Characterization of Primary and Secondary Al Alloys Injected through Vacuum Assisted HPDC and Influence of T6 Heat Treatment on Mechanical Properties

Gonçalo Crisóstomo Soares

Master Dissertation

FEUP Supervisor: Prof. Rui Jorge de Lemos Neto

INEGI Supervisor: Eng. Rui Daniel Caetano Madureira

INEGI Co-Supervisor: Eng. Rui Miguel Brás Soares

Master in Mechanical Engineering

2022-09-26

Para a minha família

Resumo

A indústria automóvel procura alternativas aos componentes estruturais em aço para minimizar o peso dos veículos. Uma das alternativas é a utilização de componentes estruturais em ligas de alumínio obtidos por fundição injetada. Devido às elevadas velocidades de injeção, o metal líquido mistura-se com o ar presente no interior da cavidade moldante e juntamente com as pressões elevadas utilizadas durante a fase de compactação formam-se porosidades gasosas colapsadas no interior das peças. Estas porosidades são prejudiciais para a ductilidade e resistência mecânica. Além disto, caso estas peças sejam tratadas termicamente para melhorar as propriedades mecânicas, quando sujeitas a um tratamento convencional de solubilização ocorre *blistering* nas peças. Para evitar/diminuir a formação de porosidades gasosas durante a injeção é realizado vácuo durante o enchimento. Assim, o objetivo deste trabalho foi estudar as diferenças que existem em termos de defeitos e propriedades mecânicas em ligas primárias de alumínio (AlSi10MnMg e AlMg4Fe2) e ligas secundárias (AlSi12(Fe) e AlSi10Mg(Fe)) na injeção com e sem vácuo, assim como a influência do tratamento térmico T6 nas propriedades mecânicas e microestrutura.

Inicialmente, foi analisada a composição química das ligas em estudo para se confirmar se estas apresentavam valores dentro daqueles que estão normalizados. Maquinaram-se provetes das peças que serviram para a medição de densidade através do método de Arquimedes e também para a caraterização mecânica das peças. Foram analisadas peças através da tomografia computorizada para se perceber a distribuição de defeitos ao longo destas e com a ajuda de um software foi possível determinar a porosidade, número e volume de defeitos nas peças, de forma a avaliar se o vácuo durante a injeção levou ou não a uma redução das porosidades. Através da análise realizada na tomografia computorizada, foi escolhida uma secção da peça onde se verifica a existência de porosidade, para esta ser analisada com recurso à metalografia e se comparar os resultados obtidos por ambas as técnicas. Foram realizadas medições de dureza nas peças, antes e após tratamento térmico, sendo depois comparados com os valores normalizados. Realizou-se um tratamento térmico T6 (solubilização durante 2 horas a 490°C seguido de um envelhecimento artificial durante 2 horas a 170°C) para se estudar a alteração das propriedades mecânicas e microestrutura das ligas em estudo, assim como avaliar a formação de blistering nas peças cuja injeção foi realizada com assistência de vácuo.

Sem tratamento térmico, as peças que foram injetadas com vácuo apresentaram uma menor percentagem de defeitos, sendo que a redução esperada para o nível de vácuo utilizado, 200 mbar, ronda os 60%. Após o tratamento térmico, houve um aumento exponencial na quantidade de defeitos e uma diminuição da média do volume dos defeitos nas peças injetadas com assistência de vácuo devido ao aumento do número de porosidades gasosas. À exceção de uma peça, as peças injetadas com assistência de vácuo apresentaram menos *blistering*. Na análise das mesmas secções através da TAC e da metalografia os resultados foram semelhantes. Sem tratamento térmico, não existiram diferenças relevantes nas propriedades mecânicas das peças injetadas com vácuo e sem vácuo e os valores obtidos foram na sua maioria inferiores aos valores normalizados. A ductilidade das ligas primárias foi superior à das ligas secundárias por não existirem tantas agulhas da fase β-Al_5FeSi. Após o tratamento térmico, a ductilidade das ligas AlSi10Mg(Fe) e Silafont-36 aumentou entre os 21% e 119% devido à globulização do silício. A tensão de cedência e a tensão de rotura diminuíram na liga AlSi10Mg(Fe) devido ao amaciamento, porém houve um aumento destas propriedades na liga Silafont-36 devido à precipitação de intermetálicos incoerentes Mg-Si na matriz de alumínio. Assim, foi possível verificar que a utilização de vácuo não trouxe melhorias relevantes na diminuição de porosidades e na melhoria das propriedades mecânicas. A monitorização do processo de injeção foi deficiente, o que não garantiu os parâmetros de injeção ótimos, e a utilização de provetes de secção retangular maquinados de peças empenadas levou à variabilidade da área de secção, o que influenciou os resultados da caraterização mecânica.

Abstract

The automotive industry is looking for alternatives to structural steel components to minimize vehicle weight. One of the alternatives is the use of structural aluminum alloy components obtained by HPDC. Due to the high injection speeds, the liquid metal mixes with the air present inside the molding cavity and together with the high pressures used during the compaction phase, collapsed gas porosities are formed inside the parts. These porosities are detrimental to ductility and mechanical strength. In addition, if these parts are heat treated to improve mechanical properties, when subjected to a conventional solution treatment blistering occurs in the parts. To prevent/reduce the formation of gas porosities during injection, vacuum is performed during filling. Thus, the objective of this work was to study the differences that existed in terms of defects and mechanical properties in primary alloys (AlSi10MnMg and AlMg4Fe2) and secondary alloys (AlSi12(Fe) and AlSi10Mg(Fe)) when injection was performed with and without vacuum and the influence of T6 heat treatment on mechanical properties and microstructure.

Initially, the chemical composition of the alloys under study was analyzed to confirm if they presented values within those that were standardized. Specimens were machined from the parts to be used for density measurement using the Archimedes method and also for the mechanical characterization of the parts. These were analyzed through computed tomography to understand the distribution of defects along them and with the help of myVGL software it was possible to determine porosity, number and volume of defects in the parts to understand whether or not the vacuum during injection led to a reduction of porosity. Using the CT scan analysis, a section of the part was chosen to be analyzed using metallography to try to understand if the results obtained were similar to those obtained in the CT scan. Hardness measurements were made on the parts to compare with the standard values and values after heat treatment. A T6 heat treatment (solution heat treatment for 2 hours at 490°C followed by artificial aging for 2 hours at 170°C) was performed to study if exists any change in the mechanical properties and microstructure of the alloys under study and to see if there was less blistering in the parts whose injection was performed with vacuum assistance. After the heat treatment, further analyses were performed in computed tomography and metallography.

Without heat treatment, the parts that were vacuum injected showed a lower percentage of defects, with the expected reduction for the vacuum level used, 200 mbar, being around 60%. After the heat treatment, there was an exponential increase in the amount of defects and a decrease in the average defect volume in the vacuum-assisted injected parts due to the increase in the number of gas porosities. With the exception of one part, the vacuum-assisted injected parts showed less blistering. When analyzing the same sections using CT and metallography the results were similar. Without heat treatment, there were no relevant differences in the mechanical properties of the vacuum and non-vacuum assisted injected parts and the values obtained were most of them lower than the standard values. The ductility of the primary alloys was higher than that of the secondary alloys because there were not as many needles of the β-Al_5FeSi phase. After heat treatment, the ductility of AlSi10Mg(Fe) and Silafont-36 alloys increased between 21% and 119% due to the spheroidization of silicon. The yield strength and ultimate tensile strength decreased in the AlSi10Mg(Fe) alloy due to softening, but there was an increase in these properties in the Silafont-36 alloy due to the precipitation of incoherent Mg-Si intermetallics in the aluminum matrix. Thus, it was possible to verify that the use of vacuum did not bring relevant improvements in reducing porosities and improving mechanical properties. The monitoring of the injection process was poor, which did not guarantee the optimal injection parameters, and the use of rectangular specimens machined from warped parts led to variability of the cross-section area, which influenced the mechanical characterization results.

Acknowledgements

I would like to thank Professor Rui Neto, supervisor at FEUP, for all the guidance and knowledge that he transmitted to me throughout this work, being always available to help me.

To my supervisors at INEGI, Engineer Rui Madureira and Engineer Rui Soares, for all the availability, help and advice that were essential to finish this project.

To Engineer José Silva for his availability and feedback given on the dissertation.

To the unit of INEGI where I made my dissertation, UTAF, especially to the technicians José Teixeira and Armanda Marques who always showed great availability to help me and for all the patience they had with me.

To Engineer Rui Amaral and technician Tiago Santos for their help in the tensile tests.

I also acknowledge CEMUP (Materials Center of the University of Porto) for expert assistance with SEM-EDS.

A special thanks to Engineer Rui Silva for having accompanied me in the SEM-EDS sessions.

I would like to thank to LET and the DEMEC workshops for their availability and the quality of the work done.

To my friends who had a lot of patience to put up with me, not only throughout this work, but whenever they are with me. Thank you for the strength and affection that you transmitted to me to finish another stage of my life.

Last but not least, to my family, especially my parents, sisters and brothers-in-law for supporting me throughout all the stages of my life and because without them I would never have gotten where I am.

Author gratefully acknowledge the funding of Project POCI-01-0247-FEDER-039920 – SMARTINJECT: DESENVOLVIMENTO DE PEÇAS DE ELEVADO DESEMPENHO INJETADAS EM LIGAS DE ALUMÍNIO, cofinanced by Programa Operacional Competitividade e Internacionalização (COMPETE 2020), through Fundo Europeu de Desenvolvimento Regional (FEDER).

Author gratefully acknowledge the funding of Project Hi-rEV – Recuperação do Setor de Componentes Automóveis (C644864375-00000002), cofinanced by Plano de Recuperação e Resiliência (PRR), through NextGeneration EU.

Contents

Abbreviations

AA – Aluminum Association

Al – Aluminum

ANSI – American National Standards Institute

Avg - Average

Cr – Chromium

CT – Computed tomography

Cu – Copper

Fe – Iron

GP – Guinier-Preston

HPDC – High pressure die-casting

HVDC – High-vacuum die casting

IACS – International Annealed Copper Standard

INEGI – Instituto de Ciência e Inovação em Engenharia Mecânica e Engenharia Industrial

Mg – Magnesium

Mn – Manganese

PVD – Physical vapor deposition

SD – Standard deviation

Si – Silicon

Sn – Tin

SONAFI – Sociedade Nacional de Fundição Injetada

UTAF- Unidade de Tecnologias Avançadas de Fabrico

UTS – Ultimate tensile strength

VADC – Vacuum-assisted die casting

VDC – Vacuum die casting

YS – Yield strength

Zn – Zinc

List of Figures

List of Tables

1 Introduction

A brief presentation of INEGI is made. The project is introduced and the objectives of this work are presented. Finally, the outline of this dissertation is presented.

1.1 Company introduction

The dissertation was developed at INEGI, Institute of Science and Innovation in Mechanical and Industrial Engineering, in the Advanced Manufacturing Processes Unit, UTAF.

INEGI is a public utility, private, non-profit institution founded in 1986. It carries out research and technological-based innovation and consulting work with the aim of contributing to the development of industry and the economy. With the development of these projects, it intends to ensure the personal and professional development of its collaborators, as well as to enrich higher education.

It is an institution that has in its base a set of specialized units per scientific and technological area that act mainly in five areas: energy and environment; new materials and structural solutions; advanced production technologies; product and systems development; biomechanics.

The growth, the conversion of knowledge into value and the maintenance of the institutional identity as a partner of companies are pillars that are part of INEGI's vision for the future.

1.2 Project presentation

This project was developed through a partnership between INEGI and SONAFI. The second one is a company that produces aluminum alloy components for internal combustion engines by high-pressure die casting for the automotive sector. However, with the increase in electric mobility, the manufacture of components for cars with internal combustion engines will have a decreasing trend. In addition, more and more automotive companies are seeking to improve the energy efficiency of vehicles by reducing vehicle weight, and therefore aluminum is replacing steel in the production of structural components. Thus, SONAFI is increasingly sought to manufacture components with higher technical requirements, mainly mechanical strength and ductility. However, the injection process and the aluminum alloys that are currently used by SONAFI do not meet the desired mechanical properties demanded by the customers.

Due to the high speeds used during the injection process there is a mixture of air with the liquid metal, which combined with the high compression pressures used, results in the appearance of collapsed gas porosities in the parts. This type of defect affects the mechanical properties obtained such as yield strength, ultimate tensile strength, and elongation. In addition, it turns out impossible to improve these properties. As conventional solution heat treatments are used, - with stages of 4 to 6 hours at temperatures of approximately 540°C – the result can be what literature refers to as blistering. This phenomenon occurs due to the increase in

temperature that leads to a decrease in the yield strength of the material and an increase in the internal pressure of the gas porosities which causes deformation or the opening of the pores near the part's surface. Due to these gas porosities, it is impossible to obtain parts with ductility and toughness properties suitable for structural components.

To meet the customers' requirements, a study of alternative alloys (when comparing to SONAFI's alloys, AlSi10Mg(Fe) and AlSi12(Fe)) will be performed. Secondary alloys are the most common. These alloys have a low cost and due to the presence of iron, which acts as a release agent, helps to extend the life of the molds. However, due to the high iron content, the ductility obtained for components in this type of alloys does not meet the requirements needed for these parts to be used in structural components. To obtain better mechanical properties, especially ductility and toughness, primary Al-Si-Mg alloys characterized by low iron content (0.2 wt.%) and primary Al-Mg alloys, which despite their lower castability, generally do not need to be heat treated, will be studied. To complement the study of these alloys, heat treatments that can guarantee the improvement of mechanical properties will be studied with the purpose of applying the produced parts in structural components.

To analyze the feasibility of using the new alloys and heat treatments for structural parts, specimens taken from parts obtained by vacuum and conventional high-pressure die casting will be studied. These include two secondary alloys used in SONAFI, AlSi10Mg(Fe) and AlSi12(Fe), a primary alloy AlSi10MnMg (Silafont-36) and a new generation alloy AlMg4Fe2 (Castaduct-42). Mechanical characterization and microstructural analysis of the specimens before and after the heat treatment will be carried out in order to study the influence of the parameters of the heat treatment process on the microstructure and mechanical properties of the components.

1.3 Objectives

The aim of this project is to study the application of heat treatments and/or introduction of primary and new generation alloys in parts obtained by vacuum and conventional high-pressure die casting. In the end, it is intended to provide SONAFI the ability to produce components with high technical demands that allow meeting the requirements imposed by current customers, but also allow entry into other markets, such as the production of structural components in aluminum alloys.

1.4 Outline

This document is divided into five chapters:

- Chapter 1 – A presentation of the company and the project that will be developed in this dissertation is made. The objectives of this work are presented.
- Chapter 2 – This chapter presents the literature review of aluminum alloys used in casting and structural components, the differences between high-pressure die casting and vacuum high-pressure die casting processes, and the main considerations to have during the high-pressure die casting process.
- Chapter 3 – This chapter presents the experimental procedures and the equipment used for the different analyses and tests performed.
- Chapter 4 – In this chapter the results obtained are presented and analyzed.
- Chapter 5 – The main conclusions of this work and future work are presented.

2 Literature review

In this chapter the literature review of the concepts that will be used throughout this work is done. The families of alloys most common in die casting, the main requirements that an alloy should have to be used in structural components and the aluminum alloys that are currently used in structural components are presented and, at the end, the distinction between HPDC, VADC and HVDC and the main precautions to be taken during the high-pressure die casting process are made.

2.1 The importance of aluminum alloys in the mobility of the future

With the emergence of new energy efficiency policies with more and more restrictions on pollution levels and waste of resources and also with the prediction that the technological development of the automotive industry in the future will focus on the following pillars: improved efficiency of internal combustion engines, electrification/energy storage and structures, powertrains and power electronics with as little weight as possible, this type of industry seeks solutions that meet those requirements [1]. One of the main solutions is the use of aluminum alloys, whose consumption has been growing year by year in this industry (Figure 1) [1-4].

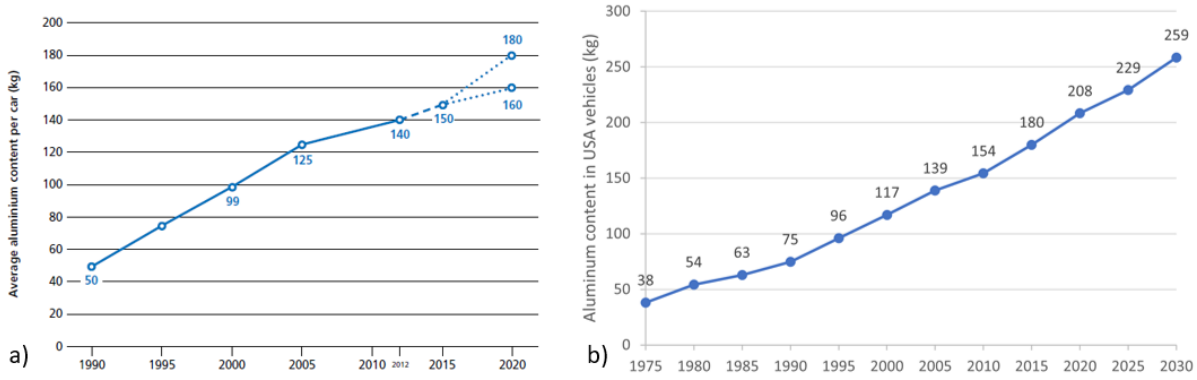

Figure 1: Amount of aluminum used in cars: a) average weight of aluminum used in each European car and b) aluminum content in each USA vehicle. Adapted from [2, 3].

The increase of the aluminum alloys consumption over the years can be justified by the excellent properties: low density, good corrosion resistance, relatively easy to recycle, good thermal conductivity, high strength stiffness to weight ratio and good formability and castability [1, 5, 6].

The industry seeks to develop lightweight designs, while using these types of alloys. This allows to reduce the material amount per part, as well as optimizing the construction, accordingly to the material strength [1]. Thus, the implementation of this type of design in the automotive industry aims to reduce the weight of vehicles, with the consequent optimization of fuel consumption and reduction of emissions of pollutants, as well as improved performance [1, 4, 5]. For vehicles with internal combustion engines, a 100 kg reduction in vehicle weight corresponds to a fuel reduction of between 0.3 and 0.5 l/100 km, and therefore a reduction of 8 to 11 g of CO_2/km [1].

The development of lightweight design for electric vehicles is of even greater or equal importance to that of vehicles with internal combustion engines. This is because more and more automotive manufacturers are presenting fully electrified models, with at least more than 100 new models expected by 2024, causing sales of electric passenger vehicles to increase 30 to 35% by 2030 [7]. Lightweighting will continue to be a focus of the automotive industry, because as electric vehicles are approximately 125% heavier than their equivalents with internal combustion engines, weight reduction is/will be a serious concern, in order to increase the range

of the vehicle on a full charge. In the case of electric vehicles, a weight reduction of roughly 10% corresponds to an increase in autonomy of nearly 13.7%. In addition to the importance that weight reduction has in increasing the range of the vehicle, it also has an impact on the cost of electric vehicles. With this, there is an opportunity to reduce the battery size and drivetrain components while still maintaining the range [1].

The lightweight design is important for the development of the circular economy in the industry. The circular economy is an opportunity for a more productive use of materials by recirculating them through reuse and recycling, thus reducing waste in production and increasing the lifetime of products. The use of aluminum is advantageous because more than 90% of its content in a car is recycled, making it a perfect material according to the circular economy philosophy. On the other hand, producing primary aluminum requires a large amount of energy, which affects the potential energy savings during its service in the vehicle [1].

2.2 Aluminum and its alloys

2.2.1 Aluminum

Aluminum is the most abundant metal on the planet. Unlike iron or copper, it does not exist as a metal in nature due to its chemical activity and its affinity for oxygen [8].

In 1886, scientists Paul Heroult and Charles Martin Hall discovered an economically feasible way to extract aluminum from aluminum oxide via the Hall-Heroult electrolytic process. In this process, metallic aluminum is extracted from alumina by melting a mixture of alumina and cryolite followed by electrolytic reduction. In 1888, the Bayer process was patented, which consists of obtaining alumina from bauxite. In this process, caustic soda is added to the bauxite at high pressure and temperature, followed by filtration and calcination to obtain the alumina [9].

Currently, the following steps are performed to obtain primary aluminum:

- Extraction of bauxite, which contains alumina in its composition;
- Performing the Bayer process to obtain alumina from bauxite;
- Finally, aluminum production through the Hall-Heroult process.

Aluminum is one of the most used metals because of its good properties, such as durability, styling, and recyclability, which make it an ideal material for many applications [10]. Considering its low density (2.7 g/cm³) - approximately one-third that of steel - it is widely used in applications that require weight to be kept as low as possible. Its formability is highlighted, as it is a metal that can be worked in virtually all processes used today. Its low melting point is an advantage for casting, but it has poor casting characteristics [10]. When used in its pure state, it has a low mechanical strength, but after cold working its strength can double [11]. Mechanical strength and other mechanical properties can be improved with the addition of certain alloying elements, such as silicon, copper, manganese, magnesium, chromium, zinc, iron, etc [11]. It has high corrosion resistance due to the thin, invisible layer of aluminum oxide (Al_2O_3) that forms when the metal in its liquid state is exposed to the atmosphere. The electrical conductivity of pure aluminum (minimum 99%) is high, approximately 60% of IACS, and has a resistivity of $2.65x10^{-8}$ ohm.m. These two properties combined with its low density mean that an aluminum conductor can conduct the same amount of current as a copper conductor, which is roughly twice as heavy, making it a much more expensive component [12]. With a reflectivity of over 80%, high corrosion resistance and low density, it is a much sought-after material for building roofing materials [12]. Table 1 shows the physical, mechanical, and thermal properties of pure aluminum.

Table 1: Properties of pure aluminum [13].

Melting Point (°C)	660
Thermal Conductivity (W/(m.K))	236
Coefficient of Linear Expansion ($x10^{-6}$/°C)	23.5
Electrical Resistivity (Ω.m)	$2.65*10^{-8}$
Density (g/cm^3)	2.7
Modulus of Elasticity (GPa)	68
Poisson Ratio	0.34

2.2.2 Aluminum alloys

2.2.2.1 Classification

As previously stated, pure aluminum due to its low mechanical strength is used in applications where mechanical strength is not an important factor [8]. However, engineering tries to find solutions for weight reduction in various components and structures and several alloying elements were added to pure aluminum that led to improved mechanical properties, castability and machinability.

With more and more aluminum alloys being created and commercialized, the Aluminum Association (AA) created a designation system to distinguish and classify the aluminum alloys that exist nowadays. This system was adopted in 1954 and was approved by the American National Standards Institute (ANSI) in 1957.

Aluminum alloys can be divided into two major classes depending on how they are processed: wrought aluminum alloys and cast aluminum alloys. The wrought alloys are used in plastic forming processes and the cast alloys are suitable for casting. As these two classes of aluminum alloys are used for different applications, their chemical composition is also quite different, ductility being important for wrought alloys and fluidity important in cast alloys to improve their castability [8].

The wrought alloys are identified by a four-digit number (XXXX). The first digit is related to the main alloying element. The second digit, if it is non-zero, means that there has been a modification of the base alloy. The third and fourth digits form an arbitrary number that identifies the alloy in the series in which it is included [8]. The series that exist for wrought alloys are shown in Table 2.

Table 2: Classification for wrought aluminum alloys according to AA [8].

Alloy Series	Major Alloying Element
1xxx	99.00% minimum aluminum
2xxx	Copper
3xxx	Manganese
4xxx	Silicon
5xxx	Magnesium
6xxx	Magnesium and silicon
7xxx	Zinc
8xxx	Other element
9xxx	Unused series

Within the category of wrought alloys there is a division: heat treatable alloys and non-heat treatable alloys. The non-heat treatable alloys are those whose strength is due to the alloying elements used, such as manganese, iron, silicon, and magnesium that still have

increased strength due to strain hardening. The alloys that belong to this group are: 1xxx, 3xxx, 4xxx and the 5xxx. Heat treatable alloys increase their strength through a solution heat treatment followed by artificial or natural aging to occur precipitation hardening. The alloys included in this group are: 2xxx, some of the 4xxx, 6xxx and 7xxx series [8].

Cast alloys are identified by a three-digit number and a decimal number (XXX.X). The first digit represents the main alloying element. The second and third digits identify the alloy in the series. The decimal number identifies whether the alloy composition is for final casting (.0) or for ingot (.1 or .2). A capital letter before the number indicates a modification of the base alloy [8]. The series that exist for cast alloys are shown in Table 3.

Table 3: Classification for cast aluminum alloys according to AA [8].

Alloy Series	Major Alloying Element
1xx.x	99.00% minimum aluminum
2xx.x	Copper
3xx.x	Silicon plus copper and/or magnesium
4xx.x	Silicon
5xx.x	Magnesium
6xx.x	Unused series
7xx.x	Zinc
8xx.x	Tin
9xx.x	Other element

2.2.2.2 Metallurgical states

For the complete characterization of an aluminum alloy, its metallurgical condition must be designated. The metallurgical condition follows the alloy designation, the two being separated by a hyphen. Metallurgical conditions are represented by letters. The most common are:

- F (as fabricated): applied to products that are obtained by forming processes, where there is no special control over thermal or strain hardening conditions. There is no limit to the mechanical properties of wrought products;
- O (annealed): in the case of wrought products, annealing is done to obtain the lowest mechanical strength, while in the case of cast products, it is done to improve ductility and dimensional stability;
- H (strain-hardened): used only in wrought products. These are the products that have their strength increased through cold plastic deformation, which may or may not be heat treated to produce partial softening;
- W (solution heat treated): applied to alloys that age naturally at room temperature after solution heat treatment;
- T (thermally treated to produce stable conditions other than F, O or H): applied to products that are heat-treated, which may or may not be hardened through further plastic deformation to obtain a stable state. This metallurgical condition has a subdivision of 10 states (numbered from 1 to 10) that represent the heat treatment to which the alloy has been subjected [8]. Table 4 shows the substates of this metallurgical condition.

Table 4: Subdivisions of metallurgical condition T according to AA [8].

T1	Cooling from a high forming temperature, followed by natural aging to a substantially stable condition
T2	Cooling from high forming temperature, followed by cold working and natural aging to a substantially stable condition
T3	Solution heat treatment followed by cold working and natural aging to a substantially stable condition
T4	Solution heat treatment followed by natural aging to a substantially stable condition
T5	Cooling from a high forming temperature, followed by artificial aging
T6	Solution heat treatment followed by artificial aging
T7	Solution heat treatment followed by over ageing or stabilization
T8	Solution heat treatment followed by cold working and artificial aging
T9	Solution heat treatment followed by artificial aging and cold working
T10	Cooling from high forming temperature, followed by cold working and artificial aging

2.2.3 Major families of aluminum alloys

In this chapter the most common aluminum alloys for casting will be discussed:

- Al-Cu (2xx);
- Al-Si-Cu (3xx);
- Al-Si (4xx);
- Al-Si-Mg (3xx);
- Al-Mg (5xx);
- Al-Zn-Mg (7xx);
- Al-Sn (8xx).

2.2.3.1 Al-Cu alloys family

Al-Cu alloys are widely used in casting and forging where strength and toughness are required. They exhibit high strength and toughness both at room temperature and at higher temperatures.

The first Al-Cu alloys contained copper percentages of about 10% and thus had high strength and hardness without requiring heat treatment.

Alloys containing between 4-5% copper can have different percentages of magnesium. By performing heat treatments they are the commercial casting alloys that have the greatest ability to achieve high strength. Combined with a low level of impurities, excellent ductility can also be obtained. The combination of good strength and ductility gives excellent toughness. The use of silver, by aging, accelerates the response of the alloy and reduces the risk of stress corrosion.

This type of alloys are very difficult to cast without hot cracking and interdendritic shrinkage, so grain refinement and selective chilling must be performed.

Copper makes aluminum alloys more susceptible to corrosion and stress corrosion. On the other hand, copper improves mechanical properties at elevated temperatures, usually with the addition of nickel [14].

2.2.3.2 Al-Si-Cu alloys family

Al-Si-Cu alloys (typically AlSi9Cu3) represent a large proportion of the aluminum alloys used for casting. Copper is responsible for increased strength and machinability, while silicon improves castability and reduces hot cracking. Alloys with high concentrations of hypoeutectic silicon are advisable for more complex castings and for the die casting process. Alloys containing a copper concentration of less than 5.6% are heat treatable. The response to heat treatment can be improved with the addition of magnesium.

Hypereutectic Al-Si alloys with 12-30% Si also contain copper. The wear resistance is ensured by the primary silicon phase and the copper helps to increase the strength for high temperatures and for matrix hardening. They are used for pistons in association with nickel, magnesium or cobalt [14].

2.2.3.3 Al-Si alloys family

Al-Si binary alloys exhibit excellent fluidity, castability, corrosion resistance, low density, and low coefficient of thermal expansion. However, they exhibit low strength, poor machinability, and ductility is highly dependent on low impurity concentration and microstructure.

The strength, ductility and castability of the hypoeutectic and eutectic alloys of this family can be improved by modification of the Al-Si eutectic. The use of antimony is recommended to achieve a lamellar eutectic. In addition, higher cooling rates promote a finer unmodified microstructure of the eutectic. As for hypereutectic Al-Si alloys, proeutectic silicon phase tuning through the addition of phosphorus is essential in casting and alloy performance [14].

2.2.3.4 Al-Si-Mg alloys family

Adding small amounts of magnesium to Al-Si alloys improves castability and mechanical properties after heat treatment. In addition, the excellent corrosion resistance and low coefficient of thermal expansion are maintained. Although these alloys do not present strength values as Al-Cu and Al-Si-Cu alloys, the values obtained are considered quite acceptable. The addition of beryllium changes the morphology of the iron-containing intermetallic, improving the strength and ductility of this type of alloys. The modification of the eutectic with sodium or strontium is important to improve strength, elongation and casting process [14].

In this family of alloys, the formation of different Fe-containing intermetallic phases is common. The appearance of the most harmful phase (β-Al_5FeSi phase) is more common in secondary alloys (for example in the AlSi10Mg(Fe) alloy), because the recycled aluminum of these alloys contains several impurities, iron being one of the main ones. In the primary alloys, the iron content is reduced and manganese is added to help combat die soldering which is also beneficial for the transformation of the β-Al_5FeSi phase into the α-$Al_{15}(Fe,Mn)_3Si_2$ phase which, because it is not needle-like, does not act as much as a stress concentrator, thus improving the ductility of the alloys. Another way to suppress the β-Al_5FeSi phase is to use high cooling speeds (typical of the high-pressure die casting process) that allow the formation of the α-Al_8Fe_2Si phase. The α-Al_8Fe_2Si and α-$Al_{15}(Fe,Mn)_3Si_2$ phases are less detrimental to mechanical properties because they form as chinese-script or compact globular particles [15].

A summary table of the Fe-containing intermetallic phases and the effect they have on the ductility of the alloy is shown in Figure 2.

Fe-rich Intermetallic	Crystal Structure	Morphology	Ductility Loss
β-Al_5FeSi	Monoclinic (Platelets)	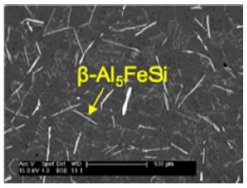	Severe
α-Al_8Fe_2Si	Hexagonal (Chinese script)	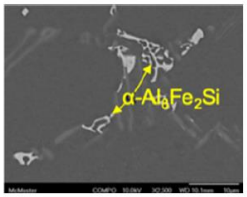	Less severe
α-$Al_{15}(Fe,Mn)_3Si_2$	Cubic (Chinese script)	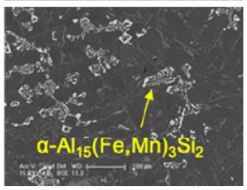	Less severe

Figure 2: Fe-containing intermetallic phases and their influence on the ductility of Al-Mg-Si alloys [4].

In the automotive industry, one of the most common choices is to use primary Al-Si-Mg alloys heat-treated to achieve the required mechanical properties. The T6 heat treatment is performed to achieve maximum strength, while the T4 or T7 heat treatments are performed when high elongation and ductility values are desired [16].

2.2.3.5 Al-Mg alloys family

Al-Mg alloys are essentially single-phase binary alloys with moderate values for strength and toughness. Due to their resistance to corrosion, these alloys can be exposed to marine environments and also due to this feature, are widely used in the food industry. In addition to good corrosion resistance they have excellent weldability, good machinability and their surface finish is very attractive after casting, machining, polishing or anodizing.

The injection of this type of alloys requires greater care and control when compared to Al-Si alloys.

During the melting state, magnesium is very reactive without a protective atmosphere, which can lead to the formation of aluminum and magnesium oxides, contaminating the bath. These slags are detrimental to the final quality of the part.

For this type of alloys, the use of heat treatments is performed to stabilize the value of some properties and not to improve them [14].

2.2.3.6 Al-Zn-Mg alloys family

Most Al-Zn-Mg alloys age naturally, reaching their maximum strength, after being left for 20 to 30 days at room temperature. However, artificial aging can also be used to accelerate the hardening process.

Since in most cases it is not necessary to perform either solution heat treatment or tempering, the cost of heat treatment, residual stresses and distortions in the parts are avoided.

Solution heat treatment may be necessary when cooling rates are high, which causes micro segregation of magnesium-zinc phases that reduce the final hardness value.

Al-Zn-Mg alloys are not suitable for casting because they are prone to hot cracking and high shrinkage during solidification [14].

2.2.3.7 Al-Sn alloys family

Tin is one of the most widely used alloying elements for bearing applications. Aluminum alloys with 5-7% tin are used in bearings and bushings where low friction, compressive, fatigue and corrosion resistance are required. The addition of copper, nickel and magnesium contributes to increased hardness and strength, while the addition of silicon improves castability, reduces hot shortness and increases compressive strength [14].

2.2.4 Alloying elements

The alloying elements play a very important role. They influence the mechanical properties of alloys, but also influence the characteristics that determine the good production of components made with a particular alloy. This chapter will describe the function and importance that the main alloying elements have in aluminum alloys, although these can change depending on the amount of elements present in the alloy and the interaction that a given element has with other alloying elements.

2.2.4.1 Copper

Copper increases strength and hardness in both cast and heat-treated alloy conditions. Alloys containing 4-5.5% copper respond better to heat treatments and their castability has a relative improvement. On the other hand, it generally reduces corrosion resistance, reduces hot cracking resistance, and increases interdendritic shrinkage [14, 17, 18].

2.2.4.2 Iron

High iron values impair ductility and increase the tendency for porosity formation. On the other hand, iron improves hot cracking resistance and acts as a release agent extending the life of dies [17, 18]. The critical iron value (in wt%) can be calculated using the following equation [19]:

$$Fe_{crit} \approx 0.075 * (wt\%\ Si) - 0.05 \quad (1)$$

The most common iron bath penetration mechanisms are:

- aluminum in the liquid state reacts with the iron present in the unprotected steel tools and/or furnace equipment;
- the addition of contaminated alloying elements or scrap containing high percentages of iron to the bath [19].

Since the solubility of iron is very low in pure aluminum and its alloys in the solid state, it combines with other elements to form different types of intermetallic phases. When silicon is not present, the Al_3Fe and Al_6Fe phases are formed, but when it is present, the most common phases are α-Al_8Fe_2Si and β-Al_5FeSi. When Si and Mg are present, the phase π-$Al_8FeMg_3Si_6$ can be formed, whereas if Si and Mn are present, the phase formed will be α-$Al_{15}(Fe,Mn)_3Si_2$. When Mn is present, the latter phase tends to form instead of the α-Al_8Fe_2Si phase. Together with manganese, chromium and other elements, iron forms sludging phases [14, 18, 19].

The α-phases (Figure 3) resemble the shape of a chinese script, but the α-$Al_{15}(Fe,Mn)_3Si_2$ phase may have the shape of a compact block, and sometimes the shape of polyhedral crystals. The π phase (Figure 3) may appear in the form of a chinese script, or it may appear attached to

the β phase through a peritectic reaction, thus forming a distinct platelet morphology. The different morphologies of these intermetallic phases have different impacts on the castability and mechanical properties of the alloys. The morphology most detrimental to ductility is that of the β-Al_5FeSi phase (Figure 3), because due to its needle-like shape, micro-cracks tend to initiate in these particles [19].

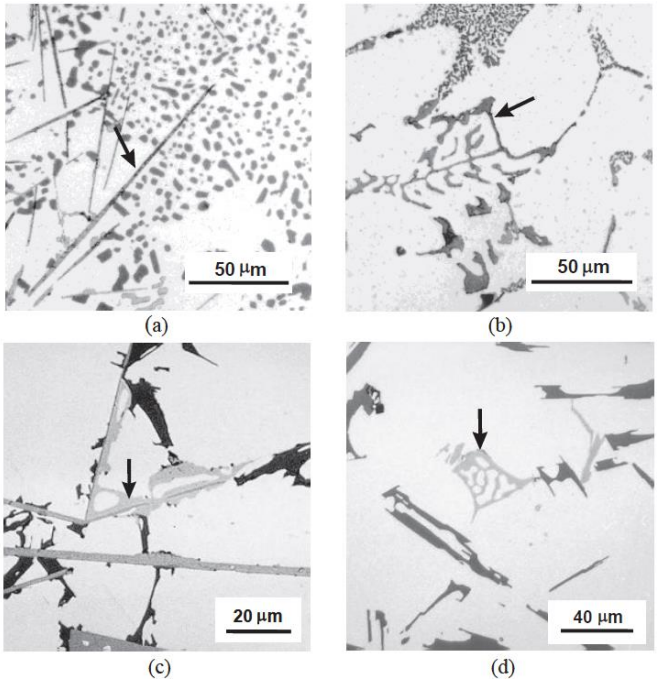

Figure 3: Typical morphologies of Fe-containing intermetallic phases: a) β-Al_5FeSi needles; b) script morphology α-Al_8Fe_2Si phase; c) π-$Al_8FeMg_3Si_6$ phase growing from β phase; d) script morphology π-$Al_8FeMg_3Si_6$ phase [19].

The α and β phases for solution temperatures up to approximately 540°C do not undergo any phase transformation changes [19].

2.2.4.3 Magnesium

Magnesium is the element that serves as the basis for increased strength and hardness in heat-treated Al-Si alloys [17, 18]. High-strength Al-Si alloys have percentages of magnesium between 0.070 and 0.40%. The phase that causes the hardening of Al-Si alloys is Mg_2Si which has a solubility limit of 0.70% Mg, above this value no further hardening occurs [14].

Al-Mg binary alloys are used in applications that require a bright surface finish, good corrosion resistance and a good combination of strength and ductility. These alloys have a Mg concentration between 4 and 10%, and above 7% Mg these alloys can be heat treated [14, 17].

2.2.4.4 Manganese

In the case of casting alloys, it has been proven that a high-volume fraction of $MnAl_6$ in alloys with more than 0.5% Mn can be a positive influence on the internal soundness. By being able to consider iron and manganese isomorphic elements, can favor the appearance of an intermetallic compound with a morphology like a Chinese script (α- Al(Fe,Mn)Si phase) that is not detrimental for the mechanical properties or the machinability of the alloy [10, 14, 17, 18]. Higher manganese values help minimize die soldering [18, 20, 21]. The main issue with Mn additions is the sludge formation at lower temperatures. The Equation (2) is used to determine the sludge factor (SF) [21]:

$$SF = (1 * wt\%Fe) + (2 * wt\%Mn) + (3 * wt\%Cr) \quad (2)$$

If SF>1.4 there is sludge formation in the holding furnace at 620°C and if SF is bigger than 2.0 it leads to sludge formation at 660°C [21].

2.2.4.5 Nickel

Nickel is usually used with copper to improve the properties of the alloy at higher temperatures [17]. In addition, it reduces the thermal expansion coefficient [14].

2.2.4.6 Phosphorus

In hypereutectic Al-Si alloys, phosphorus is used as a primary silicon refiner [17]. In hypoeutectic Al-Si alloys, phosphorus coarsens the eutectic structure and impairs the effectiveness of the most common eutectics modifiers, sodium and strontium [14].

2.2.4.7 Silicon

The main function of silicon in aluminum alloys is to improve the most important properties for casting. Silicon contributes to improved fluidity, hot cracking resistance, reducing solidification shrinkage and improving feeding characteristics. There are hypoeutectic, eutectic and hypereutectic aluminum alloys with silicon, Figure 4 [10, 14, 17, 18].

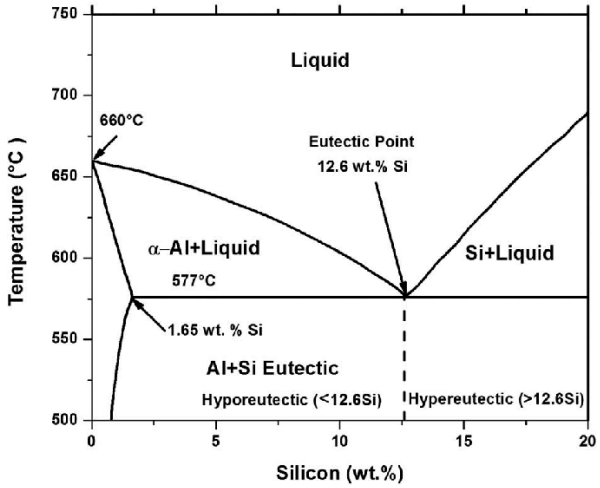

Figure 4: Al-Si phase equilibrium diagram [22].

It is recommended to use 8 to 12% silicon in Al-Si alloys used in die casting based on the relationship that exists between the cooling rate and fluidity and the effect of the percentage of eutectic in the feed as solidification progresses [14]. For percentages above 12.5% of Si, there is an increasing in the strength and hardness, but, on the other hand, the ductility and machinability decrease [10].

As stated earlier, the combination of silicon and magnesium forms the hardening phase, Mg_2Si, which enhances strength and facilitates the response to heat treatment. On the other hand, it combines with iron and other elements to form complex insoluble phases [14]. Without magnesium and copper, Al-Si alloys are not adequate for heat treatment [10].

2.2.4.8 Chromium

For certain alloys, the addition of chromium improves corrosion resistance and increases sensitivity to tempering [14].

In Al-Si alloys it modifies the morphology of the AlFeSi intermetallic phases and may form sludge containing iron, manganese, and chromium [14, 17].

2.2.4.9 Sodium

Sodium modifies the Al-Si eutectic [17]. The interaction of sodium with phosphorus causes its efficiency in eutectic modification to be reduced and also causes the effectiveness of phosphorus in refining the primary silicon phase to decrease. In contrast to other Al-Si eutectic modifiers, sodium shows high efficiency under all solidification conditions. Al-Mg alloys with less than 0.005% sodium lose their ductility and become brittle [14].

2.2.4.10 Strontium

At very low concentrations of strontium, it modifies the size and shape of the eutectic silicon particles, improving the ductility of the alloy [10, 17, 18, 20]. High strontium concentrations cause porosity and impair degassing efficiency [14, 21]. Finally, it improves resistance to die soldering [18, 21].

2.2.4.11 Zinc

Although zinc by itself brings no benefit to aluminum alloy casting, when used with copper and/or magnesium it results in compositions that are attractive for heat treatment or natural aging [14, 17].

2.2.4.12 Titanium

Titanium is widely used to refine the primary aluminum solid solution grains in the aluminum alloys microstructure [14, 17, 18, 21].

2.2.5 Alloys under study

2.2.5.1 AlSi12(Fe)

It is a binary alloy of the Al-Si family. As can be seen from the equilibrium diagram in Figure 4, its composition is very close to the eutectic composition, which guarantees excellent castability to this alloy. However, it is typical that this family of alloys contains eutectic silicon in acicular shape. This impairs the mechanical properties, and that being a secondary alloy it contains percentages of iron in its composition that lead to the appearance of the needle shaped β-AlFeSi phase, which affects the ductility of the alloys. These detrimental effects can be mitigated with the addition of small amounts of strontium or sodium that make the eutectic silicon thinner with a structure close to globular and with the addition of manganese that transforms the β-AlFeSi phase into the α-Al(Fe,Mn)Si phase which is less detrimental to the mechanical properties [23, 24].

The mechanical properties and chemical composition of the AlSi12(Fe) alloy, based on NP EN 1706 2000 standard, are shown in Table 5.

Table 5: Mechanical properties and chemical composition in the ingot (weight in %) of AlSi12(Fe) [25].

Mechanical Properties						
Yield strength (MPa)		Ultimate tensile strength (MPa)		Elongation (%)		
>130		>240		>1		
Chemical composition						
Si	Fe	Cu	Mn	Zn	Ti	Al
10.5-13.5	<1	<0.1	<0.55	<0.15	<0.15	Bal.

2.2.5.2 AlSi10Mg(Fe)

It is a secondary alloy of the Al-Si-Mg family widely used in high-pressure die casting for the production of components with complex geometry and thin walls. Its main properties are good chemical and hot cracking resistance and excellent fluidity [26]. The mechanical properties and chemical composition of this alloy, based on NP EN 1706 2000 standard, are shown in Table 6.

Table 6: Mechanical properties and chemical composition in the ingot (weight in %) of AlSi10Mg(Fe) [25].

Mechanical Properties										
Yield strength (MPa)			Ultimate tensile strength (MPa)			Elongation (%)				
>140			>240			>1				
Chemical composition										
Si	Fe	Cu	Mn	Mg	Ni	Zn	Ti	Sn	Pb	Al
9-11	<1	<0.1	<0.55	0.2-0.5	<0.15	<0.15	<0.2	<0.05	<0.15	Bal.

Because it has an iron content of approximately 1%, there is a tendency to form the needle-like β-AlFeSi phase (as was the case for the AlSi12(Fe) alloy) which is detrimental to the mechanical properties.

2.2.5.3 Silafont-36 (AlSi10MnMg)

Rheinfelden's Silafont series features alloys with excellent fluidity and with the addition of sodium or strontium it is possible to improve mechanical properties. It is used for the production of complex components where tight requirements must be met.

The alloy of this series that will be studied in this work is Silafont-36 (AlSi10MnMg). This alloy belongs to the group of primary aluminum alloys and exhibits excellent castability, has high corrosion resistance, high fatigue resistance, excellent weldability and machinability, and can be heat treated to achieve higher elongation and ductility values [20].

With this alloy it is possible to improve some of the processing properties over the secondary AlSi10Mg(Fe) alloy, considered a standard alloy for the high-pressure die casting process. With Silafont-36, the improvement of mechanical properties after heat treatment is superior and the joining potential is also superior, which is an important feature in the automotive industry. Table 7 compares some of the processing properties for AlSi10MnMg and AlSi10Mg(Fe) alloys.

Table 7: Processing properties of Silafont-36 and AlSi10Mg(Fe) [20].

	AlSi10MnMg	**AlSi10Mg(Fe)**
Improvement of properties after heat treatment	Very good	Good
Hot crack tendency	Low	Low
Sticking tendency	Low	Low
Joining potential	High	Medium
Mold working time	> 80%	> 80%
Linear shrinkage	0.4 – 0.6%	0.4 – 0.6%

The chemical composition and mechanical properties of Silafont-36 are shown in the following table:

Table 8: Mechanical properties and chemical composition in the ingot (weight in %) of AlSi10MnMg [20].

Mechanical Properties								
Yield strength (MPa)			Ultimate tensile strength (MPa)			Elongation (%)		
120-150			250-290			5-11		
Chemical composition								
Si	Fe	Cu	Mn	Mg	Zn	Ti	Sr	P
9.5-11.5	<0.15	<0.03	0.5-0.8	0.1-0.5	<0.07	0.04-0.15	0.010-0.025	0.001

The magnesium quantity that is present in this alloy has a relatively large variation range when compared to the other alloying elements, because this value is adjusted according to the type of application. The variation of the magnesium percentage affects the ductility and strength values. Rheinfelden has defined five ranges for the amount of magnesium depending on the type of application:

- For components that will be exposed to crash and flanging technology, the magnesium should range between 0.13 and 0.19%;
- For rigid components and accident safety related components exposed to fatigue loads, the magnesium should range between 0.18 and 0.28%;
- For components requiring high resistance against impact stress, the magnesium should range between 0.24 and 0.35%;
- For heat treated components with air quenching after solution heat treatment, the magnesium should range between 0.28 and 0.35%;
- For components where maximum strength is most important after injection or after O, T4 or T6, the magnesium should vary between 0.35 and 0.45% [20].

Thus, for components in the as-cast condition an increase in the magnesium percentage causes an increase in yield strength and ultimate tensile strength, but on the other hand causes a decrease in elongation. Magnesium values higher than 0.5% do not increase the yield strength value, because this excess of magnesium does not influence the hardening of the solid aluminum solution.

Small percentages of strontium are used to modify the aluminum-silicon eutectic. It makes the eutectic thinner (Figure 5) which leads to an increase in elongation from 5 to 10% in the as-cast condition and helps in the spheroidization of the silicon during heat treatments.

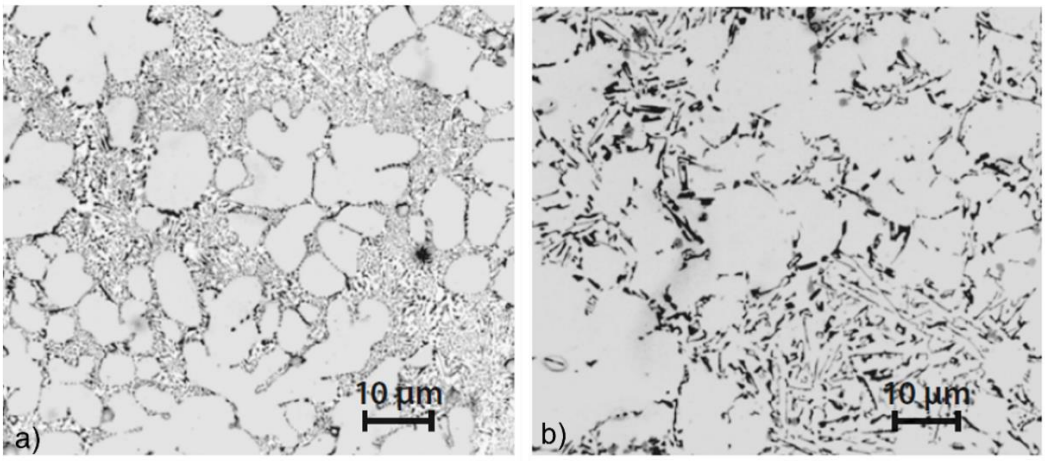

Figure 5: a) AlSi10MnMg with strontium; b) AlSi10MnMg without strontium. Adapted from [20].

Due to the low iron percentage, it is possible to decrease the amount of the AlFeSi phases that are detrimental to the ductility and strength of the parts. These needle-like phases are

typically where cracking starts when components are subjected to deformation or dynamic loading. In contrast, iron is an essential element to facilitate the demolding of the parts after injection.

As in this alloy it was tried to keep the percentage of iron as low as possible, it was necessary to find a solution to avoid die soldering. To do this, the percentage of manganese was increased, which has the same function as iron when it comes to die soldering. However, unlike iron, manganese is not so detrimental to the ductility of the parts, because the precipitates that occur during solidification are globulitic and not acicular. In the tests performed in F and T6 conditions, the yield and ultimate tensile strength are practically constant for a manganese value above 0.4%, but for manganese values below this value, the yield and ultimate tensile strength decrease due to the adhesion of the parts to the mold, which causes surface cracks and consequently deteriorates the mechanical properties. Regarding the elongation, typical values are also low when there is no manganese due to the tendency for die soldering. The elongation is maximum for manganese values between 0.4 and 0.5% for components in the F condition and between 0.2 and 0.25% for components after T6 treatment. This value decreases when a higher percentage (than those mentioned above) of manganese is present. For the same percentage of manganese, the elongation is higher after T6 treatment, because during solution heat treatment, the manganese intermetallic phases assume a globulitic form, which improves ductility [20].

2.2.5.4 Castaduct-42 (AlMg4Fe2)

Castaduct-42 (AlMg4Fe2) belongs to the AlMgFe family of alloys and is characterized by having high elongation in the as-cast condition, as well as a yield strength value similar to Silafont-36, but this one need to undergo a two-stage T7 heat treatment. Due to its high ductility, it is used for the production of large and thin-walled structural components. However, these alloys have low fluidity, which makes it difficult to fill thin parts.

Because it is a natural-harded alloy it does not need to be heat treated, as there are no structural hardening elements. This leads to lower production costs and prevents possible warping of the components produced.

The chemical composition and mechanical properties of Castaduct-42 is shown in the following table:

Table 9: Mechanical properties and chemical composition in the ingot (weight in %) of AlMg4Fe2 [27].

Mechanical Properties						
Yield strength (MPa)		Ultimate tensile strength (MPa)		Elongation (%)		
120-150		240-280		10-22		
Chemical composition						
Si	Fe	Cu	Mn	Mg	Zn	Ti
<0.2	1.5-1.7	<0.2	<0.15	4.0-4.6	<0.3	<0.2

It is the only alloy under study where silicon is not an alloying element, and so in this case, even though there is a high percentage of magnesium there will be no structural hardening caused by the Mg_2Si phase.

The amount of magnesium determines the mechanical strength that will be obtained. Higher percentages lead to increased yield strength, but, on the other hand, reduce elongation. Magnesium is always dissolved in the alpha aluminum phase.

Due to the high percentage of magnesium there tends to be an increase in dross formation when the bath is being held in the furnace for a long time at a relatively high temperature.

Oxidation inhibitors need to be added to the bath to make the oxide skin denser, reducing the oxidation of magnesium on the surface of the bath.

The percentage of iron must be kept between the values shown in Table 9, otherwise large and plate-like Fe-containing phases will form which will reduce ductility. Unlike other structural alloys, which contain lower percentages of iron to avoid the formation of these phases, Castaduct-42, has higher values of iron in its chemical composition, allowing adhesion to the mold to be lower. This allows an increase in a mold operating life and improves the flow of liquid metal inside the mold to obtain parts with thinner walls [27].

The silicon percentage should be less than 0.2% to avoid the formation of AlFeSi needles that lead to reduced elongation. In addition to silicon, the manganese values should also be strictly controlled to avoid coarse and unfavorable solid solution phase precipitations [27].

Calcium and sodium are detrimental to the hot cracking tendency and the elongation at break, so the melting fluxes used should be specific to AlMg alloys.

A stress-strain curve for this alloy is shown in Figure 6. In the plastic deformation zone, a typical behavior of this alloy is evidenced with the appearance of small peaks. These peaks correspond to strain aging. This Portevin-Chatellier effect is due to an interaction between dissolved atoms and microstructural displacements that cause stress drops over a short period of time in the stress-strain curve [27].

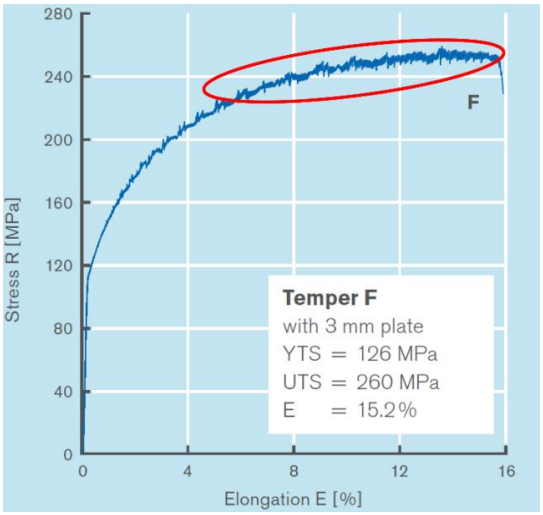

Figure 6: Stress-strain curve of Castaduct-42 with emphasis on the area where the Portevin-Chatellier effect is visible. Adapted from [27].

2.2.6 Aluminum alloys for structural applications

Structural die casting components usually have complex geometries, large dimensions and thin wall thicknesses (2-3 mm), so the alloys used must have good castability. These types of components are used in car body structure (shock towers, A or B pillars, cross members, engine cradles or inner door panels), but are also used in marine applications, motorcycle or recreational vehicle structures [21].

Structural die casting components must meet the following requirements:

- According to Casarotto et al. [16], the chassis components need to have a yield strength above 120 MPa and an elongation above 10%;
- Preferably, they should not require heat treatment;
- Must have good weldability and rivetability;
- Have high fatigue strength and high energy absorption capacity;
- Have high corrosion resistance [21].

Aluminum alloys for structural applications need to have high strength, toughness and ductility. This type of alloys is increasingly sought after by the automotive industry to replace the use of sheet steel in components such as shock tower, A or B pillars, subframes and large castings used in electric vehicles. With the exception of Castaduct-42 all structural aluminum alloys (Table 10) have low iron contents in their chemical composition to prevent the formation of phases that are adverse to ductility. However, the low iron content causes the appearance of the die soldering phenomenon that can be mitigated with the use of small amounts of manganese [4].

Table 10: Chemical composition of structural die cast aluminum alloys adapted from [4, 20, 27, 28].

Alloy	**Chemical composition** (in %wt)						
	Mg	Si	Fe	Mn	Ti	Cu	Sr
Castasil 37	<0.06	8.5-10.5	<0.15	0.35-0.6	<0.15	<0.05	0.006-0.025
Magsimal 59	5.0-6.0	1.8-2.6	<0.2	0.5-0.8	<0.2	<0.03	-
Magsimal-plus	6.0-6.4	2.1-2.6	<0.15	0.5-0.8	<0.05	<0.05	-
Aural 2	0.27-0.33	9.5-11.5	0.15-0.2	0.45-0.55	<0.08	<0.03	0.01-0.16
Aural 3	0.4-0.6	9.5-11.5	0.15-0.2	0.45-0.55	<0.08	<0.03	0.01-0.16
Aural 4	0.4-0.5	4.0-4.5	0.15-0.2	0.45-0.8	<0.08	<0.03	0.004-0.007
Aural 5	0.1-0.6	6.5-9.5	0.15-0.2	0.3-0.6	<0.08	<0.03	0.03
Mercalloy A368	0.1-0.3	8.5-9.5	<0.25	0.25-0.35	<0.2	<0.25	0.05-0.07
Mercalloy A367	0.3-0.5	8.5-9.5	<0.25	0.25-0.35	<0.2	<0.25	0.05-0.07
Mercalloy A362	0.5-0.7	10.5-11.5	<0.4	0.25-0.35	<0.2	<0.2	0.05-0.07
Alcoa EZCast 370	0.15-0.8	6.0-9.0	<0.2	0.1-0.8	<0.2	-	<0.025
Alcoa EZCast-NHT A152	3.0	n/a	n/a	n/a	n/a	n/a	n/a

Table 11: Tensile properties of structural die cast aluminum alloys adapted from [4, 20, 27, 28].

Alloy	**Tensile properties**			
	Condition	YS (MPa)	UTS (MPa)	Elongation (%)
Silafont 36	T5	155–245	275–340	4-9
	T6	210–280	290–340	7–12
Castasil 37	F	120–150	230–300	10–14
Magsimal 59	F	160–220	310–340	11–22
Magsimal-plus	F	200-220	340-360	9-12
	T5	230–250	350–380	8-12
Aural 2	F	140	310	~8.6
	T5	189–230	303–339	8–9
Aural 3	F	130–160	250–310	4–8
	T5	190–240	300–340	4–6.5
Aural 4	F	103	219	17
	T5	112	221	16
	T6	170–235	260–300	9–17
Aural 5	F	125–145	245–265	9–12
	T5	120–160	190–260	6–12
Mercalloy A368	F	125–140	260–275	10–12
	T6	185–200	280–295	14–16
Mercalloy A367	F	112-131	260-275	6-9
	T5	170–205	295–310	5–8
	T6	225–250	295–320	7.5–10.5
Mercalloy A362	F	125–140	260–275	9–11
	T6	230–250	295–315	14–16
Alcoa EZCast 370	F	105-140	250-280	7.5-13
	T5	150-220	245-310	5.5-10
	T6	135-250	195-300	7-16
Alcoa EZCast-NHT A152	F	142–150	267–283	14–17

Most of the alloys in Table 10 and Table 11 belong to the Al-Si family due to the excellent castability that these alloys have, while others belong to the Al-Mg family, which are alloys that do not require heat treatment, but are more aggressive to the molds and their castability is not so good [4].

For the Al-Si alloys in F condition it is possible to have a minimum elongation of 5%, but with low strength. Magnesium is added to these alloys to form precipitates after the T5 or T6 heat treatments that increase the strength of the alloy [4].

In Al-Mg alloys, since it is not necessary to perform heat treatments, there is a reduction in costs and warping of components is prevented. Alloys such as Castaduct-42 and Alcoa EZCast-NHT A152 have been a focus of the automotive industry for the production of injected structural components [4].

Recently new aluminum alloys have been developed for structural applications such as TensAl (AlSi3Mg0.5Cr0.15) [29], A345 (AlSi5Mg0.5Cr0.25) [30] and A379 (AlSi7Mg0.5Cr0.2) [31], which can be used in the processes of counter pressure casting, squeeze casting and high-pressure die casting, respectively. The three alloys have silicon, magnesium and chromium as their main alloying elements, and the difference between them lies in the variation in the chemical composition of silicon and chromium. Usually, chromium is not added to Al-Si alloys, because together with iron and manganese there is the formation

of undesirable coarse sludge particles. However, after some studies it has been proven that chromium can have beneficial effects on Al-Si alloys: it can replace iron or manganese as a release agent; chromium can act as a neutralizing element for the β-Al_5FeSi phase that is detrimental to ductility; during the solution heat treatment Cr-bearing dispersoids are formed that cause an increase hardness [4, 30].

Currently, secondary cast alloys are mostly used for non-structural applications, because they are recycled alloys with large amounts of impurities, the main one being iron, which leads to the appearance of the brittle intermetallic β-Al_5FeSi phase that is determinant for the decrease of ductility. On the other hand, since they are recycled alloys, there are great saving of energy in their production and because they have high amounts of iron (about 1.3%), there is a reduction of die soldering and an improvement in hot cracking resistance. Luo et al. [4] separate the die cast Al alloys into four generations according to the percentage of iron:

- First generation alloys contain at least 0.7 wt% iron and secondary alloys can also be included here. These alloys have a low tendency for die soldering, but due to brittle Fe-containing intermetallic phases ductility has very low values, and therefore components in these alloys are not used in structural applications;
- Second generation alloys use manganese as an iron substitute. Manganese prevents die soldering and in Al-Si alloys modifies the β-Al_5FeSi phase. The maximum secondary aluminum limit used for these alloys must be well below 10% due to Fe and Zn impurities. These alloys are used in the automotive and aerospace industries for the production of structural components;
- Third generation alloys use strontium (500 to 700 ppm) to prevent die soldering. It is possible to add a certain amount of iron, and therefore there is the possibility of using 100% secondary aluminum in the production of this type of alloys;
- According to the research carried out by Cinkilic et al. (Figure 7) there is the possibility of creating a fourth generation of alloys formed by recycled alloys. If the Fe/Mn ratio and the cooling rate are controlled it is possible to avoid the formation of the β-Al_5FeSi phase, and therefore it will be possible to use these alloys in structural applications with reduced costs and improved sustainability. In the case of the high-pressure die casting process, due to the high cooling rates, an Fe/Mn ratio of approximately 1.6 is required to obtain the metastable α-Al_8Fe_2Si and the stable α-$Al_{15}(Fe,Mn)_3Si_2$ phases. Higher cooling rates require lower manganese content to avoid the formation of β-Al_5FeSi phases [4, 15].

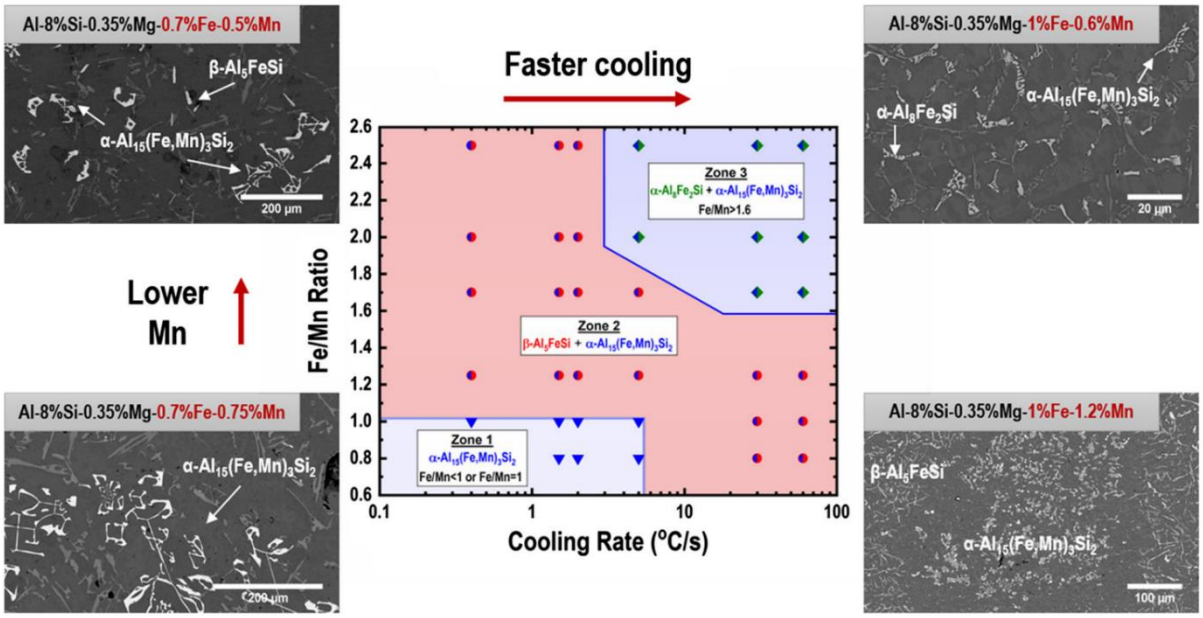

Figure 7: Graph showing the formation of different Fe-containing intermetallic phases in Al-Si-Mg casting alloys with high Fe content, depending on the variation of cooling speed and Fe/Mn ratio [15].

The future of new aluminum alloys for structural applications should involve the development of technologies that can remove impurities present in secondary alloys to bring them close to the properties of the primary alloys. The focus should be on developing alloys that do not require heat treatment to improve their strength, but at the same time have good castability to produce large and thin-walled components, especially for electric vehicles. For the case of alloys that have their strength improved through precipitation hardening, studies are being carried out to improve the results obtained by treatment T5, in order to prevent warping and residual stresses in the components typically caused by treatment T6 [4].

2.3 High-pressure die casting

2.3.1 Conventional high-pressure die casting

The HPDC process is considered the most economical and the best process for the production of large series of parts with the advantage of ensuring excellent dimensional tolerance, excellent surface finish (roughness of 1.3 µm), parts with the thinnest wall thicknesses that can be produced and parts with a competitive production cost when high production volumes are required [10, 32]. Due to its high degree of automation, it is a process that guarantees high production rates [10, 32]. About 50% of aluminum casting alloys are used in this process, and most of the components produced are used in the automotive industry [33].

The HPDC process requires alloys with superior castability and that have low tendency to hot cracking. Al-Si family alloys are the most used. Of these, the AlSi9Cu3 alloy and its variants comprise about 85% of total HPDC production. These compositions combine attractive cost with good strength, hardness, corrosion resistance, excellent fluidity, and resistance to hot cracking [14].

In this process a metal mold is used, usually machined from high quality hot working tool steels. The simplest molds consist of only two matching dies, while more complex molds contain sliding features for making holes and undercut areas. Inside the mold there are machined channels where water or oil circulates for cooling the part [14, 34].

There are two types of machines for HPDC: hot chamber machines (Figure 8) and cold chamber machines (Figure 9) [14, 35, 36]. In hot chamber machines, the shot chamber and

plunger are in contact with the liquid metal. This type of machine is used for the production of components made of magnesium and zinc alloys, which are alloys with a lower melting point, and that do not chemically attack the steel of the injection machine components. This type of machine has the advantage of having higher production rates. The injection of aluminum alloy parts is performed in cold chamber machines, where in each cycle the shot chamber is filled, thus not having a long contact between the aluminum in its liquid state and the injection machine components [14, 36].

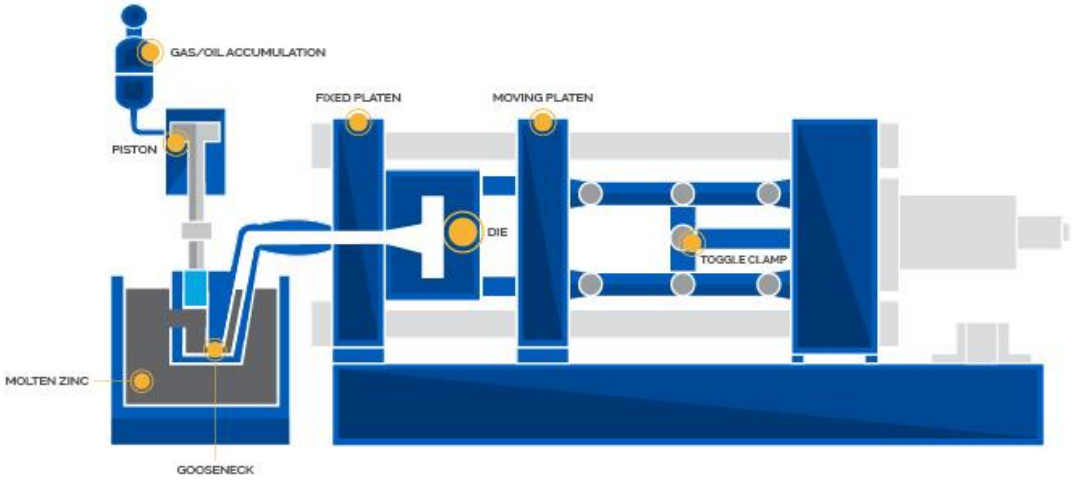

Figure 8: Schematic drawing of a hot chamber die casting machine [37].

Injection machines are characterized by their clamping forces. This defines the capability of the injection molding machine to contain the pressure generated during the injection cycle. The larger the flat area of the part to be injected and higher the injection pressure, the clamping force should be higher. Injection machines have clamping forces that typically range from 50 to 5000 tons [14, 35].

Figure 9 shows a schematic representation of a horizontal cold chamber die casting machine. The machine consists of a hollow shot sleeve (a hollow cylinder where the molten metal is deposited) with a pouring slot and a hydraulically actuated plunger. The shot sleeve is connected to an opening in the cover die half. The ejector plate and the cover die are mounted on a sturdy four-bar frame to withstand the high injection pressures. The ejector plate closes and opens against the cover die, which is activated by a hydraulic cylinder and locked in position by a toggle mechanism [10].

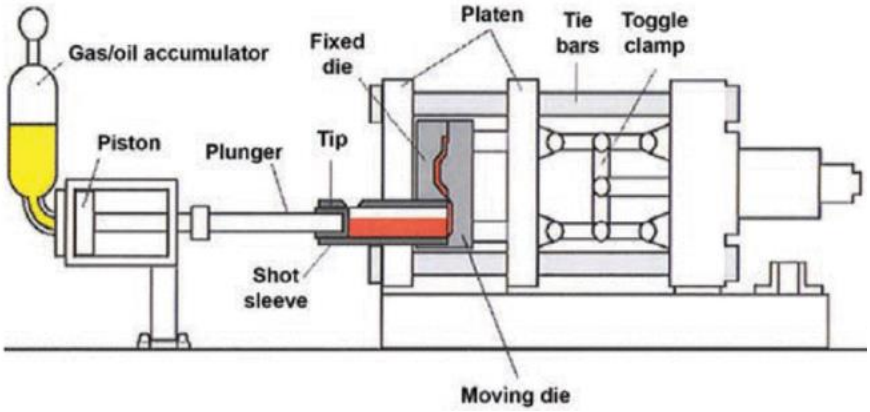

Figure 9: Schematic demonstration of the components of a horizontal cold chamber die casting machine [36].

In Figure 10 it is possible to see part of the sequence of the HPDC process. The two half dies are sprayed with a lubricant, by robot or manual application, then the mold is closed. The

cores are positioned mechanically or hydraulically. The plunger is lubricated with boron nitride to prevent friction with the sleeve. The plunger is fully retracted, and an automated pouring unit or robot pours a preset amount of liquid metal from the furnace holder into the pouring slot of the shot sleeve. The liquid metal is injected into the mold cavity [10, 36, 38].

After solidification, the moving part of the mold opens, and the ejectors are triggered. A robot grabs the part and takes it to cool in the air or in a forced air tunnel or in a cooling tank with water. Next, the part is placed in a trimming press and the gating system is cut. At the end, the part goes to the finishing section [10, 36].

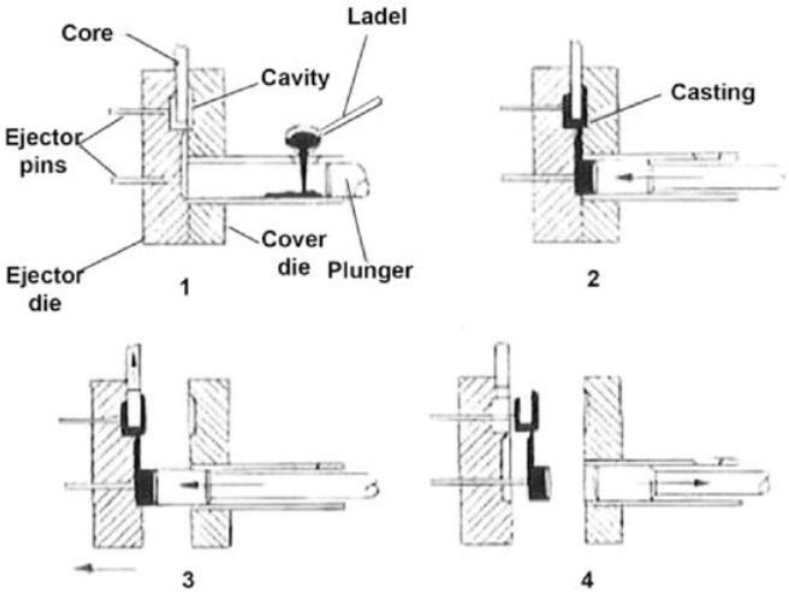

Figure 10: Sequence of the high-pressure die casting process [36].

Through the process description it is possible to list the main constituents of a die casting machine cell:

- Holding furnace;
- Injection machine;
- Mold cleaning and cooling system;
- Parts handling/extraction system;
- Cooling tank with water or forced convection tunnel;
- Trimming press [10].

In HPDC, the filling process of the molding cavity is based on three phases, Figure 11 [36].

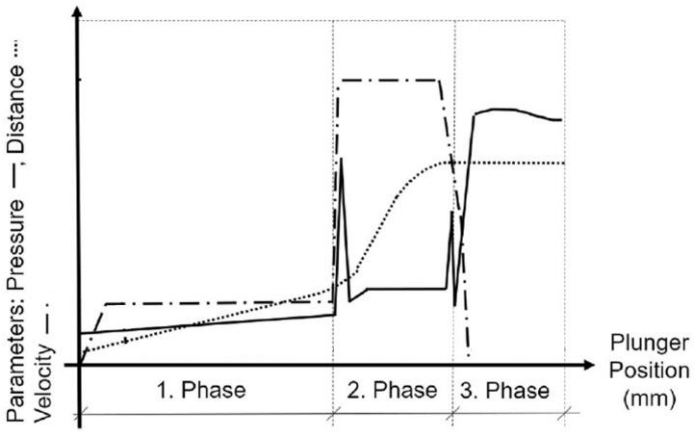

Figure 11: Phases of high-pressure die casting. Adapted from [39].

In the first phase the plunger, which is hydraulically activated, advances at very low speed inside the shot sleeve. The plunger advance in the first phase can be divided into two phases with different speeds: pour hole close speed and the speed used to fill the shot sleeve. The plunger advances at approximately 0.25 m/s from the moment the ladle mechanism finishes the pour. This movement must be performed as smoothly as possible to prevent the metal from splashing out of the shot sleeve. This first plunger speed ends when the pour hole is closed. The second part of the plunger movement (approximately 0.4 m/s) must be performed at constant acceleration (Figure 12) with adequate ventilation, once too slow or too fast velocities promote trapped gas (Figure 13). At this stage the metal advances to just before the workpiece gates [36].

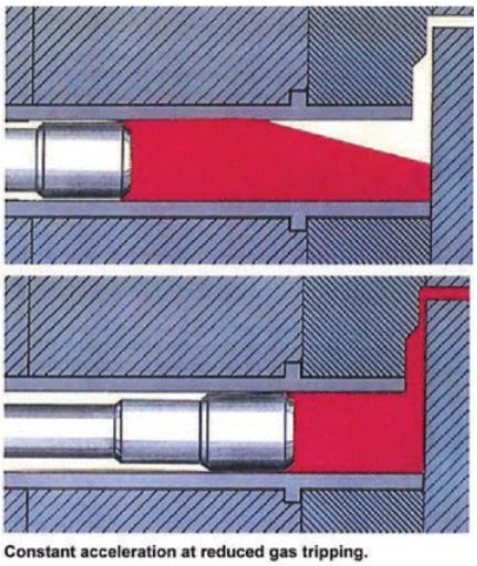

Figure 12: Reduction of trapped gas due to constant acceleration [36].

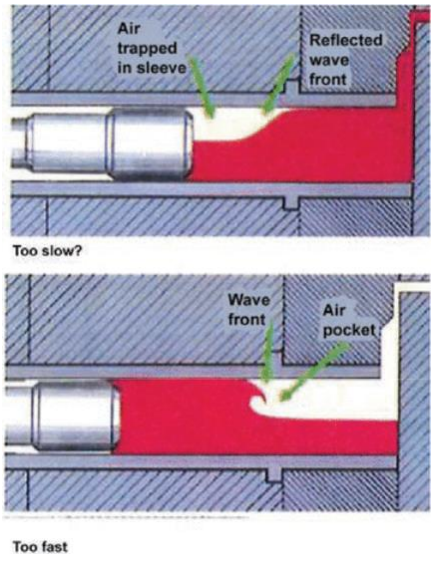

Figure 13: Trapped gas during the 1st phase. Adapted from [36].

In the second phase, the piston advances at high speeds (approximately 10 m/s), but due to the small cross-section of the gates, speeds of 60 m/s can be reached in the gates, which is much higher than the speed of transition from laminar to turbulent in aluminum alloys. This high filling speed ensures that the entire mold cavity is filled correctly, and very thin walls are obtained [32, 36]. Since the speeds are high, the injection process itself produces a non-coherent liquid metal flow, which causes at first a very thin layer of metal (called the skin) to fill the cavity, and at the end, the remaining volume of the cavity is filled with the molten alloy and gas (Figure 14) [35]. The filling takes about 20-100 ms [36].

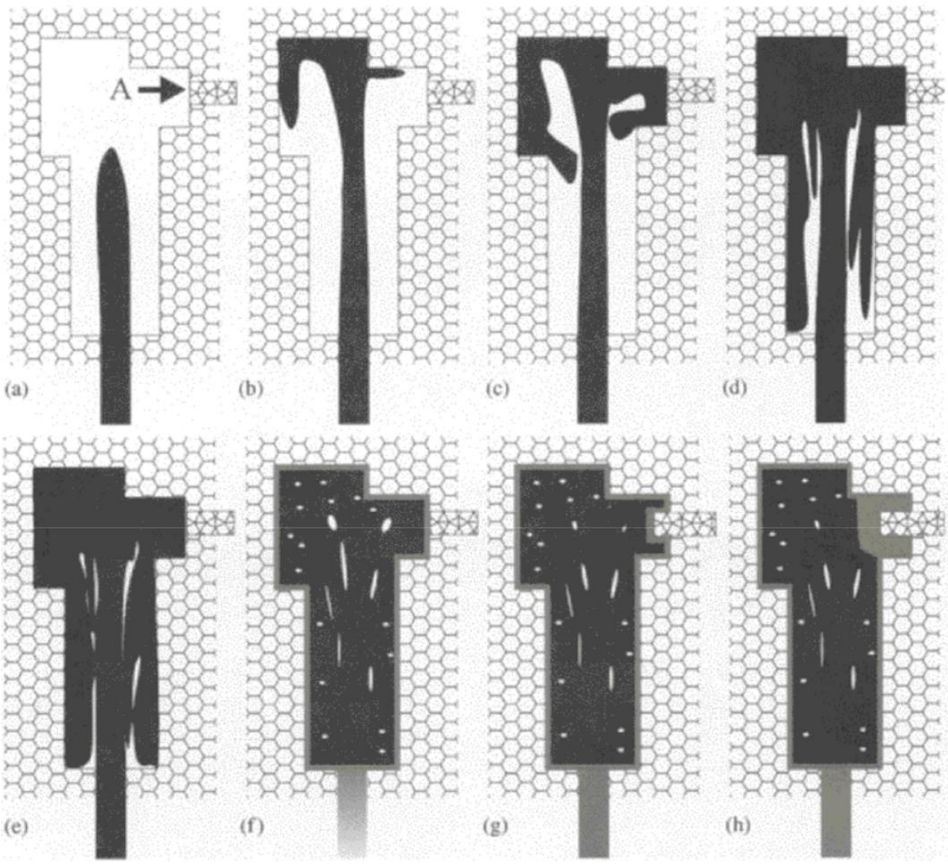

Figure 14: Schematic of the liquid metal flow during the filling phase [35].

The third and final phase is the compaction stage. In this phase, the plunger moves at very low speed, but pressures up to 1000 or 2000 bar can be reached. This high pressure serves to compensate for volumetric flaws (microporosity) that appear due to shrinkage of the alloy and to close or collapse gas porosities that are due to turbulent filling of the mold cavity. However, this phase is only most effective near the gates, and can be detrimental when performing heat treatments, as collapsed porosities appear with high gas pressures [36].

There are two major problems in aluminum alloy injection: problems related to heat treatments and die soldering [33]. Two characteristics of conventional HPDC are the high cooling rates and the high turbulence that the alloy is subjected to when injected into the mold due to the high injection speeds used. This causes the appearance of collapsed porosities, which are nothing more than gas porosities where the gas is at high pressure. This is due to the turbulent regime created by the injection speed used during the 2nd phase and the high compaction pressures used in the 3rd phase. These internal porosities contain gases such as air, hydrogen, and vapors that are formed by the decomposition of the organic lubricants in the mold wall that are trapped inside the liquid metal. These porosities combined with others due to part contraction during cooling, greatly affect the mechanical properties of the injected parts. Although, it is normal to accept a certain level of porosity in the injected parts, when they need to be heat treated, and therefore exposed to high temperatures, porosities are no longer accepted. During long exposure to high temperatures, the yield strength of the material decreases and the pressure inside the pore increases, causing surface blistering in the components (Figure 15) and dimensional instability due to deformations. Besides ruining the surface finish of the parts, it is impossible to obtain parts with ductility and toughness properties equal to those required for structural components and the ability of the parts to be watertight [14, 33, 36].

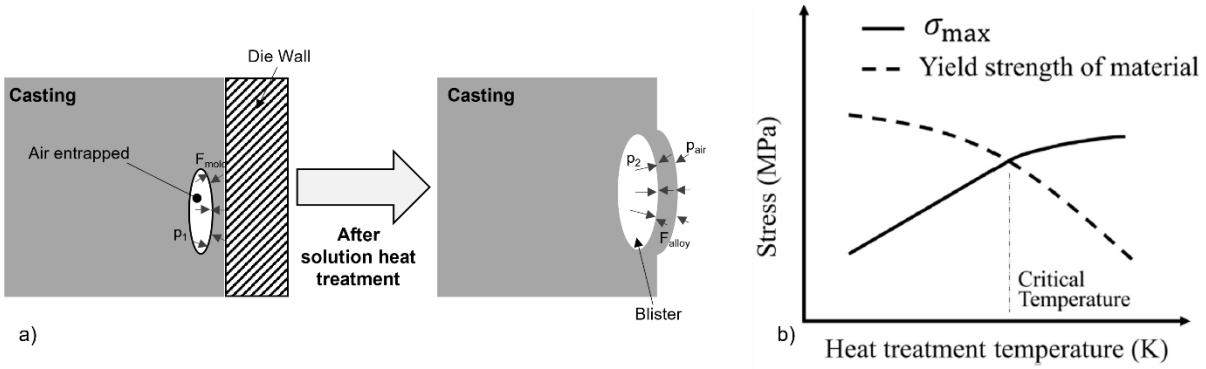

Figure 15: Blistering formation. a) Schematic drawing of the surface blistering formation; b) Schematic diagram of the evolution of the alloy yield strength and pressure inside the pore with the variation of the heat treatment temperature. Adapted from [40].

Al-Si-Cu and Al-Si-Mg family alloys are among the most commonly used in die casting and can be hardened through aging. However, up to a certain time this type of alloys were not subjected to the solution heat treatment followed by aging, because during solution they would have to stage at approximately 520°C for several hours. However, after some studies, it was concluded that the solute elements (copper, magnesium, and in some cases even silicon) dissolve in the α-aluminum grains in the early part of the solution heat treatment. Thus, reducing the temperatures and times of the solution heat treatment makes it possible to harden alloys of the families initially addressed through artificial aging without the occurrence of blistering or swelling [33].

Due to the high affinity between aluminum and iron in the liquid state, there is the possibility of the part sticking to the steel mold during cooling. Rapid interatomic diffusion is possible on contact of aluminum and iron causing the formation of intermetallic compounds on the mold surface. Die soldering can be detrimental when automatically ejecting the part from the mold, leading to production delays, and can damage the mold cavity surface, which leads to repair costs and production line downtime [33]. Adhesion is influenced by several factors:

- Chemical composition of the aluminum alloy. Iron is beneficial for unmolding parts, but affects the mechanical behavior of the injected part. Manganese and small amounts of titanium also contribute to the decrease of the die soldering effect, while nickel is detrimental. Magnesium and silicon have no significant effects;
- Chemical composition of the mold. The most commonly used steel for manufacturing injection molds is H13. Steels with higher alloying elements can better resist the chemical attack of aluminum in the liquid state, but their cost is higher, so they are not usually used;
- Injection temperature. This should be as low as possible, and it has been found that a temperature of 670°C before the molten metal enters the shot sleeve is critical to minimize the adhesion of aluminum alloy parts to steel molds;
- Coating the molds. Coatings act as diffusion barriers in the iron-aluminum reaction by slowing the welding of aluminum to the mold surface. Boron-based ceramic coatings have proven to be quite effective. Boron nitride applied through physical vapor deposition (PVD) if it is compatible with the steel substrate of the molds acts as a diffusion barrier. Alternatively, the surface of the mold can be aluminized by dipping the mold into molten aluminum at 760-800°C. After removal, the mold should be held at 300°C for 12-24 hours to form a controlled layer of iron aluminide. At the end, the surface should be polished [33].

Thus, some of the advantages of this process are:

- HPDC is a very fast process which brings some economic and dimensional advantages. The parts produced have excellent dimensional accuracy and an excellent surface finish, which minimizes the finishing processes required, thus reducing the cost. In addition, due to the high injection speed, parts are produced with reduced thicknesses, which reduces their weight and, consequently, their economic value. To increase the production speed and make maximum use of the machine's capabilities, depending on the size and geometry of the component, multi-cavity molds are used. The fast injection and high cooling rates help in the refinement of the microstructure and thus lead to maximum strength values. In addition, by optimizing the cooling channels, it is possible to improve the properties of the parts at specific points [10, 18, 34, 36];
- The high level of automation present in an injection cell ensures process repeatability and consistency of the final product with less human intervention. In addition, one operator can supervise two or three machines at the same time, reducing labor costs [10, 18];
- The HPDC process is competitive for high production volumes, around 200,000 parts per year. The high investment cost due to high machine and tooling values can be amortized over the course of large series production [10, 18].

But like all processes, it also has limitations:

- The initial investment required for HPDC is quite high due to the high costs of tooling, molds and hydraulic injection machines [18, 34];
- For the production of structural parts, the conventional injection process cannot be used, because the high injection speeds that are used during the process cause gas porosities to appear inside the parts that are detrimental to their mechanical and dynamic behavior. These porosities somewhat restrict the application of these components, for example at the structural level, because the temperatures reached during the heat treatments cause an increase in the pores that can lead to surface blisters. Components produced by sand casting and low-pressure permanent mold casting have less porosity, therefore better ductility and toughness, and more complex shapes can be produced. In addition, if there is a need to increase the hardness of the parts produced, they can already be heat treated [18, 32-34];
- When there is an increase in the size or thickness of the component being produced, there is also an increased likelihood that the properties will not be uniform throughout it [34];
- Neither sand cores can be used due to the high injection speeds, nor metal cores where they are not allowed to be removed directly. Thus, this type of process has some limitations on the design flexibility of internal passages or hollow shapes. This limitation in the simplest cases can be solved by drilling interior channels in the part or by redesigning the part so that a part can be attached to it through a bolted connection to ensure the passage of interior channels [10];
- The tendency for die soldering to occur, which leads to damage to the mold surface and poor surface quality of the part, can be minimized when the alloy has at least 0.6% iron in its constitution. However, high percentages of iron reduce the ductility, toughness and fatigue resistance of the alloy. For some components this loss of properties may be acceptable, but for structural components this situation is not acceptable [10, 18].

2.3.2 Vacuum high-pressure die casting

To prevent the appearance of gas porosities inside the parts, vacuum die casting systems have been created. By applying vacuum inside the die cavity, conceptually, there is no mixing

of the liquid metal and air, and therefore, theoretically, the gas porosities issue should be minimized. Vacuum die casting uses a vacuum pump and an accumulator to remove air and gases from the die cavity and the metal gating system before and during injection of the molten metal. The die is connected to the vacuum pump and accumulator through a combination of flexible and hard tubes. The vacuum is performed below the atmospheric pressure value [41].

Vacuum die casting (VDC) can be divided into vacuum-assisted die casting (VADC) and high-vacuum die casting (HVDC) [4, 41]. In addition, there is usually a distinction between two types of vacuum systems: valveless vacuum blocks and valve systems (Figure 16) [10, 42].

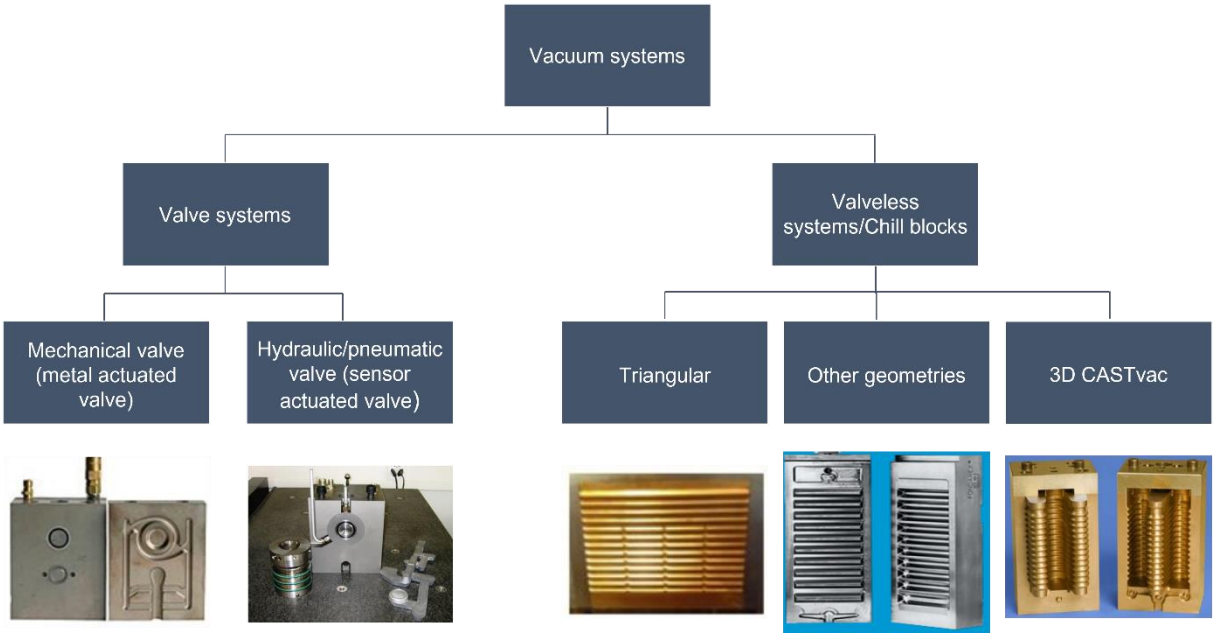

Figure 16: Types of vacuum systems. Adapted from [42].

Valve based systems allow for maximum efficiency and shut off the vacuum before the liquid metal reaches the sensor system. Their maintenance can be quite complex due to metal solidification inside the actuators. This problem is more associated with mechanically actuated valves, because in sensor actuated valves, the command to close the valve is given by the plunger position [42].

Valveless based systems use chill blocks (equipment with no moving parts) to stop the liquid metal from flowing and shut off the vacuum when the metal solidifies. They are similar to mechanical valves in the way that they use the metal flow as a trigger to shut off the vacuum. Chill blocks are classified by taking into account the geometry of the chill profile: triangular, trapezoidal, and 3D CASTvac. This last geometry by increasing the surface area for cooling becomes four times more efficient than the most usual geometries (triangular and trapezoidal). Chill blocks are less efficient than valve systems, and in addition the vacuum level, when the metal solidifies, is measured in the tank and not in the die cavity, which causes measurement errors (Figure 17) [42].

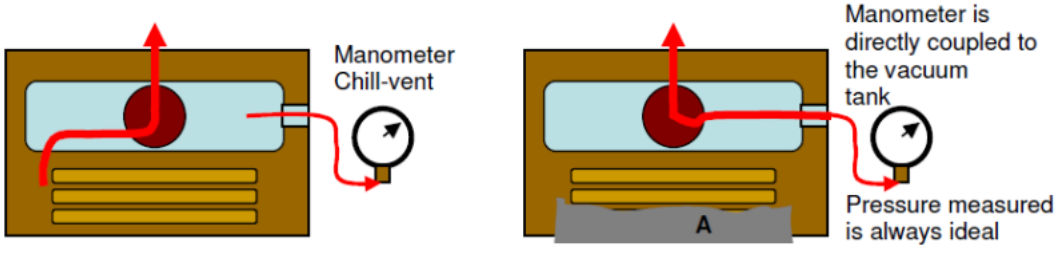

Figure 17: Wrong reading of the vacuum pressure on chill blocks [43].

Table 12 summarizes the main advantages and limitations of mechanical valves, hydraulic/pneumatic valves, and chill blocks.

Table 12: Advantages and limitations of mechanical valves, hydraulic/pneumatic valves, and chill blocks [10, 18, 36, 42].

	Advantages	Limitations
Mechanical valve	Easy to maintain; No need for an expensive controller; Biscuit size variation is not problematic; Vacuum performed through entire shot.	High cost; Less vacuum generated than in hydraulic/pneumatic valves due to smaller cross-sectional area; Maintenance must be carried out after 5000 injection cycles.
Hydraulic/pneumatic valve	Has no problems starting up, because it is not actuated by metal; Easy maintenance because there is no metal in the valve; More vacuum possible due to larger cross-sectional area.	Very high cost; Does not take into account the variation in biscuit size; Requires a better control system.
Chill block	No extra maintenance required. Can be performed when the mold is maintained; Lower cost; Vacuum can be performed until the die cavity is completely filled.	Vacuum level measurement is not accurate; Evacuation efficiency is lower than with valve systems.

Vacuum assisted die casting (VADC) (Figure 18) uses the same injection machine as HPDC with a slight modification. A vacuum valve is installed in the die to evacuate the gases inside the die cavity and is capable of generating vacuum pressures between 60 and 300 mbar. This valve is opened after the die and shot sleeve hole are closed. This variant of vacuum die casting, depending on how it is implemented, only allows the vacuum to be partial (40 to 80%), but even so it brings improvements relative to HPDC. It is then possible to produce larger parts with more complex geometries and thinner walls with less gas trapped inside. However, the consistency of this process is not yet sufficient to guarantee that all parts that undergo solution heat treatment do not exhibit blistering [4, 41].

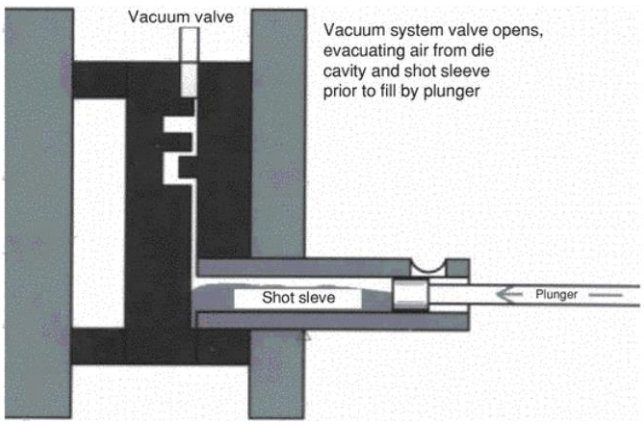

Figure 18: A typical vacuum high-pressure die casting system [41].

Hu et al. [44] injected components in the AlSi12(Fe) alloy through VADC with different vacuum levels (275 mbar, 112mbar and 72 mbar). He found that increasing the vacuum level led to a reduction in the average porosity and that for higher vacuum levels there is no major change in the number of porosities, but there is a reduction in their volume. Yield strength increased with increasing vacuum level and so did the repeatability of ultimate tensile strength and elongation, Table 13. Szalva et al. [39] injected AlSi9Cu3 alloy specimens with different vacuum levels (170 mbar, 90 mbar and 70 mbar). He found that the vacuum effectiveness is most pronounced for levels between 80 and 100 mbar. At a vacuum pressure of 70 mbar there was a 57% reduction in porosities relative to conventionally injected parts (Table 13 and Figure 19).

Table 13: Results of porosity, YS, UTS and elongation as a function of vacuum level of the references [39, 44].

Pressure (mbar)	**Porosity** (%)	**YS** (MPa)		**UTS** (MPa)		**Elongation** (%)		**Reference**
		Avg.	SD	Avg.	SD	Avg.	SD	
275	0.152	98.3	9.3	218.0	37.8	2.5	1.07	[44]
112	0.102	101.5	9.1	230.6	26.1	2.8	1.27	
72	0.046	104.1	9.9	229.5	25.3	2.5	0.99	
Atmospheric	1.10	152.9	-	253.7	-	1.31	-	[39]
170	0.71	154.0	-	258.4	-	1.43	-	
90	0.67	161.7	-	276.3	-	1.63	-	
70	0.47	167.2	-	291.6	-	2.04	-	

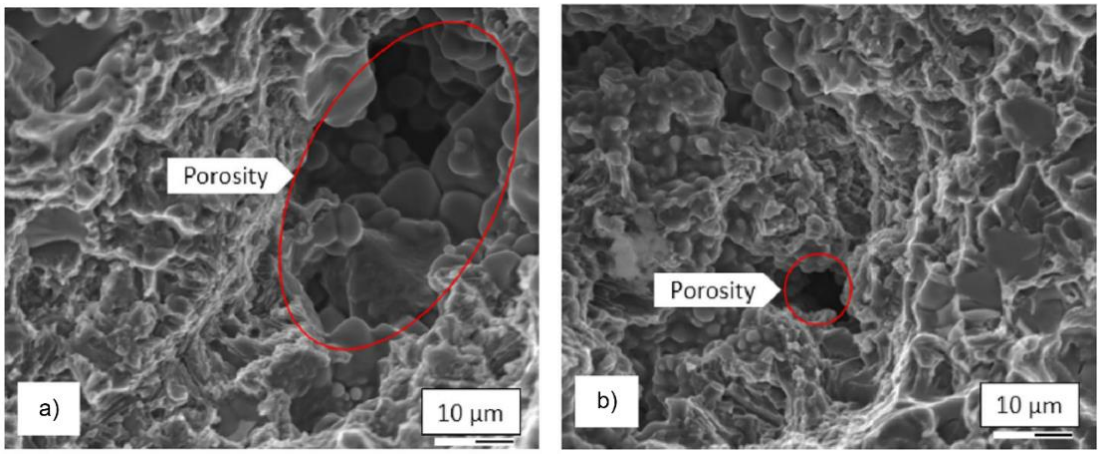

Figure 19: SEM micrograph. a) Porosity in the conventional casting; b) Porosity in the 70 mbar vacuum-assisted die casting. Adapted from [39].

High-vacuum die casting (HVDC) uses technologies capable of generating vacuum pressures of less than 60 mbar inside the die cavity and allowing tight control of the vacuum profile during die filling. From HPDC to HVDC, changes must be made to the thermal management of the shot sleeve and mold, overflows must be redesigned, and as little lubrication as possible must be used. With HVDC there is an improvement in mechanical properties over parts produced by VADC and there is already greater repeatability in obtaining treated parts without blistering [4, 36, 41]. Shock towers, A- and B-pillar components, door structures, and suspension links (Figure 20) are examples of parts that are produced using HVDC [10].

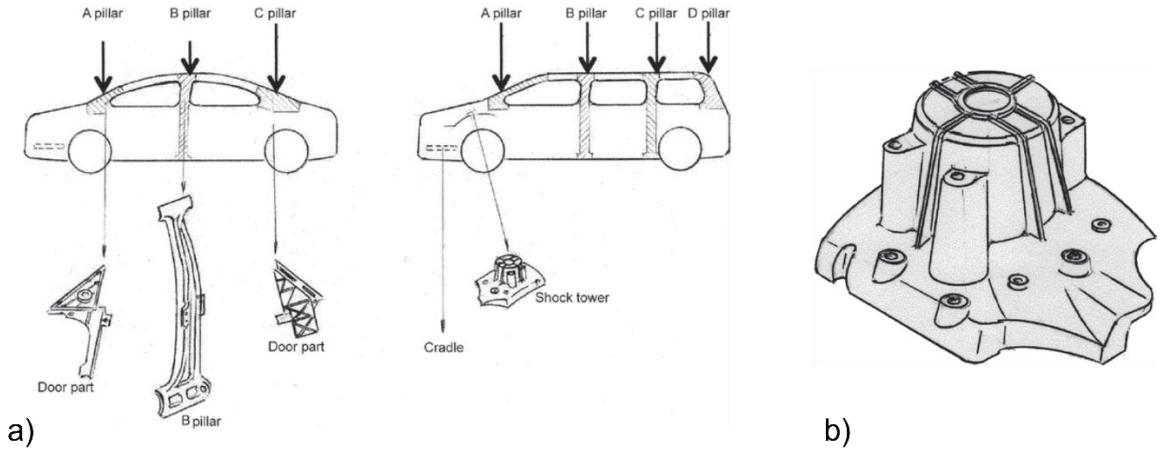

Figure 20: a) Schematic representation of structural components in a car; b) Schematic representation of a shock tower. Adapted from [10].

Dong et al. [45] was able to achieve a vacuum pressure of 19 mbar. He confirmed that HVDC increased the repeatability of the tensile properties (Table 14) of the Al-Si-Mg-Mn alloy under study. There was improvement in UTS and ductility by 5.6% and 43%, respectively, in the as-cast state when compared to the values obtained in HPDC. After the T6 treatment there was also an increase in ductility by about 21%.

Table 14: Results of YS, UTS and elongation as a function of the HPDC process [45].

State	**Process**	**YS** (MPa)		**UTS** (MPa)		**Elongation** (%)	
		Avg.	SD	Avg.	SD	Avg.	SD
As-cast	HPDC	167.7	2.4	300.9	10.0	8.1	2.1
	HVDC	169.5	1.6	317.6	1.4	11.6	0.7
T6	HPDC	297.1	4.3	355.3	3.7	9.7	1.5
	HVDC	300.2	3.4	359.0	3.1	11.7	0.3

In Table 15 a comparison is made between HPDC, VADC and HVDC.

Table 15: Process characteristics of HPDC, VADC and HVDC. Adapted from [4, 10, 36].

Process characteristics	**Conventional high-pressure die casting** (HPDC)	**Vacuum-assisted die casting** (VADC)	**High-vacuum die casting** (HVDC)
Vacuum pressure (mbar)	1000	60 - 500	< 60
Advanced systems for vacuum control	No	No	Yes
Die sealing	No	Yes	Yes
Probability of gas porosity	High	Low	Very low
Possibility to perform solution heat treatment	No	Yes	Yes
Weldability	Poor	Fair	Good
Mechanical properties	Acceptable strength, low ductility	Acceptable strength, acceptable ductility	High strength, high ductility
Minimum wall thickness (mm)	4	3	2

2.3.3 Heat treatments for Al-Si-Mg alloy components obtained by high-pressure die casting

One of the most widely used heat treatments for components produced by high-pressure die casting is the T6 heat treatment (Figure 21). This heat treatment promotes precipitation hardening. After performing this treatment, the parts have the best strength with good elongation values. The main steps of this heat treatment are:

- Solution heat treatment;
- Rapid cooling (quenching);
- Artificial aging.

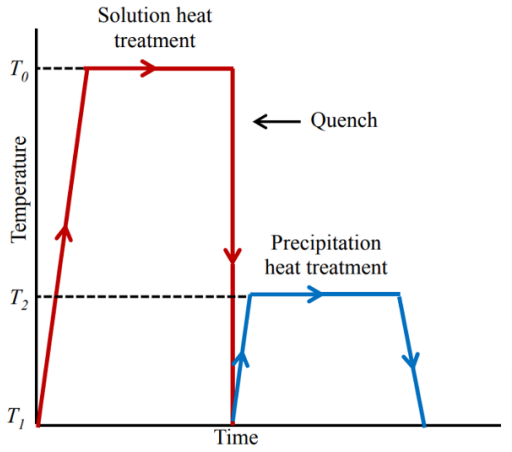

Figure 21: T6 heat treatment steps. Adapted from [46].

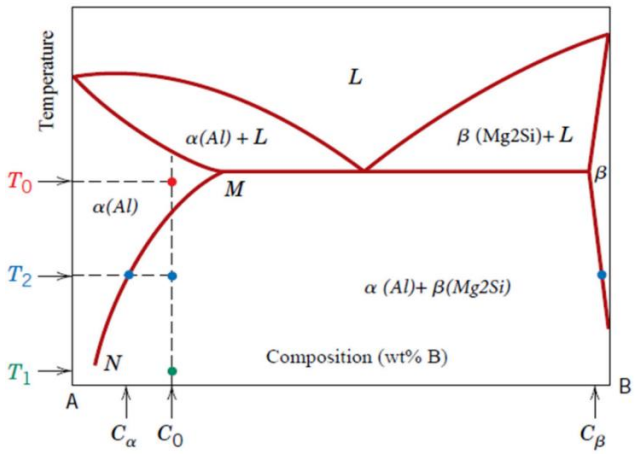

Figure 22: Schematic of the phase diagram for precipitation-hardenable Mg_2Si aluminum showing the temperatures of the different stages of the T6 heat treatment [46].

During solution heat treatment, heating is carried out to near the eutectic temperature (temperature T_0 of Figure 22). Heating to temperatures above the eutectic temperature can lead to partial melting of the alloy, resulting in a loss of mechanical properties. Temperatures below the eutectic temperature or very short stage times may not allow sufficient dissolution of alloying elements in the aluminum matrix and the desired level of homogeneity is not achieved, resulting in lower hardening. The effects of solution heat treatment are:

- the dissolution of magnesium and silicon from the Mg_2Si phase in the primary aluminum phase up to the maximum solubility limit;
- the homogenization of the microstructure;
- the spheroidization of the eutectic silicon without a decrease in the number of particles [36].

Thus, the dissolution of the alloying elements allows the creation of the optimal conditions for artificial aging and the spheroidization of the silicon particles promotes an improvement in the ductility of the alloy.

The spheroidization of silicon particles during solution heat treatment starts with the fragmentation of the eutectic silicon particles, and finally the spheroidization of these particles takes place. If the solution heat treatment is too prolonged in time, there is coarsening of the silicon particles (Figure 23) [36].

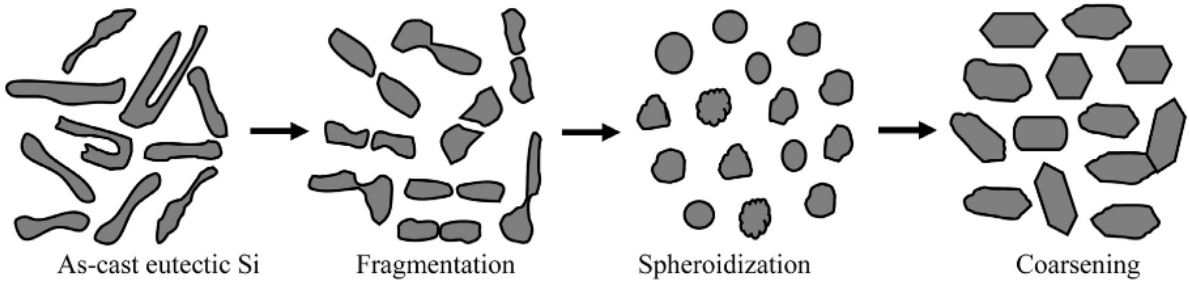

Figure 23: Morphological evolution of eutectic silicon particles [47].

After solution heat treatment, rapid cooling should be performed to prevent precipitation and formation of the Mg_2Si phase. After cooling, there is a supersaturated solid solution. The time between the end of solution heat treatment and the entry of the parts into the quench medium (e.g. water or oil) should be as short as possible. The best relationship between mechanical strength and ductility is obtained with high cooling speeds. However, the cooling speed should be optimized to achieve a perfect balance between the mechanical properties obtained and the prevention of warping, distortions, and residual stresses in the parts [36, 48].

In artificial aging, the parts should be heated up to a temperature of T_2 (Figure 22), so that there is enough diffusion to promote the nucleation of solute-rich metastable precipitates. After finishing the stage at T_2, the parts are cooled down at room temperature. The hardening results from a dense and uniform distribution of Mg-Si intermetallics that act as an obstacle to dislocation movement. This allows the mechanical strength and hardness of the parts to be improved. The mechanical strength and hardness obtained at the end depends on the aging temperature and stage time [36].

The precipitation of Al-Si-Mg alloys during aging takes place in the following sequence:

Supersaturated solid solution (α matrix) → GP zones → β'' phase → β' phase → β phase (Mg_2Si)

At the beginning of aging process decomposition of the supersaturated solid solution occurs. Separated Mg and Si clusters are initially formed, and after the diffusion of these atoms, spherical GP (Guinier–Preston) zones appear, which are composed of coherent precipitates. These zones are easily deformed by dislocations leading to localized distortions in the solid solution network. With continued diffusion of the solute into the agglomerates, the GP zones become elongated and give rise to β'' phase precipitates, composed of Mg_5Si_6 with approximately 20% aluminum and a Mg/Si ratio very close to 1. Due to the coarser size of this phase, they act as an obstacle to dislocation deformation, contributing to an increase in mechanical strength. If the stage time is prolonged, the β'' phases transform into β' phases (phase semi-coherent with the matrix) with the composition Mg_2Al. The final phase to form is the β phase (phase incoherent with the matrix), composed of Mg_2Si. As the β''→β'→β transformation takes place there is a drop in hardness and mechanical strength (Figure 24) which corresponds to the over aging of the parts (condition T7) [36, 46, 49].

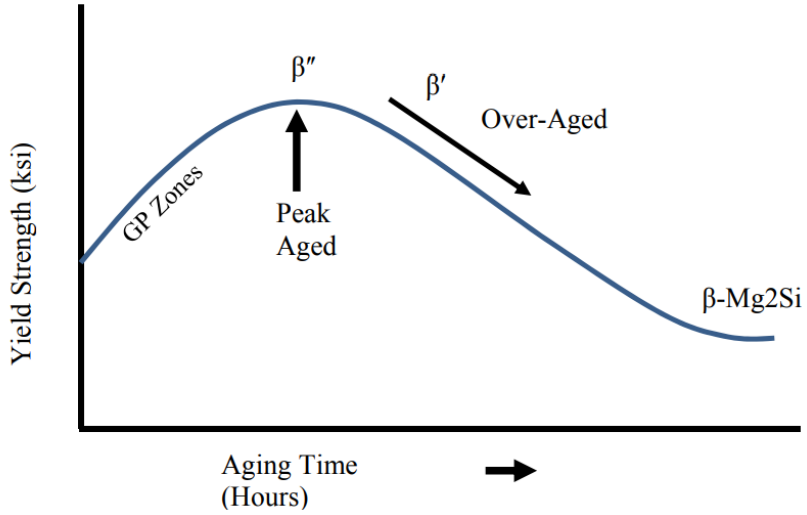

Figure 24: Yield strength evolution with increasing aging time [46].

It is common that during the formation of β-precipitates there is also the formation of silicon precipitates, and the increase in these precipitates is proportional to the increase in aging time. The formation of the silicon precipitates exists because not all of the silicon dissolved in the aluminum matrix is used in the formation of the Mg_2Si phase [50].

The formation of GP zones is inversely proportional to the temperature used for aging. If high temperatures are used, the precipitates grow faster, and therefore the peak of hardness is reached faster. However, since the precipitate density is lower, the maximum hardness obtained for higher aging temperatures is lower than that obtained for lower temperatures [26].

In addition to the T6 heat treatment, there are other heat treatments that are commonly used on die casted components. A T7 treatment can be performed if the components are subjected to high temperatures during service. Higher ductility values are achieved in this heat treatment (when compared with T6), but the strength is not as high. The T5 treatment is used to minimize costs and ensure moderate strength. As this heat treatment does not perform solution heat treatment followed by quenching, warping of the treated components is prevented [36, 41].

2.3.4 Pouring and dosing of molten metal

The most traditional method of transporting the liquid metal into the mold is to use open-top ladles, which can be manual or mechanized to transport larger quantities of material. One of the main problems with using an open-top ladle is that the slag that accumulates on the surface of the liquid metal will be poured into the holding furnace or the mold. So, in order to avoid this situation, in Figure 25, different types of ladles are shown that using a teapot spout or a bottom stopper rod and nozzle that can reduce the transfer of slag [41].

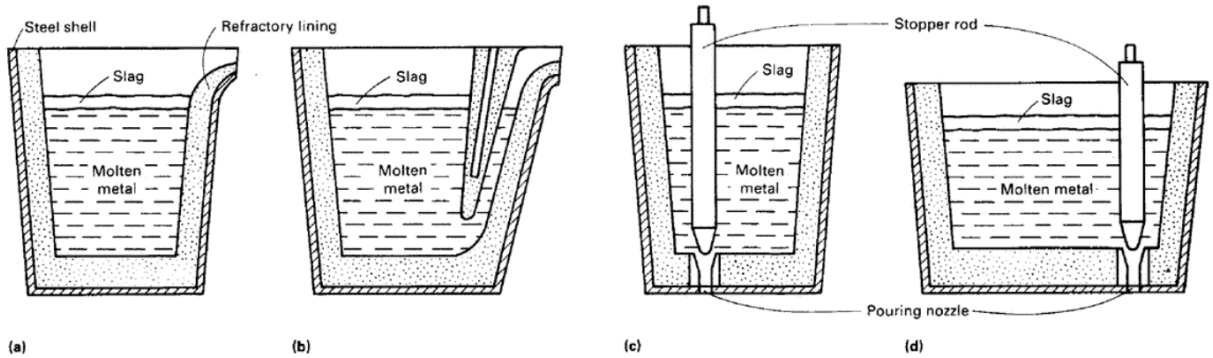

Figure 25: Four different pouring ladles. a) open lip-pour ladle; b) teapot ladle; c) and d) bottom-pour ladles [41].

As an alternative to the use of ladles or ladle furnaces that fill the shot sleeve by gravity pouring, dosing furnaces are used.

A dosing furnace not only operates as a holding furnace, but also has the advantage of directly transferring the liquid metal into the shot sleeve in precise quantities. To be able to transfer the liquid metal from the furnace to the shot sleeve through the dosing channel, it is necessary to use compressed dry air. The use of dry air is essential because the solubility of hydrogen in liquid aluminum is very high. The compressed dry air is introduced into the pressure-sealed furnace and forces the metal inside to rise through the riser tube. With an increasing pressure, the liquid metal fills the entire riser tubing until it reaches the dosing channel that is connected to the shot sleeve. The metal flow stops when the pressure is turned off [41].

At each filling of the dosing furnace, a loss of quality in the liquid metal is observed, so the filling according to that depicted in Figure 26 ensures that the drop in quality is less. Keeping the filling funnel always full, ensures that oxides are formed on the surface bath and do not contaminate the melt inside the furnace. These oxides can be skimmed off at the end of the filling operation [41].

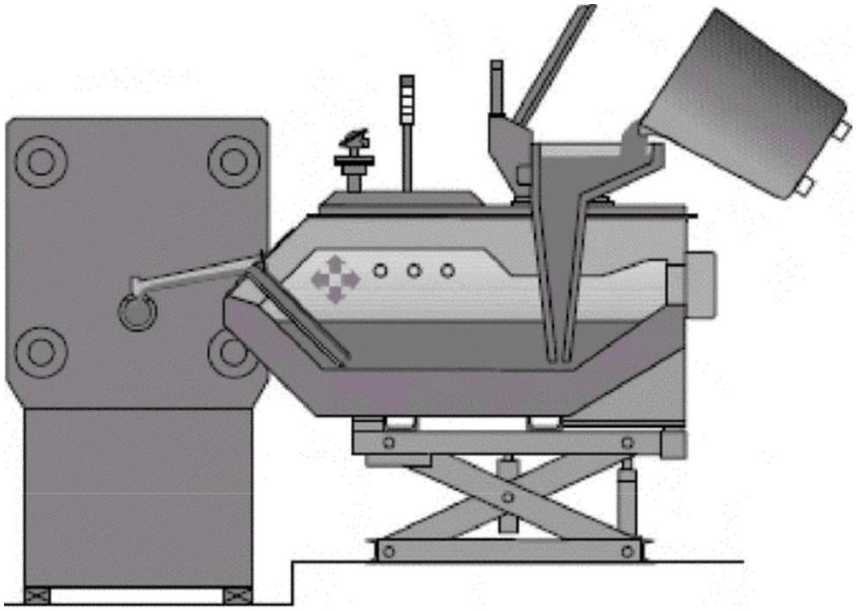

Figure 26: Refilling a dosing furnace [41].

Holding the liquid aluminum for longer periods in the dosing furnace ensures better bath properties because it allows more time for the deposition of inclusions on the surface or bottom of the bath that will then not affect the metal that is used to fill the mold. One way to improve the quality of the bath even more is to use porous plugs that are placed at the bottom of the furnace (Figure 27). These porous plugs can produce extremely small gas bubbles along the entire surface of the plug. Introducing argon or another inert gas through these plugs, allows the level of hydrogen inside the furnace to be better controlled and kept as low as possible [41, 51].

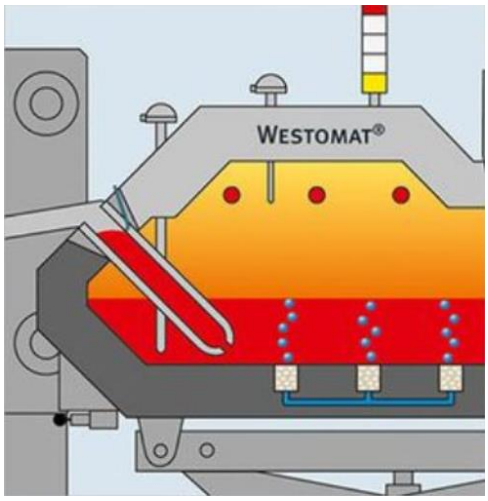

Figure 27: Porous plugs on the bottom of a dosing furnace [51].

The main advantages in using this type of furnace are:

- By controlling the flow and pressure of the injected air it is possible to control the speed of the liquid metal, thus preventing it from entering the turbulent regime and avoiding the air entrapment;
- As the liquid aluminum is in a controlled atmosphere, the solubility of hydrogen in the aluminum is prevented;
- The filling of the furnace with the metal that comes from the ladles is done by a funnel that is below the surface of the bath, so it does not come in contact with the slag that is on the surface of the bath;
- High repeatability in dosing accuracy;
- Makes the process faster [41].

It is extremely important to adopt the best solutions regarding the pouring and dosing of molten metal, because if the metal quality is not maintained in these initial steps, the mechanical requirements of the components cannot be guaranteed even when the injection process and heat treatment are excellent.

Due to the turbulence of the liquid metal flow, oxide films are formed on the bath surface, which do not allow the different ceramic film layers formed to bond (Figure 28). This lack of bonding between the ceramic films creates a fissure in the liquid, which is called a bifilm [32].

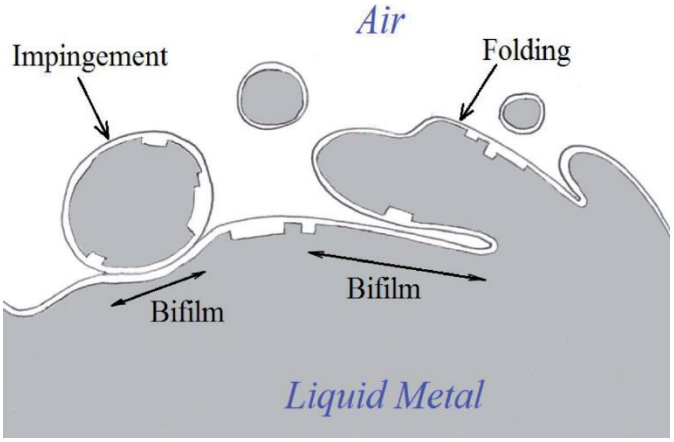

Figure 28: Production of bifilms as cracks in the liquid metal [32].

Apart from the problem of oxide films being dragged and causing cracks in the liquid metal, the dragging of air bubbles can also be problematic. As the bubbles move inside the liquid metal, a kind of oxide tail (similar to a long bifilm) is formed all the way back to the

initial point of bubble formation (Figure 29). Thus, bubbles, in addition to being gas porosity points, can also form macroscopic crack-like defects [32].

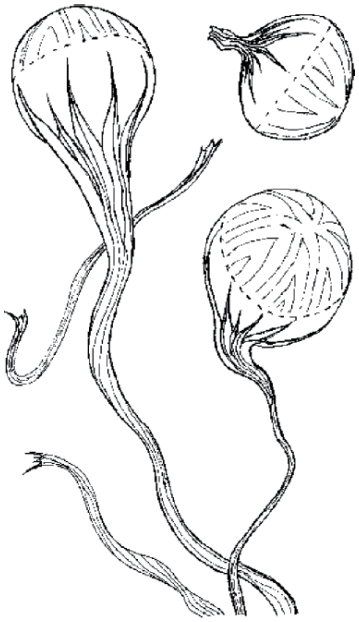

Figure 29: Bubbles and their oxide tails [32].

In the case of the high-pressure die casting process, once the mold filling takes place in milliseconds it does not allow the bifilms to grow, resulting in an extremely thin film. The reduced thickness may allow adhesion between two films due to "atomic rearrangements during their transformation from pure alumina to spinel as the magnesium in the alloy diffuses into the bifilm" [32]. The high pressure used during the 3rd stage of HPDC process also contributes to the closeness between two biofilms [32].

The entrainment defects that cause the appearance of the bifilms are independent of the environment where the injection is made whether in air, inert atmosphere or vacuum. In a vacuum atmosphere there is always some oxygen and/or nitrogen that allows the creation of oxide or nitride films on the surface of the liquid metal. Vacuum injection does not eliminate bifilms, but makes them even thinner and thus more difficult to detect in vacuum casts [32].

2.3.5 Molten-metal treatments: fluxing and degassing

The reactivity of metals combined with the high temperature of the melting bath causes the dissolution of gases and the appearance of inclusions in the molten metal [36, 41].

It is almost impossible to prevent slag formation during the melting of aluminum alloys. Usually, this slag has large amounts of Al_2O_3, because the free energy of formation of this oxide is very low. Al_2O_3 forms on the outer surface of the bath if it is exposed to the atmosphere. It floats and agglomerates on the top of the bath and can be removed by skimming. The design of the gating system should be carefully dimensioned to minimize the formation of Al_2O_3 during mold filling [36, 41].

The distribution and size of the oxides present in aluminum alloy castings influence the degradation of the mechanical properties. Rapid cooling during solidification is beneficial for decreasing the size of the oxide inclusions and for improving the distribution of these inclusions. Thus, the degradation of mechanical properties is not as pronounced [41].

There is a possibility that other alloying elements present in aluminum alloys react with oxygen and form complex oxides with Al_2O_3 as one of the components. In the case of alloys containing magnesium, magnesium oxide (MgO) is formed which then joins with Al_2O_3

forming $MgAl_2O_4$. To avoid as much as possible the formation of this type of oxides, pouring and gating system design should be done carefully [41].

Other types of inclusions can appear as a result of grain refinement operations due to uncontrolled addition of elements. Excessive additions of, for example, titanium, vanadium, and boron can lead to the formation of diborides, which are undesirable inclusions. Commercial aluminum has its chemical composition worked out to exploit age hardening but is susceptible to the formation of undesirable intermetallic particles during cooling. The control of the bath chemical composition is especially important in cases where scrap is recycled, as this is introduced into the bath and increases the levels of impurities that decreases the properties of the components [36, 41].

For cleaning the inclusions present in the bath, fluxing is performed. Chemically active solids, inert gases or chemically active gases are used. The choice of the type of fluxing depends on the chemical composition of the bath and refractories. The functions of these additives are:

- Remove inclusions, impurities and dissolved gases from the bath;
- Prevent the formation of excess solid phase inclusions;
- Cleaning the oxides that are on the walls of the furnace [36, 41].

The use of fluxes can be done both during the melting of the metal and during the transportation of the molten metal in the transfer ladles [41].

In the casting of aluminum and its alloys, the use of fluxes is important to control the amount of impurities and to remove oxides. The types of fluxes that are commonly used are:

- Cover fluxes: create a protective barrier against oxidation and moisture on the surface of the bath that is in contact with the surrounding atmosphere;
- Drossing fluxes: moisten the bath to cause coalescence of the aluminum;
- Melt-cleaning fluxes: are used to remove the oxides formed during the melting of the aluminum;
- Wall-cleaning fluxes: are used to remove the aluminum oxide buildup that exists on melting furnace walls [36, 41].

Within non-ferrous materials, aluminum is the one that is most susceptible to hydrogen-induced defects. One reason for this is that aluminum and its alloys when reacting with water vapor (Equation (3)) easily absorb hydrogen [41].

$$2Al(l) + 3H_2O(v) \rightarrow Al_2O_3(s) + 3H_2(in\ Al) \quad (3)$$

Another reason that explains the greater susceptibility of aluminum and its alloys to hydrogen-induced defects, is the fact that the partition coefficient (k) (Equation (4)) is relatively small [41]. This means that the solubility of hydrogen in liquid aluminum is much higher than the solubility of hydrogen in solid aluminum. In addition, the diffusion rate of hydrogen in solid aluminum is much lower than that in liquid aluminum [41].

$$k = \frac{S_s}{S_l} \quad (4)$$

The solubility of hydrogen in pure aluminum (Figure 30) directly indicates the possibility of porosity formation and how it evolves during solidification after casting [41].

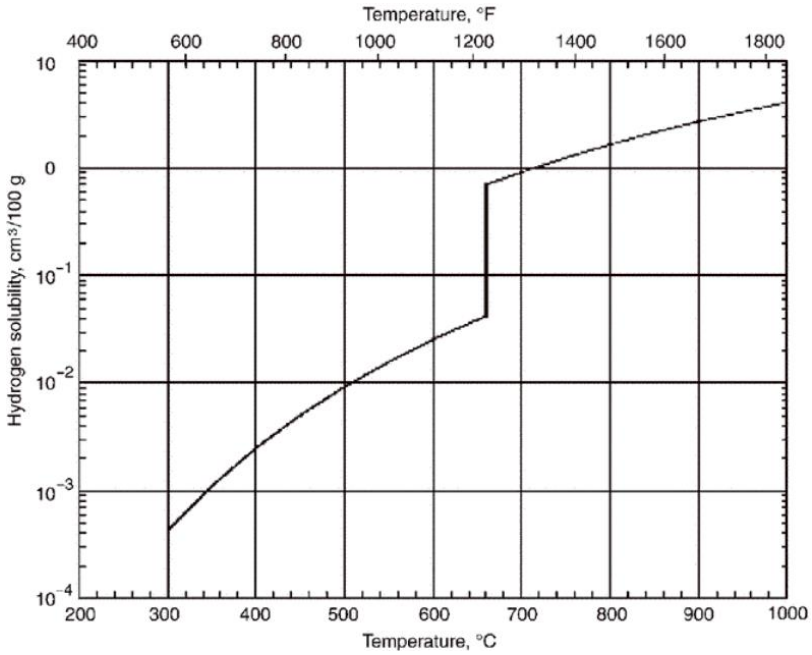

Figure 30: Solubility of hydrogen in pure aluminum in liquid and solid state [41].

Alloying elements influence the solubility of hydrogen in aluminum alloys. Although there are not as many studies of the variation of hydrogen solubility in aluminum alloys as there are for pure aluminum, it is known that silicon, copper, zinc, and iron decrease the solubility of hydrogen in liquid aluminum and that lithium, magnesium and titanium increase the solubility, as shown in Figure 31a). In aluminum in the solid state, silicon, magnesium, copper, lithium and zinc increase the solubility of hydrogen (Figure 31b)) [41].

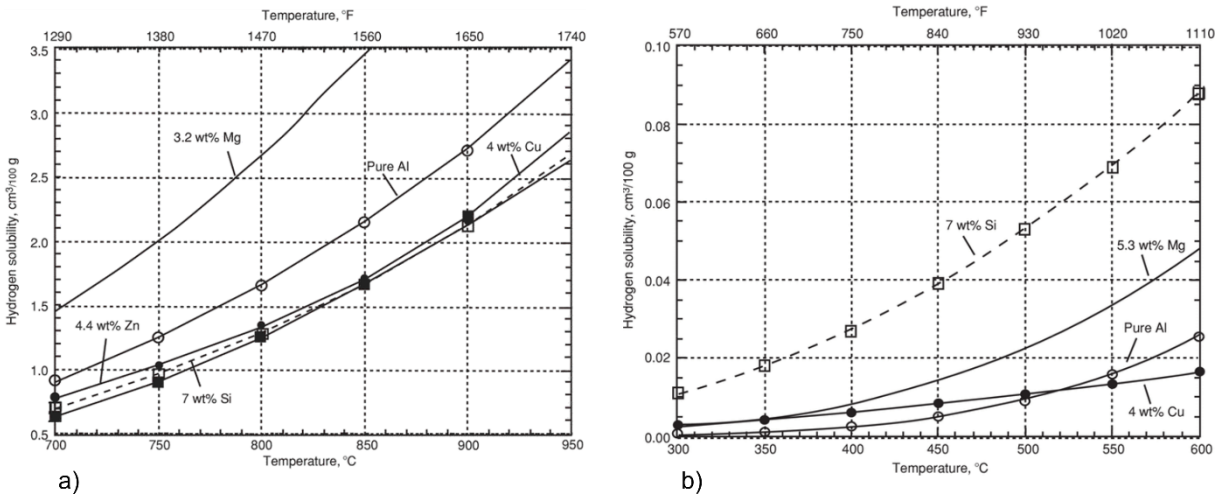

Figure 31: a) Hydrogen solubility in pure aluminum and binary alloys in the liquid state; b) Hydrogen solubility in pure aluminum and binary alloys in the solid state. Adapted from [41].

The most common method for removing hydrogen from aluminum is degassing. Due to the high solubility of hydrogen in liquid aluminum, the degassing operation is extremely important to prevent degradation of the mechanical properties (tensile strength, elongation, fatigue strength, and fracture toughness) of the casting parts [36, 41].

A defined practical value for which porosities caused by hydrogen will, in principle, not be a problem is to reach after the degassing process a level of 0.15 mL H_2/100 g Al [36, 41].

The main sources of hydrogen are, for example, fuel-fired furnaces that contain hydrogen due to the decomposition of fossil fuel, the presence of water vapor in the atmosphere, ingots,

additives and fluxes, and tools (such as plungers and ladles) that have not been properly cleaned and come into contact with liquid aluminum [24, 36, 41].

The first simple way to minimize hydrogen absorption is to decrease the melting and holding times and the temperature, as shown in Figure 30. However, since the bath is normally exposed to an atmosphere with moisture there is always hydrogen reabsorption.

The basic principle of degassing is that any gas except hydrogen is insoluble in aluminum, and therefore they can be used to collect hydrogen and inclusions by removing them by flotation (Figure 32) [24, 36, 41].

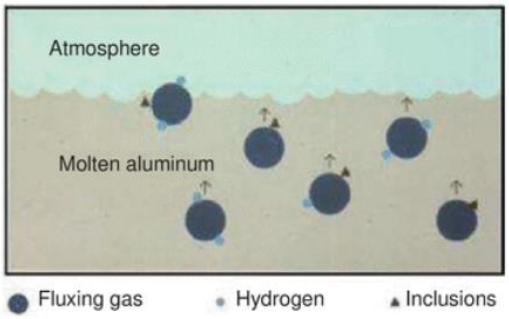

Figure 32: Schematic of gas flotation in molten aluminum [36].

The most effective method for degassing is to use a rotor. The rotor is a rotating graphite shaft with a graphite impeller. The rotating motion allows the creation of small bubbles that rise more slowly in the bath and disperse more, which improves the degassing efficiency (Figure 33). Argon or nitrogen is injected inside the rotor at low pressure (207 kPa). These gases, since they are insoluble in aluminum, will spread throughout the bath and rise to the surface. Hydrogen atoms will diffuse into these gas bubbles forming a hydrogen molecule. When this bubble reaches the surface of the melt, the hydrogen is released. After degassing there is always slag formation on the surface of the bath, which must be skimmed off so as not to impair the quality of the castings [24, 36, 41].

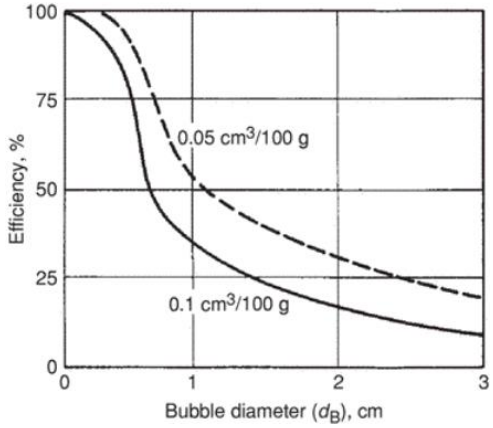

Figure 33: Degassing efficiency as a function of bubble size [41].

In terms of purge gas, despite the higher price of argon, it is preferable to nitrogen. Argon, being more inert and heavier than nitrogen, creates a protective layer on the bath surface during degassing that prevents hydrogen reabsorption and oxidation [36, 41]. It is also possible for the purge gas to be a reactive gas or a mixture of gases, however, the use of reactive gases has declined in recent years due to environmental concerns. In addition, when strontium is used to modify eutectic silicon, only inert gases can be used [24].

2.3.6 GigaPress

As the demand for new cars is growing year by year, automotive manufacturers have been forced to find new solutions that can satisfy the customers' orders. In addition to customer satisfaction, it is important for automotive companies to minimize production costs and maximize profits. To fulfill these three points, IDRA has developed in partnership with Tesla, the OL 6100 CS which is one of the die casting machines with the highest clamping force on the market and can produce large and lightweight structural parts at high production rates. This new machine belongs to the so-called GigaPress family, reducing manufacture times, which makes it possible to fulfill the three points mentioned above.

The IDRA OL 6100 CS (Figure 34), or commonly known as GigaPress, has as main specifications: a clamping force of about 6000 tons, an injection force of about 3000 kN, allows the use of molds with a maximum height of 2400 mm, a shot weight to vary between 80.7 and 116.2 kg and is a large machine with 19.8 m length and 6 m height [52].

Figure 34: IDRA OL 6100 CS [52].

For the Model 3 and Model Y, Tesla decided to replace the front and rear area of the chassis (Figure 35), each composed of about 70 stamped, cast and extruded parts and then welded together, with two structural parts obtained through high-pressure die casting. These structural parts (Figure 35) support suspension, engine, and body elements [53, 54].

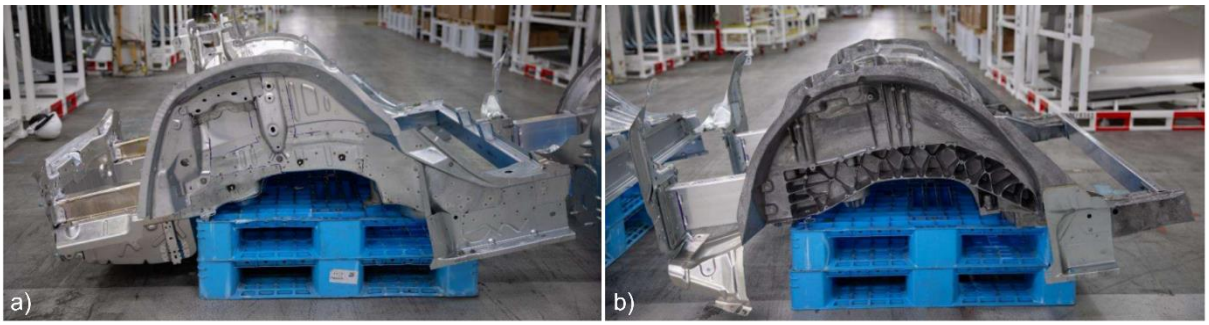

Figure 35: a) Rear underbody with 70 pieces of metal; b) Rear underbody with the new casting. Adapted from [55].

By reducing the number of parts to produce and assemble, Elon Musk said it will be possible to reduce the size of the body shop by 30% [54, 56].

Tesla intends the Model 3 and Model Y chassis to consist of only three injected parts: the front underbody, the battery pack support area, and the rear underbody (Figure 36) [57]. In the future they intend to produce the complete chassis in a single injection molding cycle. For this the new GigaPress from IDRA will be used with closing forces of up to 9225 tons (model OL 9000 CS). The Model 2 (unofficial name), which is intended to be the cheapest model marketed by Tesla, could be the first car with its entire chassis produced in an aluminum alloy injected in a single component [4, 57, 58].

Figure 36: Model Y chassis. Adapted from [58].

3 Experimental procedure

In this chapter the component to be analyzed will be presented as well as the main injection parameters adopted. The experimental procedures and the respective equipment used will also be object of study.

3.1 Component under review

Regarding this study, it was decided to analyze a power electronics casing (Figure 37) produced by SONAFI through high-pressure die casting in four different alloys: AlSi12(Fe), AlSi10Mg(Fe), AlSi10MnMg and AlMg4Fe2. For each of the alloys, there were two different batches of parts: a batch of vacuum-assisted injected parts and a batch of conventionally injected parts.

The parts were cast on a 400 ton Colosio machine. The main injection parameters are shown in Table 16. The instrumentation design to monitor the most important variables of the process is presented in Appendix A. Due to the lack of investment it was not possible to implement the designed instrumentation, and therefore there was a greater difficulty in analyzing the variables of the injection process. The mold temperature was measured with a thermal imaging camera Appendix A. For all alloys the temperature varied between the values shown in Table 16.

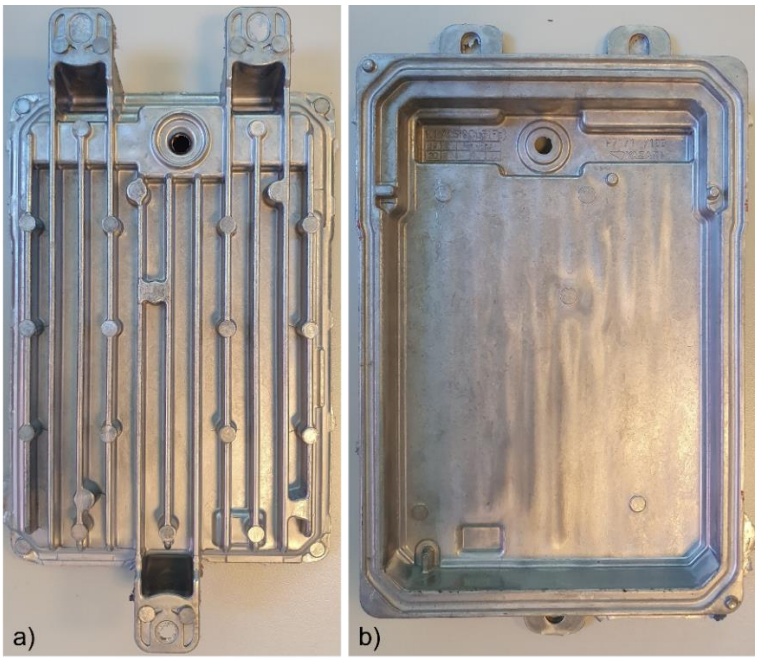

Figure 37: Power electronics casing. a) top view of the part; b) bottom view of the part.

Table 16: Main injection parameters.

	AlSi12(Fe)	**AlSi10Mg(Fe)**	**AlSi10MnMg**	**AlMg4Fe2**
Average velocity in gates during the 2nd phase (m/s)	30 - 35(*)			
Pouring temperature (°C)	670 (ΔT≈100°C)	670 (ΔT≈100°C)	670 (ΔT≈100°C)	700 (ΔT≈80°C)
Die temperature (°C)	145 - 220			
Vacuum pressure (mbar)	200			

$\Delta T = T_{Pouring} - T_{Solidus}$; *: These speeds were obtained in the ProCAST software

Figure 38 shows the average velocity at the gates as a function of filling time for the AlMg4Fe2 alloy during its vacuum-assisted injection simulated numerically in ProCAST software. These values are within the standardized range (18 - 41m/s) by NADCA.

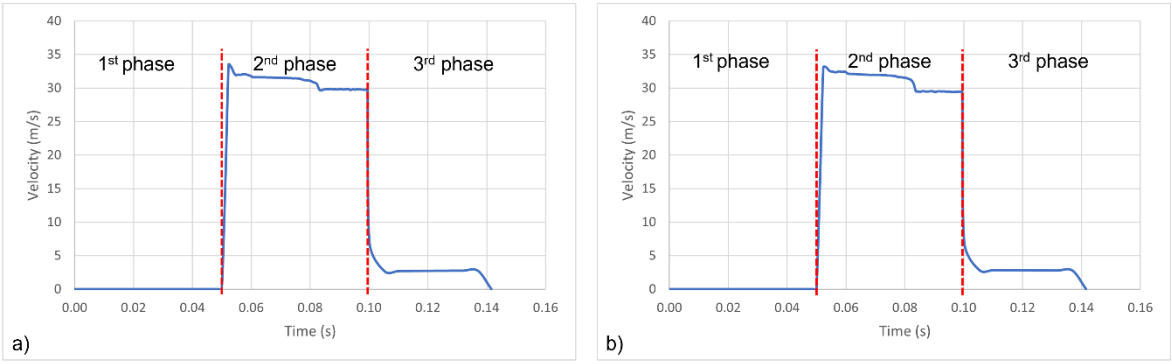

Figure 38: a) Average velocity in the left gate; b) Average velocity in the right gate.

Figure 39 shows an injected part attached to the gating system, vacuum channel and overflows.

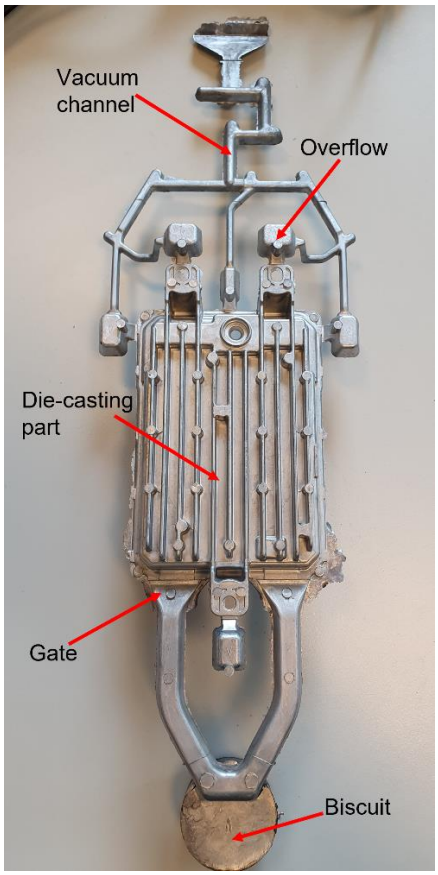

Figure 39: Die-casted part with its gating and venting system.

3.2 Procedure performed

3.2.1 Production of the specimens

Specimens for tensile testing follow the guidelines of ASTM B557M-15 [59]. The specimen dimension is shown in Figure 40.

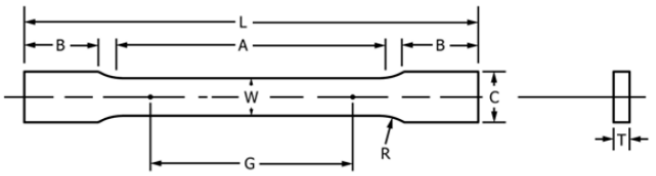

G – Gage length	25.0 ± 0.1
W – Width	6.0 ± 0.1
T – Thickness	thickness of material
R – Radius of fillet	6
L – Overall length	100
A – Length of reduced section	32
B – Length of grip section	30
C – Width of grip section	10

Figure 40: Specimen dimensions (mm) according to ASTM B557M-15. Adapted from [59].

These specimens will be used to determine the mechanical properties of the alloys under study and for density measurement, as a representative factor of the porosity present in the injected parts.

The specimens were obtained by machining the injected parts. Figure 41 shows the positioning of the specimens in the part and the support (Figure 42) used to fix the parts during machining.

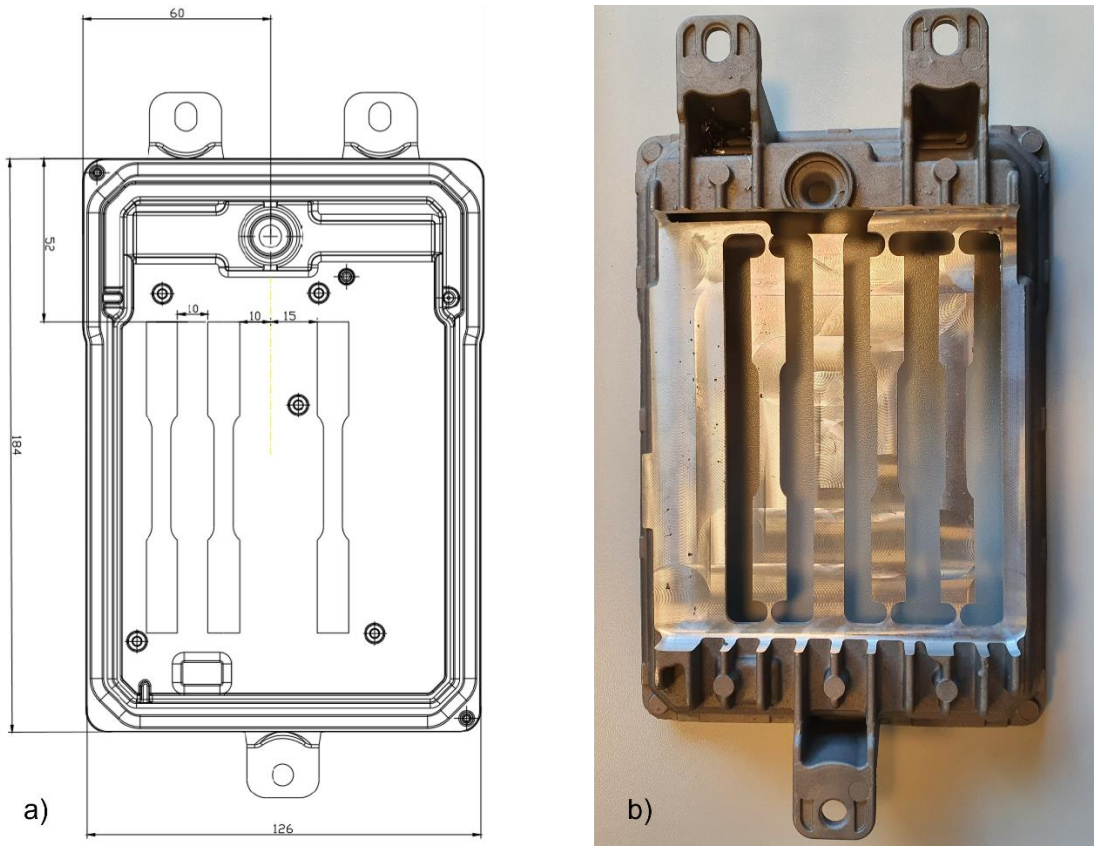

Figure 41: a) CAD model of the specimen positioning - bottom view of the part; b) Positioning the specimens after machining - top view of the part.

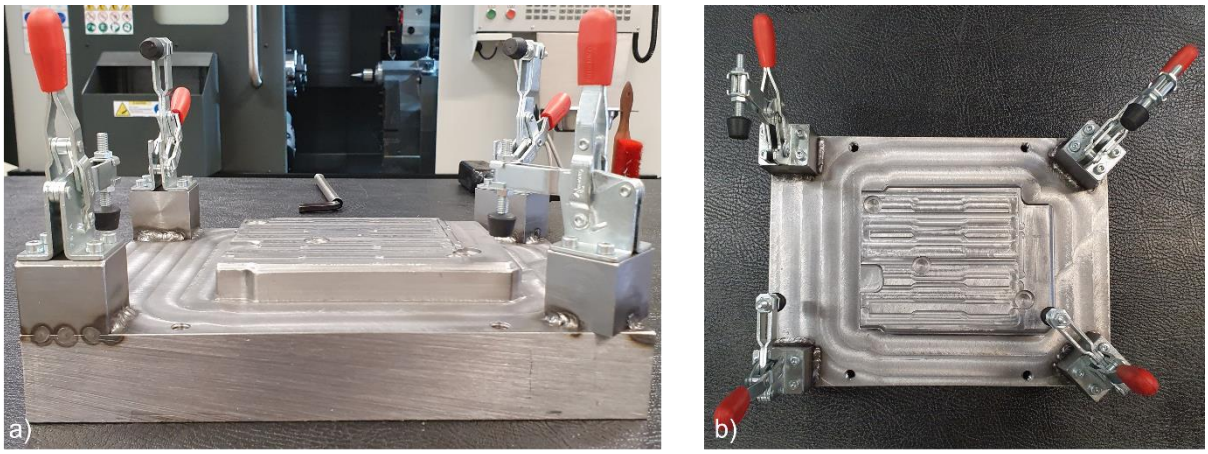

Figure 42: Support used for machining the parts. a) side view; b) top view.

Due to the warping of some parts during mold ejection (Figure 43), it was not possible to obtain a flat surface, which means that it would not be possible to obtain tensile specimens with constant thickness.

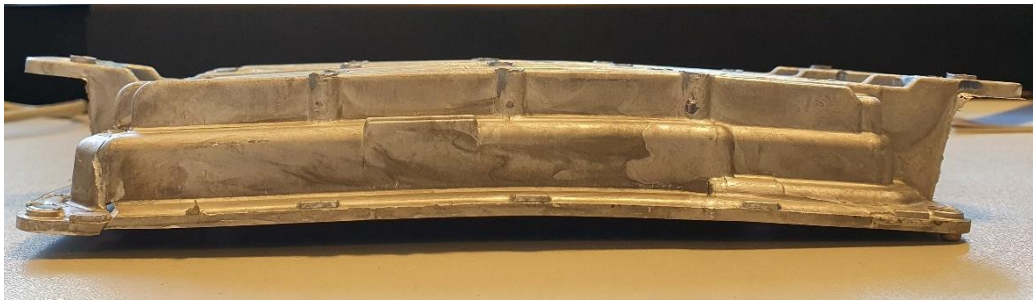

Figure 43: Example of a warped part.

In order to obtain the flattest possible parts, it was necessary to straighten them as well as possible. For the straightening, a hydraulic press was used and the assembly in this operation is shown in Figure 44. This assembly consists of three small 1.5 mm thickness plates, two of them were placed at the ends of the part and the third is placed in the area where the part has a belly due to warping. On the top surface of the part, besides the 1.5 mm plate, another plate (blue colored) and a bar were used to ensure a better load distribution.

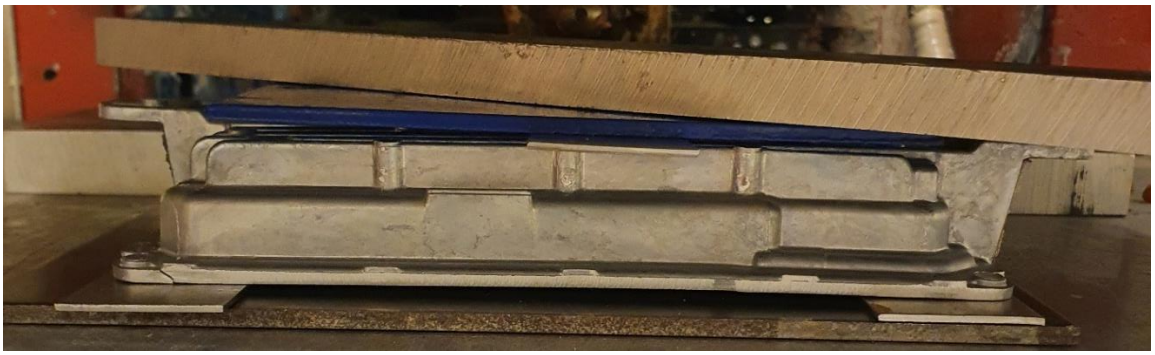

Figure 44: Assembly used to straighten the parts.

In order to have a good statistical sample, it was decided to take specimens of four injected parts with and without vacuum of each alloy, i.e., for each alloy there are twelve specimens whose parts were injected with vacuum assistance and twelve specimens whose parts were injected conventionally.

3.2.2 Density Measurement

A Foseco model BC 1500C balance (Figure 45) was used to determine the density of the specimens using the Archimedes method. Only one measurement was made for each specimen. For each alloy and injection type combination, 12 tensile test specimens were analyzed. With this system, the maximum length of the sample cannot be bigger than the diameter of the container with water.

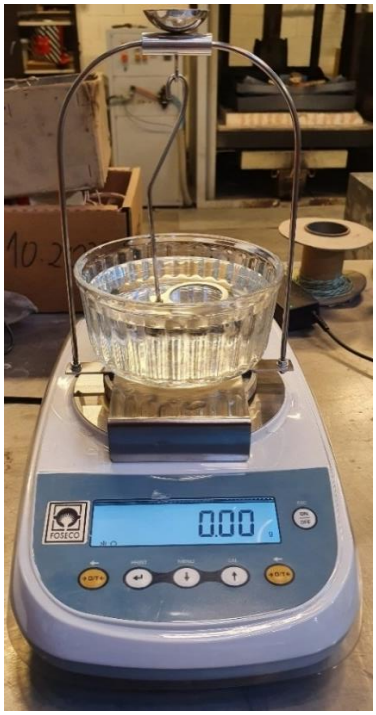

Figure 45: Foseco BC 1500C.

3.2.3 Tensile tests

For the tensile tests only nine of the twelve machined specimens were used, i.e., there were three specimens left that could be used if any of the tests were invalid.

To choose which nine specimens would be used, the thickness (Figure 46 a)) and the width (Figure 46 b)) of the cross section were measured in three different points in each of the twelve specimens. Then, the cross-sectional area of each specimen was calculated and the three specimens whose cross-sectional area was farthest from the average were removed.

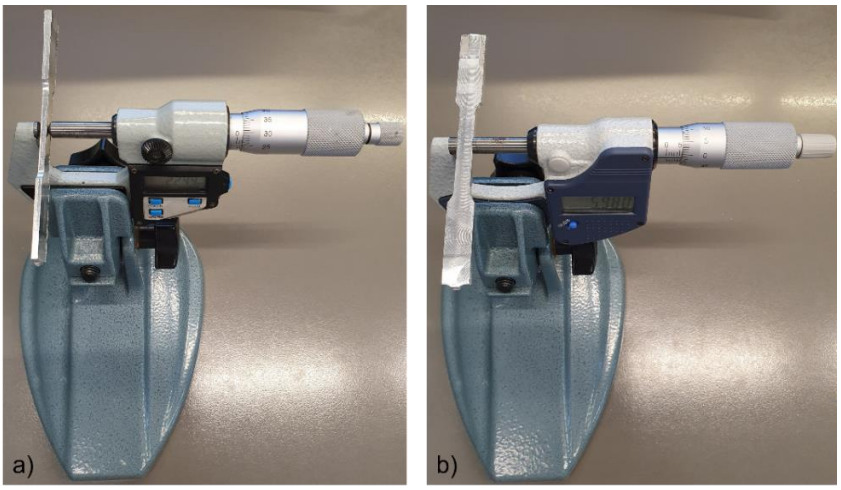

Figure 46: a) Curved-face digital micrometer; b) Flat-face digital micrometer.

The tensile tests were performed at room temperature on an Instron 5900R machine with a 5 kN load cell and at a strain rate of 0.5 mm/min. Digital Image Correlation (DIC) was used to measure the specimens' deformation throughout the test, instead of the usual strain gauges.

DIC is an optical technique that allows strains' and displacements' measurement without contact. This is done by tracking blocks of pixels that allow a data processing system to measure surface displacement and develop strain maps and deformation vector fields. In order to be able to analyze the deformation, digital photographs at different deformation stages of a given component are compared. The scattering of the pixel blocks needs to be random and unique with a certain level of contrast to ensure that this technique works properly [60, 61]. There are already DIC systems that can analyze from micro-scale to the macro-scale, thus allowing this technique to be used on large structures [62].

To be able to use this analysis technique, it was necessary to sand one of the faces of the specimens with water sandpaper, so that they could be painted. First, a layer of white paint was applied (Figure 47 a)), and then they were painted with black paint so that only black dots were formed (Figure 47 b)) to be able to track the blocks of pixels throughout the test. The acquisition of image data starts at the same time as the tensile test. For the data acquisition, it is necessary a machine to perform the tensile tests, a camera and a spotlight pointed at the gage section of the specimen (Figure 48). At the end of the test, two reports are obtained, one from the tensile testing machine and another from the DIC program (VIC-2D), which need to be combined to obtain the stress-strain curve.

Figure 47: a) specimen painted with a white layer; b) specimen with black dots on the white layer.

Figure 48: a) spotlight; b) data acquisition camera; c) Instron 5900R machine.

3.2.4 Chemical composition of alloys

The chemical composition analysis of the parts was performed on an Ametek SPECTROMAXx (Figure 49) using arc/spark optical emission spectrometry (OES).

Figure 49: Ametek SPECTROMAXx used in chemical composition analysis.

The analysis was performed on the ear of the part (Figure 50) and six parts of each alloy were used, three of them injected with vacuum assistance and the other three conventionally injected. It should be noted that the use of vacuum has no influence on the chemical composition of the parts. Then, the obtained values were compared with the standard compositions of the alloys.

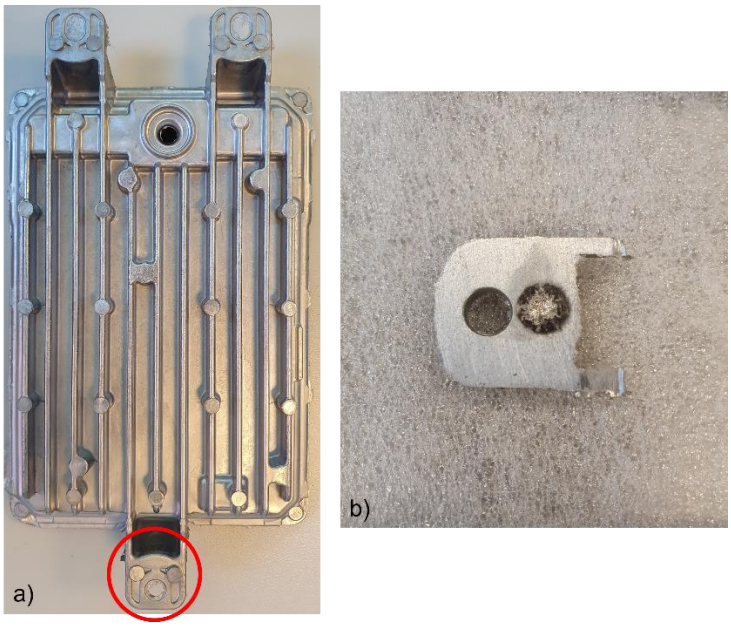

Figure 50: a) Ear location on the part; b) Ear after chemical composition analysis.

3.2.5 Microstructure

Microstructure and defect analysis was carried out using an Olympus PMG 3 optical microscope with a Leica DP12 digital camera.

The smaller samples were hot-mounted onto cylindrical blocks of phenolic resin using a Struers ProntoPress-2. These cylindrical blocks were then placed in sample holders to facilitate the polishing process on a semi-automatic polishing machine.

The samples were polished with silicon carbide sandpaper with grit sizes of 180, 320, 600, 1000 and 2400 grit. Polishing was finished with aluminum cloths impregnated with 3 μm and 1 μm diamond spray.

For the samples that were used to study porosities, images were taken on the microscope at 23x magnification and then processed and analyzed in ImageJ software.

Due to the typical microstructural refinement of the injected alloys, there was some difficulty to identify typical structures in the images observed in the optical microscope. Thus, for a better characterization of the microstructure, scanning electron microscopy (SEM) was used in conjugation with energy dispersive spectroscopy (EDS).

An Olympus SZH stereo microscope was used to analyze the fracture zone of the specimens.

The hardness measurements were performed in an EMCO M4U-075 hardness tester (Figure 51). Taking into account the hardness values that were expected, a Brinell test (HB5) was performed with a spherical tip indentor in tungsten carbide with a diameter of 2.5 mm, which corresponds to a force of 31.25 kgf. For each sample, three tests were performed and then the final hardness was taken as the average of the tests.

Figure 51: EMCO M4U-075 hardness tester.

3.2.6 TAC

In order to have a general perception of the defect level (gas porosity and shrinkage porosity) a computed tomography system was used (non-destructive test). The computed tomography was performed by NM3D Ibérica on a Nikon XT H 225 ST 2X, and then the

general defect analysis was performed at INEGI by using the myVGL software. In order to analyze the porosity on a specific section of the part, it was performed at NM3D Ibérica a 2D porosity analysis using a porosity analysis module programmed according to Volkswagen's VW50093 standard.

The above mentioned analyses were performed on parts of all alloys under study before heat treatment and after T6 heat treatment for parts of AlSi10MnMg and AlSi10Mg(Fe) alloys.

3.2.7 Heat treatment

The T6 heat treatment (solution heat treatment followed by artificial aging) was performed in a M. J. Amaral forced convection furnace (Figure 52) with a chamber of dimensions 600×600×700 mm³. The interior of the furnace has a double stainless-steel wall, so that there is no direct radiation to the components to be treated.

Figure 52: M.J. Amaral forced convection furnace with a chamber of dimensions 600×600×700 mm³.

In this furnace, the air circulates and heats from top to bottom, i.e., the lower zone of the furnace will be at a higher temperature than the upper zone of the furnace. The furnace has three thermocouples to understand the temperature distribution along its height. One is placed in the upper zone, one in an intermediate zone and the other in the lower zone. Besides reading the values of these thermocouples, three parts instrumented with a thermocouple were placed in three different locations of the furnace, (Figure 53 and Figure 54). Thus, it was possible to compare the temperatures of the parts with the furnace temperatures.

Figure 53: Thermocouple placed on test part.

M6 threaded rods and M6 nuts were used to position the parts inside the basket, Figure 54 a). Thus, there was no part-to-part contact, and the correct heating of the parts was ensured.

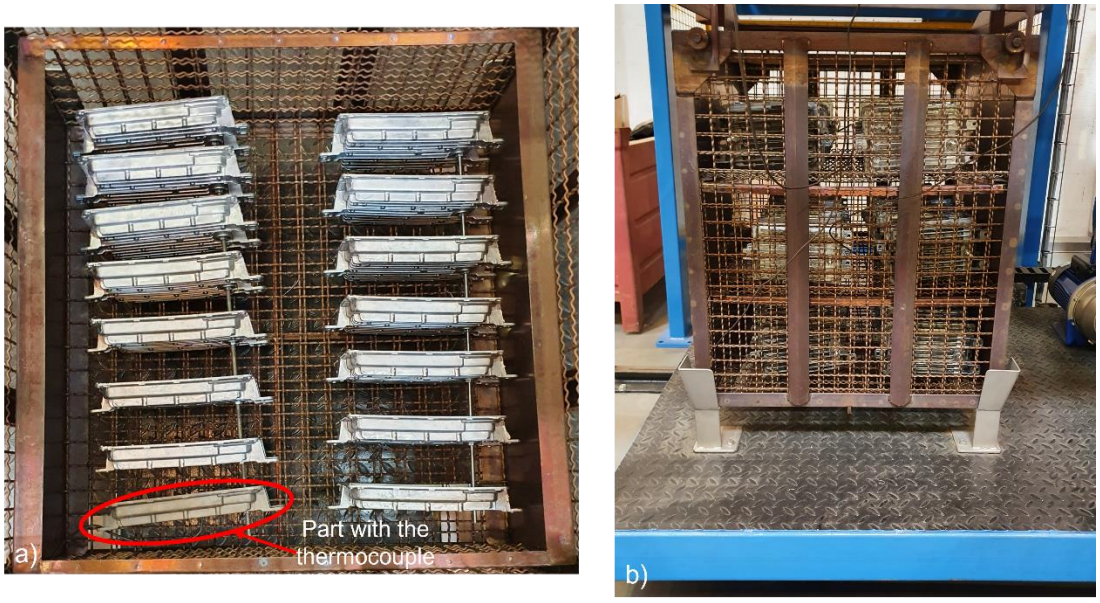

Figure 54: a) Parts placed in the basket; b) Parts before heat treatment.

In addition, 5 vacuum-assisted and 5 conventionally injected parts were heat treated for each of the alloys under study. The AlSi12(Fe) and AlMg4Fe2 alloys were treated only to verify the appearance or not of blistering on the parts, since these alloys do not react to the heat treatment performed.

The parameters of the T6 treatment performed were defined based on the Rheinfelden catalog [20]. Thus, ideally, the solution heat treatment should be carried out at 490°C for 2 hours, followed by water quenching (water temperature between 10 to 60°C). After the temperature of the parts is uniform, they should undergo a 2-hour stage at 170°C, corresponding to the artificial aging. Finally, the parts are air cooled. The Rheinfelden ideal T6 heat treatment can be seen in Figure 55.

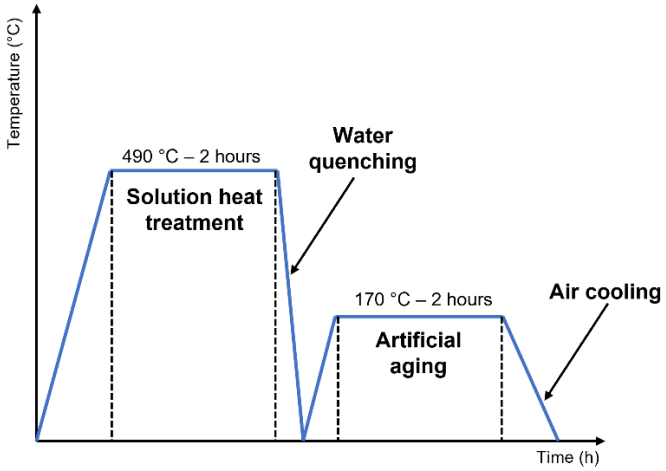

Figure 55: Theoretical T6 heat treatment.

The actual temperature curve can be seen in Figure 56. This curve was obtained from the values recorded by the thermocouples present in the furnace. The temperature curve of the upper thermocouple can be ignored because it is placed in an area of no interest for the temperature control of the parts. Note that the furnace temperature is controlled by the temperature of the thermocouple placed in the bottom zone.

The area highlighted in red in Figure 56 represents approximately the elapsed time between the quenching of the parts and the start of the artificial aging treatment. This time was approximately 1.6 hours, which is well below the maximum time (12 hours) recommended by Rheinfelden [20].

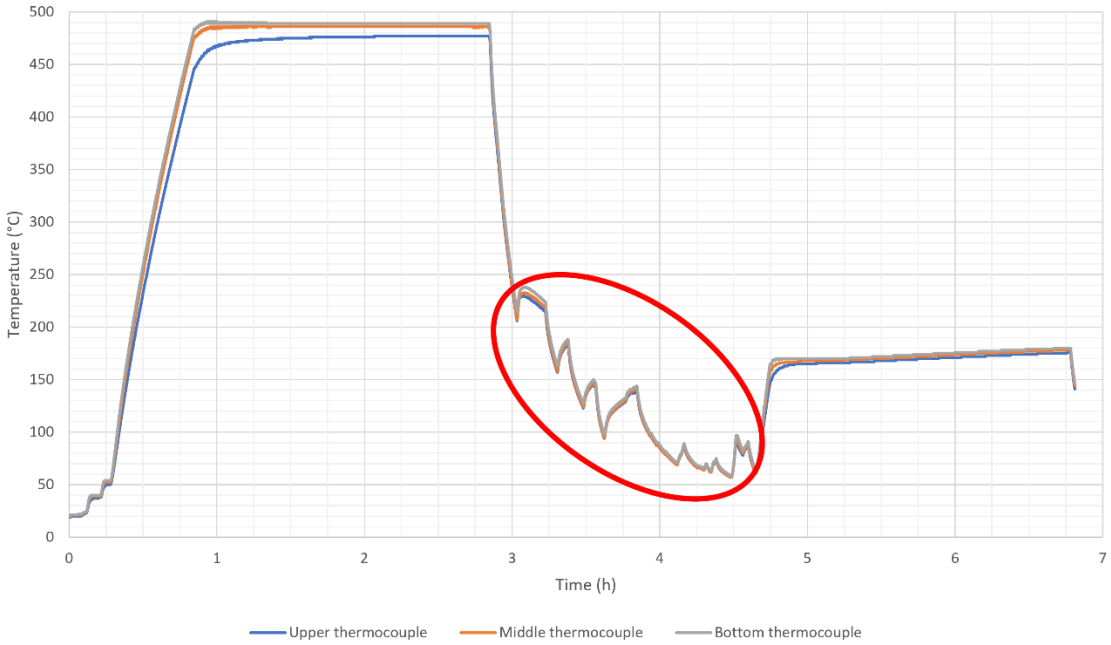

Figure 56: Temperature evolution in the furnace thermocouples during the T6 heat treatment.

To better understand the stage times and temperatures reached in the different stages of the heat treatment, the temperature evolution of the thermocouple placed in the lower zone of the furnace during the solution heat treatment is presented in Figure 57.

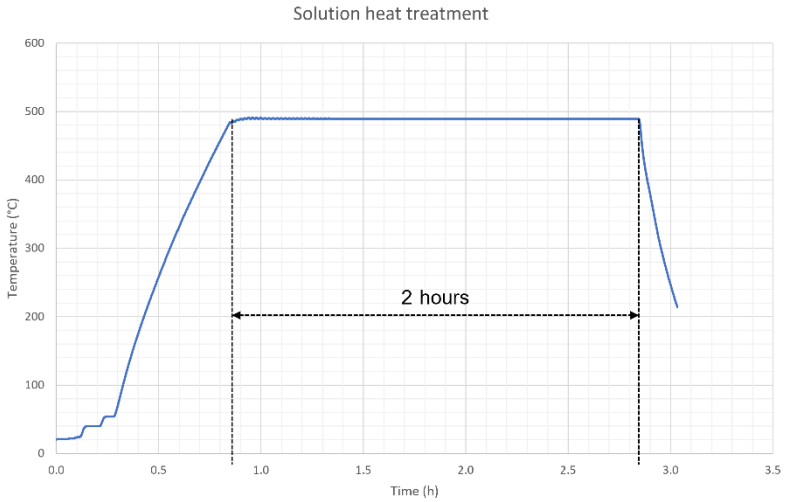

Figure 57: Temperature evolution at the bottom thermocouple during solution heat treatment.

Through Figure 57, it can be concluded that at least the temperature recorded inside the furnace, during the two hours of stage, was very close to the desired 490°C. When comparing the temperatures recorded by the furnace thermocouple with the temperatures recorded by the thermocouples that were placed in the test parts (Figure 58) it can be seen that the maximum difference between the read values is only 4°C. Between the parts that are placed on different floors inside the basket, the maximum thermal gradient is 5°C, which can be considered a practically negligible value considering the temperature range that is being used and the values of thermal gradients obtained in previous works developed at INEGI.

Figure 58: Temperature of thermocouples placed on the test parts during the solution heat treatment.

Figure 59 shows the temperature evolution of the thermocouple placed in the lower zone of the furnace during the artificial aging treatment.

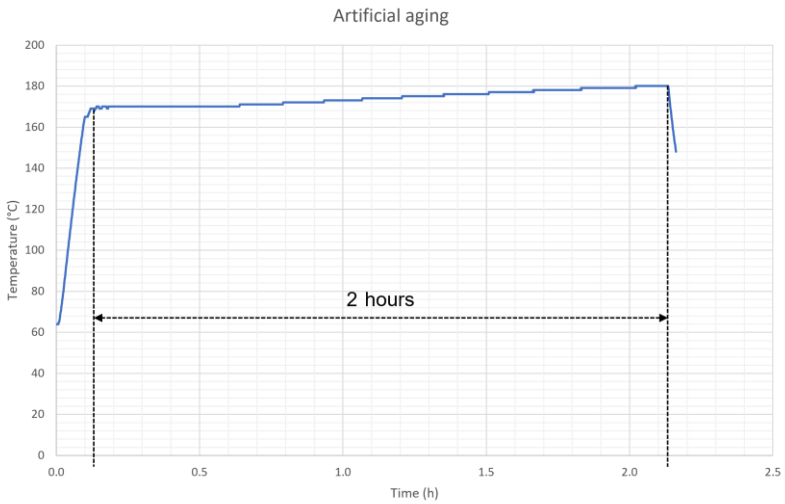

Figure 59: Temperature evolution at the bottom thermocouple during artificial aging heat treatment.

During artificial aging, the preset temperature of 170°C was increased throughout the aging time until 180°C, which was reached near the end of the cycle. This difficulty of the furnace in maintaining the temperature of 170°C can be justified by the fact that the calibration of the furnace was made for temperatures close to 500°C, so that in this temperature range the maximum thermal gradient is 5°C. The parts placed in the middle and top of the basket were at the same temperature of the furnace (180°C), while the thermocouple placed in the lower part of the basket was at 178°C, Figure 60.

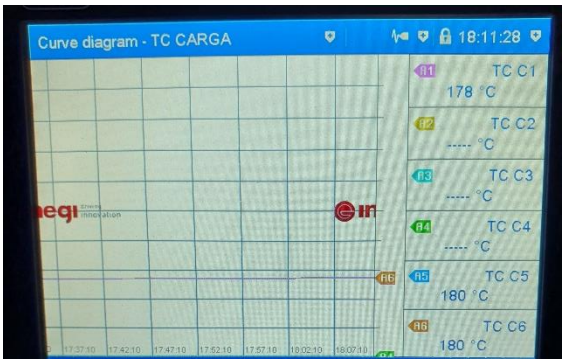

Figure 60: Temperature of thermocouples placed on the test parts during the artificial aging heat treatment.

4 Analysis and discussion of the results

In this chapter the results obtained will be presented and their analysis and discussion will be carried out. It is intended to compare the mechanical properties of the primary alloys (AlSi10MnMg and AlMg4Fe2) with those of the secondary alloys (AlSi12(Fe) and AlSi10Mg(Fe)) and to evaluate if the injection performed with vacuum assistance improves the mechanical properties of the components, especially ductility. This mechanical property is one of the most important properties in structural safety components in vehicles, because it has direct implication in the ability of a given component to absorb the greatest amount of energy during an accident. The results of the heat-treated parts (T6 heat treatment) will also be analyzed, to verify if the vacuum injected parts show less blistering than the conventionally injected parts, and, if the heat treatment improves the strength and ductility of these parts.

4.1 Analysis of the chemical composition of alloys

The chemical composition analysis was carried out on all the alloys in order to understand the possible modifications in the chemical composition of the alloys under study, from ingots melting to the obtaining of the injected parts. Modifications in the chemical composition could influence the injection conditions and affect negatively the mechanical properties.

For each of the alloys, a table will be presented where the average values obtained for the main chemical elements are compared with the standard values for the ingots of the alloy in consideration. In Appendices B to E the full reports of the analyses performed are presented. Presumably, there will be slight differences between the obtained values and the standard values because the standard chemical composition is obtained in the ingot while the experimental value was obtained in the parts. These differences can happen once the alloy has already been melted and may have been contaminated with other chemical elements or some of the initial chemical elements may have had their composition altered, for example, because there was their loss during the melting.

4.1.1 AlSi12(Fe)

Table 17 shows the chemical composition of AlSi12(Fe) alloy:

Table 17: Chemical composition of AlSi12(Fe) alloy (weight in %).

	Si	Fe	Cu	Mn	Zn	Ti	Al
a	12.1	0.81	0.25	0.40	0.10	0.03	86.22
b	10.5-13.5	<1	<0.10	<0.55	<0.15	<0.15	Bal.

a- values of the samples; b- NP EN 1706 2000 standard values [25]

All the values obtained from the chemical composition are in accordance with the standard, except for the copper value that is slightly above (0.25% vs. maximum 0.1%). Despite being slightly above than expected, the alloy under study is still considered AlSi12(Fe), because both AlSi12Cu1(Fe) and AlSi12(Cu) alloys already have Cu and Fe limit values that do not fit as well as those of AlSi12(Fe) alloy.

4.1.2 AlSi10Mg(Fe)

Table 18 shows the chemical composition of AlSi10Mg(Fe) alloy:

Table 18: Chemical composition of AlSi10Mg(Fe) alloy (weight in %).

	Si	Fe	Cu	Mn	Mg	Ni	Zn	Ti	Sn	Pb	Al
a	10.6	0.88	0.14	0.09	0.2	0.01	0.05	0.04	0.001	0.01	87.97
b	9-11	<1	<0.10	<0.55	0.2-0.5	<0.15	<0.15	<0.20	<0.050	<0.15	Bal.

a- values of the samples; b- NP EN 1706 2000 standard values [25]

Again, the only value that is slightly above the standard value is the copper value, and in this case the difference is very small (0.14% vs. maximum of 0.1%).

4.1.3 AlSi10MnMg

Table 19 shows the chemical composition of AlSi10MnMg alloy:

Table 19: Chemical composition of AlSi10MnMg alloy (weight in %).

	Si	Fe	Cu	Mn	Mg	Zn	Ti	Sr	P	Al
a	11.1	0.13	0.001	0.6	0.25	0.001	0.04	0.010	0.001	87.82
b	9.5-11.5	<0.15	<0.030	0.5-0.8	0.10-0.50	<0.070	0.04-0.15	0.010-0.025	<0.001	Bal.

a- values of the samples; b- standard values [20]

All the chemical composition values of the samples are within the standard ranges. However, the copper and zinc values are below what would be expected. Since the percentages of zinc and copper are very low, the zinc compounds with copper and/or magnesium that are attractive for heat treatment may not be formed. The iron percentage being slightly lower than the maximum standard value is optimal to prevent the formation of the harmful AlFeSi phases for ductility. Since an average content of 0.25% Mg was obtained in the parts analyzed they should show better ductility values than mechanical strength [20]. On the other hand, with a manganese percentage around 0.61% it is expected that the elongation values will be slightly lower than expected [20].

4.1.4 AlMg4Fe2

Table 20 shows the chemical composition of AlMg4Fe2 alloy:

Table 20: Chemical composition of AlMg4Fe2 alloy (weight in %).

	Si	Fe	Cu	Mn	Mg	Zn	Ti	Al
a	0.10	1.5	0.01	0.01	4.9	0.01	0.01	93.38
b	<0.20	1.5-1.7	<0.20	<0.15	4.0-4.6	<0.30	<0.20	Bal.

a- values of the samples; b- standard values [27]

The only value outside the standard value range is the magnesium percentage. This slight increase (4.9% vs. maximum 4.6%) may slightly impair the elongation values since higher percentages of Mg reduce elongation, but on the other hand causes an increase in mechanical strength. The silicon and manganese content being low is important to prevent the formation of phases that are detrimental to the mechanical properties.

4.2 Density analysis

To understand if the vacuum injected parts had less porosity than the conventionally injected parts, the density of the specimens that would be used to determine the mechanical properties was determined. In theory, the conventionally injected parts would have larger quantities of entrapped gases, and therefore their density would be lower than the density of the parts injected with vacuum assistance.

Table 21 shows the average density of each alloy injected with vacuum and without vacuum after measuring the twelve specimens as well as the standard density of each alloy.

Table 21: Density of vacuum and non-vacuum injected alloys and their theoretical density.

	Density (kg/dm³)		
Alloy	**With vacuum**	**Without vacuum**	**Standard**
AlSi12(Fe)	2.6850±0.0040	2.6806±0.0259	2.65-2.71 [25]
AlSi10Mg(Fe)	2.6874±0.0033	2.6859±0.0041	2.66-2.71 [25]
AlSi10MnMg	2.6671±0.0211	2.6661±0.0211	2.64 [20]
AlMg4Fe2	2.6411±0.0173	2.6559±0.0113	2.69 [27]

AlSi12(Fe) and AlSi10Mg(Fe) alloys are the only ones that present the closest results to the expected ones, i.e., the density is higher in the parts that were injected with vacuum and the value obtained for the density is within the standard range of values.

Also, in Silafont-36 (AlSi10MnMg), the vacuum injected parts' density is slightly higher than the conventionally injected parts' density, which is in agreement with what is expected. However, the experimentally measured density is slightly higher than the standard density value.

In contrast to AlSi10MnMg the Castaduct-42 (AlMg4Fe2) alloy has a lower experimental density than the standard density. However, it was the only alloy where the parts injected with vacuum had a lower density than the conventionally injected parts. This result, which was not expected, can be justified by the fact that three of the twelve specimens that were machined from parts injected with vacuum had voids/shrinkages (Figure 61) visible to the naked eye that caused slight drops in the density values measured.

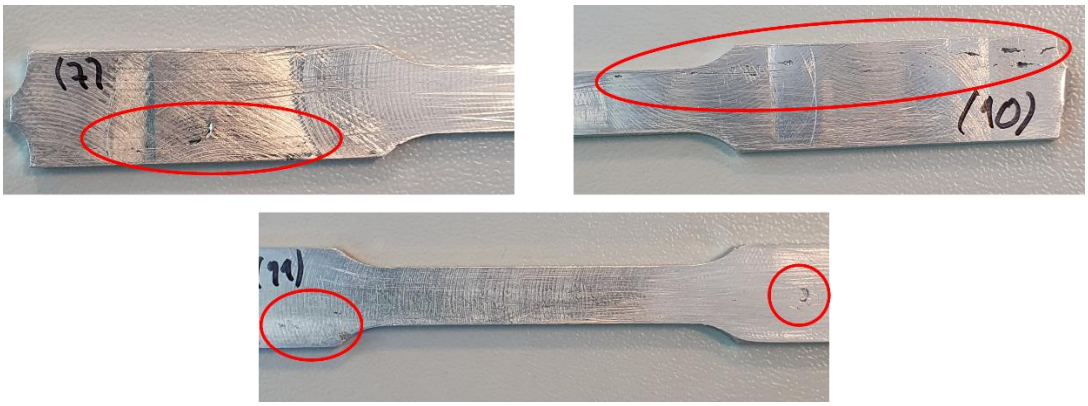

Figure 61: Specimens with defects visible to the naked eye.

This first attempt to understand if the vacuum injected parts would have a lower quantity of gas porosities was not very conclusive. In alloys where the density of the vacuum injected parts was higher than the density of the conventionally injected parts, the difference between densities ranges from 0.04% to 0.16%, which as will be seen later is an almost negligible difference. Thus, through this experimental method it was not possible to conclude that the use of vacuum during injection led to a decrease in the quantity of trapped gas.

It should be noted that the small size of the specimens may be the origin of the small variations that exist in the density values. For a more sensitive measurement, the density should be checked on the part, but due to the equipment limitations (Chapter 3.2.2) this was not possible.

4.3 Hardness tests

Initially, hardness was measured on samples (Figure 62) taken from parts in the as-cast condition. This initial measurement was performed to verify if the values obtained experimentally were in agreement with the standard values.

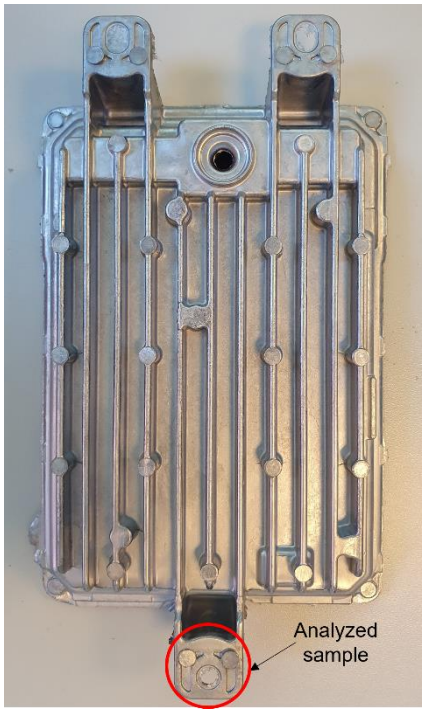

Figure 62: Sample used for hardness measurement.

Table 22 shows the results of the measurements made, the average of these results and the theoretical hardness value for each of the alloys in the as-cast condition.

Table 22: Hardness values obtained for all alloys in as-cast condition.

		Hardness (HB)				
Alloy	**Sample**	**Measure 1**	**Measure 2**	**Measure 3**	**Average**	**Standard**
AlSi12(Fe)	1	81.6	84.8	83.2	83±1.25	Min. 60 [25]
	2	82.2	83.5	84.5		
AlSi10Mg(Fe)	1	89.2	90.3	86.9	88±1.62	Min. 70 [25]
	2	87.3	88.6	85.9		
AlSi10MnMg	1	80.3	79.6	77.5	77±2.50	75-95 [20]
	2	76.8	74.2	74.6		
AlMg4Fe2	1	70.3	69.3	68.8	69±1.41	65-75 [27]
	2	71.4	67.4	68.5		

For all alloys in the as-cast condition, the experimentally obtained hardness are very close to the values that were expected. Only in the secondary alloys (AlSi12(Fe) and AlSi10Mg(Fe)) as there is no range of values for standard hardness, but only a minimum value, however the hardness value experimentally obtained is higher when compared to the standard one.

After performing the T6 heat treatment, hardness was measured again on the parts of AlSi10Mg(Fe) and AlSi10MnMg alloys, Table 23.

Table 23: Hardness values obtained for AlSi10Mg(Fe) and AlSi10MnMg alloys after T6 treatment.

		Hardness (HB)				
Alloy	**Sample**	**Measure 1**	**Measure 2**	**Measure 3**	**Average**	**Standard**
AlSi10Mg(Fe)	1	56.0	56.4	57.0	61±5.16	-
	2	67.4	65.4	64.3		
AlSi10MnMg	1	82.0	86.2	85.0	85±1.78	90-110 [20]
	2	85.5	85.2	87.3		

After the T6 heat treatment it is expected an hardness increase in AlSi10Mg(Fe) and AlSi10MnMg alloys due to the precipitation of Mg-Si intermetallics in the aluminum matrix. When comparing the hardness values from Tables 22 and 23, it is seen that the increase in hardness only occurred for the AlSi10MnMg alloy.

In the case of AlSi10MnMg alloy an average hardness value of 85 HB was obtained, thus being slightly below the expected minimum, 90 HB. This difference is almost negligible and can be justified by the fact that the artificial aging treatment was performed only for two hours, when it could have been done for three hours. That is, the peak of hardness could occur after the two hours of aging for a temperature of 170°C.

In the AlSi10Mg(Fe) alloy, there was a hardness decrease of approximately 31% between the as-cast condition and after the T6 treatment. This hardness decrease could be explained by the softening of the material caused by coarsening of the silicon during solution heat treatment. In addition, Bruno [49] studied the optimization of the T6 heat treatment for the AlSi10Mg(Fe) alloy and performed hardness measurements in the as-cast condition, after the solution treatment and during the artificial aging treatment. The hardness obtained in the as-cast condition was 84 HB, very similar to the value that was obtained (88 HB). After the two solution heat treatments performed (460°C for 15 minutes and 450°C for 15 minutes) there was a decrease in hardness to values close to 63 HB. After solution treatment at 450°C for 15 minutes, artificial aging at 180°C for 8 hours was performed. After 2 hours of the beginning of the artificial aging, the average hardness was approximately 69 HB. In the present work after artificially aging for 2 hours at 170°C a hardness of 61 HB was obtained. It is known that higher temperatures during aging lead to an earlier peak of hardness, and therefore can be explained the difference of 8 HB that is obtained between the values obtained by Bruno and those obtained in this work. In the work developed by Bruno, it is considered that the peak of hardness is reached at 5 hours and 30 minutes, and therefore if the aging treatment that was carried out at 170°C was prolonged in time, the hardness obtained would probably be higher than the one obtained in the as-cast condition.

4.4 Defect analysis by 3D X-ray computed tomography and metallography

4.4.1 3D X-ray computed tomography

Before performing the heat treatment in the injected parts, some of them were analyzed by 3D X-ray computed tomography: two AlSi12(Fe) alloy parts, one injected using vacuum and the other injected conventionally; six AlSi10Mg(Fe) alloy parts, three injected using vacuum and the other three injected conventionally; six AlSi10MnMg alloy parts, three injected using vacuum and the other three injected conventionally; two AlMg4Fe2 alloy parts, one injected using vacuum and the other injected conventionally.

This initial analysis allows to understand the distribution of defects along the part, if there is any pattern, if the injection with vacuum reduces the appearance of gas porosities and if the

location of defects meets the numerically simulated results. Since in the HPDC process there are two types of porosities, gas porosities and shrinkages, it was necessary to find a way to distinguish them [63]. Thus, the distinction was made by taking into account the sphericity of the defects. Kang et al. [63] used this distinction and defined that defects with sphericity above 0.4 would be gas porosities and sphericity values below 0.4 would be shrinkages. This will be the distinction criterion used in this work.

In the analysis performed on the myVGL software for all parts, the values of the defect quantity, defects volume (mm^3), defect volume ratio (%), sphericity, defect diameter (mm) and average defect volume (mm^3) were obtained. In the case of AlSi10Mg(Fe) and AlSi10MnMg alloys, as more than one part was analyzed, it was possible to calculate the defect volume ratio average and the standard deviation. Table 24 shows the results obtained for the parts in the as-cast condition.

Table 24: Results of porosity measurement in as-cast parts by 3D X-ray computed tomography.

Alloy	**Vacuum**	**Part No.**	**Quantities**	**Defects volume** (mm^3)	**Average defect volume** (mm^3)	**Defect volume ratio** (%)
AlSi12(Fe)	Yes	1	78	17.33	0.222	0.010
	No	1	217	52.29	0.241	0.030
AlSi10Mg(Fe)	Yes	1	79	19.19	0.242	0.013
		2	2062	85.28	0.042	0.061
		3	253	54.53	0.216	0.039
	No	1	11525	199.55	0.018	0.143
		2	15528	366.48	0.025	0.262
		3	15921	259.89	0.017	0.186
AlSi10MnMg	Yes	1	357	76.01	0.213	0.055
		2	264	57.98	0.220	0.042
		3	279	62.86	0.226	0.046
	No	1	3792	98.03	0.027	0.071
		2	6782	161.49	0.025	0.116
		3	7138	233.91	0.034	0.169
AlMg4Fe2	Yes	1	196	88.75	0.453	0.070
	No	1	1115	399.34	0.358	0.290

In the case of the AlSi12(Fe) alloy, the use of vacuum during injection caused defects to be reduced by 64%. In Figure 63, it is possible to see the difference in defects between the two parts.

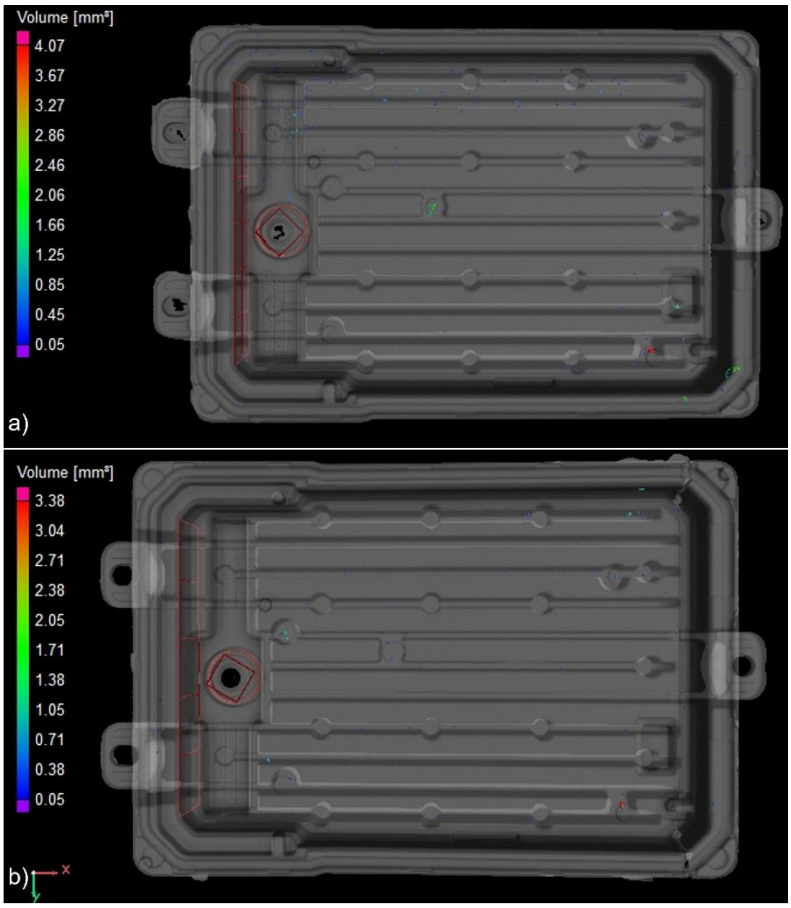

Figure 63: Results of CT analysis of AlSi12(Fe) alloy as-cast parts. a) part injected without vacuum; b) part injected with vacuum.

In both figures, the highest percentage of defects is found in areas where the volume is higher, with the conventionally injected part showing a greater quantity of defects, most of them being gas porosities (Figure 64).

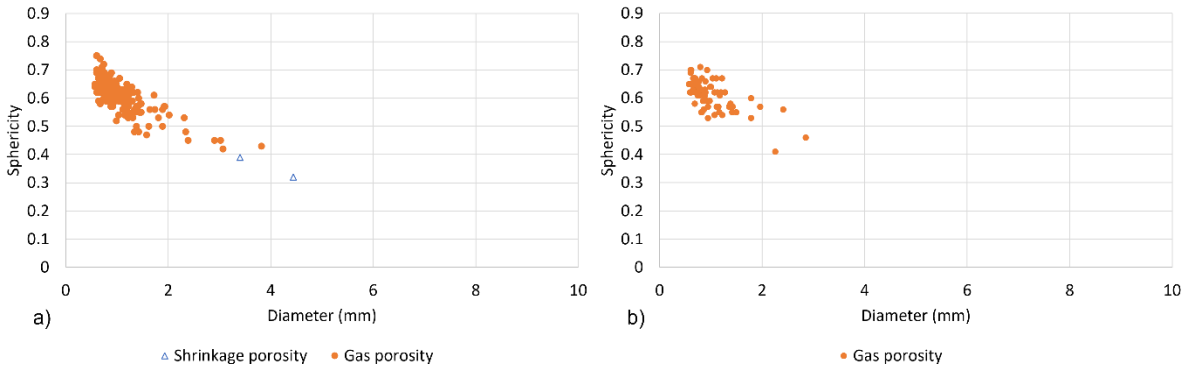

Figure 64: Sphericity and diameter of the porosities present in the AlSi12(Fe) alloy parts. a) HPDC; b) VADC.

As expected, according to Figure 65, shrinkage porosity will tend to appear in the areas with higher mass concentration. There is some similarity between the results shown in Figure 63 and those shown in Figure 65, in terms of shrinkage porosities.

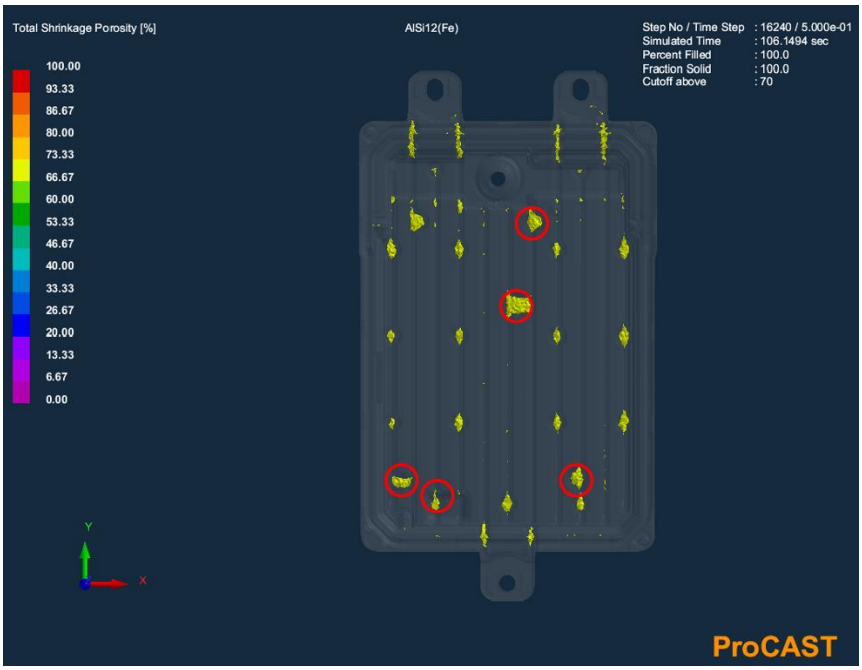

Figure 65: Numerically simulated shrinkage porosity in ProCAST software for AlSi12(Fe) alloy.

For the conventionally injected AlSi10Mg(Fe) alloy parts, the average defect volume ratio value was 0.20% with a standard deviation of 0.06. On the other hand, the parts that were not conventionally injected had an average defect volume ratio value of 0.04% and a standard deviation of 0.02. Once again, the use of vacuum during injection made it possible to reduce the percentage of defects by 81%. Since the standard deviation values are very low for both injection with vacuum and without vacuum, it can be concluded that there is some repeatability during the process, at least in these six parts analyzed. Figure 66 shows the CT results.

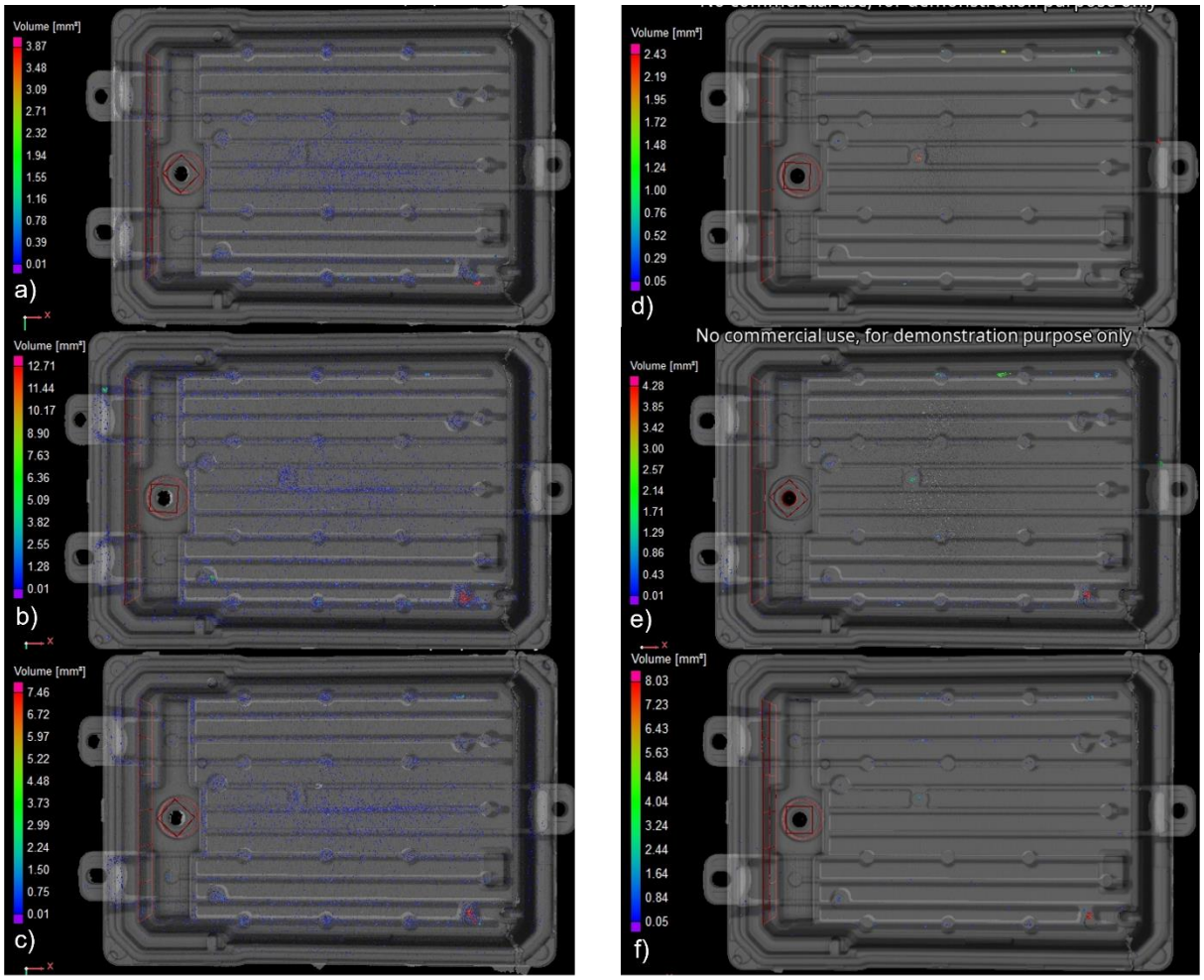

Figure 66: Results of CT analysis of AlSi10Mg(Fe) alloy as-cast parts. a), b), c) parts injected without vacuum; d), e), f) parts injected with vacuum.

The main difference between vacuum injected parts (d), e) and f)) and conventional injected parts (a), b) and c)) is the large quantity of small porosities (blue points) distributed mainly in the fin region and in the central area of the part. By analyzing the graphs in Figure 67, it can be concluded that the larger number of defects in the conventionally injected parts is due to an increase in the amount of gas porosity. The graphs for the remaining parts can be seen in Appendix F.

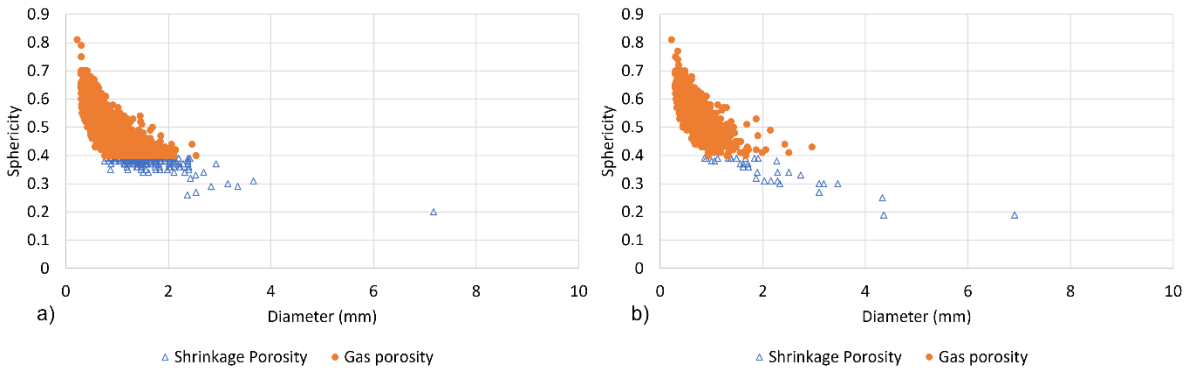

Figure 67: Sphericity and diameter of the porosities present in the AlSi10Mg(Fe) alloy parts. a) Part of Figure 66 c) (HPDC); b) Part of Figure 66 e) (VADC).

After analyzing the results obtained in the numerical simulation (Figure 68) and taking into account that the defects with the largest diameter are shrinkage porosities (Figure 67), it

can be concluded that probably the defects with the largest volume in Figure 66 are shrinkage porosities.

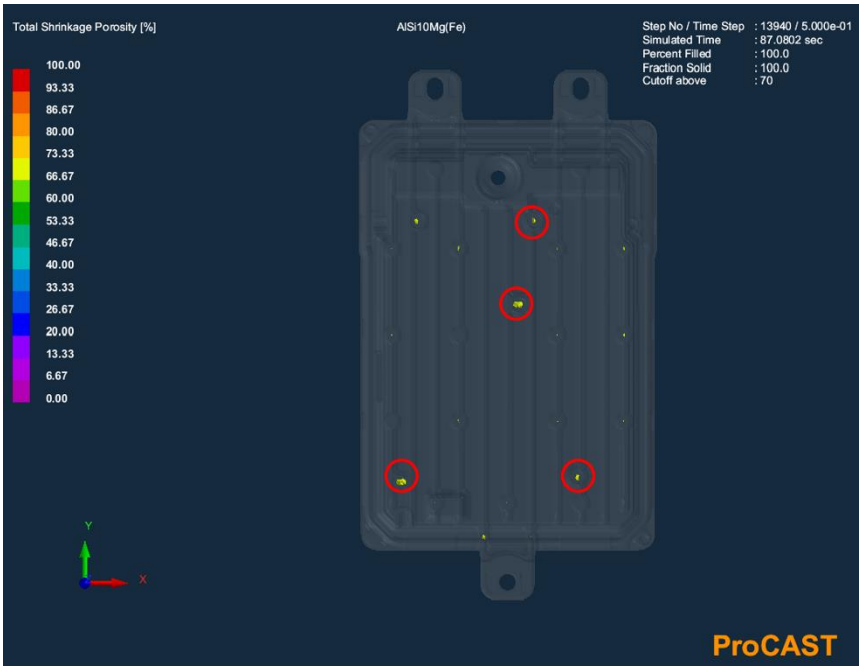

Figure 68: Numerically simulated shrinkage porosity in ProCAST software for AlSi10Mg(Fe) alloy.

The parts conventionally injected in Silafont-36 alloy (AlSi10MnMg) showed an average defect volume ratio of 0.12% and a standard deviation of 0.05. In contrast, in the vacuum injected parts there was an improvement, as the average defect volume ratio decreases to 0.05% and the standard deviation obtained was 0.01. There was a reduction of defects by about 60%, so once again the use of vacuum was beneficial for the high-pressure die casting process. As with the AlSi10Mg(Fe) alloy, the standard deviations that were obtained were low, which may indicate a certain level of repeatability during the injection process. Figure 69 shows the CT results.

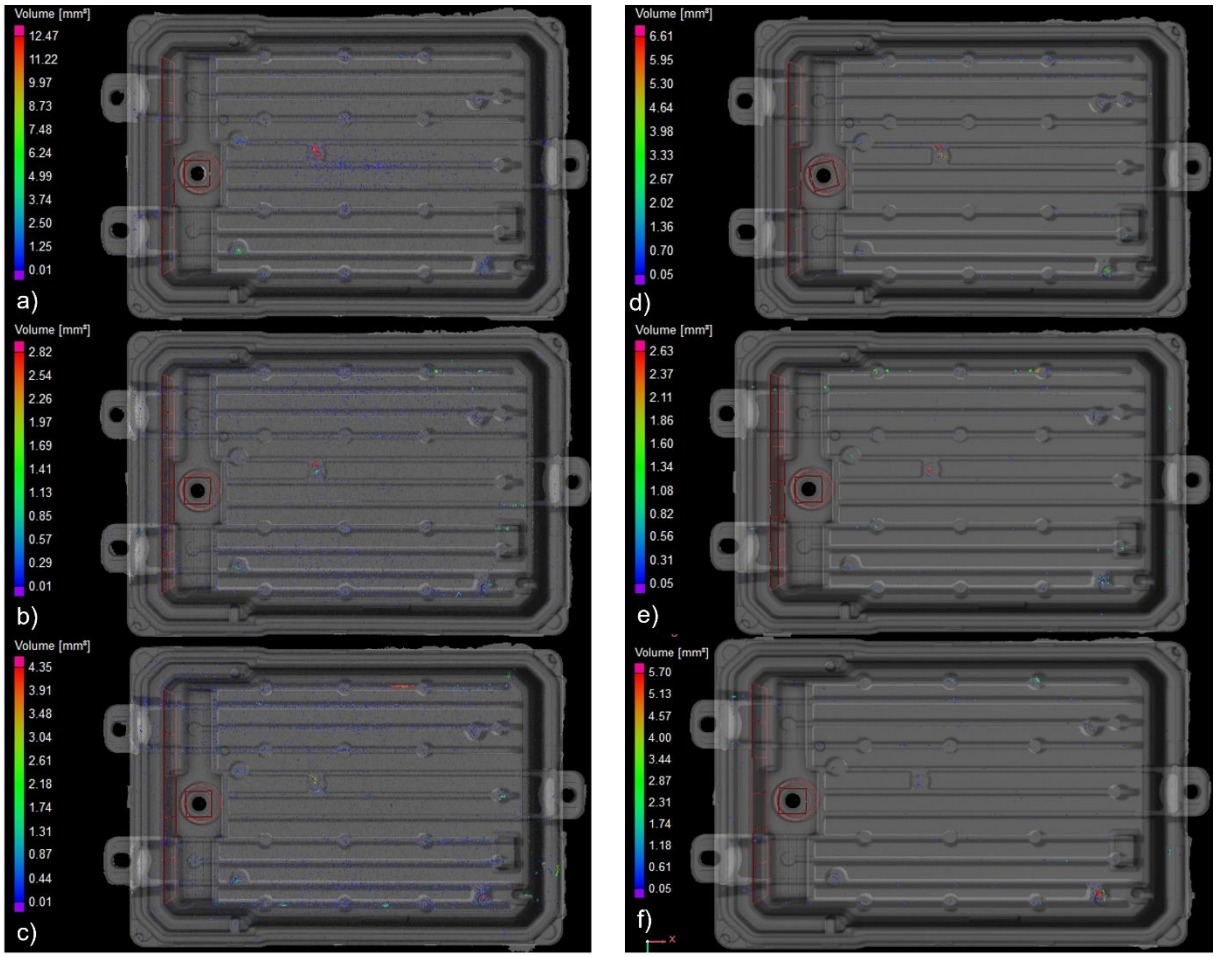

Figure 69: Results of CT analysis of AlSi10MnMg alloy as-cast parts. a), b), c) parts injected without vacuum; d), e), f) parts injected with vacuum.

Observing Figure 69, the main difference between the conventionally injected parts (a), b), and c)) and the vacuum injected parts (d), e), and f)) is that the last ones do not have so many small defects in the region of the fins, defects that correspond to gas porosities due to their greater sphericity and smaller volume (Figure 70). The graphs for the remaining parts can be seen in Appendix G.

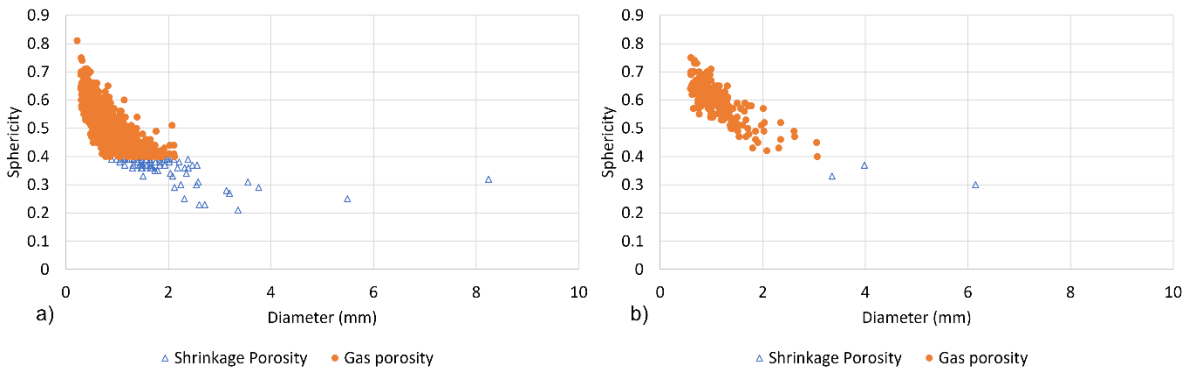

Figure 70: Sphericity and diameter of the porosities present in the AlSi10MnMg alloy parts. a) Part of Figure 69 a) (HPDC); b) Part of Figure 69 f) (VADC).

After comparing the results of Figure 69 and Figure 70 with the simulation result for shrinkage porosity (Figure 71), it is concluded that the larger defects are likely to correspond to shrinkage porosities.

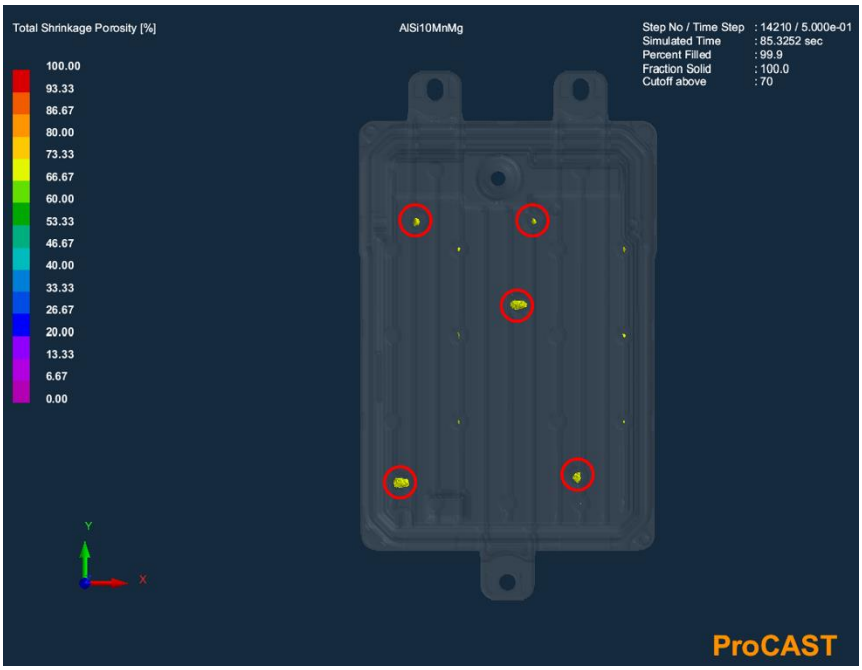

Figure 71: Numerically simulated shrinkage porosity in ProCAST software for AlSi10MnMg alloy.

Finally, as in the other alloys, the use of vacuum for AlMg4Fe2 alloy led to a decrease of defects by about 78%. After the analysis of Figure 72 and Figure 73, it can be concluded that with the use of vacuum assisted injection there is a decrease in the quantity of defects of smaller volume that correspond to gas porosities. It is not possible to analyze the process' repeatability, because not enough parts were analyzed.

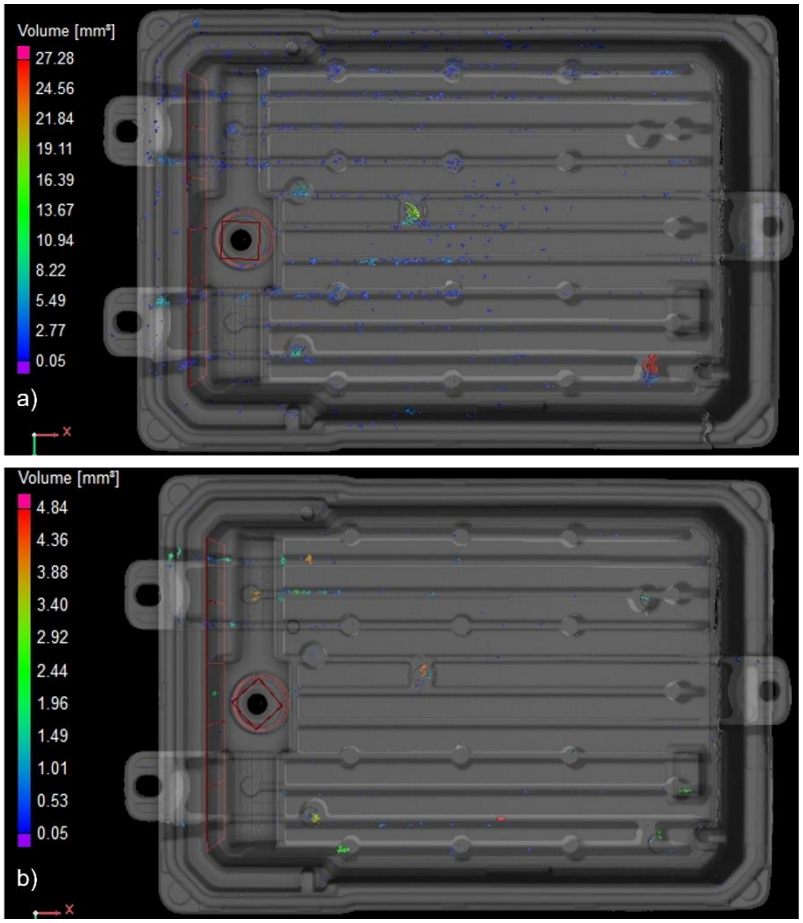

Figure 72: Results of CT analysis of AlMg4Fe2 alloy as-cast parts. a) part injected without vacuum; b) part injected with vacuum.

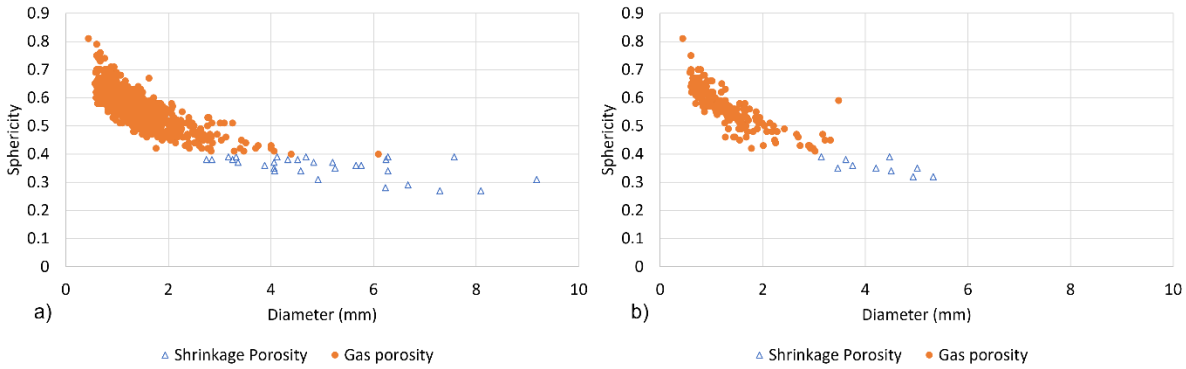

Figure 73: Sphericity and diameter of the porosities present in the AlMg4Fe2 alloy parts. a) HPDC; b) VADC.

The formation of shrinkage porosities was only predicted in two regions in the simulation (Figure 74), but by evaluating the results of Figure 72, it is possible that shrinkage porosities exist in other areas of the part, particularly in areas of higher volume, such as the pins.

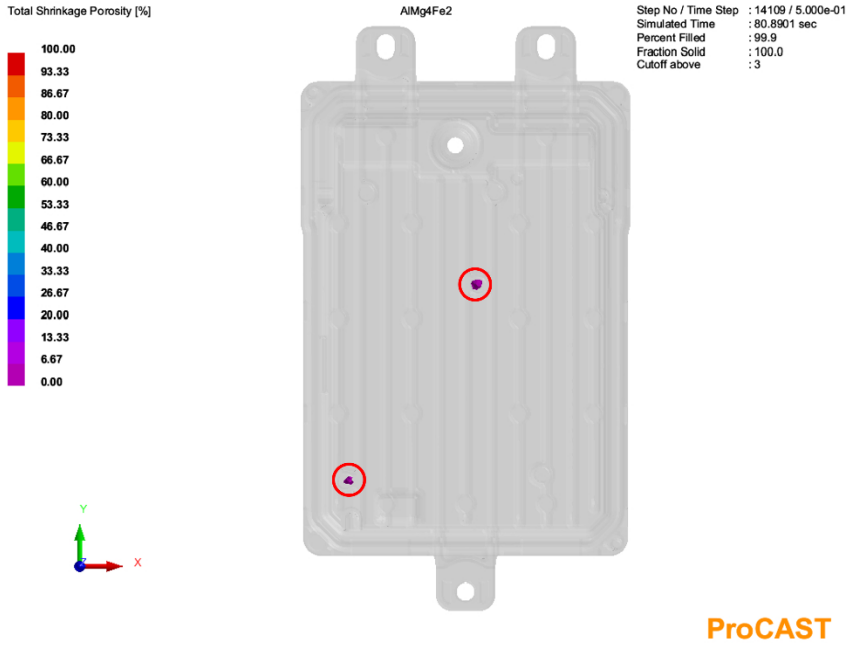

Figure 74: Numerically simulated shrinkage porosity in ProCAST software for AlMg4Fe2 alloy.

For all alloys, vacuum assisted injection led to a decrease in the percentage and quantity of defects. The silafont-36 alloy was the only one where the injection conditions were more controlled and the injection parameters were more optimized, and therefore the reduction in the percentage of defects that was obtained, approximately 60%, is what should be considered as expected for a vacuum pressure of 200 mbar. The conventionally injected parts present a larger quantity of gas and shrinkage porosities, and there is a large number of shrinkage porosities with a sphericity very close to 0.4, which may be a combination of gas and shrinkage porosities. Furthermore, after the analysis of the sphericity versus diameter graphs, it is possible to conclude that the smaller diameter of the defect, the larger its sphericity.

After the T6 heat treatment, the AlSi10Mg(Fe) and AlSi10MnMg alloy parts were again analyzed by 3D X-ray computed tomography to understand the influence that the solution heat treatment had on the gas porosities. Table 25 shows the results obtained for the analyzed parts.

Table 25: Results of porosity measurement in heat-treated parts by 3D X-ray computed tomography.

Alloy	**Vacuum**	**Part No.**	**Quantities**	**Defects volume** (mm^3)	**Average defect volume** (mm^3)	**Defect volume ratio** (%)
AlSi10Mg(Fe)	Yes	1	24192	1233.33	0.052	0.869
		2	26734	2305.23	0.087	1.618
		3	22999	1877.71	0.082	1.329
	No	1	25956	1631.46	0.063	1.147
		2	43690	3779.00	0.087	2.646
		3	27619	1835.98	0.067	1.298
AlSi10MnMg	Yes	1	26598	1701.99	0.064	1.215
		2	26138	1575.40	0.061	1.127
		3	18338	1302.17	0.071	0.935
	No	1	12450	507.47	0.041	0.361
		2	17230	856.98	0.050	0.613
		3	18112	1250.51	0.069	0.897

Figure 75 shows the CT results for AlSi10Mg(Fe) alloy parts after being heat treated.

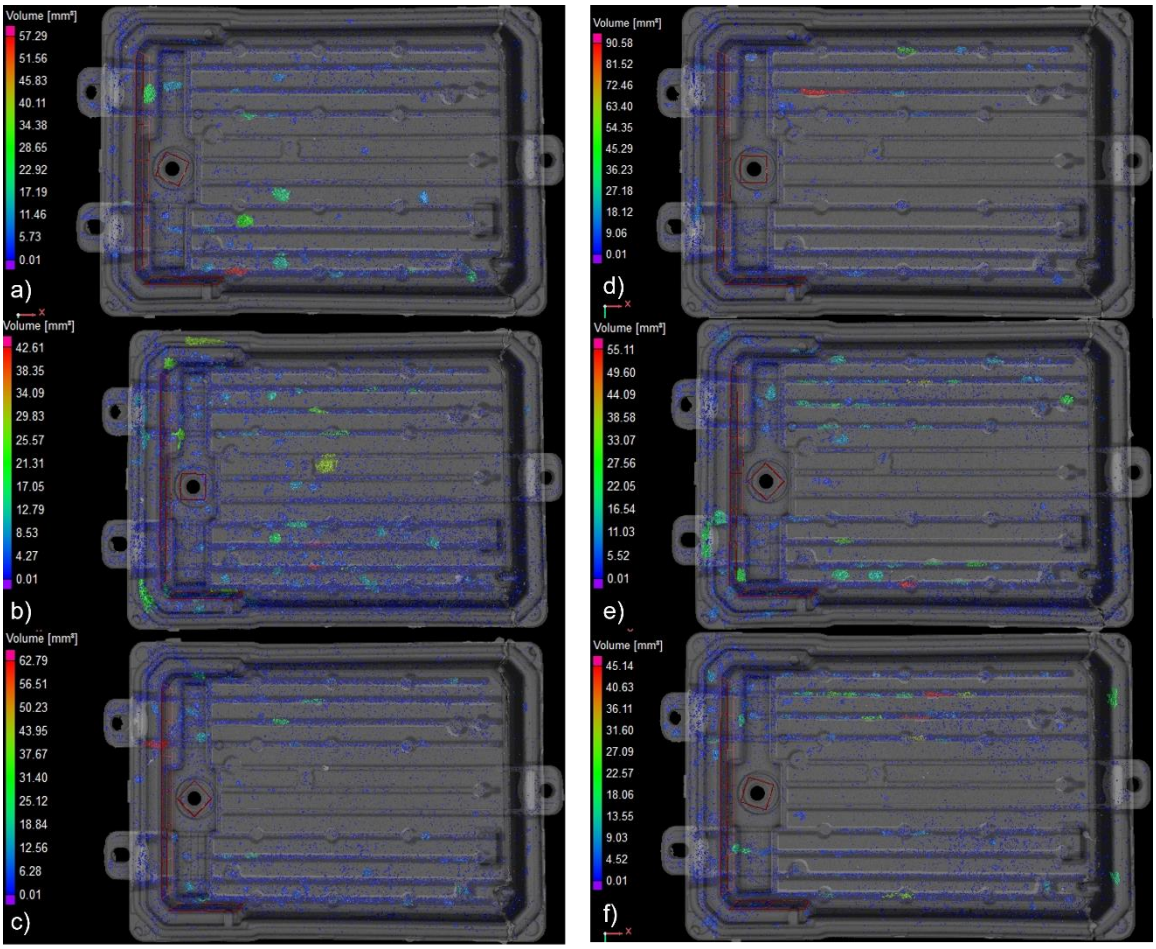

Figure 75: Results of CT analysis of AlSi10Mg(Fe) alloy heat treated parts. a), b), c) parts injected without vacuum; d), e), f) parts injected with vacuum.

Figure 76 shows the CT results for AlSi10MnMg alloy parts after being heat treated.

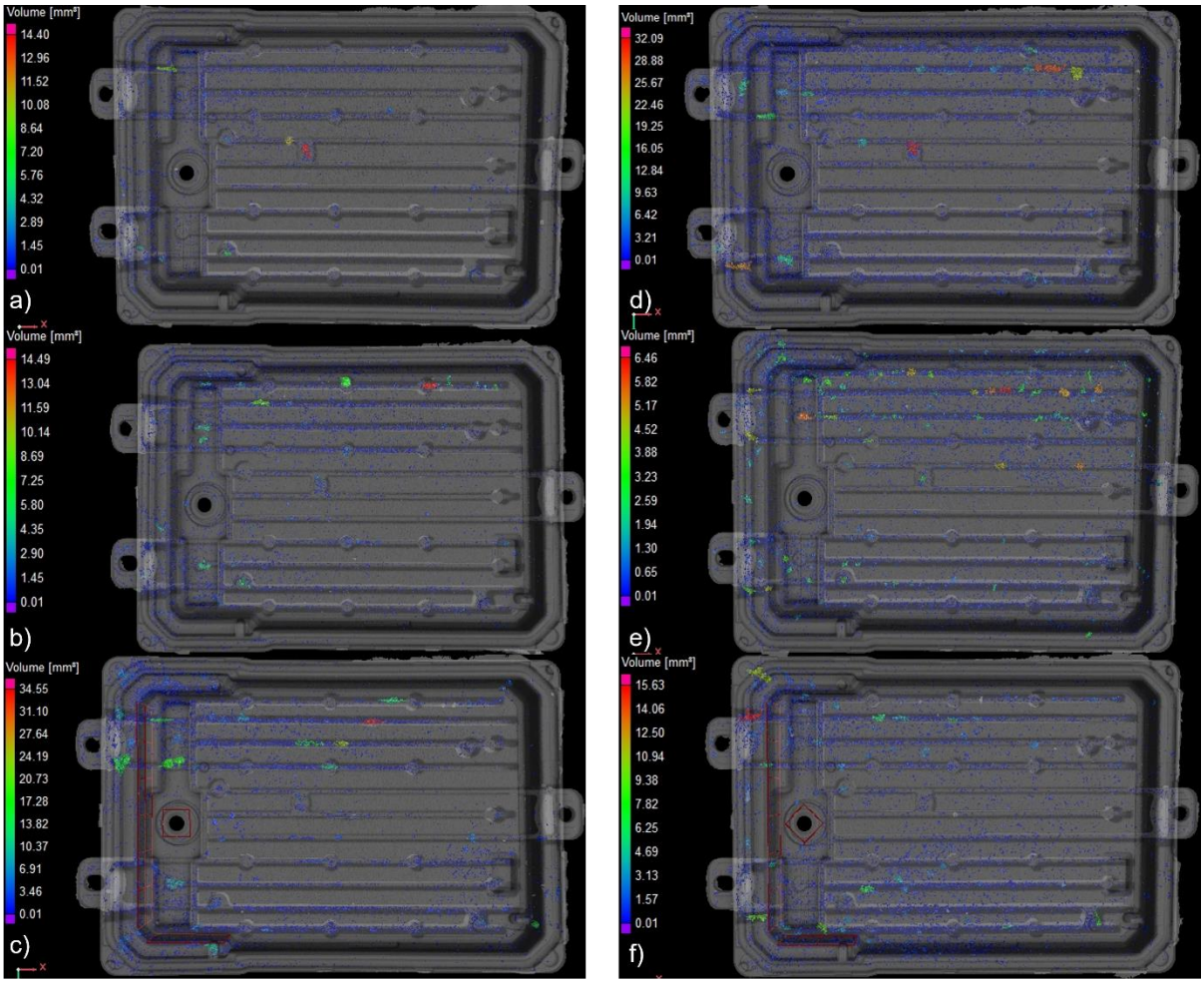

Figure 76: Results of CT analysis of AlSi10MnMg alloy heat treated parts. a), b), c) parts injected without vacuum; d), e), f) parts injected with vacuum.

Analyzing the results of Table 24 and Table 25, it can be observed that after the heat treatment, the vacuum-assisted injected parts have a higher increase in defects quantity compared to the conventionally injected parts. This higher increase can be explained by the fact that the analysis only detects defects with volume ≥0.01 mm³ and in the as-cast condition vacuum-assisted injected parts there are defects with volume <0.01 mm³ that after the solution heat treatment increase their volume and are detected in the analysis performed after the heat treatment. Furthermore, in the vacuum-assisted injected parts after the T6 heat treatment there is a high increase in defects with reduced volume, since the average defect volume has a reduction of about 56% in the case of AlSi10Mg(Fe) alloy and 70% in the case of AlSi10MnMg alloy.

For vacuum-assisted injected AlSi10Mg(Fe) alloy parts, the defect volume ratio was reduced by 25% when compared to that obtained for conventional injected parts (the graphs of sphericity as a function of diameter for AlSi10Mg(Fe) alloy parts are in Appendix H). On the other hand, for the AlSi10MnMg alloy, the average defect volume ratio of the vacuum-assisted injected parts showed an increase of 75% compared to the defect volume ratio of the conventionally injected parts. After analyzing the graphs in Figure 77, it is possible to verify that especially for the vacuum-assist injected parts no. 1 (Figure 77d)) and no. 2 (Figure 77e)), the number of defects with larger diameter is higher than for the conventionally injected parts no. 1(Figure 77a)) and no. 2 (Figure 77b)). As the defect volume ratio calculation uses the defect volume and the part volume (this being constant for all parts analyzed), an increase in the number of defects with larger diameter leads to an increase in the defect volume, which in turn implies an increase in the defect volume ratio value.

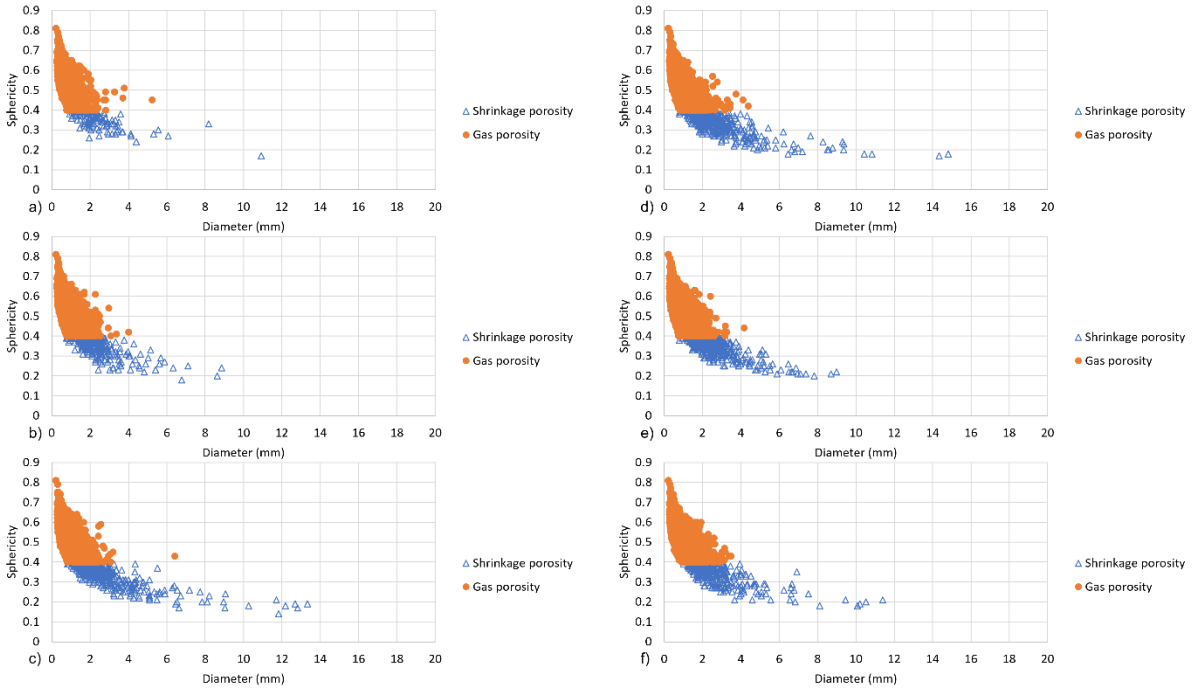

Figure 77: Sphericity and diameter of the porosities present in the AlSi10MnMg alloy heat treated parts. a), b), c) HPDC; d), e), f) VADC.

Figure 78 compares the number and type of defects for the same part in the cast condition and in the heat-treated condition. It is confirmed that after the heat treatment, the number and diameter of the gas porosities increases. However, there is also an increase in the number of shrinkages porosities. This may occur due to the expansion of the gas porosities that start to join (coalescence phenomenon) and their shape starts to become distorted thus leading to a decrease in sphericity.

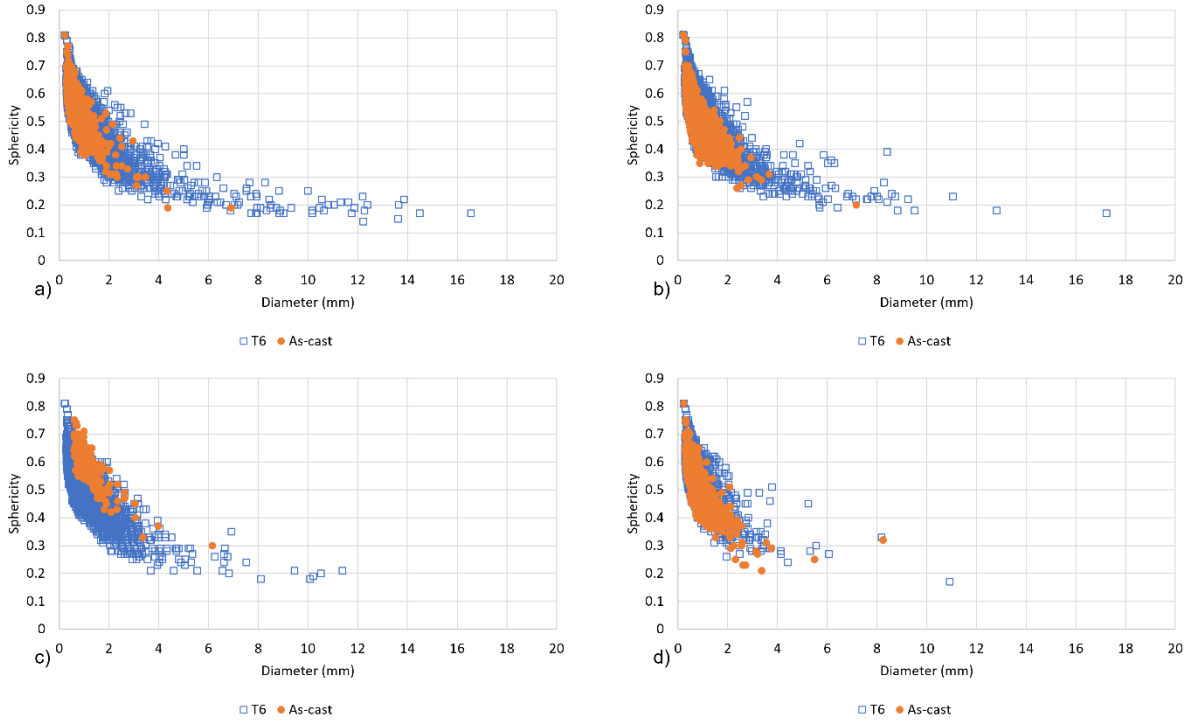

Figure 78: Comparison of porosity in the part in the cast state and after being heat-treated. a) Part No. 2 vacuum injected in AlSi10Mg(Fe) alloy; b) Part No. 3 conventionally injected in AlSi10Mg(Fe) alloy; c) Part No. 3 vacuum injected in AlSi10MnMg alloy; d) Part No. 1 conventionally injected in AlSi10MnMg alloy.

In order to compare the defects visible in CT and metallography analyses, it was necessary to define the section of the part to be analyzed. After observing the results obtained in CT for the parts in the as-cast condition, it was concluded that the fin marked in Figure 79a) had for most of the parts the highest defects' concentration. As it is not possible to scan the whole fin section with the optical microscope that was used, an analysis section of smaller area was defined in order to facilitate the analysis, Figure 79b).

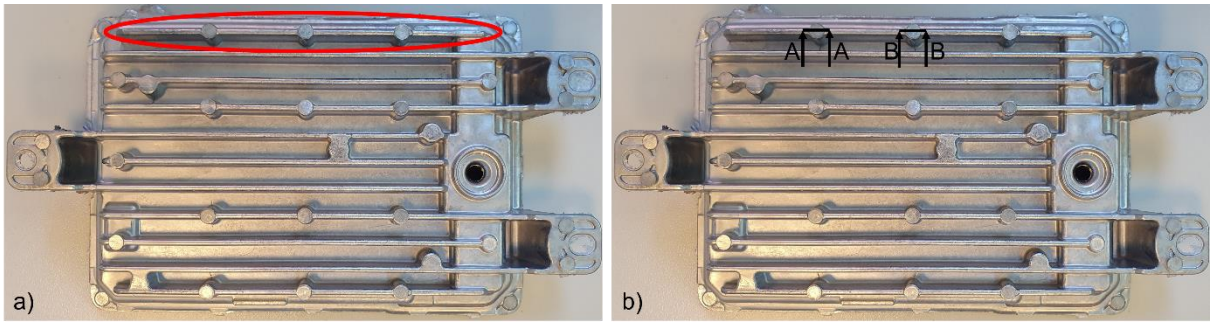

Figure 79: a) Fin chosen for the analysis; b) Analyzed sections: section A-A and section B-B.

Table 26 shows the results of the analysis of section A-A (Figure 79b)) for the parts in the as-cast condition. These parts are the same ones that were analyzed at the beginning of chapter 4.4 (full scan).

Table 26: Results of porosity measurement on a section of the as-cast parts by 3D X-ray computed tomography.

Alloy	**Vacuum**	**Part No.**	**Analyzed area** (mm^2)	**Porosity** (%)	**Average porosity** (%)
AlSi12(Fe)	Yes	1	66.20	0.00	-
	No	1	65.77	0.23	-
AlSi10Mg(Fe)	Yes	1	65.90	0.00	0.15
		2	65.58	0.16	
		3	65.54	0.30	
	No	1	71.88	0.97	1.85
		2	69.79	2.30	
		3	66.41	2.27	
AlSi10MnMg	Yes	1	65.86	2.35	1.27
		2	65.48	0.74	
		3	65.24	0.72	
	No	1	65.50	0.54	1.58
		2	65.37	1.55	
		3	65.77	2.65	
AlMg4Fe2	Yes	1	65.49	0.00	-
	No	1	65.31	3.30	-

As expected, the parts whose injection was performed with vacuum assistance have a lower percentage of defects than the conventionally injected parts. Only the AlSi10MnMg alloy part number 1 injected with vacuum has a higher porosity when compared to the other vacuum injected parts, Figure 80.

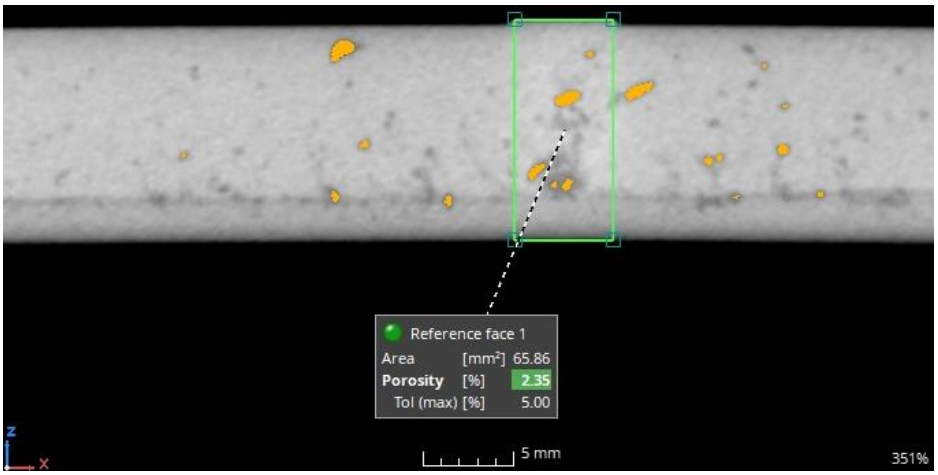

Figure 80: Porosity in the analyzed section of vacuum injected part number 1 in AlSi10MnMg alloy.

Figure 81 shows the sections for which no porosity was found.

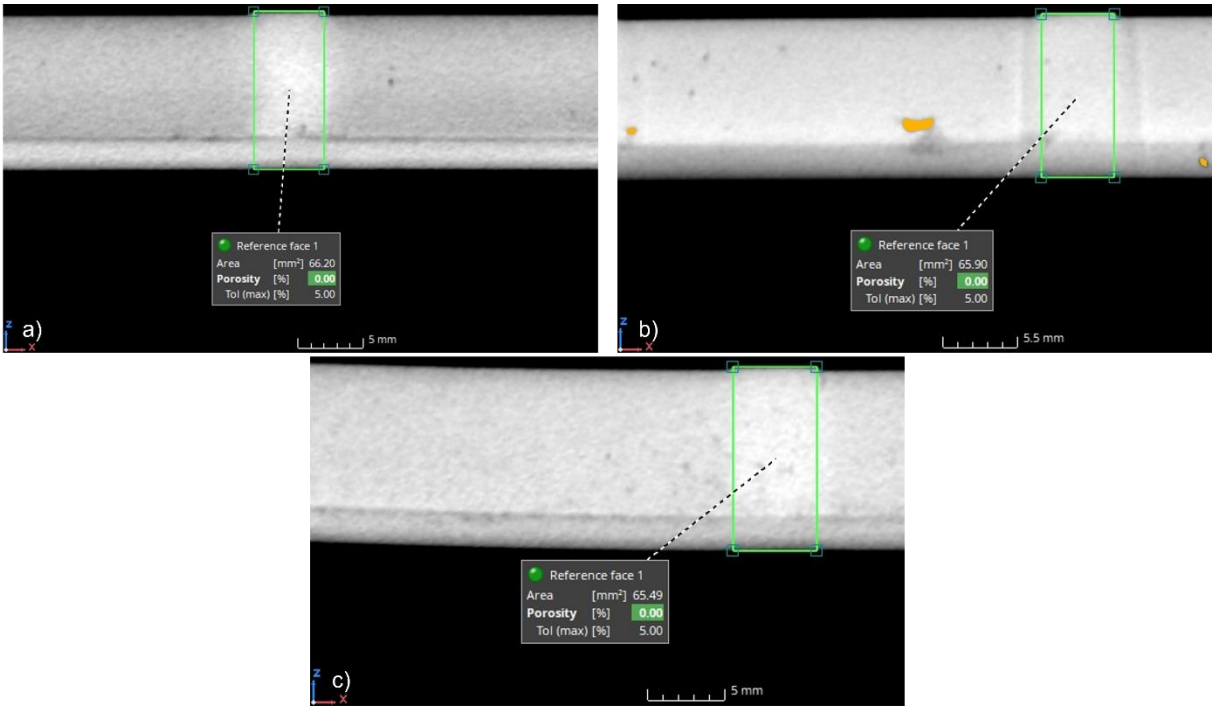

Figure 81: a) Porosity in the analyzed section of vacuum injected part number 1 in AlSi12(Fe) alloy; b) Porosity in the analyzed section of vacuum injected part number 1 in AlSi10Mg(Fe) alloy; c) Porosity in the analyzed section of vacuum injected part number 1 in AlMg4Fe2 alloy.

After the T6 heat treatment, the same sections of the same parts of the AlSi10Mg(Fe) and AlSi10MnMg alloys were analyzed. The results obtained are presented in Table 27.

Table 27: Results of porosity measurement on a section of the heat-treated parts by 3D X-ray computed tomography.

Alloy	**Vacuum**	**Part No.**	**Analyzed area** (mm^2)	**Porosity** (%)	**Average porosity** (%)
AlSi10Mg(Fe)	Yes	1	65.46	1.28	5.09
		2	65.58	9.09	
		3	65.48	4.90	
	No	1	65.68	1.60	4.61
		2	65.73	2.65	
		3	65.38	9.57	
AlSi10MnMg	Yes	1	65.64	19.69	9.64
		2	65.41	6.24	
		3	65.37	3.00	
	No	1	65.76	1.17	4.06
		2	65.37	6.52	
		3	65.55	4.49	

After the solution heat treatment, it is expected that there is an increase in porosity due to the gas porosities' expansion. Taking into account the results obtained for the sections of the parts without heat treatment, it was expected that the ones from the vacuum injected parts would present a lower average value of porosity than the conventionally injected parts, but this was not observed (Table 27).

As in the full parts analysis, the increase in porosity after heat treatment is much higher in the sections of the vacuum injected parts than in the sections of the conventionally injected parts. Figure 82 shows the sections of the vacuum injected parts number 1 of both alloys. When comparing the section (Figure 82a)) of the AlSi10MnMg alloy with that in Figure 80, it can be seen that the pores in darker gray in Figure 80, expanded during the solution heat treatment and coalesced, thus occupying a larger area.

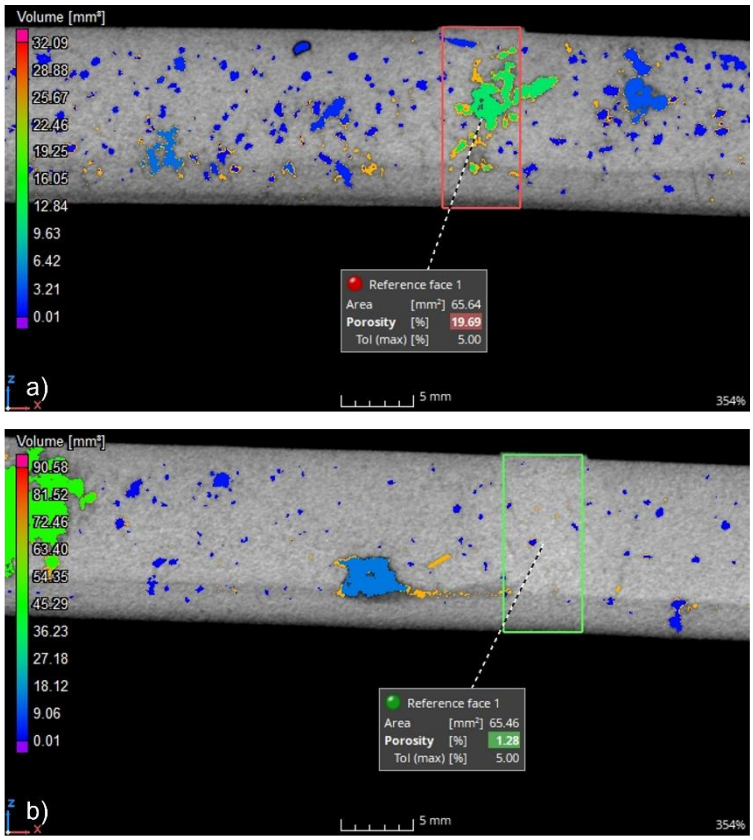

Figure 82: a) Porosity in the analyzed section of vacuum injected part number 1 in AlSi10MnMg alloy after heat treatment; b) Porosity in the analyzed section of vacuum injected part number 1 in AlSi10Mg(Fe) alloy after heat treatment.

4.4.2 Metallography

Regarding the parts without heat treatment, in order to analyze the porosity in section A-A, the entire fin was cut (Figure 83a)) and then only the section previously defined was analyzed. However, due to the size of the fins it was not easy to polish them. In some fins, the section that should be analyzed contained several scratches (Figure 83b)) that influenced the results obtained in the ImageJ software.

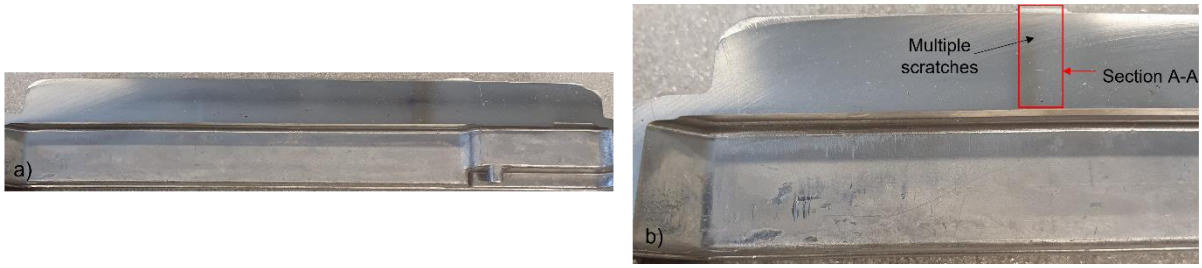

Figure 83: a) Fin cut and polished; b) Section A-A with surface scratches.

In order to have standardized analysis performed with ImageJ software, the following parameters were set as constants:

- Image type: 32-bit;
- Image threshold: 90;
- Scale: 196 pixels/mm;
- Particles size (mm²): 0.00-∞;
- Particles circularity: 0.40-1.00.

Considering that the gas porosity was previously defined as a particle with sphericity ≥0.4, it was also defined that only particles with circularity above 0.4 were detected.

The results obtained for the percentage of defects, amount of gas porosities and average area of the gas porosities are presented in Table 28.

Table 28: Results of porosity measurement on a section of the as-cast parts by metallography.

Alloy	**Vacuum**	**Sample No.**	**Analyzed area** (mm^2)	**Porosity** (%)	**No. of gas porosities**	**Average area of gas porosities** (mm^2)
AlSi12(Fe)	Yes	1	54.98	0.119	107	5.68E-04
		2	70.81	1.081	2012	2.00E-04
		3	64.35	0.178	676	1.50E-04
	No	1	75.21	0.167	304	3.53E-04
		2	65.22	0.651	935	2.65E-04
		3	35.59	0.074	135	1.54E-04
AlSi10Mg(Fe)	Yes	1	35.39	0.201	335	2.03E-04
		2	45.02	0.180	165	2.41E-04
		3	56.60	0.129	91	4.02E-04
	No	1	63.08	2.770	2326	2.03E-04
		2	54.09	0.776	516	2.70E-04
		3	58.36	2.834	5557	1.40E-04
AlSi10MnMg	Yes	1	46.41	8.109	369	2.00E-03
		2	70.86	0.837	3099	1.35E-04
		3	79.35	2.557	3137	3.90E-04
	No	1	59.92	1.780	1065	3.81E-04
		2	41.47	0.555	391	4.11E-04
		3	47.88	1.171	1160	3.48E-04
AlMg4Fe2	Yes	1	16.23	0.035	18	2.53E-04
		2	74.05	0.230	408	1.94E-04
		3	69.58	5.121	3741	1.60E-04
	No	1	61.57	0.936	931	4.44E-04
		2	65.47	1.780	2882	1.77E-04
		3	65.07	0.401	673	2.37E-04

Analyzing Table 28, it can be seen that the values of the analyzed area in the optical microscope have a much greater dispersion when compared to the ones that are obtained in the analysis performed at the myVGL software. The scratches on the samples and the difficulty in scanning the entire section with the optical microscope can justify the greater dispersion of the values.

The average value of porosity was only higher in conventional injection in the case of AlSi10Mg(Fe) alloy. This was a result that was not expected considering the results that were obtained by computed tomography. This percentage of defects is determined taking into account the threshold value. Since this value was fixed for all the analyses, in certain analyzed images there may have been some contamination or scratches of the samples that were considered as defect, thus increasing the value of the percentage of defects.

There is also some variation in the number of gas porosities which again may be related to identification of small scratches or contamination as gas porosities.

Regarding the average value of the area of the gas porosities, the verified values were considerably low in every samples, which was expected because the high compaction pressures used in the third injection phase have the function of collapsing the voids present inside the parts. It is expected that the value of the average area of the gas porosities will increase after the heat treatment.

The analyzed parts after heat treatment were not the same as those analyzed without heat treatment, as such a direct comparison cannot be made as it was done in the computed tomography case. The results obtained after heat treatment are presented in Table 29.

Table 29: Results of porosity measurement on a section of the heat-treated parts by metallography.

Alloy	**Vacuum**	**Sample No.**	**Analyzed area** (mm^2)	**Porosity** (%)	**No. of gas porosities**	**Average area of gas porosities** (mm^2)
AlSi12(Fe)	Yes	1	70.40	3.435	548	3.00E-03
	No	1	67.92	1.591	222	4.00E-03
AlSi10Mg(Fe)	Yes	1	53.72	16.965	1210	4.00E-03
	No	1	62.55	5.209	895	3.00E-03
AlSi10MnMg	Yes	1	66.40	8.794	618	5.00E-03
	No	1	67.77	7.877	1167	3.00E-03
AlMg4Fe2	Yes	1	67.59	2.115	1471	7.59E-04
	No	1	68.74	14.207	2857	1.00E-03

In the heat treated samples, the values of the analyzed area are no longer as scattered as in the as-cast samples and already have values closer to those that were obtained in the myVGL software, because the entire fin was not cut, but only the pin where the B-B section crosses (Figure 79b)).

As mentioned earlier, the average area value of the gas porosities increases after the solution heat treatment, because the strength of aluminum alloys decreases when they are kept at high temperature and the pressure of the gas porosity eventually exceeds the strength of the alloy, leading to an expansion of the porosity.

On average, there was an increase in porosity (%) after the heat treatment. This fact can be explained by the increase in the average area value of the gas porosities that occupy a larger area in the analyzed section and increase the porosity percentage.

4.4.3 Computed tomography VS metallography

To understand if there was any similarity between the porosity values obtained in computed tomography and metallography, the sections of part number 1 of AlSi10MnMg alloy injected with vacuum assistance and part number 3 of AlSi10Mg(Fe) alloy injected conventionally after heat treatment were analyzed.

Figure 84 shows the analyses performed on the sections with ImageJ and myVGL software.

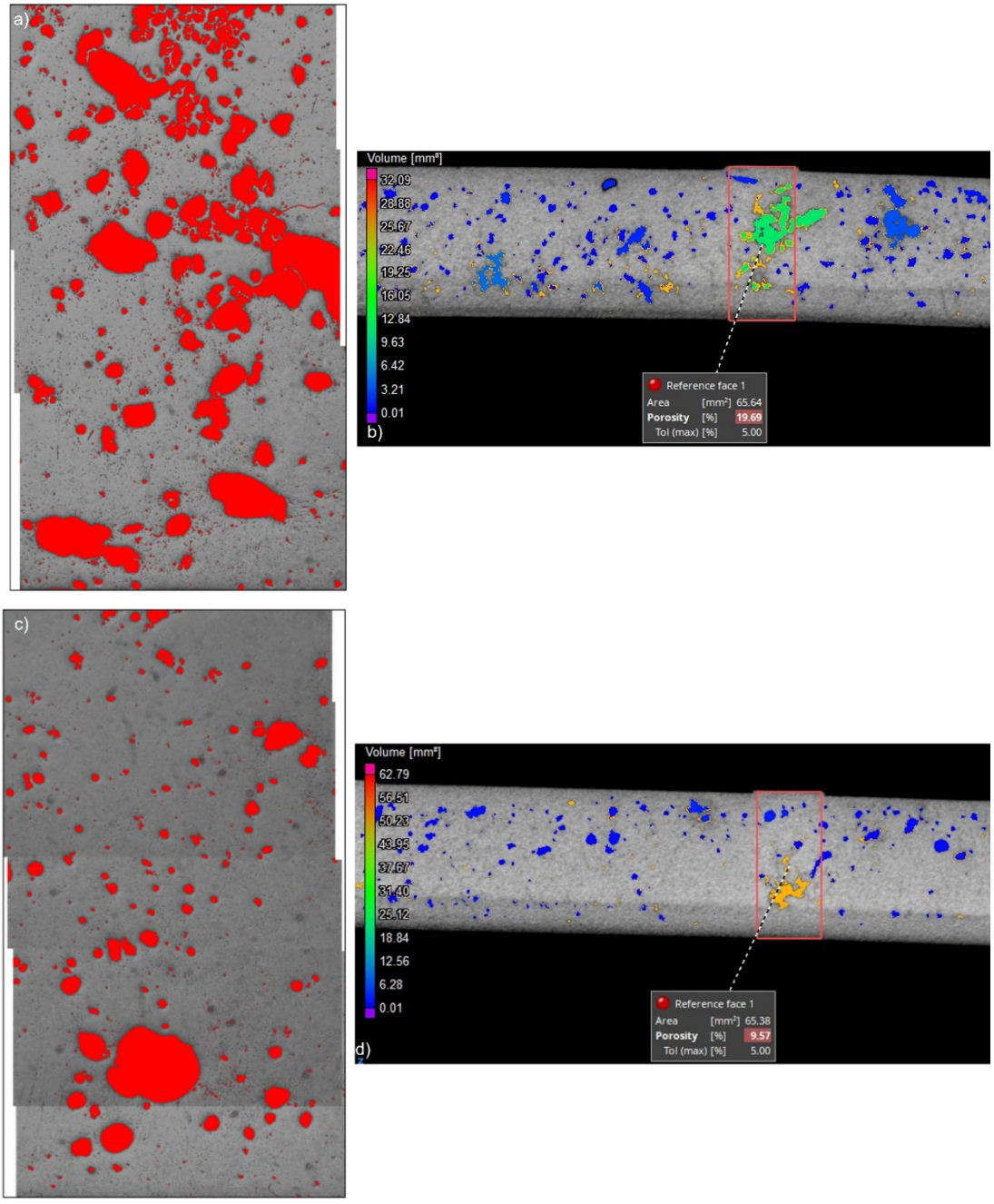

Figure 84: Analysis of porosities. a) Analysis performed in ImageJ on section of part no. 1 injected with vacuum assistance (AlSi10MnMg); b) Analysis performed in myVGL on section of part no. 1 injected with vacuum assistance (AlSi10MnMg); c) Analysis performed in ImageJ on section of part no. 3 conventionally injected (AlSi10Mg(Fe)); d) Analysis performed in myVGL on section of part no. 3 conventionally injected (AlSi10Mg(Fe)).

Table 30 shows the values of the analyzed area and porosity (%).

Table 30: Porosity analysis in ImageJ and myVGL software.

Alloy	**Software**	**Analyzed area** (mm²)	**Porosity** (%)
AlSi10MnMg	ImageJ	61.05	20.60
	myVGL	65.64	19.69
AlSi10Mg(Fe)	ImageJ	61.27	7.36
	myVGL	65.38	9.57

Considering the results in Figure 84 it can be seen that most likely the analysis plane used in metallography and CT is not the same, because the distribution of porosities is different in both alloys. However, the porosity values (Table 30) obtained using metallography and CT are very similar. CT is a nondestructive testing to detect internal defects and it is easier to analyze different planes along the part, but the cost is much higher than metallography.

4.5 Blistering

After the heat treatment, besides having analyzed the internal porosities using CT and metallography, the visual inspection of the blistering was performed.

In order to facilitate the analysis, only the images of the parts with the lowest and highest defect volume ratio for each alloy will be presented, based on the values shown in Table 25. The images of the remaining parts are in Appendices I to J.

After analyzing the Figures 85-88, it is concluded that the parts that have a higher defect volume ratio (Figure 86 and Figure 87) present a larger number of blisters and with larger size when compared to the parts of the same alloy with a lower defect volume ratio value. Knowing that the part in Figure 86 has the highest defect volume ratio and the part in Figure 88 has the lowest defect volume ratio, there may be a relationship between the defect volume ratio and the number and size of blisters, i.e., the higher the defect volume ratio, the larger the number of blisters formed. Furthermore, with the exception of the part in Figure 86, there is a tendency for the bottom of the parts to have smaller blisters than the ones on the top of the part.

AlSi10Mg(Fe) alloy

Figure 85: Blistering on vacuum injected part no.1.

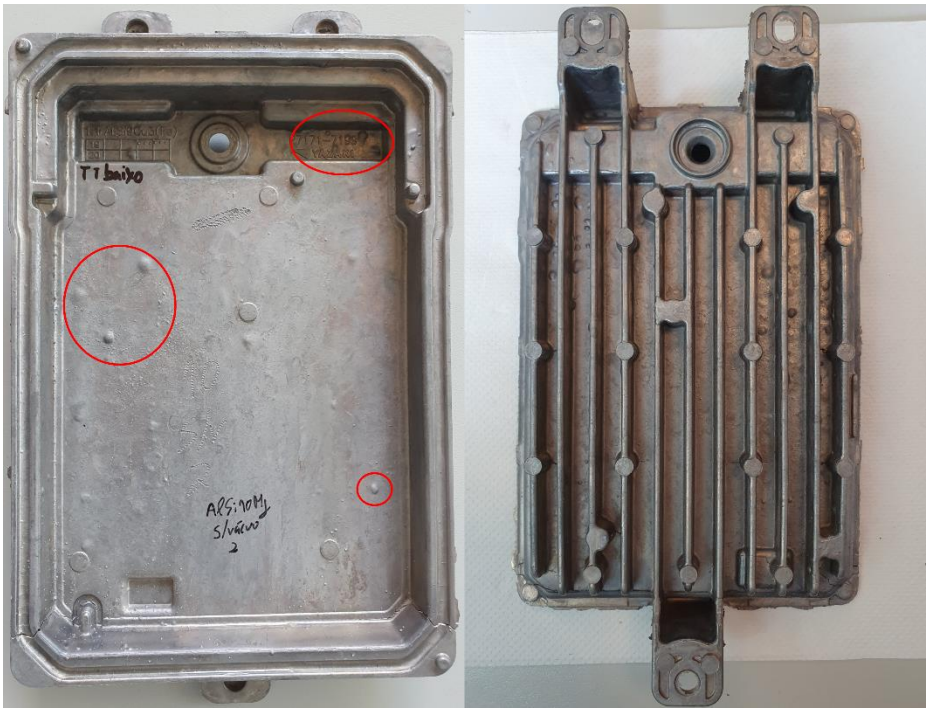

Figure 86: Blistering on conventionally injected part no.2.

AlSi10MnMg alloy

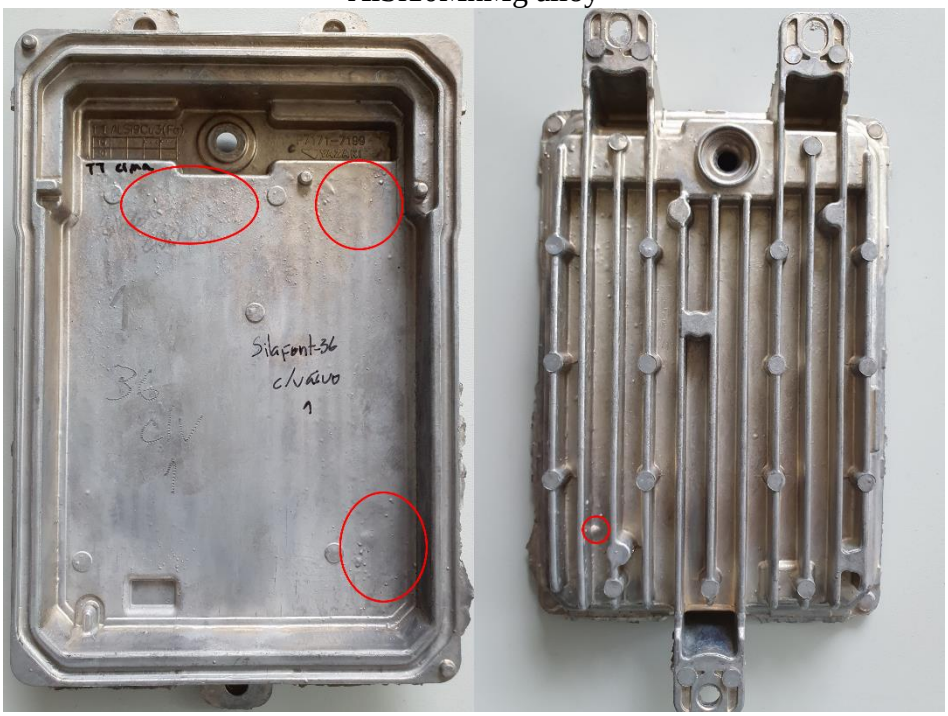

Figure 87: Blistering on vacuum injected part no.1.

Figure 88: Blistering on conventionally injected part no.1.

Although the AlSi12(Fe) and AlMg4Fe2 alloys did not respond to the heat treatment performed, parts of these alloys were also heat treated to understand if the quantity of blistering was lower in the vacuum injected parts. Figures 89-92 show the images of the parts (after heat treatment) that were used for the porosity measurement using computed tomography.

AlSi12(Fe)

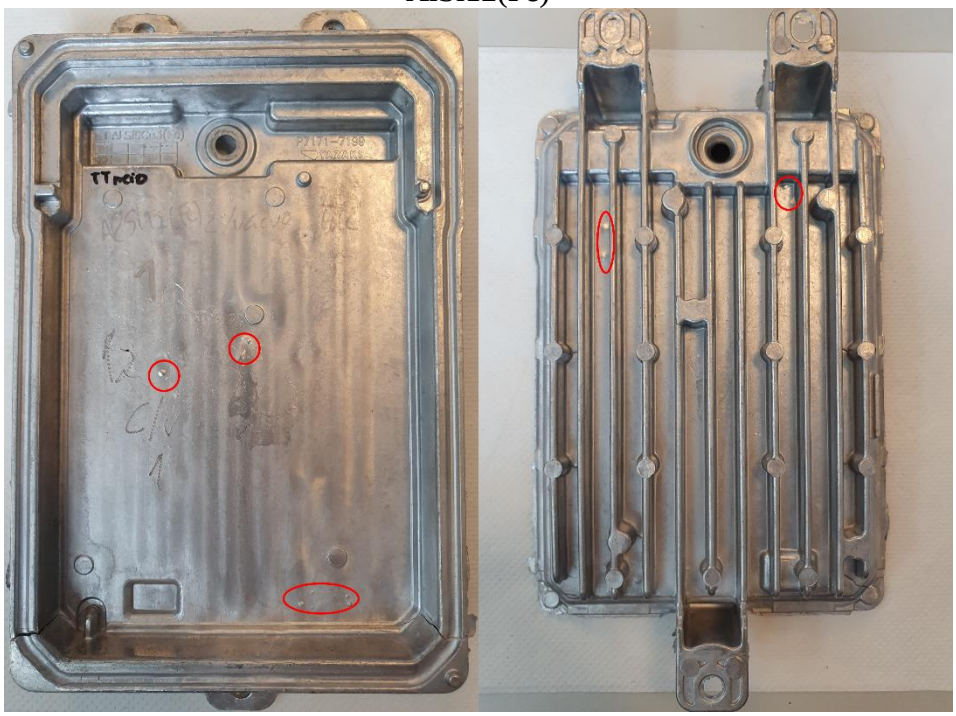

Figure 89: Blistering on vacuum injected part no.1.

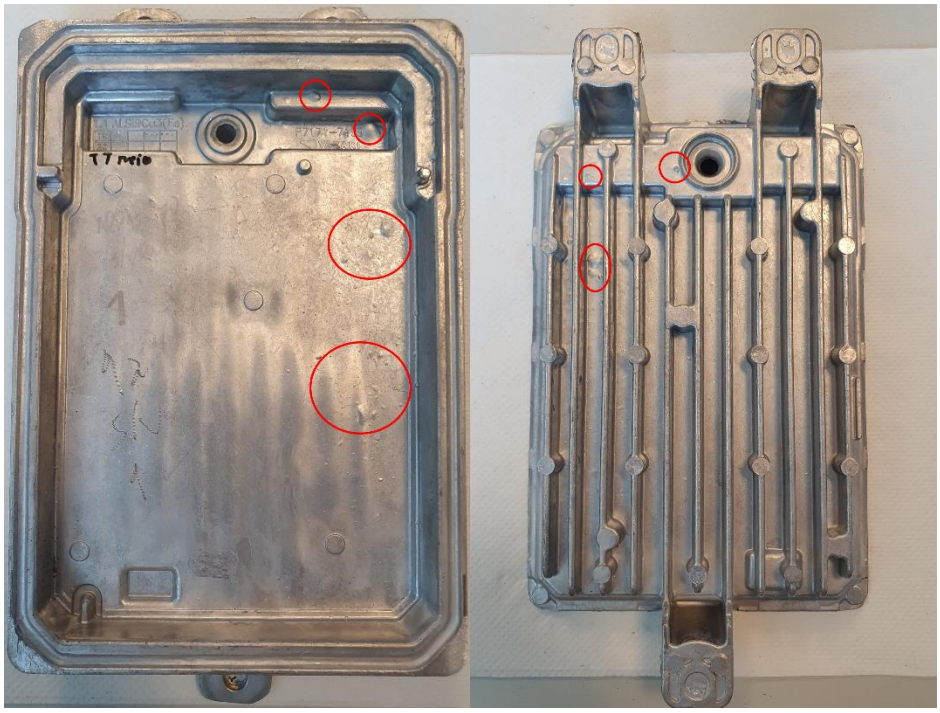

Figure 90: Blistering on conventionally injected part no.1.

AlMg4Fe2

Figure 91: Blistering on vacuum injected part no.1.

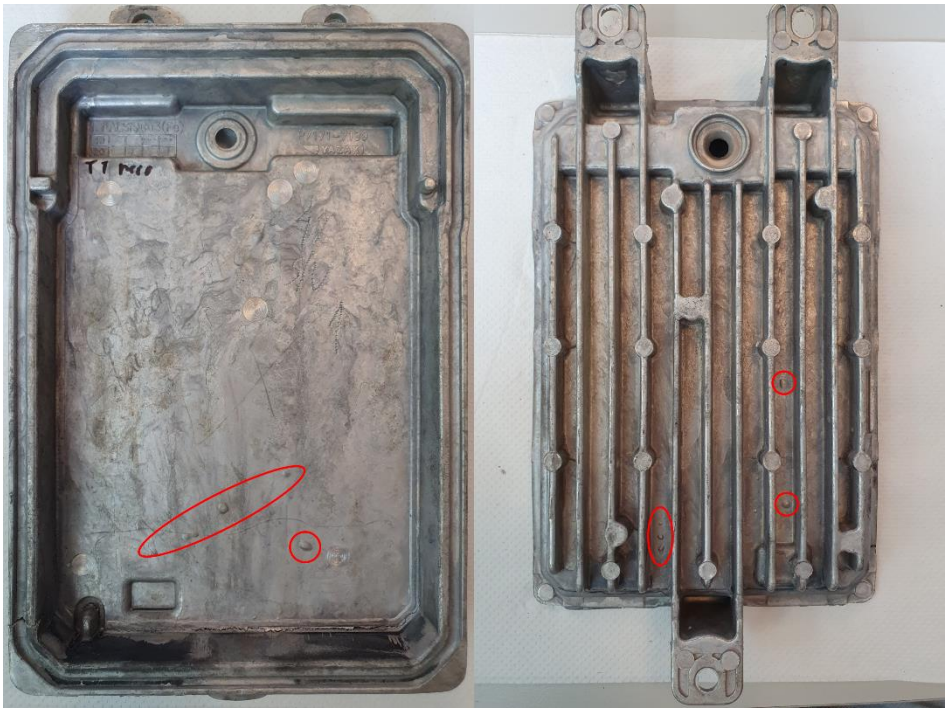

Figure 92: Blistering on conventionally injected part no.1.

Both the vacuum-assisted and the conventionally injected parts had blistering. However, analyzing all the parts presented, the use of vacuum seems to have contributed to a decrease in blistering, with the exception of the part in Figure 87. The fact that blisters appear both in vacuum-assisted and conventionally injected parts can be justified by the fact that there was a problem in vacuum efficiency during injection. If the vacuum generation has occurred before the plunger closes the pouring slot of the shot sleeve or if there are gaps between the plunger and the shot sleeve, entrapment of a larger amount of air can occur. This air can no longer be removed from the liquid metal and will be detrimental to the appearance of blistering.

The number of blisters can be reduced by optimizing the solution heat treatment. Minimizing the temperature and/or the time of solution heat treatment may lead to a reduction

in the number of blisters but may also lead to a minimization of the mechanical properties value relative to what is expected.

4.6 Tensile tests

Tensile tests were performed on specimens taken from as-cast state parts in order to perform the mechanical characterization of the parts under study. The yield strength, ultimate tensile strength and elongation values obtained will be compared with the standard values. The mechanical properties of machined specimens of conventionally injected parts and vacuum-assisted injected parts will be compared, in order to assess whether the use of vacuum during injection improves the mechanical properties.

Figure 93 shows the stress-strain plot for the AlSi12(Fe) alloy specimens injected with vacuum assistance.

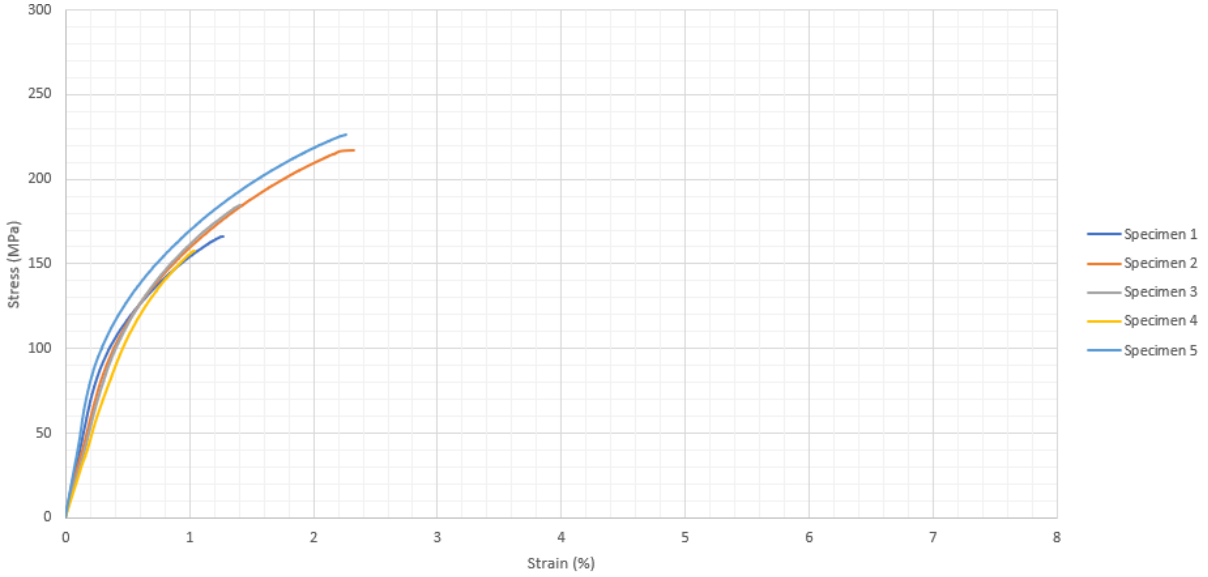

	Section area (mm^2)	Yield Strength (MPa)	Ultimate Tensile Strength (MPa)	Elongation (%)
Average	11.835	137±11	190±30	1.02±0.52
Standard	-	>130	>240	>1

Figure 93: Stress-strain plot of AlSi12(Fe) alloy specimens - Vacuum-assisted injection.

Figure 94 shows the stress-strain plot for the AlSi12(Fe) alloy specimens conventional injected.

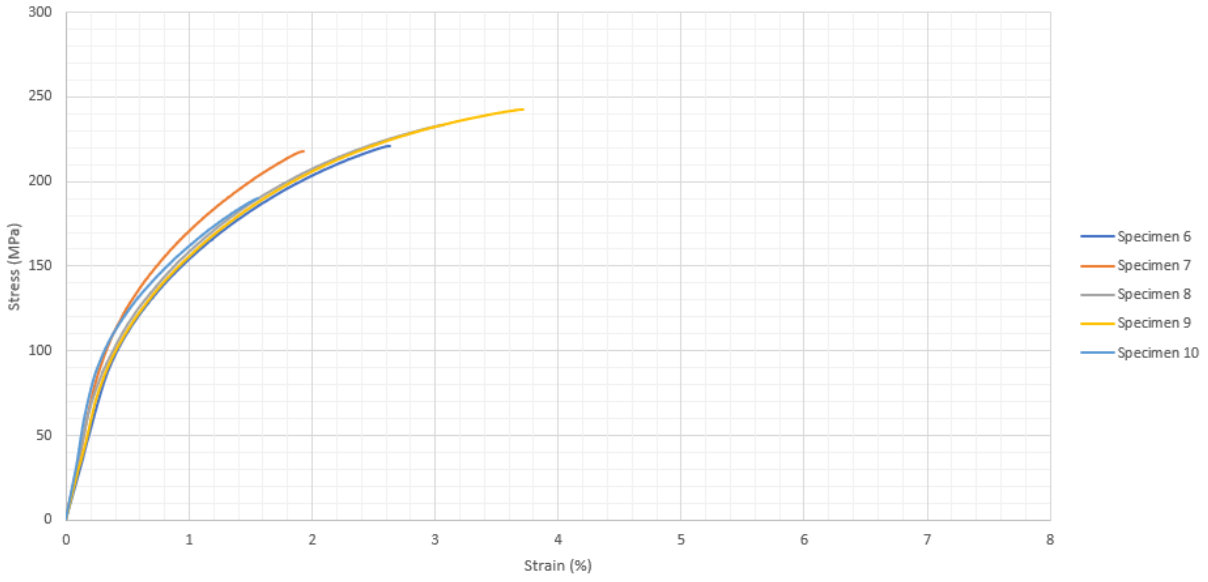

	Section area (mm²)	Yield Strength (MPa)	Ultimate Tensile Strength (MPa)	Elongation (%)
Average	11.421	128±5	221±20	1.93±0.81
Standard	-	>130	>240	>1

Figure 94: Stress-strain plot of AlSi12(Fe) alloy specimens - Conventional injected.

The average value of the yield strength was higher in the specimens where the injection was performed with vacuum assistance, but the variability of the values obtained was higher. On the other hand, the mean value of the ultimate tensile strength and the elongation was higher in the specimens where the injection was performed without vacuum assistance, however the standard deviation of the elongation values was slightly higher. When comparing the average values of yield strength, ultimate tensile strength and elongation obtained with the values indicated in the standard, the ultimate tensile strength is below the theoretical value (min. 240 MPa) and the yield strength for the specimens where the injection was performed without vacuum assistance is also slightly below the theoretical value (128 MPa vs. min. 130 MPa).

Figure 95 shows the stress-strain plot for the AlSi10Mg(Fe) alloy specimens injected with vacuum assistance.

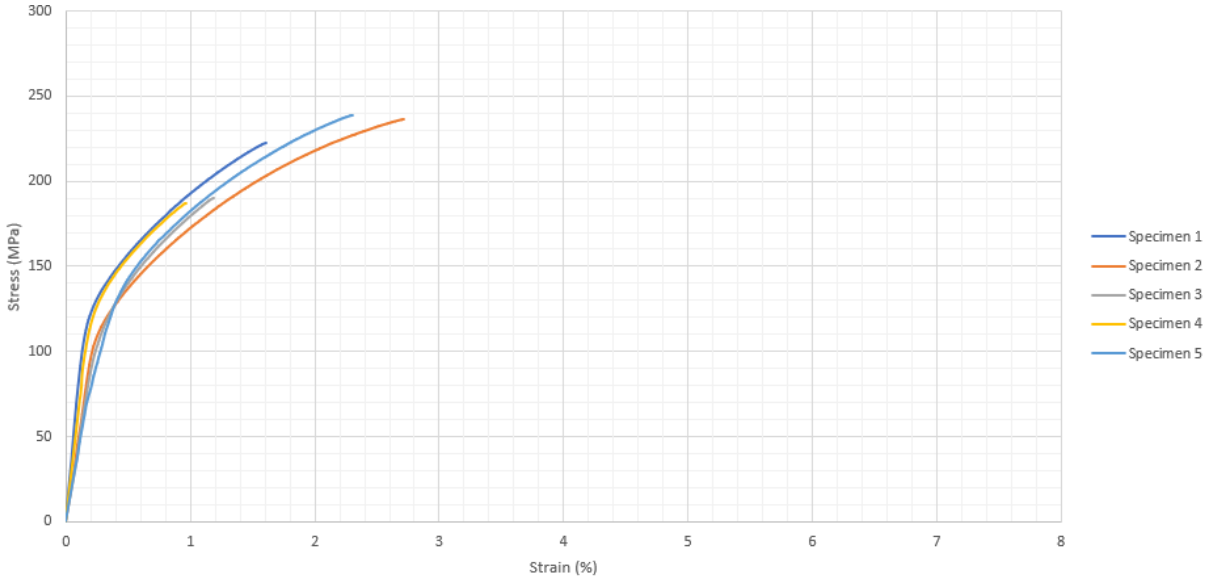

	Section area (mm²)	Yield Strength (MPa)	Ultimate Tensile Strength (MPa)	Elongation (%)
Average	12.194	143±7	215±25	1.34±0.65
Standard	-	>140	>240	>1

Figure 95: Stress-strain plot of AlSi10Mg(Fe) alloy specimens - Vacuum-assisted injection.

Figure 96 shows the stress-strain plot for the AlSi10Mg(Fe) alloy specimens conventional injected.

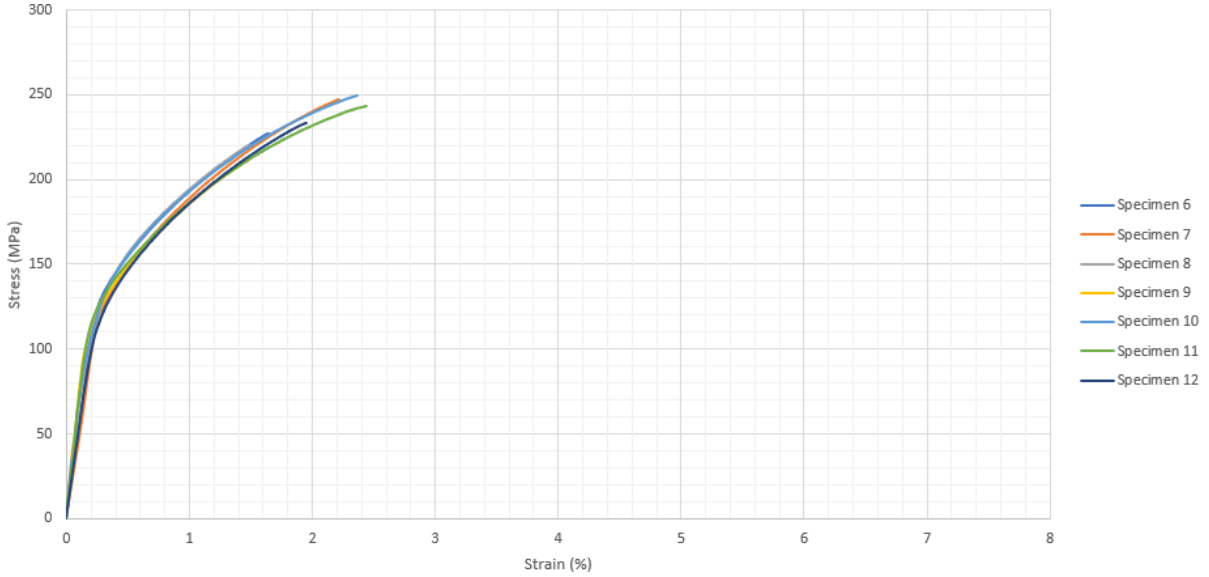

	Section area (mm²)	Yield Strength (MPa)	Ultimate Tensile Strength (MPa)	Elongation (%)
Average	11.537	147±4	233±15	1.54±0.40
Standard	-	>140	>240	>1

Figure 96: Stress-strain plot of AlSi10Mg(Fe) alloy specimens - Conventional injected.

In this alloy, the average value of the three mechanical properties under study (yield strength, ultimate tensile strength and elongation) was higher in specimens where the injection was conventionally performed and the variability of the results obtained was lower. When comparing the average values of yield strength, ultimate tensile strength and elongation obtained with the standard ones, only the ultimate tensile strength is below the theoretical value (min. 240 MPa).

Figure 97 shows the stress-strain plot for the AlSi10MnMg alloy specimens injected with vacuum assistance.

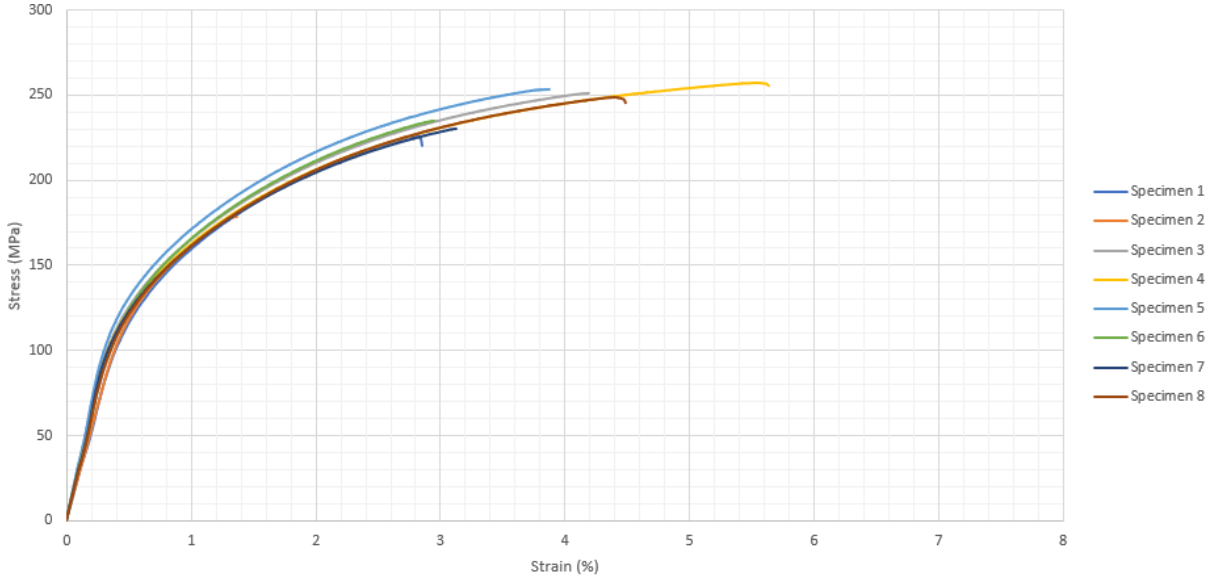

	Section area (mm²)	Yield Strength (MPa)	Ultimate Tensile Strength (MPa)	Elongation (%)
Average	11.860	138±3	235±26	2.66±1.20
Standard	-	120-150	250-290	5-11

Figure 97: Stress-strain plot of AlSi10MnMg alloy specimens - Vacuum-assisted injection.

Figure 98 shows the stress-strain plot for the AlSi10MnMg alloy specimens conventional injected.

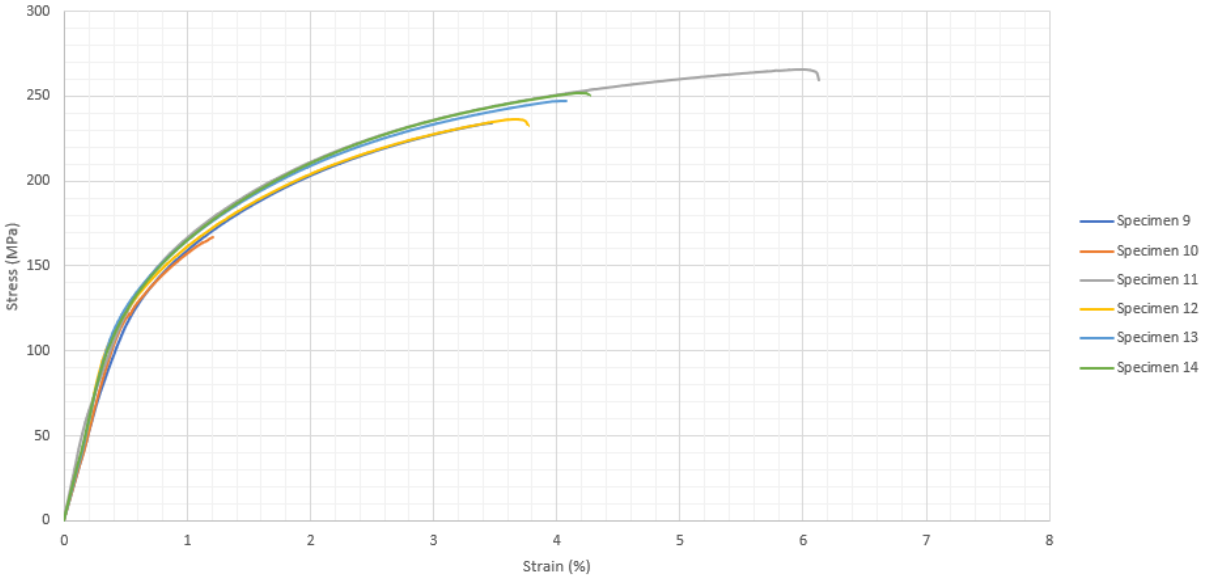

	Section area (mm^2)	Yield Strength (MPa)	Ultimate Tensile Strength (MPa)	Elongation (%)
Average	11.701	136±3	234±35	3.01±1.48
Standard	-	120-150	250-290	5-11

Figure 98: Stress-strain plot of AlSi10MnMg alloy specimens - Conventional injected.

The average value of YS and UTS was higher for the specimens taken from the vacuum-assisted injected parts and for these two properties, the variability of the results obtained was lower. For the elongation, the average value was higher for the specimens where the injection was performed conventionally, but the variability of the results obtained was lower for the injection with vacuum assistance. Only the yield strength values are within the standard value range. Regarding the elongation values obtained, these are about half of the minimum standard value.

Figure 99 shows the stress-strain plot for the AlMg4Fe2 alloy specimens injected with vacuum assistance.

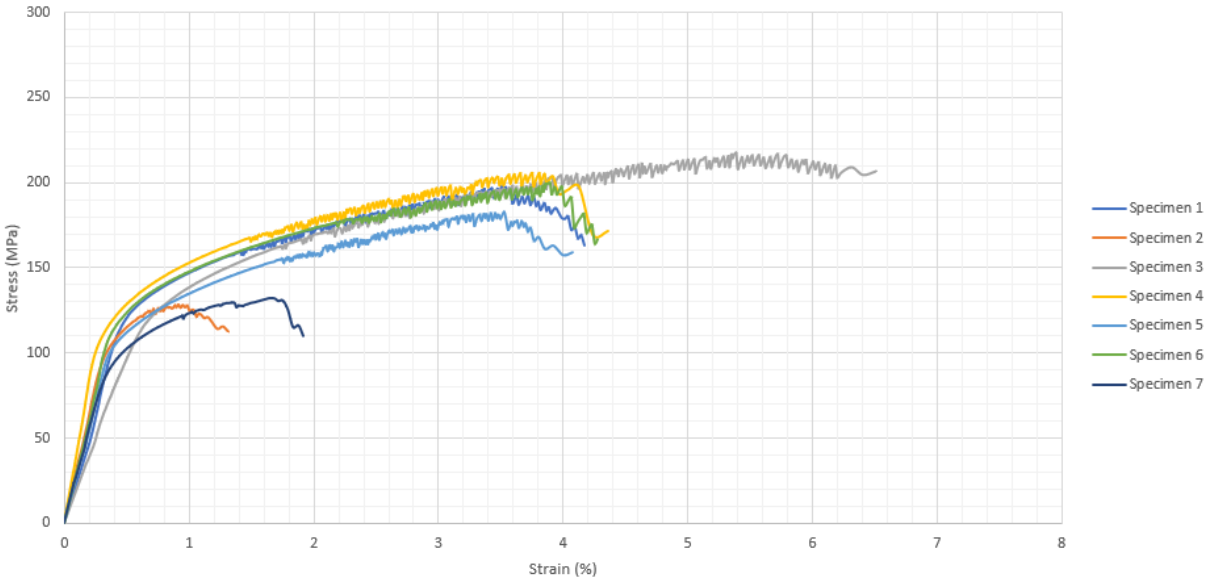

	Section area (mm^2)	Yield Strength (MPa)	Ultimate Tensile Strength (MPa)	Elongation (%)
Average	11.369	124±9	180±36	3.23±1.60
Standard	-	120-150	240-280	10-22

Figure 99: Stress-strain plot of AlMg4Fe2 alloy specimens - Vacuum-assisted injection.

Figure 100 shows the stress-strain plot for the AlMg4Fe2 alloy specimens conventional injected.

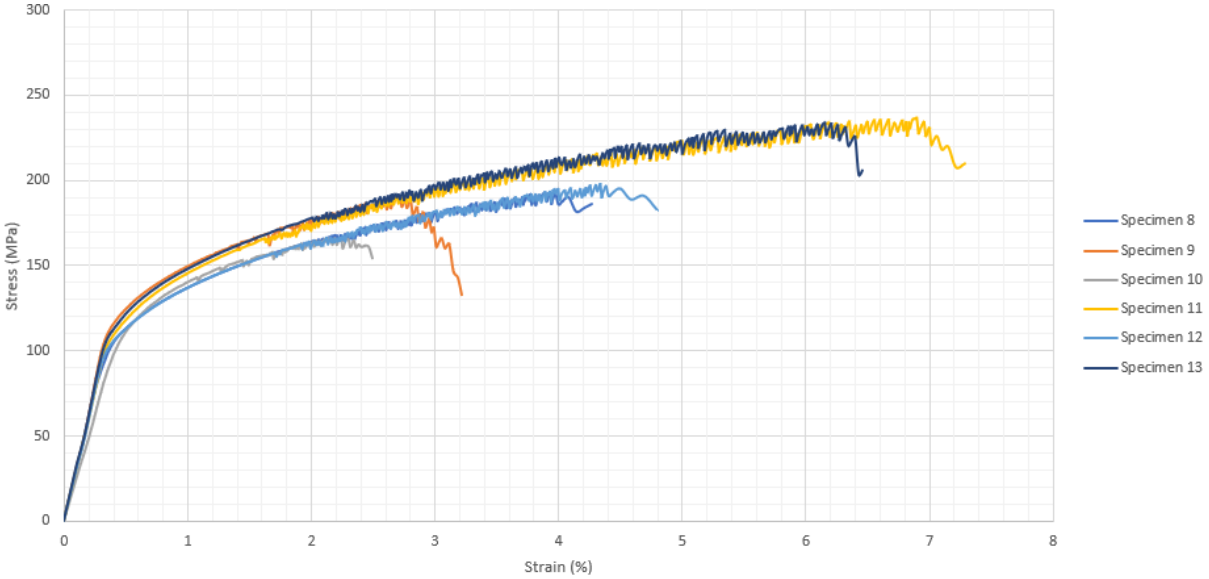

	Section area (mm^2)	Yield Strength (MPa)	Ultimate Tensile Strength (MPa)	Elongation (%)
Average	11.530	126±6	203±27	4.15±1.76
Standard	-	120-150	240-280	10-22

Figure 100: Stress-strain plot of AlMg4Fe2 alloy specimens - Conventional injected.

For the AlMg4Fe2 alloy, the average values of the three mechanical properties under study were higher when the injection was performed conventionally and the variability of the results obtained was lower, except for the elongation, where it was lower when the injection was performed with vacuum assistance. When comparing the average values of yield strength, ultimate tensile strength and elongation obtained with the standard ones, only the yield strength is within the standard values, the remaining properties are well below the standard values. For the average elongation values obtained there was a decrease of about 60-70% from the minimum standard value.

After the tensile tests, the fracture zone of the specimens was analyzed in a stereo microscope. Figure 101 shows the fracture zones of the specimens with the best and worst elongation values for each alloy.

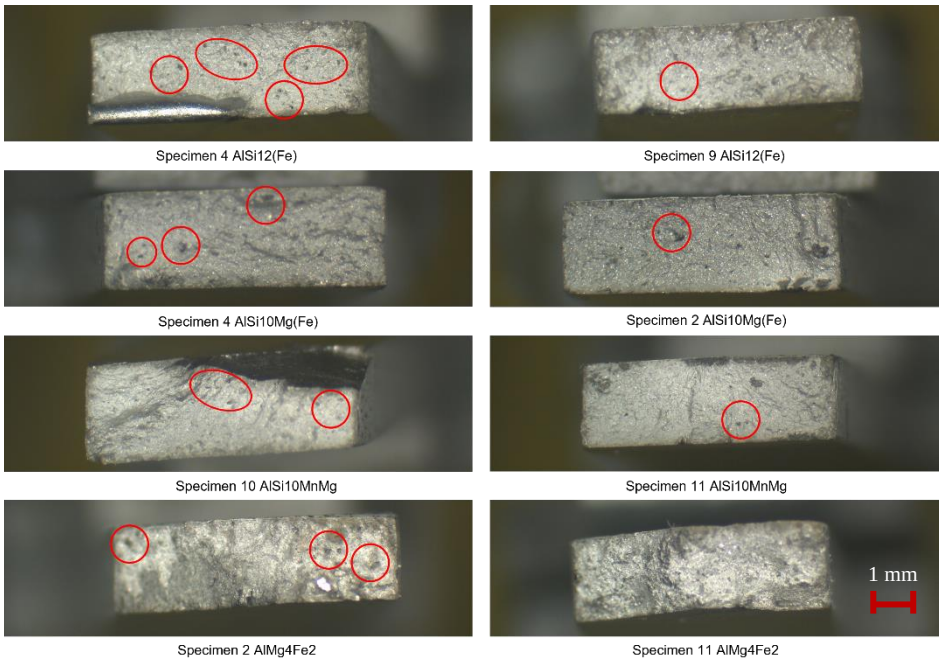

Figure 101: Analysis of defects in the fracture zone of the specimens in the as-cast condition.

The specimens on the left side of Figure 101 have more defects in the fracture zone, which explains the lower elongation values obtained.

In order to better understand the influence of vacuum on the mechanical properties and if there was any difference between the primary and secondary alloys, three graphs are presented in Figure 102, where for each of the three mechanical properties under study are compared the average values and standard deviations obtained for each of the alloys (with and without vacuum).

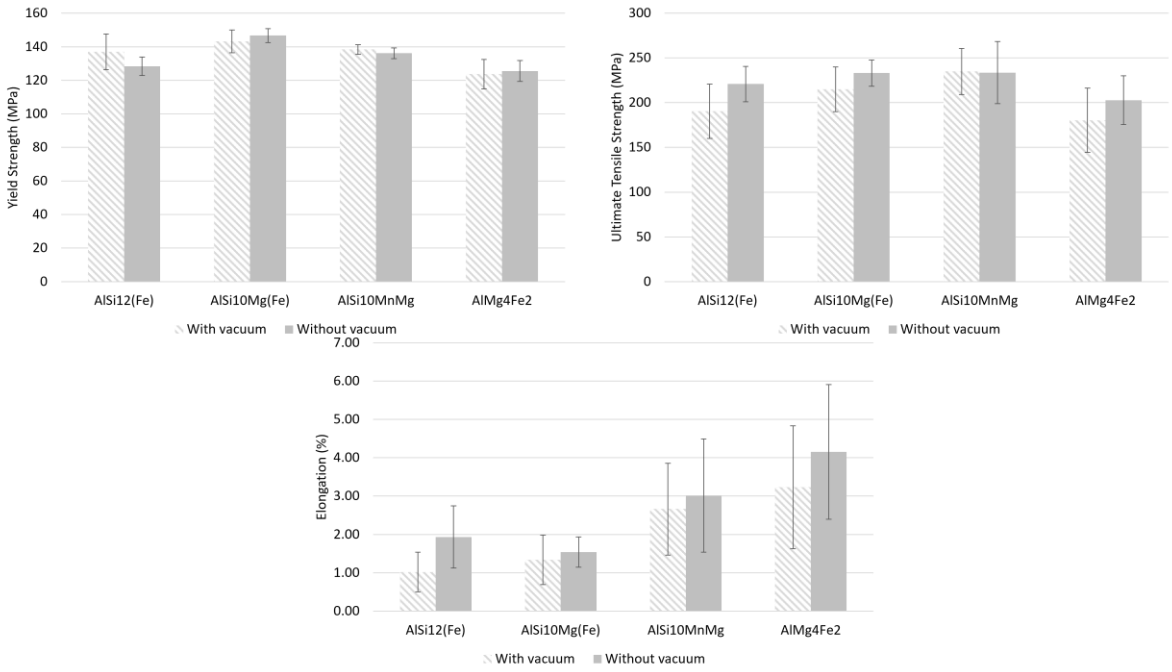

Figure 102: Values of yield strength, ultimate tensile strength and elongation and their standard deviations for the alloys under study in the as-cast condition.

Analyzing the graphs of the previous figure, it can be seen that the use of vacuum during injection only slightly improved the yield strength of AlSi12(Fe) and AlSi10MnMg alloys and the ultimate tensile strength of AlSi10MnMg alloy. It is therefore concluded that the use of

vacuum during injection did not cause any significant improvement in the mechanical properties, which was not the expected result after consulting the literature. This result may be related to the injection conditions and parameters not being optimal. If only the results for AlSi10MnMg alloy are observed, since this was the alloy where the best and most constant injection conditions were obtained, vacuum assisted injection led to a slight improvement in yield strength and ultimate tensile strength and elongation had no improvement, but the average value obtained for vacuum assisted injection (2.66%) was very close to the average elongation value for conventional injection (3.01%). Furthermore, it was the only alloy where for the three mechanical properties under analysis, it was found that the injection performed with vacuum assistance reduces the variability of the results obtained, which is in line with the conclusions obtained by Hu et al. and Dong et al. [44, 45].

Comparing the results of the primary alloys (AlSi10MnMg and AlMg4Fe2) with those of the secondary alloys (AlSi12(Fe) and AlSi10Mg(Fe)), it can be seen, as expected, that the elongation of the primary alloys is higher. The decrease in the iron percentage in the AlSi10MnMg alloy and the absence of high percentages of silicon in the AlMg4Fe2 alloy cause a decrease in the appearance of the β-Al_5FeSi phase, which is quite detrimental to the ductility of the alloys. Within the primary alloys, the AlMg4Fe2 alloy, as expected, showed higher elongation values than the AlSi10MnMg alloy, but the values obtained were much lower than expected. Again, this result can be explained by the injection conditions and parameters used for the AlMg4Fe2 alloy. It was the first time that this alloy was injected at SONAFI, and therefore the injection conditions and parameters used might not be the best.

After the T6 heat treatment, 24 specimens were tested (12 specimens machined from conventionally injected parts and the rest from vacuum-assisted injected parts) of each of AlSi10Mg(Fe) and AlSi10MnMg alloys. It is intended to evaluate whether due to the heat treatment performed there was an increase in yield strength and ultimate tensile strength or whether the mechanical properties deteriorated due to blistering or coalescence of gas porosities caused by the solution heat treatment.

Figure 103 shows the stress-strain plot for the AlSi10Mg(Fe) alloy specimens injected with vacuum assistance after T6 heat treatment.

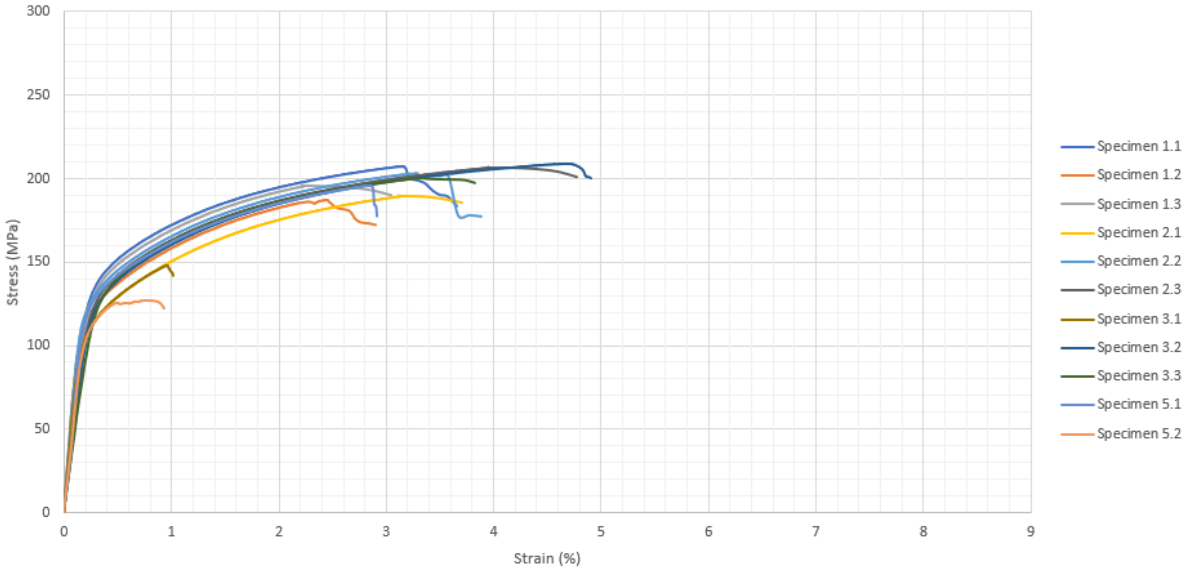

	Section area (mm^2)	Yield Strength (MPa)	Ultimate Tensile Strength (MPa)	Elongation (%)
Average	10.773	134±9	188±26	2.94±1.25
Standard	-	-	-	-

Figure 103: Stress-strain plot of AlSi10Mg(Fe) alloy specimens after T6 heat treatment - Vacuum-assisted injection.

Figure 104 shows the stress-strain plot for the AlSi10Mg(Fe) alloy specimens conventional injected after T6 heat treatment.

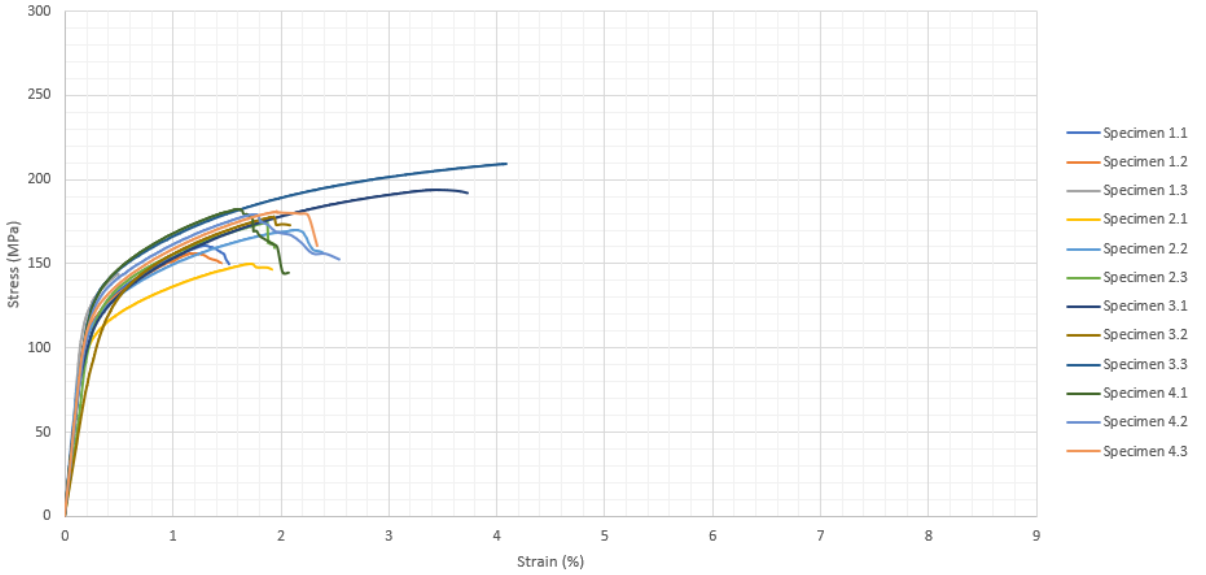

	Section area (mm²)	Yield Strength (MPa)	Ultimate Tensile Strength (MPa)	Elongation (%)
Average	10.688	132±9	173±19	1.93±0.94
Standard	-	-	-	-

Figure 104: Stress-strain plot of AlSi10Mg(Fe) alloy specimens after T6 heat treatment - Conventional injected.

Figure 105 shows the stress-strain plot for the AlSi10MnMg alloy specimens injected with vacuum assistance after T6 heat treatment.

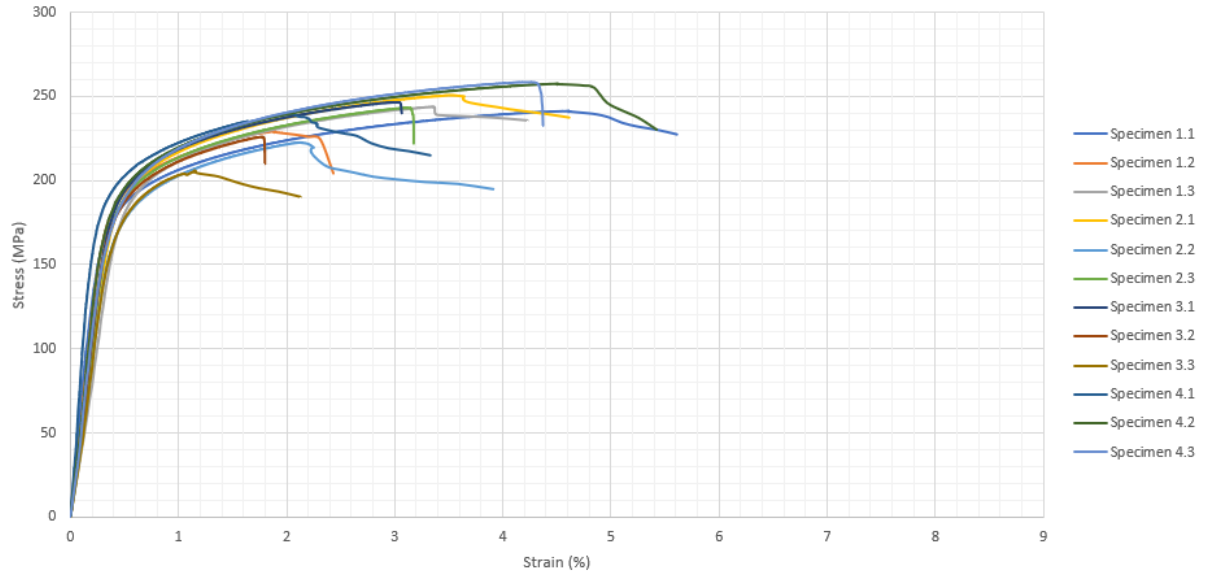

	Section area (mm²)	Yield Strength (MPa)	Ultimate Tensile Strength (MPa)	Elongation (%)
Average	12.109	193±6	239±15	3.23±1.27
Standard	-	210-280	290-340	7-12

Figure 105: Stress-strain plot of AlSi10MnMg alloy specimens after T6 heat treatment - Vacuum-assisted injection.

Figure 106 shows the stress-strain plot for the AlSi10MnMg alloy specimens conventional injected after T6 heat treatment.

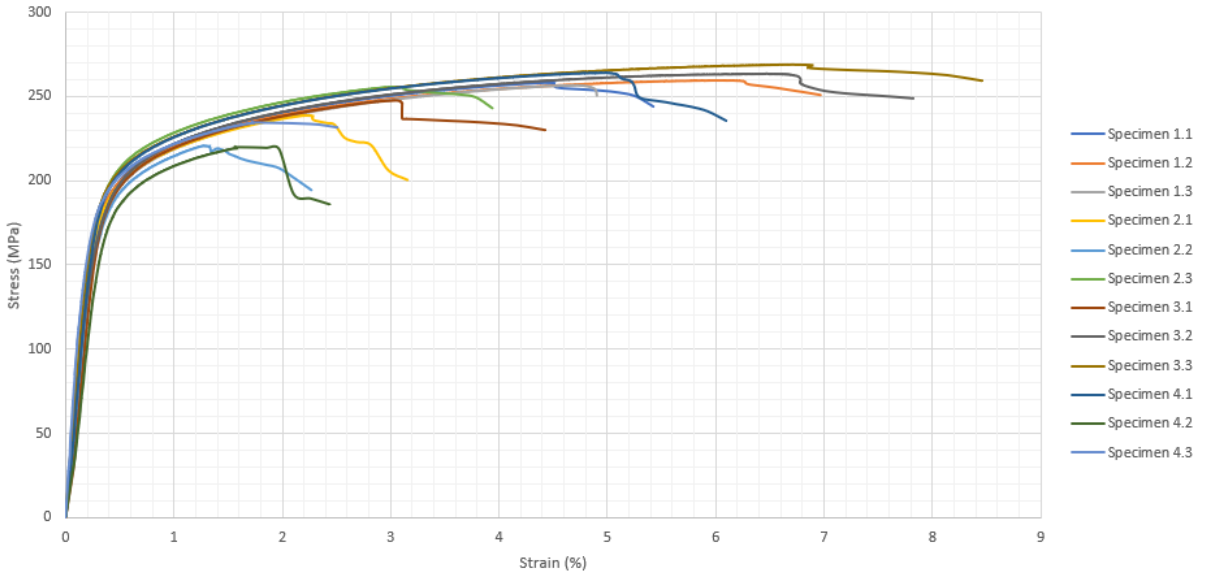

	Section area (mm^2)	Yield Strength (MPa)	Ultimate Tensile Strength (MPa)	Elongation (%)
Average	12.224	196±5	249±17	4.50±2.10
Standard	-	210-280	290-340	7-12

Figure 106: Stress-strain plot of AlSi10MnMg alloy specimens after T6 heat treatment - Conventional injected.

To better understand the effect of the T6 heat treatment on the AlSi10Mg(Fe) and AlSi10MnMg alloys mechanical properties, a summary table (Table 31) with the mechanical properties of the alloys before and after heat treatment is presented.

Table 31: Mechanical properties of AlSi10Mg(Fe) and AlSi10MnMg alloys before and after heat treatment.

Alloy	**State**	**YS** (MPa)	**UTS** (MPa)	**Elongation** (%)
AlSi10Mg(Fe)	As-cast VADC	143	215	1.34
	As-cast HPDC	147	233	1.54
	T6 VADC	134	188	2.94
	T6 HPDC	132	173	1.93
AlSi10MnMg	As-cast VADC	138	235	2.66
	As-cast HPDC	136	234	3.01
	T6 VADC	193	239	3.23
	T6 HPDC	196	249	4.50

For the AlSi10Mg(Fe) alloy there was a decrease of YS and UTS after the heat treatment. Taking into account this result and the result obtained for hardness in Chapter 4.3, it is possible to say that the alloy has softened after the solution heat treatment and that the time or temperature of artificial aging have not been ideal for the structural hardening of the alloy and consequent increase in YS and UTS. The increase in elongation by 119% in the vacuum-assisted injected parts and by 25% in the conventionally injected parts after heat treatment can be explained by the spheroidization of silicon during the solution heat treatment.

In the AlSi10MnMg alloy, there was an improvement in the mechanical properties after the heat treatment, but they turned out to be lower than the minimum standardized value. The YS increased by about 40% after the heat treatment due to structural hardening. The elongation increased by 21% in the vacuum-assisted injected parts and by 50% in the conventionally injected parts after heat treatment, an increase probably justified by silicon spheroidization. The mechanical properties of the conventionally injected parts were higher than the vacuum-assisted injected parts because 3 of the 4 vacuum-assisted injected parts had a higher percentage of defects than the conventionally injected parts (Table 25). This higher quantity of defects leads to a reduction of the specimen's cross-sectional area and thus to a lower mechanical strength.

4.7 Characterization of the microstructure

The microstructure of the different alloys under study was observed in the C-C section, Figure 107.

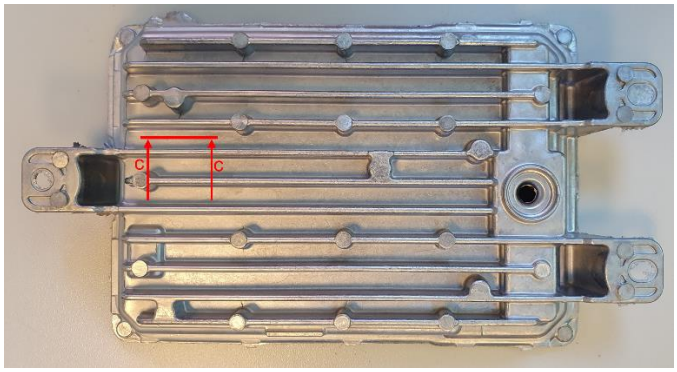

Figure 107: Analyzed section of the part for microstructure characterization.

Initially, the microstructure of the as-casted parts was characterized to serve as a basis for comparison with the microstructures obtained after heat treatment. In Figure 108, it can be seen that the AlSi12(Fe), AlSi10Mg(Fe) and AlSi10MnMg alloys present the two phases typical of AlSi alloys: the primary aluminum phase (αAl) with dendritic morphology and the eutectic (αAl+Si).

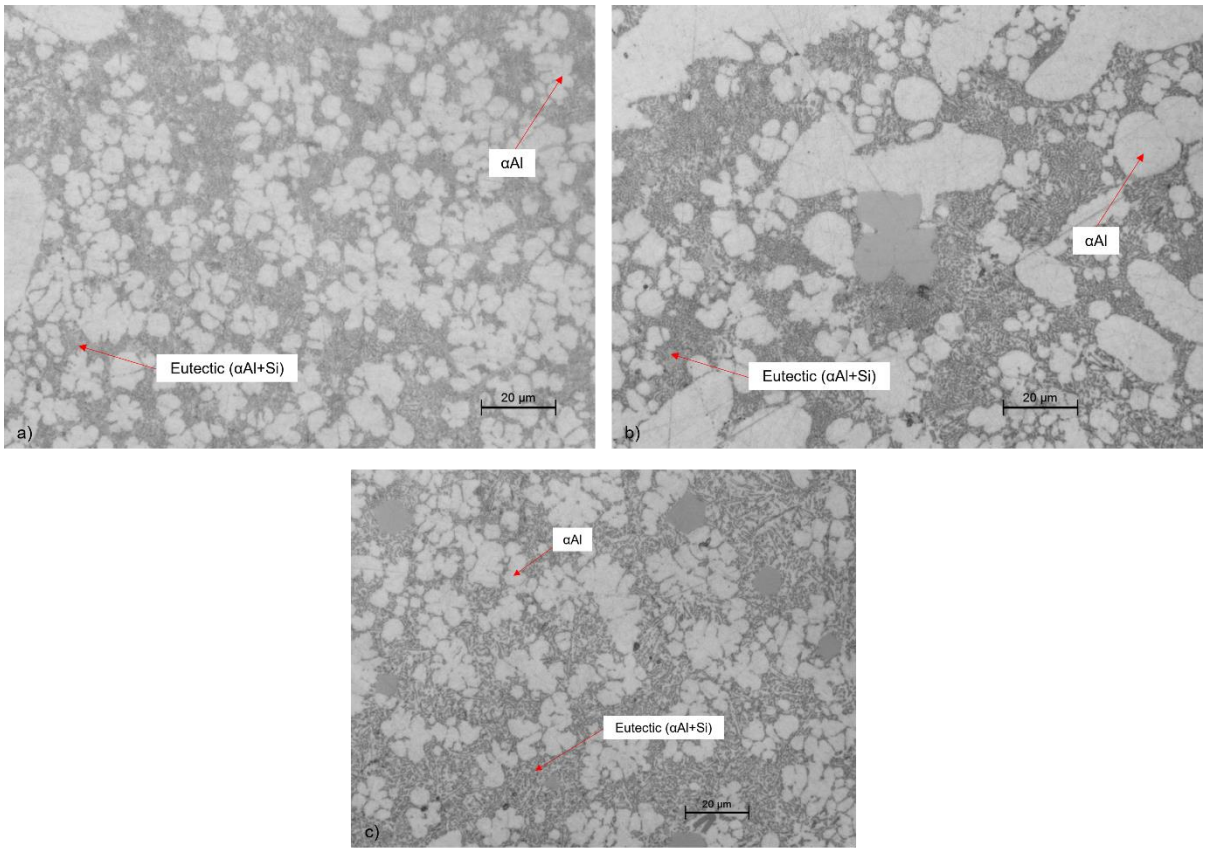

Figure 108: Microstructure of the alloy in the as-cast condition: a) AlSi10Mg(Fe) magnification 500x; b) AlSi10MnMg magnification 500x; c) AlSi12(Fe) magnification 500x.

The microstructure (Figure 109) of the AlMg4Fe2 alloy has a morphology quite different from the other alloys, as it belongs to the AlMg family.

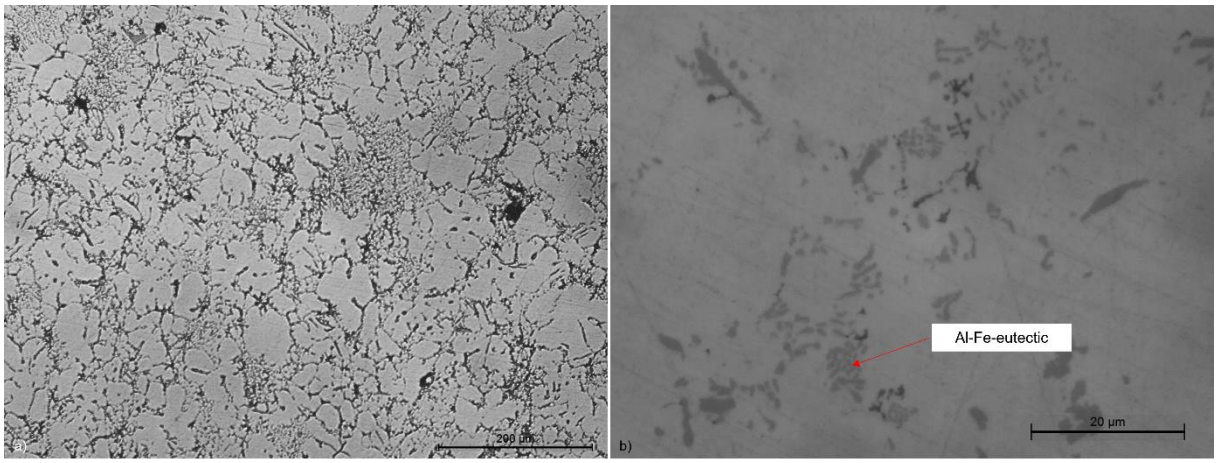

Figure 109: Microstructure of AlMg4Fe2in the as-cast condition. a) magnification 100x; b) magnification 1000x.

Due to the high cooling rates of the HPDC process that cause the refinement of the different phases of the microstructure there was some difficulty in identifying typical phases such as: the β-Al_5FeSi phase and the α-$Al_{15}(Fe,Mn)_3Si_2$ phase. To facilitate this identification, samples of the alloys under study were observed in SEM and an EDS analysis was performed on some of the identified structures.

The images in Figure 110 were obtained through backscatter electrons, and therefore the higher the atomic number of the element, the brighter it will be in the image. Comparing the images in Figure 110, knowing that iron has a higher atomic number than silicon, magnesium, aluminum and manganese and that the β-Al_5FeSi phase has a morphology that resembles a needle, it is possible to conclude that as expected because the AlSi10Mg(Fe) alloy (Figure 110a)) is a secondary alloy it would have a higher amount of needles (detrimental to ductility) than the primary AlSi10MnMg alloy (Figure 110b)).

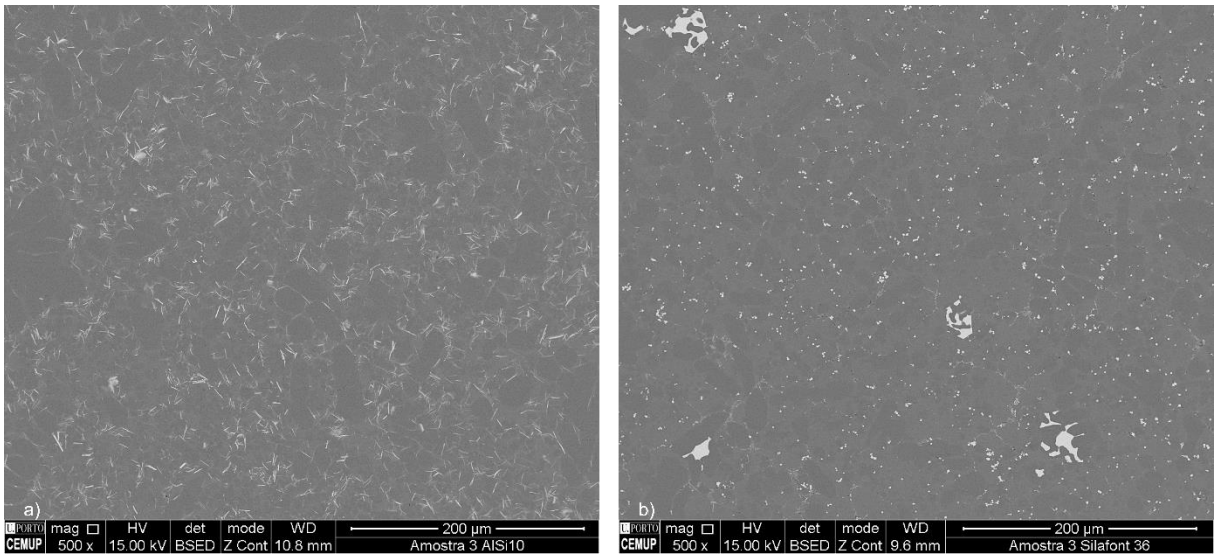

Figure 110: The as-cast SEM microstructure. a) AlSi10Mg(Fe) alloy; b) AlSi10MnMg alloy.

As can be seen in Figure 111 (Z8 and Z4), the addition of manganese leads to the formation of intermetallics that do not have needle morphology, and thus are not as detrimental to the mechanical properties of the alloys.

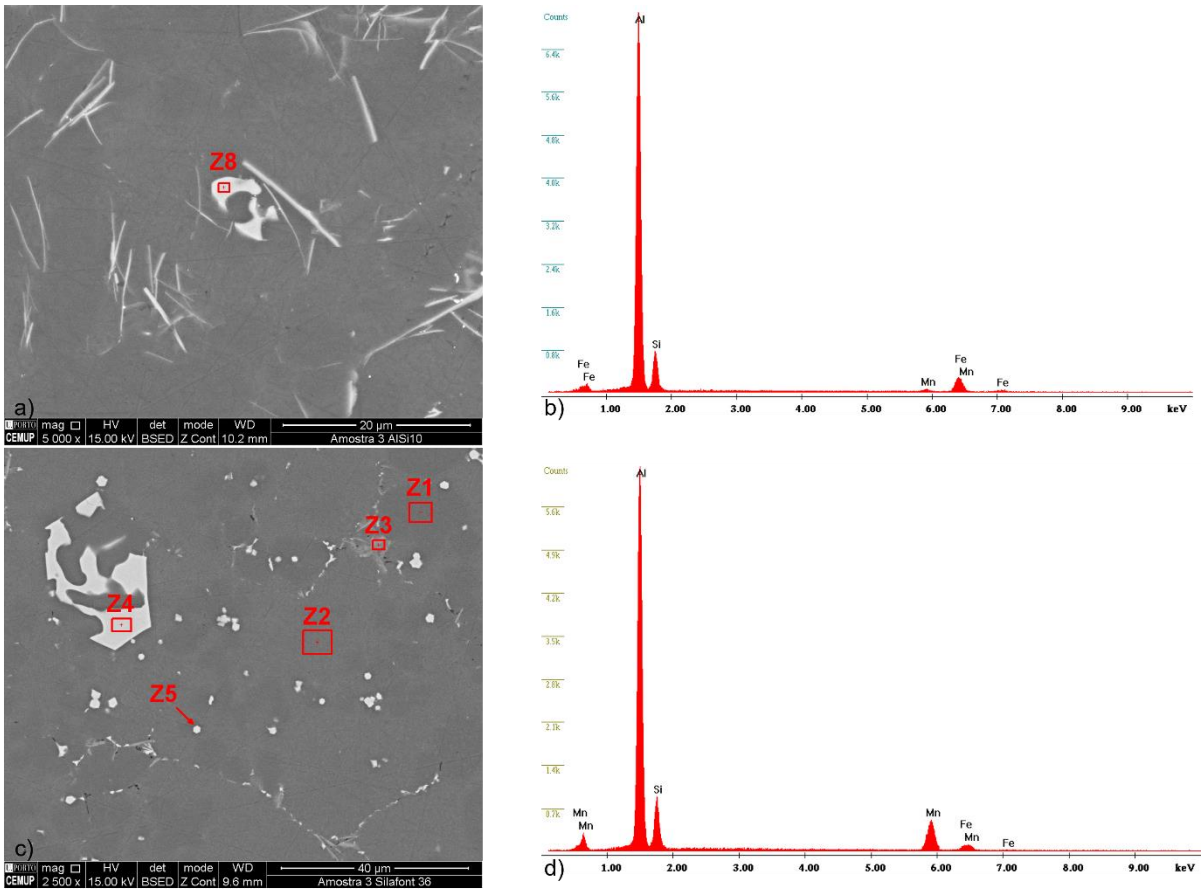

Figure 111: AlFeMnSi phases. a) Z8 - AlFeMnSi phase in AlSi10Mg(Fe) alloy; b) Spectrum of the EDS analysis of Z8; c) Z4 - AlFeMnSi phase in AlSi10MnMg alloy; d) Spectrum of the EDS analysis of Z4.

In Figure 112 is shown an intermetallic constituent with a morphology very similar to a chinese-script, which may correspond to the α-$Al_{15}(Fe,Mn)_3Si_2$ phase.

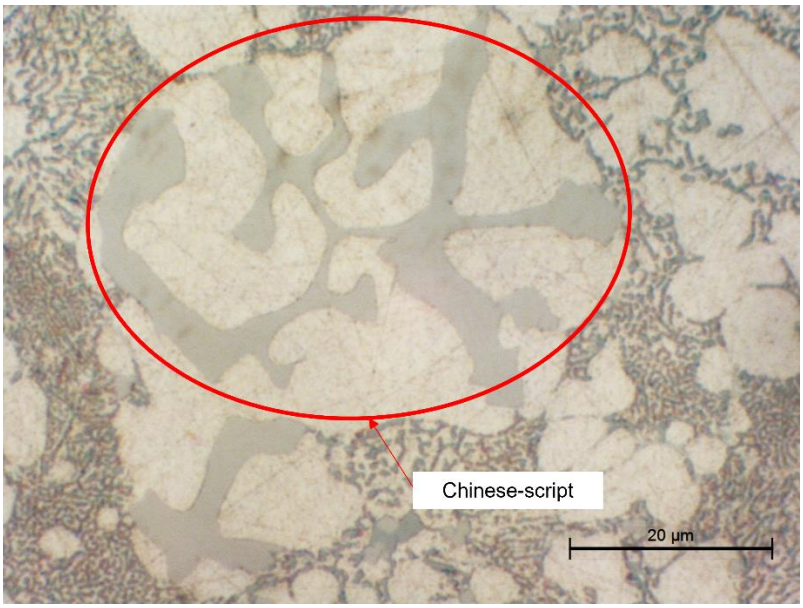

Figure 112: Chinese-script in AlSi10MnMg alloy (magnification 1500x).

After the T6 heat treatment due to solution heat treatment, silicon fragmentation and spheroidization occurred in both alloys (AlSi10Mg(Fe) and AlSi10MnMg). Figure 113 shows the microstructure of AlSi10MnMg alloy after heat treatment.

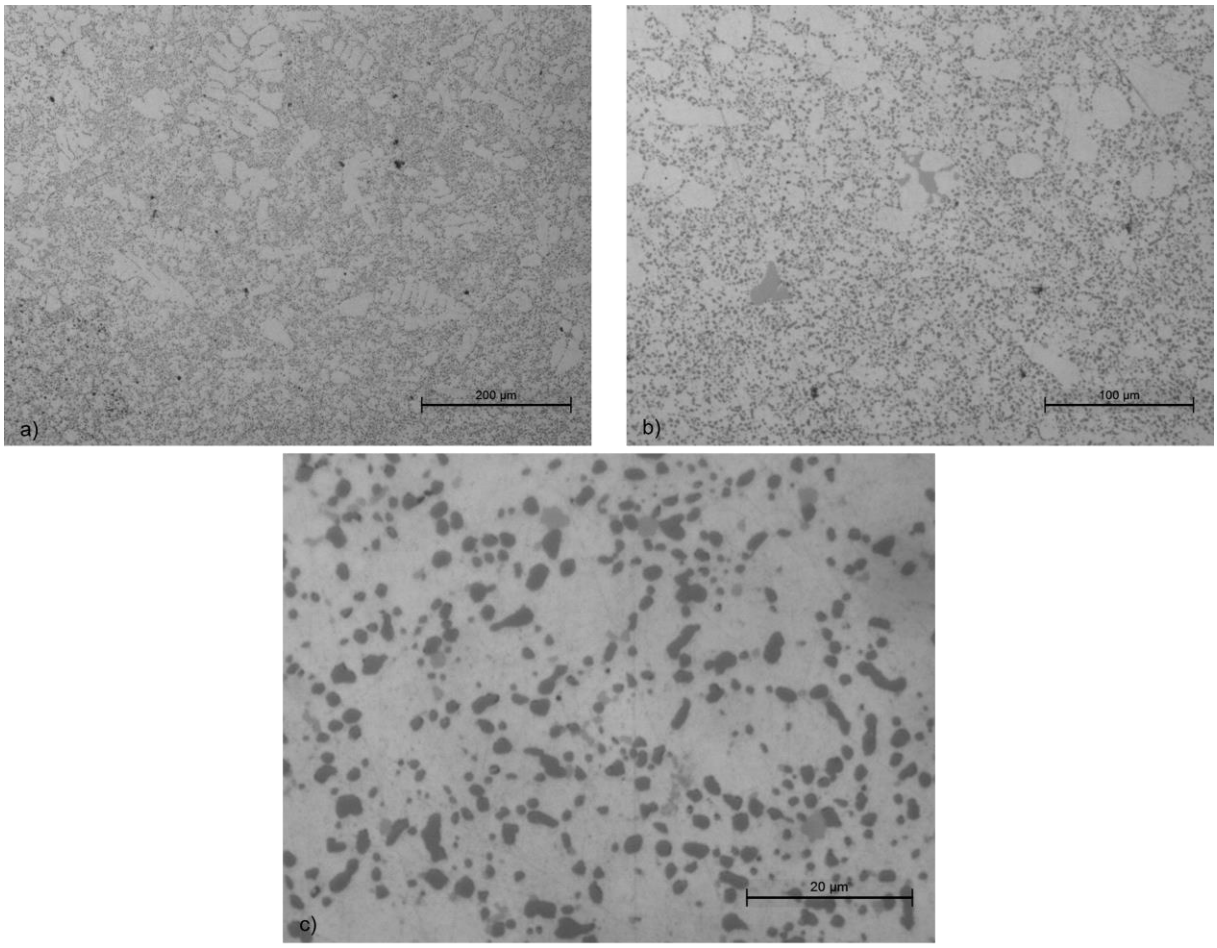

Figure 113: Silicon fragmentation and spheroidization in AlSi10MnMg alloy. a) magnification 100x; b) magnification 200x; c) magnification 1000x.

With the EDS analysis it was possible to verify that there was precipitation of Mg-Si intermetallics in the aluminum matrix during the artificial aging heat treatment because it is detected in the Z1 zones (αAl phase) of Figures 114c) and 115c) when without heat treatment it was not detected Figures 114a) and 115a).

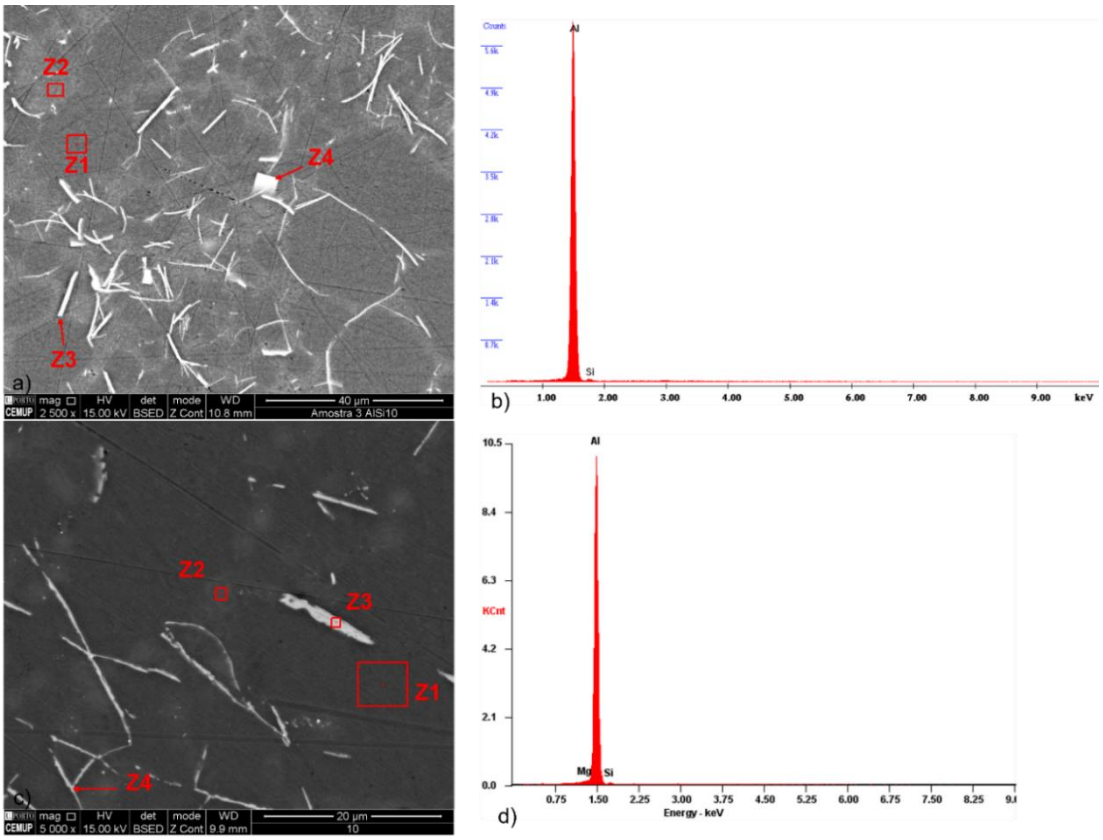

Figure 114: Precipitation of Mg-Si intermetallics in the aluminum matrix in AlSi10Mg(Fe) alloy. a) Z1 - αAl phase before heat treatment; b) Spectrum of the EDS analysis of Z1 before heat treatment; c) Z1 - αAl phase after heat treatment; d) Spectrum of the EDS analysis of Z1 after heat treatment.

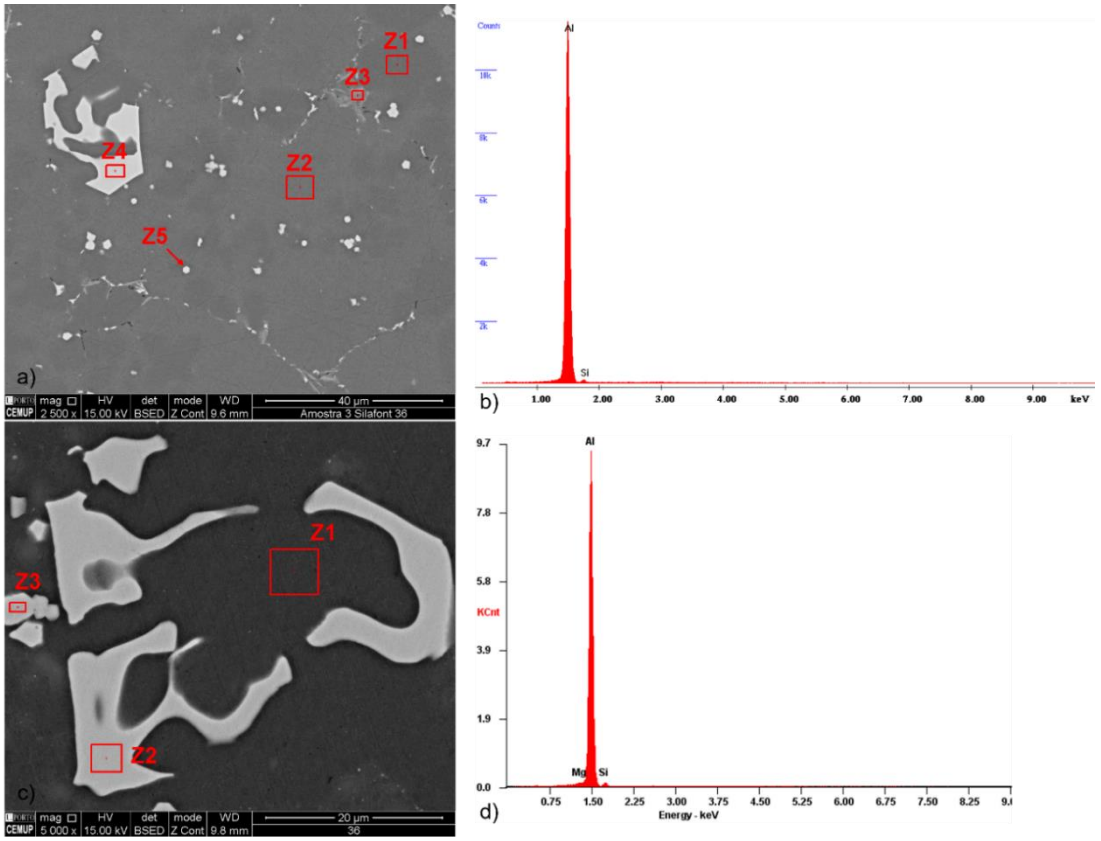

Figure 115: Precipitation of Mg-Si intermetallics in the aluminum matrix in AlSi10MnMg alloy. a) Z1 - αAl phase before heat treatment; b) Spectrum of the EDS analysis of Z1 before heat treatment; c) Z1 - αAl phase after heat treatment; d) Spectrum of the EDS analysis of Z1 after heat treatment.

5 Conclusions and future work

In Chapter 5.1, the conclusions drawn after the accomplished work are presented. Some suggestions for future works are also shown in Chapter 5.2.

5.1 Conclusions

The main conclusions to be drawn from this work are:

- In the as-cast condition, VADC led to a reduction in the amount and percentage of defects (64% reduction for AlSi12(Fe) alloy parts, 81% reduction for AlSi10Mg(Fe) alloy parts, 60% reduction for AlSi10MnMg alloy parts, and 78% reduction for AlMg4Fe2 alloy parts). Considering that the injection conditions for AlSi10MnMg alloy were the most constant and optimized, it can be concluded that for a vacuum level of 200 mbar, the defect reduction will be around 60%.
- After the heat treatment, in the vacuum injected parts there was an exponential increase in the quantity of defects and a decrease in the average defect volume due to the appearance of a larger number of gas porosities (small volume and sphericity greater than 0.4). The solution heat treatment led to an increase in the number and diameter of the gas porosities and an increase in the number of shrinkage porosities due to the coalescence of the gas porosities. This coalescence causes distortion of the porosities and consequent decrease in sphericity.
- For the analyzed sections using metallography and computed tomography, the porosity values were similar, however CT has the advantage of being a non-destructive method that enables an analysis of defects throughout the part with the ability to analyze different sections in different planes.
- The highest amount of blistering occurred in parts where the defect volume ratio was higher, which means that they may be related. The parts that were analyzed, those that were vacuum injected showed generally less blistering. As there was blistering in both vacuum injected and conventionally injected parts, it means that vacuum generation during injection was not efficient. Furthermore, the parameters used in the heat treatment were not optimized to minimize blistering.
- In the as-cast condition, taking into account the mean values and standard deviations obtained for the mechanical properties, it can be concluded that these are similar for HPDC and VADC, which is more or less in agreement with the results obtained by Szalva et al. [39]. By not being able to make an efficient control of the injection process conditions and the generation of vacuum, it was not possible to observe significant differences between injection with and without vacuum. In addition, the cross-sectional area of the specimens was variable, as they were machined from warped parts, and therefore it was difficult to obtain specimens with uniform thickness. This variation in area also had an influence on the mechanical properties obtained. As expected, the primary aluminum alloys presented higher elongation values than the secondary aluminum alloys due to the reduced amount of needles of the β-Al_5FeSi phase.
- In AlSi10Mg(Fe) and AlSi10MnMg alloys after heat treatment the elongation improved between 21% and 119% due to silicon spheroidization during solution heat treatment. The YS and UTS decreased in AlSi10Mg(Fe) alloy after T6 due to its softening. On the other hand, in the AlSi10MnMg alloy, there was an increase in YS and UTS due to the precipitation of Mg-Si intermetallics in the aluminum matrix. In the conventionally injected parts of AlSi10MnMg alloy, the mechanical properties were higher than in the vacuum injected parts because 3 of the 4 parts tested showed a higher quantity of defects. This higher number of

defects leads to a reduction in the cross-sectional area of the specimens which causes a reduction in mechanical strength and ductility.

5.2 Future work

In order to improve the results that were obtained in this work, the following could be done:

- The injection parameters, as well as, vacuum cycle - should be properly monitored so that they can be optimized;
- Perform two-stage vacuum by evacuating in the die cavity and shot sleeve to increase the vacuum level;
- Tests to optimize injection conditions, especially in primary alloys;
- Tighter control of the metallurgical quality of the bath to prevent oxide formation and hydrogen absorption;
- Control the quantity of lubricant/release agent applied to the mold to prevent gas porosity caused by hydrogen;
- Optimization of the heat treatment cycles. Shorter stage times and/or lower temperatures during the solution heat treatment should lead to a reduction of blistering. Extend the artificial aging time to achieve peak hardness;
- The numbering of the specimens according to their positioning in the part, in order to understand if there is an area of the part where the concentration of defects is higher;
- Designing a mold to inject specimens. Thus, in theory, the mechanical properties obtained will be close to the standard mechanical properties.

References

[1] F. Czerwinski, "Current Trends in Automotive Lightweighting Strategies and Materials," *Materials,* vol. 14, no. 21, p. 6631, 2021, doi: https://doi.org/10.3390/ma14216631.

[2] "Aluminium in Cars - Unlocking the Light-Weighting Potential," European Aluminium Association, Belgium, 2013. [Online]. Available: https://www.european-aluminium.eu/media/3371/aluminium-in-cars-unlocking-the-lightweighting-potential.pdf

[3] A. Svendsen. "Aluminum Continues Unprecedented Growth in Automotive Applications." Light Metal Age. www.lightmetalage.com (accessed 9 March, 2022).

[4] A. A. Luo, A. K. Sachdev, and D. Apelian, "Alloy development and process innovations for light metals casting," *Journal of Materials Processing Technology,* vol. 306, p. 117606, 2022, doi: https://doi.org/10.1016/j.jmatprotec.2022.117606.

[5] B. Stojanovic and I. Epler, "Application of aluminum and aluminum alloys in engineering," *Applied Engineering Letters,* vol. 3, pp. 52-62, 2018, doi: https://doi.org/10.18485/aeletters.2018.3.2.2.

[6] A. Musfirah and A. Jaharah, "Magnesium and aluminum alloys in automotive industry," *Journal of Applied Sciences Research,* vol. 8, no. 9, pp. 4865-4875, 2012.

[7] EccoMelt_Admin. "Electric Vehicles to Transform Aluminum Demand by 2035." Eccomelt LLC. https://eccomelt.com/electric-vehicles-transform-aluminum-demand-2035/ (accessed 10 March, 2022).

[8] S. G. Epstein, J. G. Kaufman, and P. Pollak, "Aluminum and Its Alloys," in *Mechanical Engineers' Handbook*, M. Kutz Ed., 2nd ed.: Wiley, 1998, ch. 3, pp. 45-58.

[9] F. Habashi, "Extractive Metallurgy of Aluminum," in *Handbook of Aluminum: Alloy Production and Materials Manufacturing* vol. 2, G. E. Totten and D. S. MacKenzie Eds., 1st ed.: Marcel Dekker, 2003, ch. 1, pp. 1-45.

[10] J. Nath, *Aluminum Castings Engineering Guide*. Materials Park, Ohio: ASM International, 2018.

[11] ABAL. *Fundamentos e Aplicações do Alumínio*, 2007.

[12] M. R. Gomes and E. B. Filho, *Propriedades e Usos de Metais Não Ferrosos*. Associação Brasileira de Metais, 1986.

[13] Azom. "Aluminium: Specifications, properties, classifications and classes." Azom. https://www.azom.com/article.aspx?ArticleID=2863 (accessed 21 March, 2022).

[14] J. G. Kaufman and E. L. Rooy, *Aluminum Alloy Castings: Properties, Processes, and Applications*. Materials Park, Ohio: ASM International, 2004.

[15] E. Cinkilic, C. Ridgeway, X. Yan *et al.*, "A formation map of iron-containing intermetallic phases in recycled cast aluminum alloys," *Metallurgical and Materials Transactions A,* vol. 50, no. 12, pp. 5945-5956, 2019, doi: https://doi.org/10.1007/s11661-019-05469-6.

[16] F. Casarotto, A. J. Franke, and R. Franke, "High-pressure die-cast (HPDC) aluminium alloys for automotive applications," in *Advanced materials in automotive engineering*, J. Rowe Ed.: Elsevier, 2012, ch. 6, pp. 109-149.

[17] M. Warmuzek, *Aluminum-Silicon Casting Alloys: Atlas of Microstructures*. Materials Park, Ohio: ASM International, 2017.

[18] M. Hartlieb, "High Integrity Diecasting for Structural Applications," ed, 2013. [Online]. Available: https://www.visi-trak.com/pdf/High%20Integrity%20Die%20Casting%20-%20iMdc%20Dec%202013.pdf

[19] J. A. Taylor, "Iron-containing intermetallic phases in Al-Si based casting alloys," *Procedia Materials Science,* vol. 1, pp. 19-33, 2012, doi: https://doi.org/10.1016/j.mspro.2012.06.004.

[20] R. Alloys. "Primary Aluminium Alloys for Pressure Die Casting." Rheinfelden Alloys. https://rheinfelden-alloys.eu/en/ (accessed March, 2022).

[21] M. Hartlieb, "Aluminum alloys for structural die casting," *Die Casting Engineer,* vol. 57, no. 3, pp. 40-43, 2013.

[22] P. Biswas, S. Patra, and M. Kumar Mondal, "Structure-property correlation of eutectic Al-12.4 Si alloys with and without Zirconium (Zr) addition," *International Journal of Cast Metals Research,* vol. 33, no. 2-3, pp. 134-145, 2020, doi: https://doi.org/10.1080/13640461.2020.1769319.

[23] X. Ai, J. Wang, T. Wen *et al.*, "A high Fe-containing AlSi12 alloy fabricated by laser powder bed fusion," *Journal of Materials Research and Technology,* vol. 18, pp. 4513-4521, 2022, doi: https://doi.org/10.1016/j.jmrt.2022.04.008.

[24] J. E. Gruzleski and B. M. Closset, *The treatment of liquid aluminum-silicon alloys*. Inc. Des Plaines, Illinois, USA: American Foundrymen's Society, 1990.

[25] *Alumínio e ligas de alumínio,* NP EN1706, 2000.

[26] N. A. G. Lima, "Tratamento térmico de envelhecimento da liga de fundição AlSi10Mg (Fe)," M.S. thesis, Porto Univ., Porto, 2012. [Online]. Available: https://hdl.handle.net/10216/72551

[27] R. Alloys. "Primary Aluminum HPDC Alloys for Structural Casts in Vehicle Construction." Rheinfelden Alloys. https://rheinfelden-alloys.eu/en/ (accessed March, 2022).

[28] Alcoa. "Foundry Aluminum Alloys." Alcoa. https://www.alcoa.com/global/en/what-we-do/aluminum/cast-products/foundry-aluminum-alloys (accessed June, 2022).

[29] K. Greven and M. Loganathan, "Aluminum Casting Alloy," United States Patent 9982329B2, May 29, 2018.

[30] H. Zhan and B. Hu, "Analyzing the microstructural evolution and hardening response of an Al-Si-Mg casting alloy with Cr addition," *Materials Characterization,* vol. 142, pp. 602-612, 2018, doi: https://doi.org/10.1016/j.matchar.2018.06.026.

[31] X. Deng, Y. Wang, J. Wang *et al.*, "Quench sensitivity of A379 alloy under high-pressure die-casting and gravity-casting processes," *Proceedings of the Institution of Mechanical Engineers, Part L: Journal of Materials: Design and Applications,* vol. 236, no. 9, pp. 1715-1723, 2022, doi: https://doi.org/10.1177/14644207221081620.

[32] J. Campbell, "Perspective Chapter: A Personal Overview of Casting Processes," in *Casting Processes and Modelling of Metallic Materials*, Z. Abdallah Ed.: IntechOpen, 2021, ch. 1, pp. 1-17.

[33] I. Polmear, D. StJohn, J.-F. Nie *et al.*, "High-pressure die casting," in *Light Alloys - Metallurgy of the Light Metals*, 5th ed.: Elsevier, 2017, ch. 3.5.3, pp. 134-139.

[34] P. K. Mallick, *Materials, Design and Manufacturing for Lightweight Vehicles*. Woodhead Publishing, 2010.

[35] M. Jolly, "Die-Casting (High-Pressure Die-Casting)," in *Comprehensive Structural Integrity*, vol. 1, I. Milne, R. O. Ritchie, and B. Karihaloo Eds.: Elsevier, 2003, ch. 1.18.3.2.5, pp. 413-415.

[36] K. Anderson, J. Weritz, and J. G. Kaufman, *ASM Handbook, Volume 2A: Aluminum Science and Technology*. Materials Park, Ohio: ASM International, 2018.

[37] Dynacast. "Hot chamber die casting process: Hot chamber casting." Dynacast. https://www.dynacast.com/en/specialty-die-casting/die-cast-process/hot-chamber-die-casting (accessed 18 April, 2022).

[38] P. Robbins and L. Chun (Ken) Chien, "High Pressure Die Casting Structural Aluminum," ed, 2014. [Online]. Available: https://castool.com/wp-content/uploads/2018/08/High-Pressure-Die-Casting-Links-2014.pdf

[39] P. Szalva and I. N. Orbulov, "The effect of vacuum on the mechanical properties of die cast aluminum AlSi9Cu3 (Fe) alloy," *International Journal of Metalcasting*, vol. 13, no. 4, pp. 853-864, 2019, doi: https://doi.org/10.1007/s40962-018-00302-z.

[40] X. Hu, Q. Zhu, S. Midson *et al.*, "Blistering in semi-solid die casting of aluminium alloys and its avoidance," *Acta Materialia*, vol. 124, pp. 446-455, 2017, doi: https://doi.org/10.1016/j.actamat.2016.11.032.

[41] A. I. H. Committee, *ASM Handbook, Volume 15: Casting*. Materials Park, Ohio: ASM International, 2008.

[42] V. Nandakumar, "Process and Tool Design for the High Integrity Die Casting of Aluminum and Magnesium Alloys," M.S. thesis, Ohio State Univ., Ohio, 2014. [Online]. Available: http://rave.ohiolink.edu/etdc/view?acc_num=osu1409032627

[43] C. Bagnoud and R. Bigger, "Die evacuation: Valve or chill vent?," ed, 2008. [Online]. Available: http://www.soundcastproject.eu/files/2013/10/Evacuation_performance_of_a_ProVac_vacuum_valve_and_a_chill-vent.pdf

[44] C. Hu, H. Zhao, X. Wang *et al.*, "Microstructure and properties of AlSi12Fe alloy high pressure die-castings under different vacuum levels," *Vacuum*, vol. 180, p. 109561, 2020, doi: https://doi.org/10.1016/j.vacuum.2020.109561.

[45] X. Dong, X. Zhu, and S. Ji, "Effect of super vacuum assisted high pressure die casting on the repeatability of mechanical properties of Al-Si-Mg-Mn die-cast alloys," *Journal of Materials Processing Technology*, vol. 266, pp. 105-113, 2019, doi: https://doi.org/10.1016/j.jmatprotec.2018.10.030.

[46] Z. Arhumah, "Characterization of microstructure and mechanical behaviour of heat affected zones in robotic arc welding of AA6061-T6," M.S. thesis, Quebec Univ., Montreal, 2019. [Online]. Available: https://espace.etsmtl.ca/id/eprint/2303/1/ARHUMAH_Zeli.pdf

[47] Y. Lin, S.-C. Luo, J. Huang *et al.*, "Effects of solution treatment on microstructures and micro-hardness of a Sr-modified Al-Si-Mg alloy," *Materials Science and Engineering: A*, vol. 725, pp. 530-540, 2018, doi: https://doi.org/10.1016/j.msea.2018.04.049.

[48] H.-J. Kang, J.-Y. Park, Y.-S. Choi *et al.*, "Influence of the Solution and Artificial Aging Treatments on the Microstructure and Mechanical Properties of Die-Cast Al–Si–Mg Alloys," *Metals*, vol. 12, no. 1, p. 71, 2021, doi: https://doi.org/10.3390/met12010071.

[49] B. M. P. T. Ferreira, "Tratamentos Térmicos de Peças Obtidas por Fundição Injetada," M.S. thesis, Porto Univ., Porto, 2018. [Online]. Available: https://hdl.handle.net/10216/113792

[50] E. Sjölander and S. Seifeddine, "The heat treatment of Al–Si–Cu–Mg casting alloys," *Journal of materials processing technology*, vol. 210, no. 10, pp. 1249-1259, 2010, doi: https://doi.org/10.1016/j.jmatprotec.2010.03.020.

[51] StrikoWestofen. "Westomat: Available options." StrikoWestofen. https://www.strikowestofen.com/en-us/transfer-and-dosing-systems/dosing-furnaces/westomat-classic/westomat-options (accessed 29 April, 2022).

[52] I. Group. "Welcome to the era of the GigaPress." Idra Group. https://www.idragroup.com/en/gigapress (accessed 22 June, 2022).

[53] M. Naor, A. Coman, and A. Wiznizer, "Vertically Integrated Supply Chain of Batteries, Electric Vehicles, and Charging Infrastructure: A Review of Three Milestone Projects from Theory of Constraints Perspective," *Sustainability*, vol. 13, no. 7, p. 3632, 2021, doi: https://doi.org/10.3390/su13073632.

[54] S. International. "Tesla model Y giga-press aluminum casting." sae.org. https://www.sae.org/news/2020/06/tesla-model-y-big-castings (accessed 16 May, 2022).

[55] S. Hanley. "Tesla model Y built in Germany will use large front casting." CleanTechnica. https://cleantechnica.com/2020/09/19/tesla-model-y-germany-large-front-casting/ (accessed 22 June, 2022).

[56] A. Lavrador. "Gigapress, o trunfo da Tesla, não é uma prensa. É uma nova revolução." Observador. https://observador.pt/2021/02/06/gigapress-o-trunfo-da-tesla-nao-e-prensa-e-uma-nova-revolucao/ (accessed 22 June, 2022).

[57] A. Lavrador. "Elon Musk mostra máquina que vai produzir a Cybertruck." Observador. https://observador.pt/2022/06/05/elon-musk-mostra-maquina-que-vai-produzir-a-cybertruck/ (accessed 22 June, 2022).

[58] A. Lavrador. "Tesla Produzirá a plataforma do model 2 numa peça só." Observador. https://observador.pt/2021/10/17/tesla-produzira-a-plataforma-do-model-2-numa-peca-so/ (accessed 22 June, 2022).

[59] *Standard Test Methods for Tension Testing Wrought and Cast Aluminum- and Magnesium-Alloy Products (Metric)*, ASTM B557M-15, 2016.

[60] N. McCormick and J. Lord, "Digital image correlation," *Materials today*, vol. 13, no. 12, pp. 52-54, 2010, doi: https://doi.org/10.1016/S1369-7021(10)70235-2.

[61] A. F. Molland and S. R. Turnock, "Rudder experimental data," in *Marine Rudders, Hydrofoils and Control Surfaces (Second Edition)*: Butterworth-Heinemann, 2022, ch. 6, pp. 105-296.

[62] W. Broughton, "Testing the mechanical, thermal and chemical properties of adhesives for marine environments," in *Adhesives in marine engineering*, J. R. Weitzenböck Ed.: Elsevier, 2012, ch. 6, pp. 99-154.

[63] H.-j. Kang, H.-s. Jang, S.-h. Oh *et al.*, "Effects of solution treatment temperature and time on the porosities and mechanical properties of vacuum die-casted and T6 heat-treated Al–Si–Mg alloy," *Vacuum*, vol. 193, p. 110536, 2021, doi: https://doi.org/10.1016/j.vacuum.2021.110536.

Appendix A: Instrumentation design

Table 32: Identification of variables to be monitored, locations, ranges and critical points - requirements and specifications.

Variables to be monitored	Unit of measurement	Ranges	Location	Critical point
Plunger displacement	mm	0-500	Injection machine	Injection machine - plunger
Plunger speed	m/s	0-5	Injection machine	-
Pressures	bar	0-1000	Hydraulic piston pressure	Injection machine - plunger
	bar	0-1000	Mold cavity	On the mold cavity surface Zone away from the gates
Metal temperature	℃	500-800	Holding furnace	Holding furnace
	℃	500-800	Plunger	Injection machine
	℃	100-800	Mold cavity	2 points on the mold cavity surface
Mold temperature	℃	50-500	Mold	Inside the mold
Vacuum level	mbar	1-1000	Tank	Vacuum machine tank
	mbar	1-1000	Vacuum valve	Connecting the valve to the machine piping
Metal detection	Binary signal	On/Off	Mold cavity	2 points on the mold cavity surface Next to the gates and in a more distant point

Selected sensors:

- Metal front contact sensor;
- Mold cavity pressure measurement;
- Metal front temperature sensor.

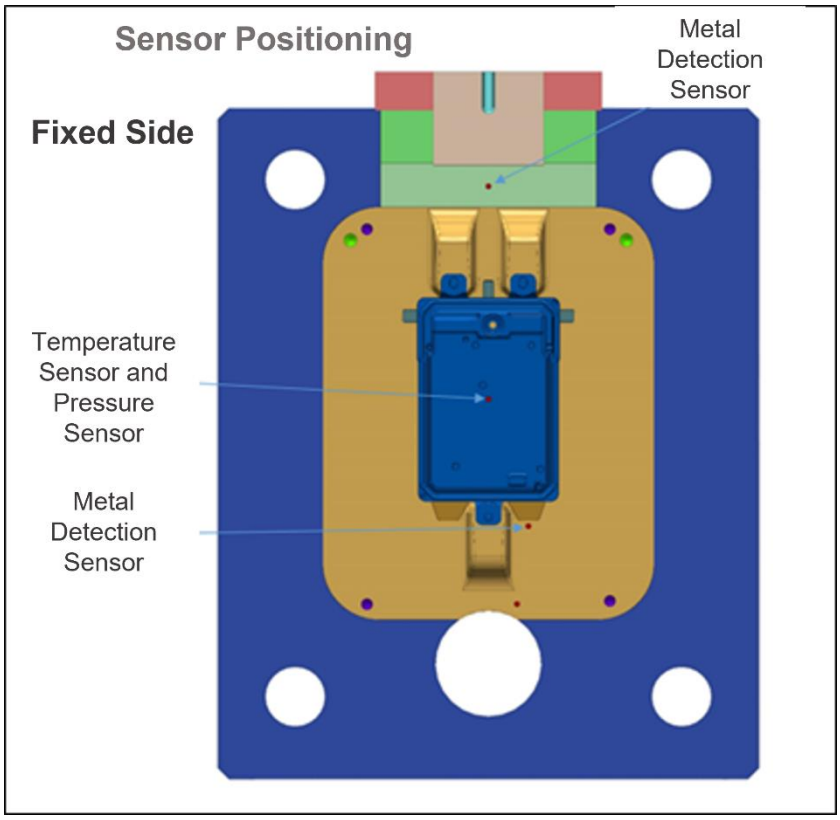

Figure 116: Sensor location schematic.

Vacuum system:

- Vacuum valve – Fondarex Supervac Medio P;
- Vacuum system – Fondarex HIGHVAC PROGRESS 2C 200 ().

Table 33: Specifications of the vacuum system to be implemented.

Tank capacity (l)	200
Tank vacuum capacity (mbar)	1
Clamping force of the injection machine (ton)	<600
BUSCH Vacuum Pump RA Series (m^3/h)	25
Vacuum channels	2
Suction section of the channels (mm^2)	500

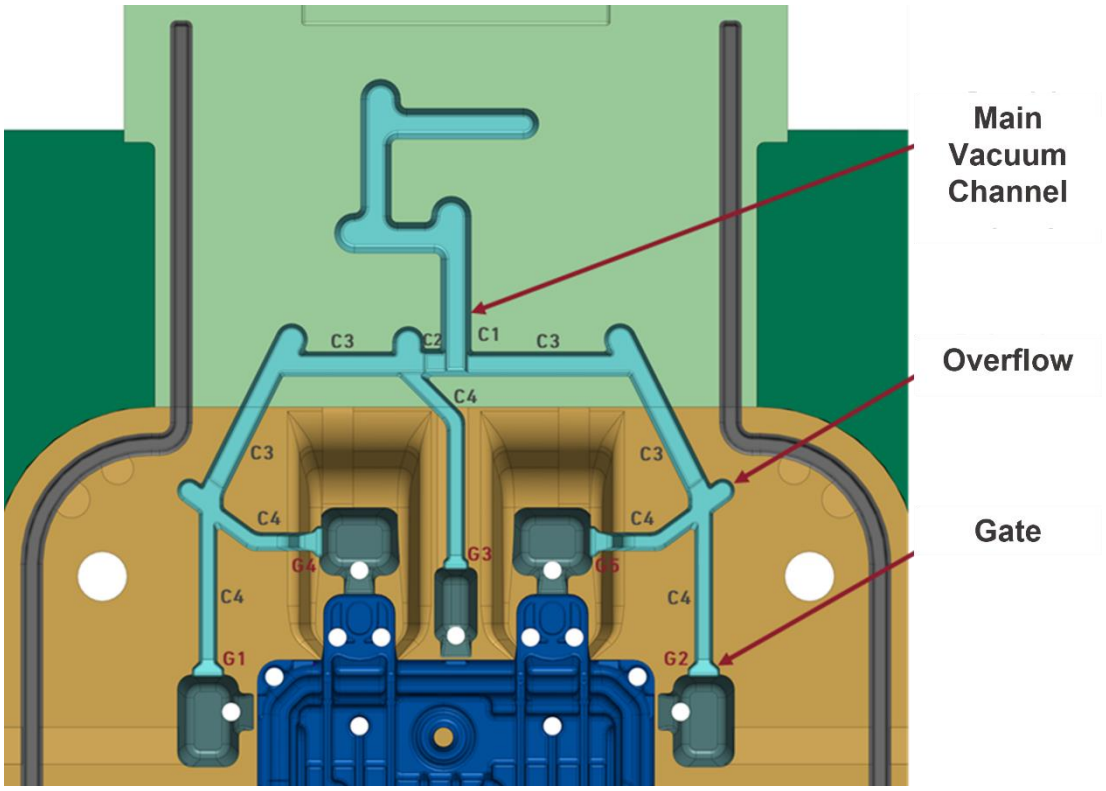

Figure 117: Sizing/Geometry of the vacuum channels of the prototype mold.

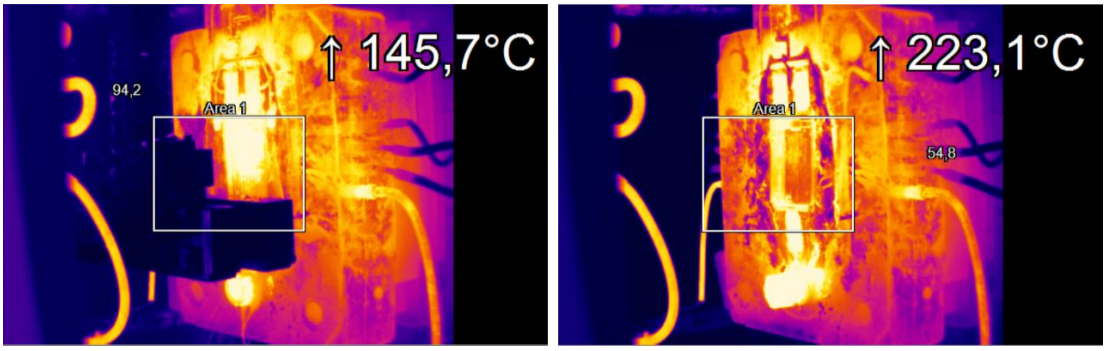

Figure 118: Thermographic images of the mold surface.

Appendix B: Analysis of the chemical composition – AlSi12(Fe)

SPECTRO AMETEK MATERIALS ANALYSIS DIVISION

Sample Result Name	Type	Measure Date Time	Recalculation Date Time	Origin	Method Name	Method Version	Operator Name	Correction Type	Type Corr Sample Name
1_AlSi12(Fe)_alv	Unknown	03-05-2022 15:45:41	03-05-2022 15:49:01	Measured	Al-20-F			None	

Check Type	Check Status	Grade Verification Name	Grade Verification Similarity	Grade Search Name	Grade Search Similarity
None	NotUsed		0 %		0 %

Nome amostra	Referencia	Cliente							
1_AlSi12(Fe)_alv									

Elements **Conc.**

Meas.	Si	Fe	Cu	Mn	Mg	Cr	Ni	Zn	Ti	Be
	%	%	%	%	%	%	%	%	%	%
	Conc.	Conc.	Conc.	Conc.	Conc.	Conc.	Conc.	Conc.	Conc.	Conc.
1	12,67	0,832	0,155	0,427	0,0118	0,0114	0,0080	0,0720	0,0291	0,00086
2	12,75	0,881	0,158	0,458	0,0115	0,0121	0,0085	0,0725	0,0279	0,00090
3	12,41	0,843	0,157	0,442	0,0110	0,0115	0,0081	0,0717	0,0280	0,00088
<x>	*12,61*	*0,852*	*0,157*	*0,443*	*0,0114*	*0,0117*	*0,0082*	*0,0720*	*0,0283*	*0,00088*

Meas.	Bi	Ca	Cd	Co	Ga	Li	Na	P	Pb	Sn
	%	%	%	%	%	%	%	%	%	%
	Conc.	Conc.	Conc.	Conc.	Conc.	Conc.	Conc.	Conc.	Conc.	Conc.
1	0,0022	0,0012	0,00054	<0,00050	0,0100	<0,00010	<0,00010	<0,00100	0,0077	<0,00100
2	0,0023	0,0011	0,00059	<0,00050	0,0102	<0,00010	0,00012	<0,00100	0,0081	<0,00100
3	0,0025	0,00094	0,00051	<0,00050	0,0100	<0,00010	<0,00010	<0,00100	0,0079	<0,00100
<x>	*0,0023*	*0,0011*	*0,00054*	*<0,00050*	*0,0100*	*<0,00010*	*0,00011*	*<0,00100*	*0,0079*	*<0,00100*

Meas.	Sr	V	Zr	Bg	Al					
	%	%	%		%					
	Conc.	Conc.	Conc.		Conc.					
1	<0,00010	0,0051	0,0044		85,8					
2	<0,00010	0,0052	0,0045		85,6					
3	<0,00010	0,0048	0,0042		86,0					
<x>	*<0,00010*	*0,0051*	*0,0044*		*85,8*					

SPECTRO AMETEK MATERIALS ANALYSIS DIVISION

Sample Result Name	Type	Measure Date Time	Recalculation Date Time	Origin	Method Name	Method Version	Operator Name	Correction Type	Type Corr Sample Name
2_AlSi12(fe)_alv	Unknown	03-05-2022 15:59:24	03-05-2022 16:02:07	Measured	Al-20-F			None	

Check Type	Check Status	Grade Verification Name	Grade Verification Similarity	Grade Search Name	Grade Search Similarity
None	NotUsed		0 %		0 %

Nome amostra	Referencia	Cliente							
2_AlSi12(fe)_alv									

Elements **Conc.**

Meas.	Si	Fe	Cu	Mn	Mg	Cr	Ni	Zn	Ti	Be
	%	%	%	%	%	%	%	%	%	%
	Conc.	Conc.	Conc.	Conc.	Conc.	Conc.	Conc.	Conc.	Conc.	Conc.
1	12,22	0,807	0,152	0,432	0,0104	0,0115	0,0081	0,0721	0,0292	0,00087
2	12,41	0,859	0,152	0,437	0,0116	0,0114	0,0081	0,0713	0,0302	0,00084
3	12,03	0,836	0,149	0,444	0,0109	0,0119	0,0076	0,0712	0,0300	0,00086
<x>	*12,22*	*0,834*	*0,151*	*0,438*	*0,0110*	*0,0116*	*0,0079*	*0,0715*	*0,0298*	*0,00086*

Meas.	Bi	Ca	Cd	Co	Ga	Li	Na	P	Pb	Sn
	%	%	%	%	%	%	%	%	%	%
	Conc.	Conc.	Conc.	Conc.	Conc.	Conc.	Conc.	Conc.	Conc.	Conc.
1	0,0024	0,00089	0,00046	<0,00050	0,0098	<0,00010	<0,00010	<0,00100	0,0084	<0,00100
2	0,0020	0,0011	0,00071	<0,00050	0,0100	<0,00010	<0,00010	<0,00100	0,0073	<0,00100
3	0,0022	0,0011	0,00056	<0,00050	0,0097	<0,00010	<0,00010	<0,00100	0,0076	<0,00100
<x>	*0,0022*	*0,0010*	*0,00058*	*<0,00050*	*0,0098*	*<0,00010*	*<0,00010*	*<0,00100*	*0,0078*	*<0,00100*

Meas.	Sr	V	Zr	Bg	Al					
	%	%	%		%					
	Conc.	Conc.	Conc.		Conc.					
1	<0,00010	0,0050	0,0045		86,2					
2	<0,00010	0,0050	0,0043		86,0					
3	<0,00010	0,0052	0,0042		86,4					
<x>	*<0,00010*	*0,0051*	*0,0043*		*86,2*					

SPECTRO

AMETEK
MATERIALS ANALYSIS DIVISION

Sample Result Name	Type	Measure Date Time	Recalculation Date Time	Origin	Method Name	Method Version	Operator Name	Correction Type	Type Corr Sample Name
3_AlSi12(Fe)_a/v	Unknown	03-05-2022 16:05:19	03-05-2022 16:06:36	Measured	Al-20-F			None	

Check Type	Check Status	Grade Verification Name	Grade Verification Similarity	Grade Search Name	Grade Search Similarity
None	NotUsed		0 %		0 %

Nome amostra	Referencia	Cliente
3_AlSi12(Fe)_a/v		

Elements **Conc.**

Meas.	Si	Fe	Cu	Mn	Mg	Cr	Ni	Zn	Ti	Be
	%	%	%	%	%	%	%	%	%	%
	Conc.	Conc.	Conc.	Conc.	Conc.	Conc.	Conc.	Conc.	Conc.	Conc.
1	12,27	0,869	0,153	0,458	0,0116	0,0128	0,0081	0,0728	0,0280	0,00090
2	12,24	0,877	0,151	0,452	0,0118	0,0123	0,0080	0,0722	0,0296	0,00086
3	11,99	0,880	0,149	0,454	0,0114	0,0124	0,0078	0,0713	0,0289	0,00085
<x>	*12,16*	*0,875*	*0,151*	*0,455*	*0,0116*	*0,0125*	*0,0080*	*0,0721*	*0,0288*	*0,00087*

Meas.	Bi	Ca	Cd	Co	Ga	Li	Na	P	Pb	Sn
	%	%	%	%	%	%	%	%	%	%
	Conc.	Conc.	Conc.	Conc.	Conc.	Conc.	Conc.	Conc.	Conc.	Conc.
1	0,0022	0,0011	0,00028	<0,00050	0,0098	<0,00010	<0,00010	<0,00100	0,0079	<0,00100
2	0,0019	0,00099	0,00053	<0,00050	0,0100	<0,00010	<0,00010	<0,00100	0,0073	<0,00100
3	0,0020	0,00099	0,00025	<0,00050	0,0097	<0,00010	<0,00010	<0,00100	0,0075	<0,00100
<x>	*0,0020*	*0,0010*	*0,00035*	*<0,00050*	*0,0098*	*<0,00010*	*<0,00010*	*<0,00100*	*0,0076*	*<0,00100*

Meas.	Sr	V	Zr	Bg	Al					
	%	%	%		%					
	Conc.	Conc.	Conc.		Conc.					
1	<0,00010	0,0058	0,0045		86,1					
2	<0,00010	0,0055	0,0043		86,1					
3	<0,00010	0,0054	0,0043		86,4					
<x>	*<0,00010*	*0,0056*	*0,0044*		*86,2*					

SPECTRO

AMETEK
MATERIALS ANALYSIS DIVISION

Sample Result Name	Type	Measure Date Time	Recalculation Date Time	Origin	Method Name	Method Version	Operator Name	Correction Type	Type Corr Sample Name
4_AlSi12(Fe)_a/v	Unknown	03-05-2022 16:10:23	03-05-2022 16:12:08	Measured	Al-20-F			None	

Check Type	Check Status	Grade Verification Name	Grade Verification Similarity	Grade Search Name	Grade Search Similarity
None	NotUsed		0 %		0 %

Nome amostra	Referencia	Cliente
4_AlSi12(Fe)_a/v		

Elements **Conc.**

Meas.	Si	Fe	Cu	Mn	Mg	Cr	Ni	Zn	Ti	Be
	%	%	%	%	%	%	%	%	%	%
	Conc.	Conc.	Conc.	Conc.	Conc.	Conc.	Conc.	Conc.	Conc.	Conc.
1	12,58	0,743	0,208	0,352	0,0056	0,0089	0,0094	0,0916	0,0335	0,00077
2	12,16	0,741	0,207	0,358	0,0054	0,0091	0,0090	0,0915	0,0313	0,00076
3	11,97	0,725	0,203	0,356	0,0055	0,0092	0,0089	0,0908	0,0319	0,00076
<x>	*12,24*	*0,736*	*0,206*	*0,356*	*0,0055*	*0,0090*	*0,0091*	*0,0913*	*0,0322*	*0,00077*

Meas.	Bi	Ca	Cd	Co	Ga	Li	Na	P	Pb	Sn
	%	%	%	%	%	%	%	%	%	%
	Conc.	Conc.	Conc.	Conc.	Conc.	Conc.	Conc.	Conc.	Conc.	Conc.
1	0,0022	0,00010	0,00069	<0,00050	0,0107	<0,00010	<0,00010	<0,00100	0,0090	<0,00100
2	0,0022	0,00011	0,00053	<0,00050	0,0099	<0,00010	<0,00010	<0,00100	0,0088	<0,00100
3	0,0022	<0,00010	0,00045	<0,00050	0,0099	<0,00010	<0,00010	<0,00100	0,0089	<0,00100
<x>	*0,0022*	*0,00010*	*0,00056*	*<0,00050*	*0,0102*	*<0,00010*	*<0,00010*	*<0,00100*	*0,0089*	*<0,00100*

Meas.	Sr	V	Zr	Bg	Al					
	%	%	%		%					
	Conc.	Conc.	Conc.		Conc.					
1	<0,00010	0,0042	0,0046		85,9					
2	<0,00010	0,0042	0,0044		86,4					
3	<0,00010	0,0044	0,0043		86,6					
<x>	*<0,00010*	*0,0042*	*0,0044*		*86,3*					

SPECTRO

AMETEK MATERIALS ANALYSIS DIVISION

Sample Result Name	Type	Measure Date Time	Recalculation Date Time	Origin	Method Name	Method Version	Operator Name	Correction Type	Type Corr Sample Name
5_AlSi12(Fe)_a/v	Unknown	03-05-2022 16:15:37	03-05-2022 16:17:09	Measured	Al-20-F			None	

Check Type	Check Status	Grade Verification Name	Grade Verification Similarity	Grade Search Name	Grade Search Similarity
None	NotUsed		0 %		0 %

Nome amostra	Referencia	Cliente							
5_AlSi12(Fe)_a/v									

Elements **Conc.**

Meas.	Si	Fe	Cu	Mn	Mg	Cr	Ni	Zn	Ti	Be
	%	%	%	%	%	%	%	%	%	%
	Conc.	Conc.	Conc.	Conc.	Conc.	Conc.	Conc.	Conc.	Conc.	Conc.
1	11,55	0,752	0,407	0,340	0,0073	0,0121	0,0127	0,153	0,0319	0,00081
2	11,55	0,762	0,414	0,343	0,0073	0,0121	0,0127	0,153	0,0305	0,00080
3	11,41	0,772	0,411	0,345	0,0073	0,0119	0,0124	0,152	0,0301	0,00079
<x>	*11,54*	*0,762*	*0,410*	*0,342*	*0,0073*	*0,0120*	*0,0126*	*0,153*	*0,0308*	*0,00080*

Meas.	Bi	Ca	Cd	Co	Ga	Li	Na	P	Pb	Sn
	%	%	%	%	%	%	%	%	%	%
	Conc.	Conc.	Conc.	Conc.	Conc.	Conc.	Conc.	Conc.	Conc.	Conc.
1	0,0026	<0,00010	0,00049	<0,00050	0,0100	<0,00010	<0,00010	<0,00100	0,0127	0,0017
2	0,0025	0,00012	0,00044	<0,00050	0,0099	<0,00010	<0,00010	<0,00100	0,0129	0,0019
3	0,0026	<0,00010	0,00041	<0,00050	0,0098	<0,00010	<0,00010	<0,00100	0,0122	0,0023
<x>	*0,0026*	*0,00011*	*0,00045*	*<0,00050*	*0,0099*	*<0,00010*	*<0,00010*	*<0,00100*	*0,0126*	*0,0020*

Meas.	Sr	V	Zr	Bg	Al					
	%	%	%		%					
	Conc.	Conc.	Conc.		Conc.					
1	<0,00010	0,0043	0,0045		86,5					
2	<0,00010	0,0040	0,0043		86,7					
3	<0,00010	0,0041	0,0042		86,8					
<x>	*<0,00010*	*0,0041*	*0,0043*		*86,7*					

SPECTRO

AMETEK MATERIALS ANALYSIS DIVISION

Sample Result Name	Type	Measure Date Time	Recalculation Date Time	Origin	Method Name	Method Version	Operator Name	Correction Type	Type Corr Sample Name
6_AlSi12(Fe)-a/v	Unknown	03-05-2022 16:29:37	03-05-2022 16:33:32	Measured	Al-20-F			None	

Check Type	Check Status	Grade Verification Name	Grade Verification Similarity	Grade Search Name	Grade Search Similarity
None	NotUsed		0 %		0 %

Nome amostra	Referencia	Cliente							
6_AlSi12(Fe)-a/v									

Elements **Conc.**

Meas.	Si	Fe	Cu	Mn	Mg	Cr	Ni	Zn	Ti	Be
	%	%	%	%	%	%	%	%	%	%
	Conc.	Conc.	Conc.	Conc.	Conc.	Conc.	Conc.	Conc.	Conc.	Conc.
1	12,07	0,813	0,440	0,353	0,0128	0,0136	0,0136	0,167	0,0288	0,00080
2	12,04	0,808	0,439	0,349	0,0125	0,0136	0,0134	0,164	0,0287	0,00081
3	11,88	0,809	0,442	0,351	0,0124	0,0139	0,0133	0,164	0,0289	0,00081
<x>	*12,00*	*0,810*	*0,440*	*0,351*	*0,0126*	*0,0137*	*0,0135*	*0,165*	*0,0288*	*0,00081*

Meas.	Bi	Ca	Cd	Co	Ga	Li	Na	P	Pb	Sn
	%	%	%	%	%	%	%	%	%	%
	Conc.	Conc.	Conc.	Conc.	Conc.	Conc.	Conc.	Conc.	Conc.	Conc.
1	0,0023	0,00031	0,00026	<0,00050	0,0100	<0,00010	<0,00010	<0,00100	0,0132	0,0016
2	0,0023	0,00028	0,00029	<0,00050	0,0098	<0,00010	<0,00010	<0,00100	0,0131	0,0021
3	0,0024	0,00022	0,00048	<0,00050	0,0098	<0,00010	<0,00010	<0,00100	0,0128	0,0021
<x>	*0,0023*	*0,00027*	*0,00034*	*<0,00050*	*0,0098*	*<0,00010*	*<0,00010*	*<0,00100*	*0,0131*	*0,0019*

Meas.	Sr	V	Zr	Bg	Al					
	%	%	%		%					
	Conc.	Conc.	Conc.		Conc.					
1	<0,00010	0,0042	0,0043		86,0					
2	<0,00010	0,0042	0,0043		86,1					
3	<0,00010	0,0042	0,0043		86,2					
<x>	*<0,00010*	*0,0042*	*0,0043*		*86,1*					

Appendix C: Analysis of the chemical composition – AlSi10Mg(Fe)

SPECTRO

AMETEK
MATERIALS ANALYSIS DIVISION

Sample Result Name	Type	Measure Date Time	Recalculation Date Time	Origin	Method Name	Method Version	Operator Name	Correction Type	Type Corr Sample Name
1_wLSi10MG(FE)	Unknown	03-05-2022 17:20:18	03-05-2022 17:23:08	Measured	Al-20-F			None	

Check Type	Check Status	Grade Verification Name	Grade Verification Similarity	Grade Search Name	Grade Search Similarity
None	Not Used		0 %		0 %

Nome amostra	Referencia	Cliente							
1_wLSi10MG(FE)									

Elements **Conc.**

Meas.	Si	Fe	Cu	Mn	Mg	Cr	Ni	Zn	Ti	Be
	%	%	%	%	%	%	%	%	%	%
	Conc.	Conc.	Conc.	Conc.	Conc.	Conc.	Conc.	Conc.	Conc.	Conc.
1	9,82	0,767	0,138	0,0939	0,163	0,0106	0,0058	0,0517	0,0361	0,00094
2	9,70	0,776	0,138	0,0933	0,167	0,0105	0,0053	0,0502	0,0356	0,00091
3	9,60	0,781	0,136	0,0931	0,168	0,0103	0,0054	0,0508	0,0351	0,00090
4	9,59	0,788	0,134	0,0930	0,166	0,0106	0,0055	0,0501	0,0345	0,00092
<x>	*9,68*	*0,778*	*0,137*	*0,0933*	*0,166*	*0,0105*	*0,0056*	*0,0507*	*0,0353*	*0,00092*

Meas.	Bi	Ca	Cd	Co	Ga	Li	Na	P	Pb	Sn
	%	%	%	%	%	%	%	%	%	%
	Conc.	Conc.	Conc.	Conc.	Conc.	Conc.	Conc.	Conc.	Conc.	Conc.
1	0,0042	0,00074	<0,00010	<0,00050	0,0090	<0,00010	0,00010	<0,00100	0,0107	0,0012
2	0,0041	0,00076	<0,00010	<0,00050	0,0089	<0,00010	<0,00010	<0,00100	0,0096	<0,00100
3	0,0039	0,00077	A 0,00028	<0,00050	0,0088	<0,00010	<0,00010	<0,00100	0,0098	<0,00100
4	0,0040	0,00074	A <0,00010	<0,00050	0,0086	<0,00010	<0,00010	A 0,0040	0,0099	<0,00100
<x>	*0,0040*	*0,00075*	*A 0,00014*	*<0,00050*	*0,0088*	*<0,00010*	*0,00010*	*A 0,0018*	*0,0100*	*0,0010*

Meas.	Sr	V	Zr	Bg	Al					
	%	%	%		%					
	Conc.	Conc.	Conc.		Conc.					
1	<0,00010	0,0062	0,0019		88,9					
2	<0,00010	0,0061	0,0018		89,0					
3	<0,00010	0,0061	0,0018		89,1					

SPECTRO

AMETEK
MATERIALS ANALYSIS DIVISION

Sample Result Name	Type	Measure Date Time	Recalculation Date Time	Origin	Method Name	Method Version	Operator Name	Correction Type	Type Corr Sample Name
2_Alsi10mg(FE)_SiV	Unknown	03-05-2022 17:29:52	03-05-2022 17:31:29	Measured	Al-20-F			None	

Check Type	Check Status	Grade Verification Name	Grade Verification Similarity	Grade Search Name	Grade Search Similarity
None	Not Used		0 %		0 %

Nome amostra	Referencia	Cliente							
2_Alsi10mg(FE)_SiV									

Elements **Conc.**

Meas.	Si	Fe	Cu	Mn	Mg	Cr	Ni	Zn	Ti	Be
	%	%	%	%	%	%	%	%	%	%
	Conc.	Conc.	Conc.	Conc.	Conc.	Conc.	Conc.	Conc.	Conc.	Conc.
1	10,85	0,870	0,137	0,0940	0,243	0,0101	0,0063	0,0520	0,0417	0,00086
2	11,09	0,910	0,144	0,0969	0,253	0,0104	0,0065	0,0523	0,0401	0,00088
3	11,07	0,899	0,141	0,0949	0,248	0,0101	0,0061	0,0517	0,0392	0,00087
<x>	*11,00*	*0,893*	*0,141*	*0,0953*	*0,248*	*0,0102*	*0,0063*	*0,0520*	*0,0403*	*0,00087*

Meas.	Bi	Ca	Cd	Co	Ga	Li	Na	P	Pb	Sn
	%	%	%	%	%	%	%	%	%	%
	Conc.	Conc.	Conc.	Conc.	Conc.	Conc.	Conc.	Conc.	Conc.	Conc.
1	0,0023	0,0014	0,00057	<0,00050	0,0103	<0,00010	<0,00010	<0,00100	0,0079	<0,00100
2	0,0023	0,0013	0,00062	<0,00050	0,0104	<0,00010	<0,00010	<0,00100	0,0084	<0,00100
3	0,0023	0,0016	0,00049	<0,00050	0,0100	<0,00010	<0,00010	<0,00100	0,0076	<0,00100
<x>	*0,0023*	*0,0014*	*0,00056*	*<0,00050*	*0,0102*	*<0,00010*	*<0,00010*	*<0,00100*	*0,0080*	*<0,00100*

Meas.	Sr	V	Zr	Bg	Al					
	%	%	%		%					
	Conc.	Conc.	Conc.		Conc.					
1	<0,00010	0,0063	0,0019		87,7					
2	<0,00010	0,0062	0,0017		87,4					
3	<0,00010	0,0065	0,0017		87,4					
<x>	*<0,00010*	*0,0063*	*0,0017*		*87,5*					

SPECTRO

AMETEK
MATERIALS ANALYSIS DIVISION

Sample Result Name	Type	Measure Date Time	Recalculation Date Time	Origin	Method Name	Method Version	Operator Name	Correction Type	Type Corr Sample Name
3_al_SI10MG(fE)_SIV	Unknown	03-05-2022 17:34:36	03-05-2022 17:36:47	Measured	Al-20-P			None	

Check Type	Check Status	Grade Verification Name	Grade Verification Similarity	Grade Search Name	Grade Search Similarity
None	NotUsed		0 %		0 %

Nome amostra	Referencia	Cliente							
3_al_SI10MG(fE)_SIV									

Elements **Conc.**

Meas.	Si	Fe	Cu	Mn	Mg	Cr	Ni	Zn	Ti	Be
	%	%	%	%	%	%	%	%	%	%
	Conc.	Conc.	Conc.	Conc.	Conc.	Conc.	Conc.	Conc.	Conc.	Conc.
1	11,55	0,963	0,147	0,0981	0,274	0,0106	0,0065	0,0528	0,0373	0,00089
2	11,11	0,915	0,145	0,0968	0,242	0,0105	0,0062	0,0518	0,0373	0,00090
3	10,83	0,893	0,143	0,0959	0,235	0,0103	0,0059	0,0509	0,0372	0,00088
4	10,64	0,891	0,142	0,0946	0,232	0,0102	0,0058	0,0508	0,0367	0,00086
<x>	***11,03***	***0,916***	***0,144***	***0,0964***	***0,246***	***0,0104***	***0,0061***	***0,0516***	***0,0371***	***0,00088***

Meas.	Bi	Ca	Cd	Co	Ga	Li	Na	P	Pb	Sn
	%	%	%	%	%	%	%	%	%	%
	Conc.	Conc.	Conc.	Conc.	Conc.	Conc.	Conc.	Conc.	Conc.	Conc.
1	0,0020	0,0016	0,00036	<0,00050	0,0105	<0,00010	<0,00010	<0,00100	0,0078	<0,00100
2	0,0025	0,0016	0,00050	<0,00050	0,0102	<0,00010	<0,00010	<0,00100	0,0084	<0,00100
3	0,0024	0,0014	0,00045	<0,00050	0,0100	<0,00010	<0,00010	<0,00100	0,0081	<0,00100
4	0,0025	0,0013	0,00025	<0,00050	0,0098	<0,00010	<0,00010	<0,00100	0,0079	<0,00100
<x>	***0,0023***	***0,0015***	***0,00039***	***<0,00050***	***0,0102***	***<0,00010***	***<0,00010***	***<0,00100***	***0,0080***	***<0,00100***

Meas.	Sr	V	Zr	Bg	Al					
	%	%	%		%					
	Conc.	Conc.	Conc.		Conc.					
1	<0,00010	0,0061	0,0018		86,8					
2	<0,00010	0,0061	0,0018		87,3					
3	<0,00010	0,0061	0,0018		87,7					

SPECTRO

AMETEK
MATERIALS ANALYSIS DIVISION

Sample Result Name	Type	Measure Date Time	Recalculation Date Time	Origin	Method Name	Method Version	Operator Name	Correction Type	Type Corr Sample Name
4_al_si10mg(fe) oiv	Unknown	05-05-2022 10:40:37	05-05-2022 10:45:14	Measured	Al-20-P			None	

Check Type	Check Status	Grade Verification Name	Grade Verification Similarity	Grade Search Name	Grade Search Similarity
None	NotUsed		0 %		0 %

Nome amostra	Referencia	Cliente							
4_al_si10mg(fe) oiv									

Elements **Conc.**

Meas.	Si	Fe	Cu	Mn	Mg	Cr	Ni	Zn	Ti	Be
	%	%	%	%	%	%	%	%	%	%
	Conc.	Conc.	Conc.	Conc.	Conc.	Conc.	Conc.	Conc.	Conc.	Conc.
1	11,00	0,937	0,141	0,0896	0,215	0,0101	0,0065	0,0501	0,0352	0,00082
2	11,18	0,964	0,146	0,0923	0,217	0,0105	0,0068	0,0506	0,0335	0,00085
3	10,83	0,940	0,141	0,0911	0,205	0,0104	0,0064	0,0497	0,0331	0,00084
<x>	***11,00***	***0,947***	***0,143***	***0,0910***	***0,212***	***0,0104***	***0,0066***	***0,0501***	***0,0339***	***0,00084***

Meas.	Bi	Ca	Cd	Co	Ga	Li	Na	P	Pb	Sn
	%	%	%	%	%	%	%	%	%	%
	Conc.	Conc.	Conc.	Conc.	Conc.	Conc.	Conc.	Conc.	Conc.	Conc.
1	0,0020	0,0011	0,00052	<0,00050	0,0107	<0,00010	<0,00010	<0,00100	0,0112	<0,00100
2	0,0021	0,0011	0,00047	<0,00050	0,0109	<0,00010	<0,00010	<0,00100	0,0120	<0,00100
3	0,0022	0,0011	0,00033	<0,00050	0,0104	<0,00010	<0,00010	<0,00100	0,0115	<0,00100
<x>	***0,0021***	***0,0011***	***0,00044***	***<0,00050***	***0,0107***	***<0,00010***	***<0,00010***	***<0,00100***	***0,0116***	***<0,00100***

Meas.	Sr	V	Zr	Bg	Al					
	%	%	%		%					
	Conc.	Conc.	Conc.		Conc.					
1	<0,00010	0,0063	0,0016		87,5					
2	<0,00010	0,0063	0,0017		87,3					
3	<0,00010	0,0064	0,0018		87,7					
<x>	***<0,00010***	***0,0063***	***0,0017***		***87,5***					

SPECTRO

AMETEK
MATERIALS ANALYSIS DIVISION

Sample Result Name	Type	Measure Date Time	Recalculation Date Time	Origin	Method Name	Method Version	Operator Name	Correction Type	Type Corr Sample Name
5_ALSI10MG(FE)_C/V	Unknown	05-05-2022 10:51:49	05-05-2022 10:53:10	Measured	Al-20-F			None	

Check Type	Check Status	Grade Verification Name	Grade Verification Similarity	Grade Search Name	Grade Search Similarity
None	NotUsed		0 %		0 %

Nome amostra	Referencia	Cliente							
5_ALSI10MG(FE)_C/V									

Elements **Conc.**

Meas.	Si	Fe	Cu	Mn	Mg	Cr	Ni	Zn	Ti	Be
	%	%	%	%	%	%	%	%	%	%
	Conc.	Conc.	Conc.	Conc.	Conc.	Conc.	Conc.	Conc.	Conc.	Conc.
1	10,30	0,854	0,141	0,0877	0,171	0,0101	0,0059	0,0468	0,0328	0,00083
2	10,66	0,904	0,147	0,0914	0,176	0,0105	0,0061	0,0478	0,0309	0,00089
3	10,18	0,872	0,143	0,0889	0,171	0,0101	0,0060	0,0479	0,0315	0,00084
<x>	*10,38*	*0,877*	*0,144*	*0,0893*	*0,173*	*0,0102*	*0,0060*	*0,0475*	*0,0318*	*0,00085*

Meas.	Bi	Ca	Cd	Co	Ga	Li	Na	P	Pb	Sn
	%	%	%	%	%	%	%	%	%	%
	Conc.	Conc.	Conc.	Conc.	Conc.	Conc.	Conc.	Conc.	Conc.	Conc.
1	0,0024	0,0011	0,00031	<0,00050	0,0094	<0,00010	0,00043	<0,00100	0,0110	<0,00100
2	0,0028	0,00099	<0,00010	<0,00050	0,0100	<0,00010	0,00058	<0,00100	0,0116	<0,00100
3	0,0027	0,00090	0,00018	<0,00050	0,0098	<0,00010	0,00020	<0,00100	0,0115	<0,00100
<x>	*0,0026*	*0,00098*	*0,00020*	*<0,00050*	*0,0097*	*<0,00010*	*0,00040*	*<0,00100*	*0,0113*	*<0,00100*

Meas.	Sr	V	Zr	Bg	Al					
	%	%	%		%					
	Conc.	Conc.	Conc.		Conc.					
1	<0,00010	0,0063	0,0016		88,3					
2	<0,00010	0,0062	0,0017		87,9					
3	<0,00010	0,0062	0,0015		88,4					
<x>	*<0,00010*	*0,0062*	*0,0016*		*88,2*					

SPECTRO

AMETEK
MATERIALS ANALYSIS DIVISION

Sample Result Name	Type	Measure Date Time	Recalculation Date Time	Origin	Method Name	Method Version	Operator Name	Correction Type	Type Corr Sample Name
6_AlSi10Mg(Fe) o/v	Unknown	05-05-2022 11:01:54	05-05-2022 11:03:29	Measured	Al-20-F			None	

Check Type	Check Status	Grade Verification Name	Grade Verification Similarity	Grade Search Name	Grade Search Similarity
None	NotUsed		0 %		0 %

Nome amostra	Referencia	Cliente							
6_AlSi10Mg(Fe) o/v									

Elements **Conc.**

Meas.	Si	Fe	Cu	Mn	Mg	Cr	Ni	Zn	Ti	Be
	%	%	%	%	%	%	%	%	%	%
	Conc.	Conc.	Conc.	Conc.	Conc.	Conc.	Conc.	Conc.	Conc.	Conc.
1	10,52	0,899	0,139	0,0877	0,203	0,0097	0,0062	0,0479	0,0359	0,00080
2	10,28	0,890	0,135	0,0870	0,199	0,0100	0,0061	0,0477	0,0348	0,00080
3	10,23	0,899	0,138	0,0873	0,195	0,0099	0,0061	0,0484	0,0335	0,00080
<x>	*10,34*	*0,896*	*0,137*	*0,0873*	*0,199*	*0,0099*	*0,0061*	*0,0480*	*0,0347*	*0,00080*

Meas.	Bi	Ca	Cd	Co	Ga	Li	Na	P	Pb	Sn
	%	%	%	%	%	%	%	%	%	%
	Conc.	Conc.	Conc.	Conc.	Conc.	Conc.	Conc.	Conc.	Conc.	Conc.
1	0,0022	0,0012	0,00041	<0,00050	0,0104	<0,00010	0,00013	<0,00100	0,0104	<0,00100
2	0,0022	0,0012	0,00033	<0,00050	0,0100	<0,00010	<0,00010	<0,00100	0,0105	<0,00100
3	0,0020	0,00099	<0,00010	<0,00050	0,0098	<0,00010	<0,00010	<0,00100	0,0104	<0,00100
<x>	*0,0022*	*0,0011*	*0,00028*	*<0,00050*	*0,0101*	*<0,00010*	*0,00011*	*<0,00100*	*0,0104*	*<0,00100*

Meas.	Sr	V	Zr	Bg	Al					
	%	%	%		%					
	Conc.	Conc.	Conc.		Conc.					
1	<0,00010	0,0063	0,0016		88,0					
2	<0,00010	0,0063	0,0016		88,3					
3	<0,00010	0,0063	0,0016		88,3					
<x>	*<0,00010*	*0,0063*	*0,0016*		*88,2*					

Appendix D: Analysis of the chemical composition – AlSi10MnMg

SPECTRO AMETEK MATERIALS ANALYSIS DIVISION

Sample Result Name	Type	Measure Date Time	Recalculation Date Time	Origin	Method Name	Method Version	Operator Name	Correction Type	Type Corr Sample Name
1_allaflont_36_a/v	Unknown	03-05-2022 15:03:41	03-05-2022 15:05:01	Measured	Al-20-P			None	

Check Type	Check Status	Grade Verification Name	Grade Verification Similarity	Grade Search Name	Grade Search Similarity
None	NotUsed		0 %		0 %

Nome amostra	Referencia	Cliente
1_allaflont_36_a/v		

Elements Conc.

Meas.	Si	Fe	Cu	Mn	Mg	Cr	Ni	Zn	Ti	Be
	%	%	%	%	%	%	%	%	%	%
	Conc.	Conc.	Conc.	Conc.	Conc.	Conc.	Conc.	Conc.	Conc.	Conc.
1	11,15	0,127	0,0013	0,596	0,258	0,00095	0,0034	<0,00100	0,0493	0,00015
2	11,00	0,124	0,00091	0,584	0,249	0,00085	0,0032	<0,00100	0,0481	0,00015
3	10,94	0,122	0,00080	0,594	0,244	0,00082	0,0033	<0,00100	0,0469	0,00015
<x>	*11,03*	*0,124*	*0,00099*	*0,591*	*0,250*	*0,00087*	*0,0033*	*<0,00100*	*0,0481*	*0,00015*

Meas.	Bi	Ca	Cd	Co	Ga	Li	Na	P	Pb	Sn
	%	%	%	%	%	%	%	%	%	%
	Conc.	Conc.	Conc.	Conc.	Conc.	Conc.	Conc.	Conc.	Conc.	Conc.
1	0,0012	0,00046	0,00053	<0,00050	0,0090	<0,00010	<0,00010	<0,00100	0,0039	<0,00100
2	0,0013	0,00039	0,00034	<0,00050	0,0086	<0,00010	<0,00010	<0,00100	0,0037	<0,00100
3	0,0016	0,00037	0,00051	<0,00050	0,0088	<0,00010	<0,00010	<0,00100	0,0040	<0,00100
<x>	*0,0014*	*0,00040*	*0,00046*	*<0,00050*	*0,0088*	*<0,00010*	*<0,00010*	*<0,00100*	*0,0039*	*<0,00100*

Meas.	Sr	V	Zr	Bg	Al					
	%	%	%		%					
	Conc.	Conc.	Conc.		Conc.					
1	0,0093	0,0046	0,0028		87,8					
2	0,0087	0,0043	0,0027		88,0					
3	0,0092	0,0045	0,0028		88,0					
<x>	*0,0091*	*0,0045*	*0,0028*		*87,9*					

SPECTRO AMETEK MATERIALS ANALYSIS DIVISION

Sample Result Name	Type	Measure Date Time	Recalculation Date Time	Origin	Method Name	Method Version	Operator Name	Correction Type	Type Corr Sample Name
2_allaflont_36_a/v	Unknown	03-05-2022 15:07:56	03-05-2022 15:12:41	Measured	Al-20-P			None	

Check Type	Check Status	Grade Verification Name	Grade Verification Similarity	Grade Search Name	Grade Search Similarity
None	NotUsed		0 %		0 %

Nome amostra	Referencia	Cliente
2_allaflont_36_a/v		

Elements Conc.

Meas.	Si	Fe	Cu	Mn	Mg	Cr	Ni	Zn	Ti	Be
	%	%	%	%	%	%	%	%	%	%
	Conc.	Conc.	Conc.	Conc.	Conc.	Conc.	Conc.	Conc.	Conc.	Conc.
1	10,98	0,124	0,00079	0,613	0,221	0,0013	0,0033	<0,00100	0,0430	0,00017
2	11,71	0,135	0,00093	0,638	0,267	0,00084	0,0034	<0,00100	0,0450	0,00016
3	11,40	0,130	0,00095	0,624	0,252	0,0012	0,0035	0,0010	0,0413	0,00016
<x>	*11,36*	*0,129*	*0,00089*	*0,625*	*0,247*	*0,0011*	*0,0034*	*0,0010*	*0,0431*	*0,00016*

Meas.	Bi	Ca	Cd	Co	Ga	Li	Na	P	Pb	Sn
	%	%	%	%	%	%	%	%	%	%
	Conc.	Conc.	Conc.	Conc.	Conc.	Conc.	Conc.	Conc.	Conc.	Conc.
1	0,0019	0,00024	0,00031	<0,00050	0,0084	<0,00010	<0,00010	<0,00100	0,0048	<0,00100
2	0,0013	0,00032	0,00031	<0,00050	0,0091	<0,00010	<0,00010	<0,00100	0,0038	<0,00100
3	0,0017	0,00030	0,00036	<0,00050	0,0086	<0,00010	<0,00010	<0,00100	0,0044	<0,00100
<x>	*0,0016*	*0,00029*	*0,00033*	*<0,00050*	*0,0087*	*<0,00010*	*<0,00010*	*<0,00100*	*0,0043*	*<0,00100*

Meas.	Sr	V	Zr	Bg	Al					
	%	%	%		%					
	Conc.	Conc.	Conc.		Conc.					
1	0,0087	0,0045	0,0028		88,0					
2	0,0090	0,0046	0,0028		87,2					
3	0,0088	0,0045	0,0028		87,5					
<x>	*0,0088*	*0,0045*	*0,0028*		*87,6*					

SPECTRO

AMETEK
MATERIALS ANALYSIS DIVISION

Sample Result Name	Type	Measure Date Time	Recalculation Date Time	Origin	Method Name	Method Version	Operator Name	Correction Type	Type Corr Sample Name
3_silafont_36_s/v	Unknown	05-05-2022 12:28:37	05-05-2022 12:30:04	Measured	Al-01-F			None	

Check Type	Check Status	Grade Verification Name	Grade Verification Similarity	Grade Search Name	Grade Search Similarity
None	Not Used		0 %		0 %

Nome amostra	Referencia	Cliente							
3_silafont_36_s/v									

Elements **Conc.**

Meas.	Si	Fe	Cu	Mn	Mg	Cr	Ni	Zn	Ti	Ag
	%	%	%	%	%	%	%	%	%	%
	Conc.	Conc.	Conc.	Conc.	Conc.	Conc.	Conc.	Conc.	Conc.	Conc.
1	10,92	0,125	0,00081	0,604	0,254	<0,00030	0,0030	0,0014	0,0383	<0,00010
2	10,92	0,125	0,00085	0,608	0,245	<0,00030	0,0032	0,0012	0,0379	<0,00010
3	10,54	0,123	0,00080	0,603	0,233	<0,00030	0,0029	<0,00100	0,0378	<0,00010
<x>	**10,79**	**0,124**	**0,00082**	**0,605**	**0,244**	**<0,00030**	**0,0030**	**0,0012**	**0,0380**	**<0,00010**

Meas.	B	Ba	Be	Bi	Ca	Cd	Ce	Co	Ga	Hg
	%	%	%	%	%	%	%	%	%	%
	Conc.	Conc.	Conc.	Conc.	Conc.	Conc.	Conc.	Conc.	Conc.	Conc.
1	0,0014	<0,00010	0,00014	0,0011	0,00034	<0,00010	<0,0015	<0,00050	0,0084	0,0012
2	0,0015	<0,00010	0,00015	0,0013	0,00034	<0,00010	<0,0015	<0,00050	0,0084	0,0014
3	0,0015	<0,00010	0,00014	0,0015	0,00027	<0,00010	<0,0015	<0,00050	0,0083	0,0012
<x>	**0,0015**	**<0,00010**	**0,00015**	**0,0013**	**0,00032**	**<0,00010**	**<0,0015**	**<0,00050**	**0,0084**	**0,0013**

Meas.	In	La	Li	Na	P	Pb	Sn	Sr	V	Zr
	%	%	%	%	%	%	%	%	%	%
	Conc.	Conc.	Conc.	Conc.	Conc.	Conc.	Conc.	Conc.	Conc.	Conc.
1	<0,00030	<0,00030	<0,00010	<0,00010	<0,00100	0,0036	<0,00100	0,0124	0,0056	0,0024
2	<0,00030	<0,00030	<0,00010	<0,00010	<0,00100	0,0040	<0,00100	0,0133	0,0055	0,0024
3	<0,00030	<0,00030	<0,00010	<0,00010	<0,00100	0,0039	<0,00100	0,0129	0,0054	0,0022
<x>	**<0,00030**	**<0,00030**	**<0,00010**	**<0,00010**	**<0,00100**	**0,0038**	**<0,00100**	**0,0129**	**0,0055**	**0,0023**

SPECTRO

AMETEK
MATERIALS ANALYSIS DIVISION

Sample Result Name	Type	Measure Date Time	Recalculation Date Time	Origin	Method Name	Method Version	Operator Name	Correction Type	Type Corr Sample Name
4_Silafont_36_c/v	Unknown	03-05-2022 15:19:23	03-05-2022 15:20:59	Measured	Al-20-F			None	

Check Type	Check Status	Grade Verification Name	Grade Verification Similarity	Grade Search Name	Grade Search Similarity
None	Not Used		0 %		0 %

Nome amostra	Referencia	Cliente							
4_Silafont_36_c/v									

Elements **Conc.**

Meas.	Si	Fe	Cu	Mn	Mg	Cr	Ni	Zn	Ti	Be
	%	%	%	%	%	%	%	%	%	%
	Conc.	Conc.	Conc.	Conc.	Conc.	Conc.	Conc.	Conc.	Conc.	Conc.
1	10,93	0,127	0,00082	0,603	0,254	0,00089	0,0033	<0,00100	0,0471	0,00015
2	11,46	0,132	0,0012	0,624	0,253	0,0011	0,0034	<0,00100	0,0426	0,00017
3	11,41	0,132	0,00100	0,603	0,271	0,00066	0,0033	<0,00100	0,0477	0,00015
<x>	**11,27**	**0,130**	**0,00099**	**0,610**	**0,259**	**0,00088**	**0,0033**	**<0,00100**	**0,0458**	**0,00016**

Meas.	Bi	Ca	Cd	Co	Ga	Li	Na	P	Pb	Sn
	%	%	%	%	%	%	%	%	%	%
	Conc.	Conc.	Conc.	Conc.	Conc.	Conc.	Conc.	Conc.	Conc.	Conc.
1	0,0014	0,00024	0,00064	<0,00050	0,0087	<0,00010	<0,00010	<0,00100	0,0045	<0,00100
2	0,0016	0,00045	0,00016	<0,00050	0,0087	<0,00010	<0,00010	<0,00100	0,0042	<0,00100
3	0,0012	0,00050	0,00038	<0,00050	0,0089	<0,00010	<0,00010	<0,00100	0,0031	<0,00100
<x>	**0,0014**	**0,00040**	**0,00039**	**<0,00050**	**0,0087**	**<0,00010**	**<0,00010**	**<0,00100**	**0,0040**	**<0,00100**

Meas.	Sr	V	Zr	Bg	Al					
	%	%	%		%					
	Conc.	Conc.	Conc.		Conc.					
1	0,0092	0,0048	0,0028		88,0					
2	0,0099	0,0044	0,0027		87,4					
3	0,0093	0,0047	0,0027		87,5					
<x>	**0,0095**	**0,0046**	**0,0027**		**87,6**					

SPECTRO

AMETEK
MATERIALS ANALYSIS DIVISION

Sample Result Name	Type	Measure Date Time	Recalculation Date Time	Origin	Method Name	Method Version	Operator Name	Correction Type	Type Corr Sample Name
5_Stilafont_36_o/v	Unknown	03-05-2022 15:29:59	03-05-2022 15:26:05	Measured	Al-20-F			None	

Check Type	Check Status	Grade Verification Name	Grade Verification Similarity	Grade Search Name	Grade Search Similarity
None	NotUsed		0 %		0 %

Nome amostra	Referencia	Cliente							
5_Stilafont_36_o/v									

Elements **Conc.**

Meas.	Si	Fe	Cu	Mn	Mg	Cr	Ni	Zn	Ti	Be
	%	%	%	%	%	%	%	%	%	%
	Conc.	Conc.	Conc.	Conc.	Conc.	Conc.	Conc.	Conc.	Conc.	Conc.
1	11,28	0,130	0,0012	0,589	0,263	0,00075	0,0035	<0,00100	0,0479	0,00015
2	11,04	0,126	0,0011	0,607	0,254	0,00090	0,0034	<0,00100	0,0477	0,00015
3	11,33	0,133	0,0013	0,620	0,257	0,00096	0,0034	<0,00100	0,0438	0,00016
<x>	*11,22*	*0,130*	*0,0012*	*0,606*	*0,258*	*0,00087*	*0,0034*	*<0,00100*	*0,0464*	*0,00015*

Meas.	Bi	Ca	Cd	Co	Ga	Li	Na	P	Pb	Sn
	%	%	%	%	%	%	%	%	%	%
	Conc.	Conc.	Conc.	Conc.	Conc.	Conc.	Conc.	Conc.	Conc.	Conc.
1	0,0012	0,00047	0,00034	<0,00050	0,0088	<0,00010	<0,00010	<0,00100	0,0035	<0,00100
2	0,0013	0,00028	0,00053	<0,00050	0,0087	<0,00010	<0,00010	<0,00100	0,0038	<0,00100
3	0,0016	0,00029	0,00029	<0,00050	0,0087	<0,00010	<0,00010	<0,00100	0,0040	<0,00100
<x>	*0,0014*	*0,00035*	*0,00039*	*<0,00050*	*0,0087*	*<0,00010*	*<0,00010*	*<0,00100*	*0,0038*	*<0,00100*

Meas.	Sr	V	Zr	Bg	Al					
	%	%	%		%					
	Conc.	Conc.	Conc.		Conc.					
1	0,0094	0,0045	0,0028		87,7					
2	0,0095	0,0047	0,0027		87,9					
3	0,0085	0,0045	0,0027		87,6					
<x>	*0,0091*	*0,0046*	*0,0027*		*87,7*					

SPECTRO

AMETEK
MATERIALS ANALYSIS DIVISION

Sample Result Name	Type	Measure Date Time	Recalculation Date Time	Origin	Method Name	Method Version	Operator Name	Correction Type	Type Corr Sample Name
6_Stilafont_36_o/v	Unknown	03-05-2022 15:30:53	03-05-2022 15:33:09	Measured	Al-20-F			None	

Check Type	Check Status	Grade Verification Name	Grade Verification Similarity	Grade Search Name	Grade Search Similarity
None	NotUsed		0 %		0 %

Nome amostra	Referencia	Cliente							
6_Stilafont_36_o/v									

Elements **Conc.**

Meas.	Si	Fe	Cu	Mn	Mg	Cr	Ni	Zn	Ti	Be
	%	%	%	%	%	%	%	%	%	%
	Conc.	Conc.	Conc.	Conc.	Conc.	Conc.	Conc.	Conc.	Conc.	Conc.
1	11,22	0,130	0,0010	0,618	0,259	0,00081	0,0034	<0,00100	0,0444	0,00015
2	10,89	0,129	0,00088	0,613	0,253	0,00096	0,0032	<0,00100	0,0438	0,00015
3	10,82	0,121	0,00081	0,606	0,218	0,0011	0,0033	<0,00100	0,0417	0,00017
<x>	*10,98*	*0,127*	*0,00091*	*0,612*	*0,243*	*0,00097*	*0,0033*	*<0,00100*	*0,0433*	*0,00016*

Meas.	Bi	Ca	Cd	Co	Ga	Li	Na	P	Pb	Sn
	%	%	%	%	%	%	%	%	%	%
	Conc.	Conc.	Conc.	Conc.	Conc.	Conc.	Conc.	Conc.	Conc.	Conc.
1	0,0014	0,00034	0,00038	<0,00050	0,0090	<0,00010	<0,00010	<0,00100	0,0036	<0,00100
2	0,0014	0,00025	0,00027	<0,00050	0,0087	<0,00010	<0,00010	<0,00100	0,0039	<0,00100
3	0,0019	0,00015	<0,00010	<0,00050	0,0083	<0,00010	<0,00010	<0,00100	0,0050	<0,00100
<x>	*0,0016*	*0,00025*	*0,00025*	*<0,00050*	*0,0087*	*<0,00010*	*<0,00010*	*<0,00100*	*0,0042*	*<0,00100*

Meas.	Sr	V	Zr	Bg	Al					
	%	%	%		%					
	Conc.	Conc.	Conc.		Conc.					
1	0,0089	0,0044	0,0027		87,7					
2	0,0086	0,0045	0,0027		88,0					
3	0,0077	0,0045	0,0028		88,2					
<x>	*0,0084*	*0,0045*	*0,0027*		*88,0*					

Appendix E: Analysis of the chemical composition – AlMg4Fe2

SPECTRO

AMETEK
MATERIALS ANALYSIS DIVISION

Sample Result Name	Type	Measure Date Time	Recalculation Date Time	Origin	Method Name	Method Version	Operator Name	Correction Type	Type Corr Sample Name
1_Castaduct_42_avacuo	Unknown	03-05-2022 11:24:58	03-05-2022 11:26:33	Measured	Al-01-F			None	

Check Type	Check Status	Grade Verification Name	Grade Verification Similarity	Grade Search Name	Grade Search Similarity
None	Not Used		0 %		0 %

Nome amostra	Referencia	Cliente							
1_Castaduct_42_avacuo									

Elements **Conc.**

Meas.	Si	Fe	Cu	Mn	Mg	Cr	Ni	Zn	Ti	Ag
	%	%	%	%	%	%	%	%	%	%
	Conc.	Conc.	Conc.	Conc.	Conc.	Conc.	Conc.	Conc.	Conc.	Conc.
1	0,0886	1,59	0,0076	0,0115	5,23	0,0030	0,0039	0,0078	0,0103	<0,00010
2	0,0809	1,61	0,0077	0,0111	5,11	0,0024	0,0035	0,0063	0,0101	<0,00010
3	0,0831	1,46	0,0066	0,0110	5,07	0,0022	0,0035	0,0070	0,0104	<0,00010
<x>	*0,0842*	*1,55*	*0,0073*	*0,0112*	*5,13*	*0,0026*	*0,0036*	*0,0070*	*0,0103*	*<0,00010*

Meas.	B	Ba	Be	Bi	Ca	Cd	Ce	Co	Ga	Hg
	%	%	%	%	%	%	%	%	%	%
	Conc.	Conc.	Conc.	Conc.	Conc.	Conc.	Conc.	Conc.	Conc.	Conc.
1	0,0018	<0,00010	0,0049	0,0021	0,00026	<0,00010	<0,0015	<0,00050	0,0129	<0,00100
2	0,0017	<0,00010	0,0047	0,0019	0,00026	<0,00010	<0,0015	<0,00050	0,0122	<0,00100
3	0,0020	<0,00010	0,0046	0,0024	0,00036	<0,00010	<0,0015	<0,00050	0,0120	<0,00100
<x>	*0,0019*	*<0,00010*	*0,0047*	*0,0021*	*0,00029*	*<0,00010*	*<0,0015*	*<0,00050*	*0,0124*	*<0,00100*

Meas.	In	La	Li	Na	P	Pb	Sn	Sr	V	Zr
	%	%	%	%	%	%	%	%	%	%
	Conc.	Conc.	Conc.	Conc.	Conc.	Conc.	Conc.	Conc.	Conc.	Conc.
1	<0,00030	<0,00030	<0,00010	0,00041	<0,00100	<0,00050	<0,00100	<0,00010	0,0068	<0,00030
2	<0,00030	<0,00030	<0,00010	0,00034	<0,00100	<0,00050	<0,00100	<0,00010	0,0066	<0,00030
3	<0,00030	<0,00030	<0,00010	0,00048	<0,00100	<0,00050	<0,00100	<0,00010	0,0071	<0,00030
<x>	*<0,00030*	*<0,00030*	*<0,00010*	*0,00041*	*<0,00100*	*<0,00050*	*<0,00100*	*<0,00010*	*0,0068*	*<0,00030*

SPECTRO

AMETEK
MATERIALS ANALYSIS DIVISION

Sample Result Name	Type	Measure Date Time	Recalculation Date Time	Origin	Method Name	Method Version	Operator Name	Correction Type	Type Corr Sample Name
2_Castaduct_42_aVacuo	Unknown	03-05-2022 11:30:50	03-05-2022 11:32:03	Measured	Al-01-F			None	

Check Type	Check Status	Grade Verification Name	Grade Verification Similarity	Grade Search Name	Grade Search Similarity
None	Not Used		0 %		0 %

Nome amostra	Referencia	Cliente							
2_Castaduct_42_aVacuo									

Elements **Conc.**

Meas.	Si	Fe	Cu	Mn	Mg	Cr	Ni	Zn	Ti	Ag
	%	%	%	%	%	%	%	%	%	%
	Conc.	Conc.	Conc.	Conc.	Conc.	Conc.	Conc.	Conc.	Conc.	Conc.
1	0,0899	1,51	0,0077	0,0112	5,58	0,0027	0,0040	0,0084	0,0103	<0,00010
2	0,0818	1,60	0,0069	0,0111	5,10	0,0022	0,0037	0,0069	0,0103	<0,00010
3	0,0832	1,50	0,0062	0,0110	4,90	0,0022	0,0031	0,0065	0,0105	<0,00010
<x>	*0,0850*	*1,57*	*0,0069*	*0,0111*	*5,19*	*0,0023*	*0,0036*	*0,0073*	*0,0104*	*<0,00010*

Meas.	B	Ba	Be	Bi	Ca	Cd	Ce	Co	Ga	Hg
	%	%	%	%	%	%	%	%	%	%
	Conc.	Conc.	Conc.	Conc.	Conc.	Conc.	Conc.	Conc.	Conc.	Conc.
1	0,0017	<0,00010	0,0050	0,0014	0,00021	<0,00010	<0,0015	<0,00050	0,0132	<0,00100
2	0,0017	<0,00010	0,0047	0,0018	<0,00010	<0,00010	<0,0015	<0,00050	0,0121	0,0012
3	0,0018	<0,00010	0,0045	0,0024	0,00013	<0,00010	<0,0015	<0,00050	0,0114	<0,00100
<x>	*0,0017*	*<0,00010*	*0,0047*	*0,0019*	*0,00015*	*<0,00010*	*<0,0015*	*<0,00050*	*0,0122*	*0,0011*

Meas.	In	La	Li	Na	P	Pb	Sn	Sr	V	Zr
	%	%	%	%	%	%	%	%	%	%
	Conc.	Conc.	Conc.	Conc.	Conc.	Conc.	Conc.	Conc.	Conc.	Conc.
1	<0,00030	<0,00030	<0,00010	0,00044	<0,00100	<0,00050	<0,00100	<0,00010	0,0064	<0,00030
2	<0,00030	<0,00030	<0,00010	0,00028	<0,00100	<0,00050	<0,00100	<0,00010	0,0065	<0,00030
3	<0,00030	<0,00030	<0,00010	0,00044	<0,00100	<0,00050	<0,00100	<0,00010	0,0073	<0,00030
<x>	*<0,00030*	*<0,00030*	*<0,00010*	*0,00038*	*<0,00100*	*<0,00050*	*<0,00100*	*<0,00010*	*0,0067*	*<0,00030*

SPECTRO

AMETEK
MATERIALS ANALYSIS DIVISION

Sample Result Name	Type	Measure Date Time	Recalculation Date Time	Origin	Method Name	Method Version	Operator Name	Correction Type	Type Corr Sample Name
3_Casteaduct_42_s vacuo	Unknown	03-05-2022 11:47:22	03-05-2022 11:50:06	Measured	Al-01-P			None	

Check Type	Check Status	Grade Verification Name	Grade Verification Similarity	Grade Search Name	Grade Search Similarity
None	NotUsed		0 %		0 %

Nome amostra	Referencia	Cliente							
3_Casteaduct_42_s vacuo									

Elements Conc.

Meas.	Si	Fe	Cu	Mn	Mg	Cr	Ni	Zn	Ti	Ag
	%	%	%	%	%	%	%	%	%	%
	Conc.	Conc.	Conc.	Conc.	Conc.	Conc.	Conc.	Conc.	Conc.	Conc.
1	0,0909	1,46	0,0066	0,0107	4,61	0,0020	0,0028	0,0049	0,0121	<0,00010
2	0,0934	1,51	0,0070	0,0117	4,58	0,0023	0,0031	0,0052	0,0123	<0,00010
3	0,0948	1,46	0,0070	0,0107	4,52	0,0020	0,0031	0,0052	0,0125	<0,00010
<x>	*0,0930*	*1,47*	*0,0069*	*0,0110*	*4,57*	*0,0021*	*0,0030*	*0,0054*	*0,0123*	*<0,00010*

Meas.	B	Ba	Be	Bi	Ca	Cd	Ce	Co	Ga	Hg
	%	%	%	%	%	%	%	%	%	%
	Conc.	Conc.	Conc.	Conc.	Conc.	Conc.	Conc.	Conc.	Conc.	Conc.
1	0,0017	<0,00010	0,0044	0,0019	0,00089	<0,00010	<0,0015	<0,00050	0,0113	<0,00100
2	0,0019	<0,00010	0,0045	0,0020	0,00040	<0,00010	<0,0015	<0,00050	0,0116	<0,00100
3	0,0019	<0,00010	0,0044	0,0019	0,00033	<0,00010	<0,0015	<0,00050	0,0116	0,0011
<x>	*0,0018*	*<0,00010*	*0,0045*	*0,0019*	*0,00054*	*<0,00010*	*<0,0015*	*<0,00050*	*0,0115*	*0,0010*

Meas.	In	La	Li	Na	P	Pb	Sn	Sr	V	Zr
	%	%	%	%	%	%	%	%	%	%
	Conc.	Conc.	Conc.	Conc.	Conc.	Conc.	Conc.	Conc.	Conc.	Conc.
1	<0,00030	<0,00030	<0,00010	0,00055	<0,00100	<0,00050	<0,00100	<0,00010	0,0070	<0,00030
2	<0,00030	<0,00030	<0,00010	0,00070	<0,00100	<0,00050	<0,00100	<0,00010	0,0073	<0,00030
3	<0,00030	<0,00030	<0,00010	0,00052	<0,00100	<0,00050	<0,00100	<0,00010	0,0073	<0,00030
<x>	*<0,00030*	*<0,00030*	*<0,00010*	*0,00062*	*<0,00100*	*<0,00050*	*<0,00100*	*<0,00010*	*0,0072*	*<0,00030*

SPECTRO

AMETEK
MATERIALS ANALYSIS DIVISION

Sample Result Name	Type	Measure Date Time	Recalculation Date Time	Origin	Method Name	Method Version	Operator Name	Correction Type	Type Corr Sample Name
4_casteaduct_42_cf _vacuo	Unknown	03-05-2022 11:54:18	03-05-2022 12:01:15	Measured	Al-01-P			None	

Check Type	Check Status	Grade Verification Name	Grade Verification Similarity	Grade Search Name	Grade Search Similarity
None	NotUsed		0 %		0 %

Nome amostra	Referencia	Cliente							
4_casteaduct_42_cf _vacuo									

Elements Conc.

Meas.	Si	Fe	Cu	Mn	Mg	Cr	Ni	Zn	Ti	Ag
	%	%	%	%	%	%	%	%	%	%
	Conc.	Conc.	Conc.	Conc.	Conc.	Conc.	Conc.	Conc.	Conc.	Conc.
1	0,114	1,58	0,0075	0,0116	5,07	0,0023	0,0040	0,0072	0,0099	<0,00010
2	0,104	1,58	0,0071	0,0114	4,56	0,0021	0,0038	0,0068	0,0104	<0,00010
3	0,109	1,61	0,0079	0,0113	5,01	0,0023	0,0038	0,0073	0,0112	<0,00010
<x>	*0,109*	*1,59*	*0,0075*	*0,0114*	*4,88*	*0,0022*	*0,0039*	*0,0071*	*0,0105*	*<0,00010*

Meas.	B	Ba	Be	Bi	Ca	Cd	Ce	Co	Ga	Hg
	%	%	%	%	%	%	%	%	%	%
	Conc.	Conc.	Conc.	Conc.	Conc.	Conc.	Conc.	Conc.	Conc.	Conc.
1	0,0020	<0,00010	0,0049	0,0023	0,00021	<0,00010	<0,0015	<0,00050	0,0133	<0,00100
2	0,0019	<0,00010	0,0048	0,0025	0,00011	<0,00010	<0,0015	<0,00050	0,0127	<0,00100
3	0,0019	<0,00010	0,0050	0,0019	0,00021	<0,00010	<0,0015	<0,00050	0,0131	<0,00100
<x>	*0,0019*	*<0,00010*	*0,0049*	*0,0023*	*0,00017*	*<0,00010*	*<0,0015*	*<0,00050*	*0,0130*	*<0,00100*

Meas.	In	La	Li	Na	P	Pb	Sn	Sr	V	Zr
	%	%	%	%	%	%	%	%	%	%
	Conc.	Conc.	Conc.	Conc.	Conc.	Conc.	Conc.	Conc.	Conc.	Conc.
1	<0,00030	<0,00030	<0,00010	0,00079	<0,00100	<0,00050	<0,00100	<0,00010	0,0070	<0,00030
2	<0,00030	<0,00030	<0,00010	0,00055	<0,00100	0,0024	<0,00100	<0,00010	0,0070	<0,00030
3	<0,00030	<0,00030	<0,00010	0,00048	<0,00100	<0,00050	<0,00100	<0,00010	0,0070	<0,00030
<x>	*<0,00030*	*<0,00030*	*<0,00010*	*0,00061*	*<0,00100*	*0,0011*	*<0,00100*	*<0,00010*	*0,0070*	*<0,00030*

Sample Result Name	Type	Measure Date Time	Recalculation Date Time	Origin	Method Name	Method Version	Operator Name	Correction Type	Type Corr Sample Name
5_castarduct_42 _vivacuo	Unknown	03-05-2022 12:04:56	03-05-2022 12:17:39	Measured	Al-01-F			None	

Check Type	Check Status	Grade Verification Name	Grade Verification Similarity	Grade Search Name	Grade Search Similarity
None	Not Used		0 %		0 %

Nome amostra	Referencia	Cliente							
5_castarduct_42 _vivacuo									

Elements **Conc.**

Meas.	Si	Fe	Cu	Mn	Mg	Cr	Ni	Zn	Ti	Ag
	%	%	%	%	%	%	%	%	%	%
	Conc.	Conc.	Conc.	Conc.	Conc.	Conc.	Conc.	Conc.	Conc.	Conc.
1	0,125	1,57	0,0079	0,0110	4,91	0,0021	0,0037	0,0072	0,0083	<0,00010
2	0,124	1,47	0,0075	0,0111	4,74	0,0022	0,0035	0,0078	0,0107	<0,00010
3	0,113	1,49	0,0074	0,0114	4,66	0,0025	0,0036	0,0073	0,0077	<0,00010
4	0,104	1,57	0,0090	0,0113	4,85	0,0028	0,0037	0,0072	0,0100	<0,00010
<x>	*0,116*	*1,52*	*0,0079*	*0,0112*	*4,79*	*0,0024*	*0,0036*	*0,0074*	*0,0092*	*<0,00010*

Meas.	B	Ba	Be	Bi	Ca	Cd	Ce	Co	Ga	Hg
	%	%	%	%	%	%	%	%	%	%
	Conc.	Conc.	Conc.	Conc.	Conc.	Conc.	Conc.	Conc.	Conc.	Conc.
1	0,0018	<0,00010	0,0047	0,0022	0,00038	<0,00010	<0,0015	<0,00050	0,0130	0,0011
2	0,0020	<0,00010	0,0046	0,0027	0,00041	<0,00010	<0,0015	<0,00050	0,0123	<0,00100
3	0,0020	<0,00010	0,0046	0,0033	0,00021	<0,00010	<0,0015	<0,00050	0,0119	<0,00100
4	0,0017	<0,00010	0,0046	0,0017	0,00052	<0,00010	<0,0015	<0,00050	0,0123	<0,00100
<x>	*0,0019*	*<0,00010*	*0,0046*	*0,0025*	*0,00039*	*<0,00010*	*<0,0015*	*<0,00050*	*0,0124*	*0,0010*

Meas.	In	La	Li	Na	P	Pb	Sn	Sr	V	Zr
	%	%	%	%	%	%	%	%	%	%
	Conc.	Conc.	Conc.	Conc.	Conc.	Conc.	Conc.	Conc.	Conc.	Conc.
1	<0,00030	<0,00030	<0,00010	0,00075	<0,00100	<0,00050	<0,00100	<0,00010	0,0065	<0,00030
2	<0,00030	<0,00030	<0,00010	0,00071	<0,00100	0,0021	<0,00100	<0,00010	0,0074	<0,00030

Sample Result Name	Type	Measure Date Time	Recalculation Date Time	Origin	Method Name	Method Version	Operator Name	Correction Type	Type Corr Sample Name
6_castarduct_42 _vivacuo	Unknown	03-05-2022 12:21:05	03-05-2022 12:22:22	Measured	Al-01-F			None	

Check Type	Check Status	Grade Verification Name	Grade Verification Similarity	Grade Search Name	Grade Search Similarity
None	Not Used		0 %		0 %

Nome amostra	Referencia	Cliente							
6_castarduct_42 _vivacuo									

Elements **Conc.**

Meas.	Si	Fe	Cu	Mn	Mg	Cr	Ni	Zn	Ti	Ag
	%	%	%	%	%	%	%	%	%	%
	Conc.	Conc.	Conc.	Conc.	Conc.	Conc.	Conc.	Conc.	Conc.	Conc.
1	0,117	1,48	0,0072	0,0110	4,66	0,0022	0,0038	0,0080	0,0098	<0,00010
2	0,147	1,55	0,0078	0,0114	5,06	0,0023	0,0043	0,0092	0,0069	<0,00010
3	0,128	1,56	0,0074	0,0113	4,78	0,0022	0,0038	0,0080	0,0068	<0,00010
<x>	*0,131*	*1,53*	*0,0075*	*0,0112*	*4,83*	*0,0022*	*0,0040*	*0,0084*	*0,0078*	*<0,00010*

Meas.	B	Ba	Be	Bi	Ca	Cd	Ce	Co	Ga	Hg
	%	%	%	%	%	%	%	%	%	%
	Conc.	Conc.	Conc.	Conc.	Conc.	Conc.	Conc.	Conc.	Conc.	Conc.
1	0,0019	<0,00010	0,0049	0,0024	0,00017	<0,00010	<0,0015	<0,00050	0,0129	<0,00100
2	0,0020	<0,00010	0,0054	0,0030	0,00015	<0,00010	<0,0015	<0,00050	0,0145	<0,00100
3	0,0019	<0,00010	0,0051	0,0033	0,00012	<0,00010	<0,0015	<0,00050	0,0134	<0,00100
<x>	*0,0019*	*<0,00010*	*0,0051*	*0,0029*	*0,00015*	*<0,00010*	*<0,0015*	*<0,00050*	*0,0136*	*<0,00100*

Meas.	In	La	Li	Na	P	Pb	Sn	Sr	V	Zr
	%	%	%	%	%	%	%	%	%	%
	Conc.	Conc.	Conc.	Conc.	Conc.	Conc.	Conc.	Conc.	Conc.	Conc.
1	<0,00030	<0,00030	<0,00010	0,00054	<0,00100	0,0032	<0,00100	<0,00010	0,0072	<0,00030
2	<0,00030	<0,00030	<0,00010	0,00065	<0,00100	0,0042	<0,00100	<0,00010	0,0071	<0,00030
3	<0,00030	<0,00030	<0,00010	0,00045	<0,00100	0,0050	<0,00100	<0,00010	0,0071	<0,00030
<x>	*<0,00030*	*<0,00030*	*<0,00010*	*0,00054*	*<0,00100*	*0,0041*	*<0,00100*	*<0,00010*	*0,0071*	*<0,00030*

Appendix F: Porosity graphs for non-heat treated AlSi10Mg(Fe) alloy parts

HPDC

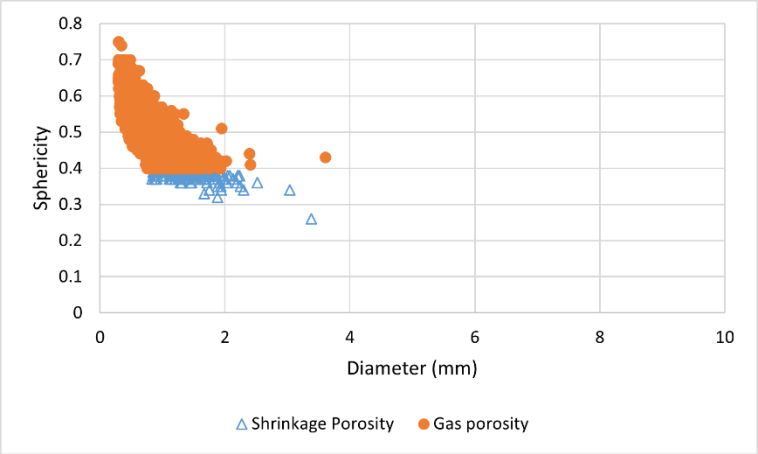

Figure 119: Sphericity and diameter of the porosities present in the part no.1.

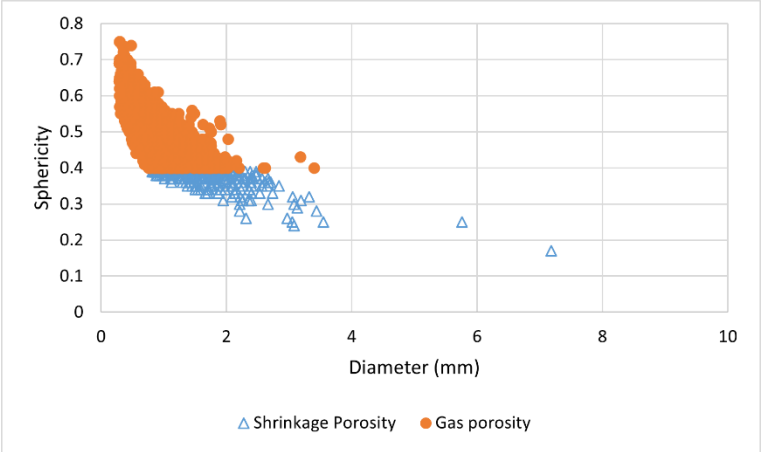

Figure 120: Sphericity and diameter of the porosities present in the part no.2.

VADC

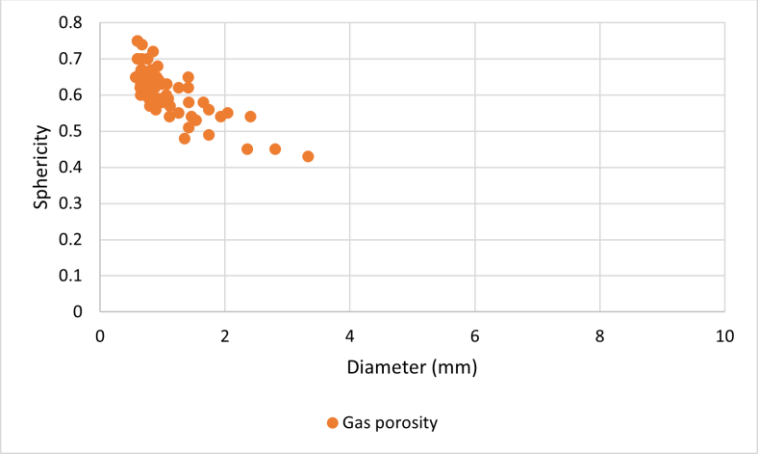

Figure 121: Sphericity and diameter of the porosities present in the part no.1.

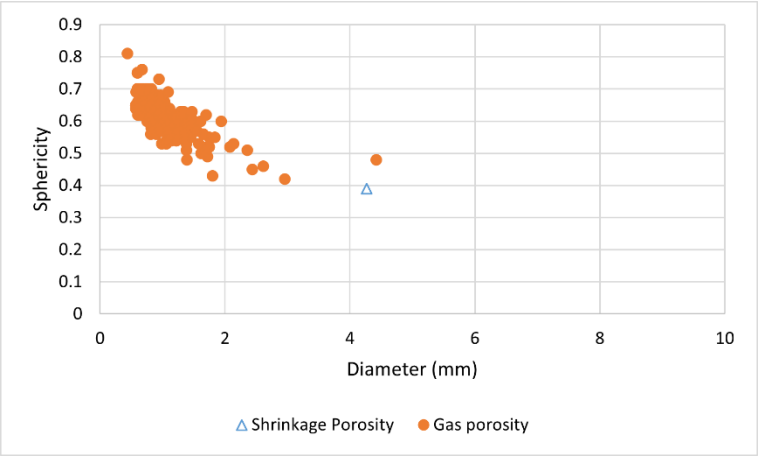

Figure 122: Sphericity and diameter of the porosities present in the part no.3.

Appendix G: Porosity graphs for non-heat treated AlSi10MnMg alloy parts

HPDC

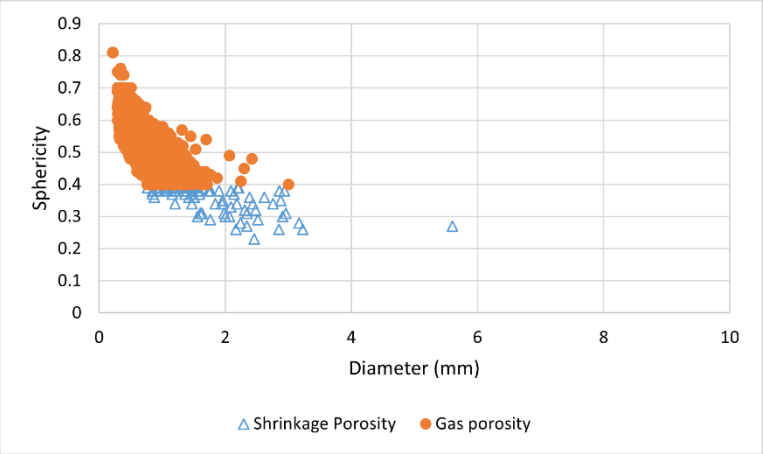

Figure 123: Sphericity and diameter of the porosities present in the part no.2.

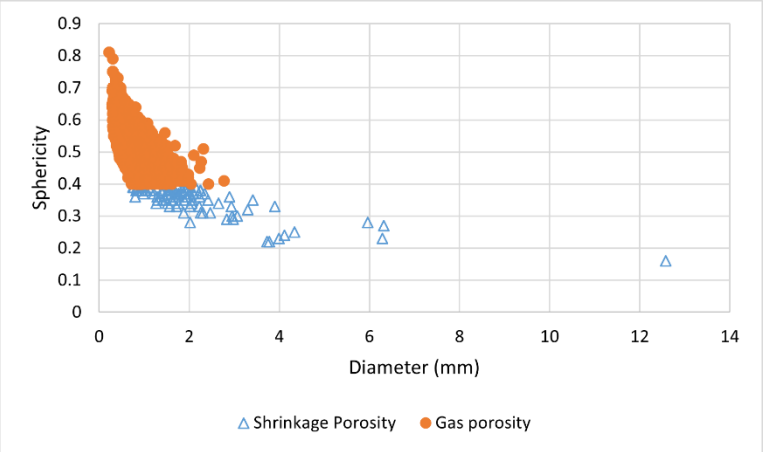

Figure 124: Sphericity and diameter of the porosities present in the part no.3.

VADC

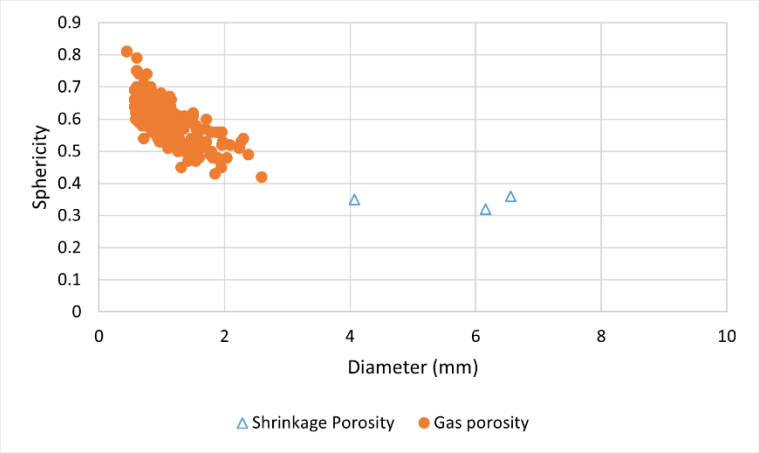

Figure 125: Sphericity and diameter of the porosities present in the part no.1.

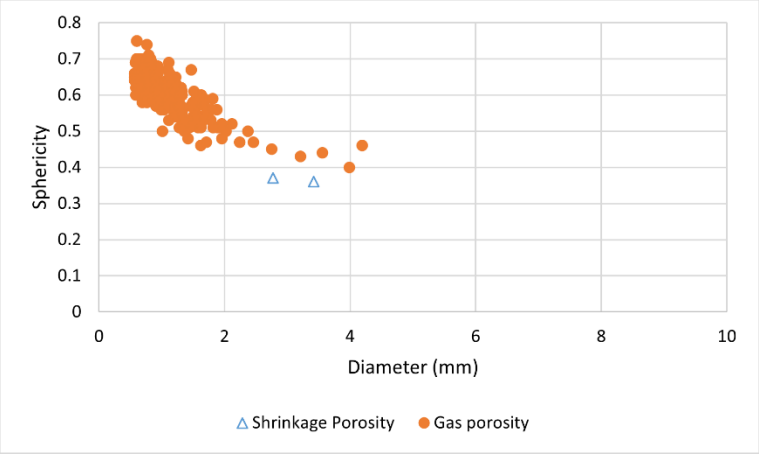

Figure 126: Sphericity and diameter of the porosities present in the part no.2.

Appendix H: Porosity graphs for heat treated AlSi10Mg(Fe) alloy parts

HPDC

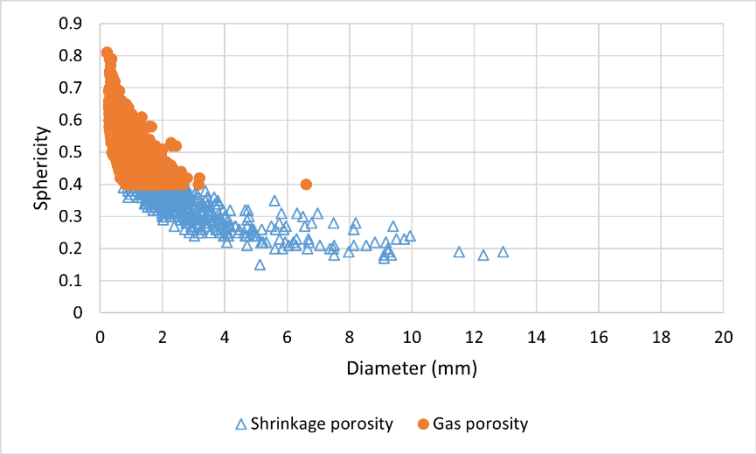

Figure 127: Sphericity and diameter of the porosities present in the part no.1.

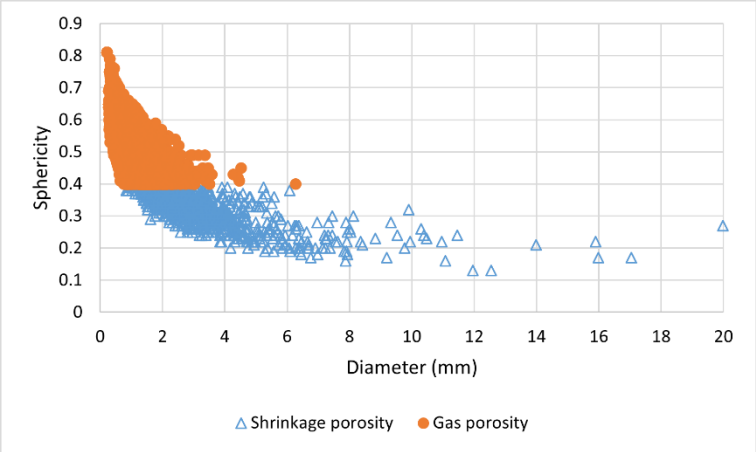

Figure 128: Sphericity and diameter of the porosities present in the part no.2.

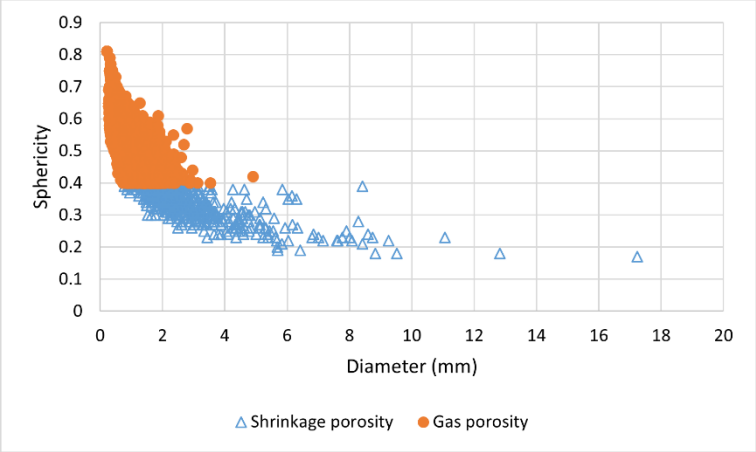

Figure 129: Sphericity and diameter of the porosities present in the part no.3.

VADC

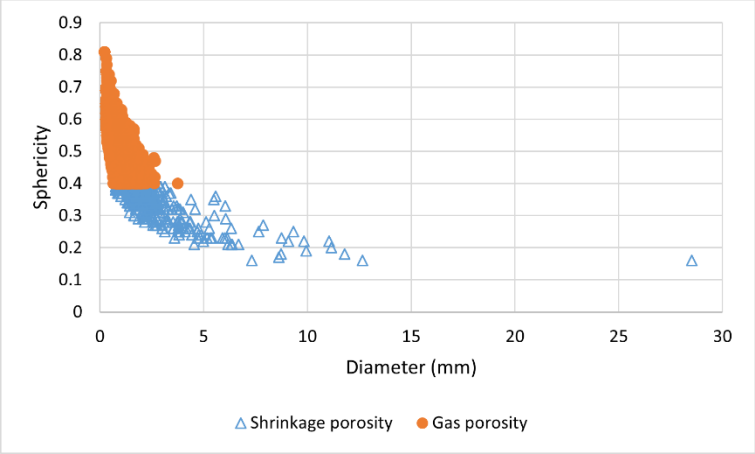

Figure 130: Sphericity and diameter of the porosities present in the part no.1.

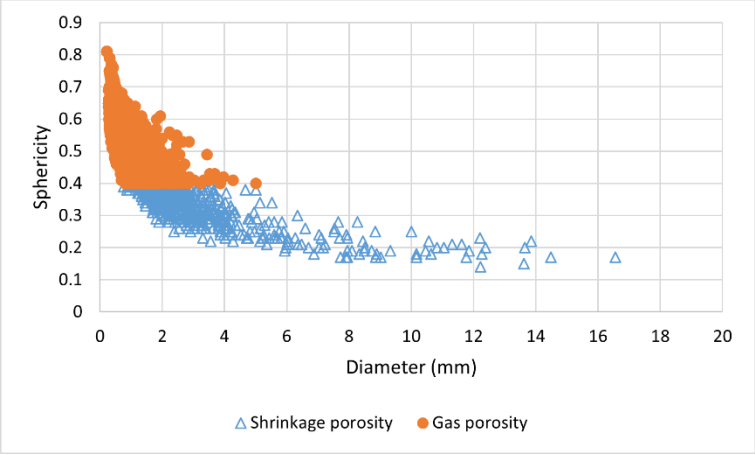

Figure 131: Sphericity and diameter of the porosities present in the part no.2.

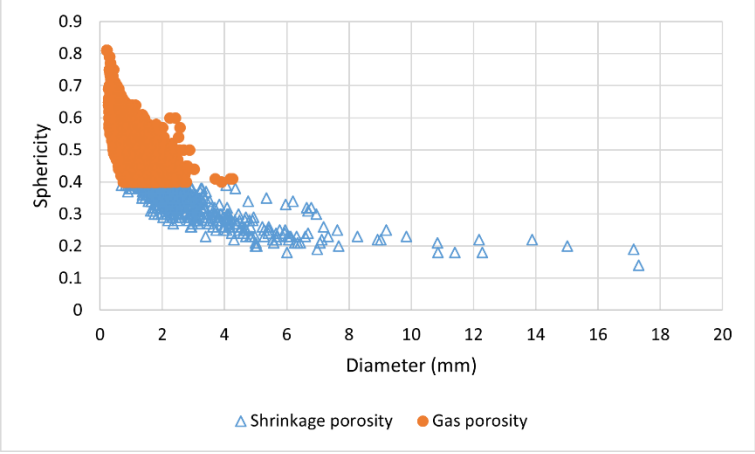

Figure 132: Sphericity and diameter of the porosities present in the part no.3.

Appendix I: Blistering in heat treated AlSi10Mg(Fe) alloy parts

Figure 133: Blistering on vacuum injected part no.2.

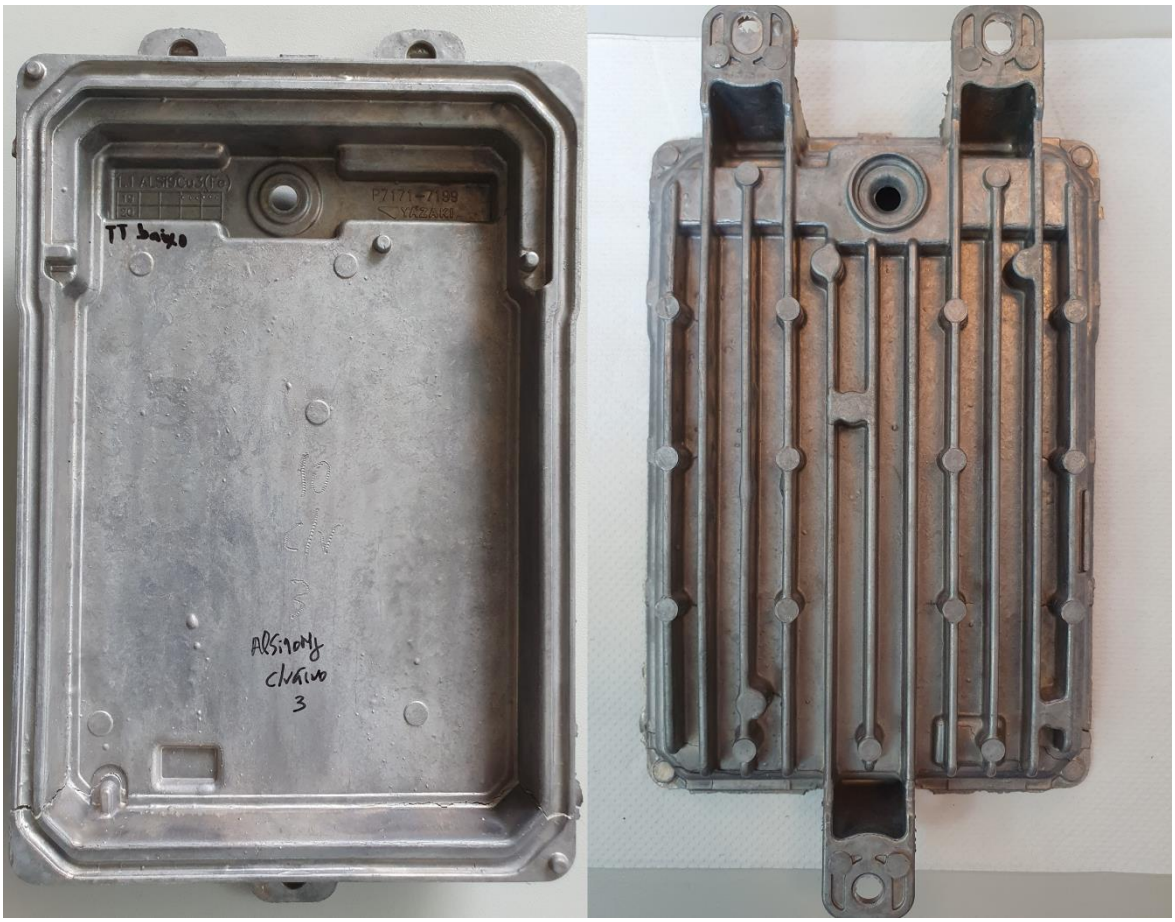

Figure 134: Blistering on vacuum injected part no.3.

Figure 135: Blistering on conventionally injected part no.1.

Figure 136: Blistering on conventionally injected part no.3.

Appendix J: Blistering in heat treated AlSi10MnMg alloy parts

Figure 137: Blistering on vacuum injected part no.2.

Figure 138: Blistering on vacuum injected part no.3.

Figure 139: Blistering on conventionally injected part no.2.

Figure 140: Blistering on conventionally injected part no.3.